STUDIA

UNIVERSITATIS BABEŞ-BOLYAI

Chemia

CLUJ-NAPOCA 1999

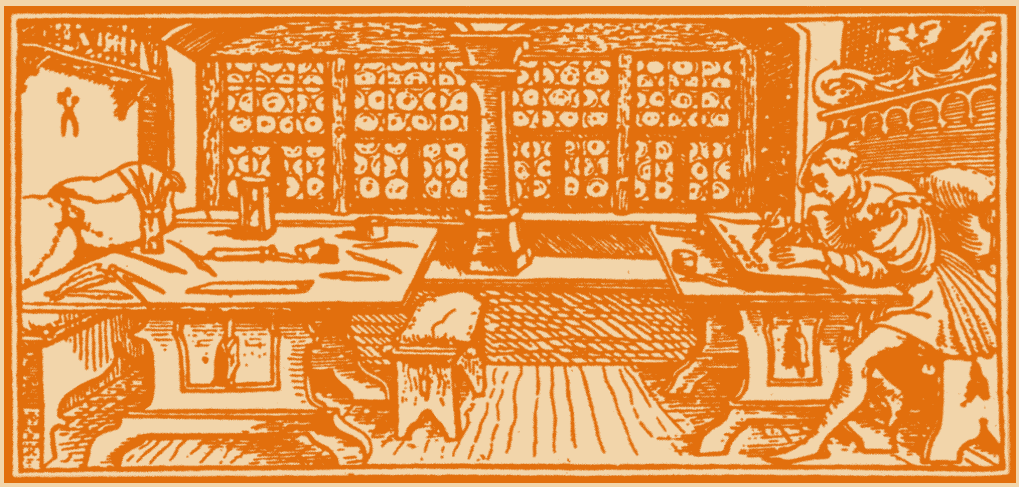

1-2

Anul XLIV **1999**

STUDIA
UNIVERSITATIS BABEŞ - BOLYAI

CHEMIA

1-2

Editorial Office: 3400 Cluj - Napoca, Gh. Bilaşcu str. no. 24 ♦ Phone: 064-405352

SUMAR - SOMMAIRE - CONTENTS - INHALT

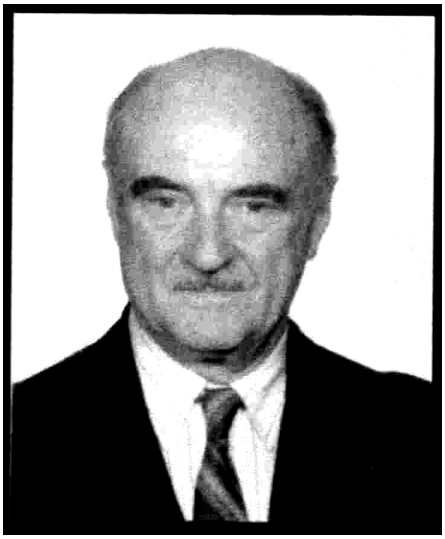

IN MEMORIAM
Prof. Dr. doc. Liviu ONICIU

On November 27, 1999, the distinguished Professor Liviu Oniciu, founder of the School of Electrochemistry in Cluj, passed away peacefully, at the age of 72. An outstanding scientific personality and author of a large and authentic scientific creation, with national and international recognition, Prof. Oniociu had a significant contribution to the development of the Physical Chemistry in our country.

Prof. Liciu Oniciu was born, on 11th of February 1927 in Cluj. In 1946 he finished his high school education in Cluj, at the University Pedagogical Seminar and became a student in Chemistry at the Faculty of Science of "Victor Babe¿" University in Cluj. He gr aduated in 1950 and in September 1950 he was appointed assistant at the Chair of Physical Chemistry. In 1961 he was promoted lecturer and obtained the Ph. D. with a thesis on aluminum complexes with organic hydroxy acids, under the supervision of Prof. Ioan Cadariu. In 1965 he obtained the position of associated professor and in 1970 became full professor. In 1971 he abtained the title of docent in science and in 1984 the Ministry of Education offered him the Award of Excellence in Teaching. He contributed much to the modernisation and development of chemical education in our university wich abnegation and strenght, being famous by his interesting and attracting courses, very much appreciated by his students, as well as by his involvement. Being an excellent organizer and a born leader, he was elected several times as Dean of the Faculty of Chemistry (between 1968-1976 and 1984-1987) as well as the Head of the Department of Physical Chemistry (between 1976-1984 and 1990-1996). He was a member of Faculty Council for 32 years and a member of the University Senate for 24 years.

In 1997 he retired at the age of 70, but continued to work as a consulting Professor, until the last days of his life. Professor Oniciu was a member of the International Society of Electrochemistry and the representative for Romanian of this Society, a member of the American Society of Electrochemistry and a member in the Council of European Academy os Surface Technology.

He founded and coordinated the Cluj-section of the Institute of Chemical and Biochemical Energetics, being his Director during 10 years. Since 1990 he functioned as Director of the Research Centre in Electrochemistry at "Babe¿-Bolyai" University, until he passed away.

As a Ph. D advisor since 1969, he supervised more than 40 doctoral students and promoted 35 of them to the award of Ph. D in Physical Chemistry. Two of them were guided together with professors from Brussels and Paris.

During his prodigious teaching and scientific career, Prof. Oniciu published 6 books, two of them abroad. He also published 8 monographs, one of them being translated abroad. He was the author of more than 220 scientific papers, published in Romanian of international journals and he succeeded in obtaining 19 patents.

In 1980 the Romanian Academy of Science awarded him with "Nicolae Teclu" prise for the book "Electrochemical Conversion of Energy", published by the Scientific and Encyclopedic Publishing House in Bucharest.

The scientific activity of Professor Oniciu started with the physico-chemical sutdies of the complexes of aluminium with various hydroxy acids, but he became famous by his papers in the field of electrochemistry. He approached the electrochemical conversion of energy, being the first in this field in our country. He was concerned with the anodic oxidation of methanol on various electrocatalysts in order to develop an indirect fuel cell. Then, he further investigation the fuel cells hydrazine/hydrogen peroxide, hydrogen/ oxygen and the alcaline batteries nickel - iron and nickel - cadmium as well as the sodium - sulfur battery and lithium anode batteries.

Since 1981, with the organization of the Institute of Chemical and Biochemical Energetics, he diversified his research directions, by including new areas of applied electrochemistry as organic electrosynthesis, electrodeposition of metals, and photoelectroctrochemical conversion of energy. His contributions to the field were theoretical and experimental ones. He directed the research concerning the electrosynthesis of adiponitrile from acrylonytrile, the electrosynthesis of propionitrile and the electrowinning various metals as lead, zinc and manganese from different raw solid materials, aiming at the elucidation of fundamental aspects concerning them.

By his entire activity as teacher and scientist and by his priseworthy results in both fields, Prof. Liviu Oniciu became prominent among the great personalities of our University, working here faithfully, for more than 49 years. With his passing away the teaching-staff of our faculty and the Romanian scientific community lost a great personality and a man of great heart.

May he rest in peace!

STUDIA UNIVERSITATIS BABEŞ-BOLYAI, CHEMIA, XLIV, 1-2, 1999

ABOUT THE POSSIBLE SHAPES OF THE EXPERIMENTAL VOLTAMMOGRAMS OBTAINED BY APPLYING THE VOLTAMMETRY WITH LINEAR SCANNING OF THE POTENTIAL TO REDOX UNIELECTRODES

N. BONCIOCAT

National Institute for Electrochemistry and Condensed Matter, Electrochemical Research Center, Spl. Independenței 202, 77208 Bucharest

ABSTRACT. In this paper, a theoretical analysis of the shapes that the experimental voltammograms obtained by applying the direct linear voltammetry to redox unielectrodes may have, has been carried out. The analysis is based on a recently deduced ordinary differential equation describing, by its solutions, the experimental voltammograms. From this analysis has resulted that in the case of quasireversible redox reactions, although at an unielectrode occurs only one redox reaction $0 + e \leftrightarrow R$, the experimental voltammogram may present, excepting the normal peak (cathodic, or anodic), two additional peaks, one before, the second after, the normal one; such voltammograms may appear only if some restrictive conditions regarding the values of the symmetry factor β and of the ratio $r=(D_O/D_R)^{1/2}(c_O/c_R)$ are fulfilled. Thus, the appearance of a succeeding peak after the normal one doesn't mean that at interface occurs a second electrode reaction, or that the electrode redox reaction occurs in two steps, and in order to give a correct answer one must change the quasireversible kinetic behaviour of the electrode reaction in a reversible kinetic behaviour, by adequately changing the values of c_O, c_R (and thus of r), respective of the scanning rate v.

INTRODUCTION

In a series of recent papers [1-6] it has been shown that the faradaic current density $i_F(t)$ of an electrode redox reaction $0 + e \leftrightarrow R$, occurring with combined overtension of charge transfer and nonstationary, linear, semiinfinite diffusion of the species 0, R is the solution of the following integral equation of Volterra type:

$$i_F(t) = \lambda \frac{i^0 N^*(t)}{\pi^{1/2}} \int_0^t \frac{i_F(u)}{(t-u)^{1/2}} du + f(t) \qquad (1)$$

where:

$$N^{*}(t)=\frac{\exp\left[-\beta f\eta(t)\right]}{F\sqrt{D_O}a_O}+\frac{\exp\left[(1-\beta)f\eta(t)\right]}{F\sqrt{D_R}a_R} \tag{1'}$$

$$f(t)=i^0\left(\exp\left[-\beta f\eta(t)\right]-\exp\left[(1-\beta)f\eta(t)\right]\right) \tag{1''}$$

$$\left(\lambda=-1;\quad f=F/RT\right) \tag{1'''}$$

$\eta(t)$ represents the overtension at the moment of time t, and the other quantities have the usual meanings: β - symmetry factor, i^0 - exchange current density, D_O, D_R - diffusion coefficients, a_O, a_R - activities.

Further, eq. (1) has been applied to the voltammetry with linear scanning of the potential, when, considering the cathodic voltammetry, $N^{*}(t)$ and f(t) may be put in the forms:

$$N^{*}(t)=\bar{N}\left[1/r+\exp\left(-f|v|t\right)\right]\exp\left(\beta f|v|t\right) \tag{2}$$

$$f(t)=i^0\left[1-\exp\left(-f|v|t\right)\right]\exp\left(\beta f|v|t\right) \tag{2'}$$

where:

$$\bar{N}=1/F\sqrt{D_R}a_R;\quad r=\sqrt{\frac{D_O}{D_R}}\cdot\frac{a_O}{a_R} \tag{2''}$$

and |v| is the magnitude of the scanning rate. An important conclusion has come out, namely: although a rigorous description of the experimental voltammograms is given only by the solutions of the integral eq. (1), one may get a sufficient accurate description by solving the following ordinary differential equation of the first order [7]:

$$\frac{1}{S(i^0\bar{N})^2}\left\{\frac{dI(t)}{dt}-\left[\beta+\frac{\exp\left(-f|v|t\right)}{1-\exp\left(-f|v|t\right)}\right]f|v|I(t)\right\}=\left\{1+2\left[\beta-\frac{\exp\left(-f|v|t\right)}{1/r+\exp\left(-f|v|t\right)}\right]f|v|t\right\}$$
$$\left[\exp\left(2\beta f|v|t\right)\right]\left[1/r+\exp\left(-f|v|t\right)\right]\cdot\left\{\left[1/r+\exp\left(-f|v|t\right)\right]\frac{I(t)}{S}-\frac{1-\exp\left(-f|v|t\right)}{\pi^{1/2}\bar{N}t^{1/2}}\right\} \tag{3}$$

where S is the electrode area and I the current intensity as measured in the external circuit (i.e., one supposes that the capacity current may be neglected). In a succeeding paper [8], it has been shown that the solutions of eq. (3) are, abstraction of some constant factors in perfect agreement with- the prediction given in the literature (but using totally different mathematical approach and, also, numerical methods). More, on the basis of eq. (3) it was possible to elaborate new direct-voltammetry methods for determining the diffusion coefficients D_O, D_R (or the concentrations c_O, c_R) [9, 10], the standard

exchange current densities i^{00} [11] and the symmetry factors β [12] of the electrode redox reactions, as well as for studying the high temperature superconductor/redox electrolyte interface [13, 14].

The above mentioned applications of the differential eq. (3), successfully verified experimentally, prove that the solutions of eq. (3) give correctly the explicit dependencies of the current intensity on all other quantities and, consequently, eq. (3) may be used to discuss the possible shapes of the experimental voltammograms obtained by applying the direct voltammetry technique to the redox unielectrodes. In the following, we shall discuss the general case of quasireversible electrode redox reactions, when i^0 has a finite value.

IN WHAT CONDITIONS THE FIRST MEMBER OF THE DIFFRENTIAL EQUATION (3) CANCELS?

From eq. (3) one sees that its second member is the product of four factors, the second and the third being always different of zero. It follows that the first member of eq. (3) may cancel, either when:

$$1+2\left[\beta-\frac{\exp\left(-f|\eta|\right)}{1/r+\exp\left(-f|\eta|\right)}\right]f|\eta|=0 \tag{4}$$

or:

$$I\left(|\eta|\right)=\frac{1-\exp\left(-f|\eta|\right)}{|\eta|^{1/2}\left[1+r\exp\left(-f|\eta|\right)\right]}\cdot\frac{SF\sqrt{D_O|v|}a_O}{\pi^{1/2}} \tag{5}$$

where we have introduced the magnitude of the cathodic overtension $|\eta|=|v|t$.

Let's start with equation (4). It shows that the relation between r and $|\eta|$, for which eq. (4) holds true, depends on the value of the symmetry factor β, which plays the role of a parameter. Indeed, eq. (4) may be written:

$$r\left(|\eta|;\beta\right)=e^{f|\eta|}\frac{\beta+1/2\,f|\eta|}{1-\beta-1/2\,f|\eta|} \tag{4'}$$

and some values of the function $r(|\eta|;\beta)$ are given in table 1.

Table 1.

Examples of values r(|η|; β) for which, eq. (4) being satisfied, the first member of eq. (3) cancels

$10^2\|\eta\|$ (V)	$10^{-2}r(\|\eta\|;\beta)$						
	β=0.0	β=0.2	β=0.4	β=0.5	β=0.6	β=0.8	β=1.0
1.00	<0	<0	<0	<0	<0	<0	<0
1.25	∞	"	"	"	"	"	"
1.60	.076	∞	"	"	"	"	"
2.00	.038	.109	"	"	"	"	"
2.10	.034	.093	∞	"	"	"	"
2.50	.027	.064	.245	∞	"	"	"
2.60	.026	.060	.206	1.390	"	"	"
2.70	.026	.060	.197	.810	"	"	"
2.80	.025	.057	.174	.525	"	"	"
2.90	.024	.054	.156	.424	"	"	"
3.00	.024	.054	.152	.357	"	"	"
3.10	.023	.052	.138	.328	∞	"	"
3.50	.023	.052	.128	.240	.975	"	"
4.00	.022	.052	.122	.214	.495	"	"
4.50	.024	.057	.128	.217	.442	"	"
5.00	.024	.063	.137	.222	.422	"	"
6.00	.029	.078	.172	.268	.470	"	"
6.30	.031	.083	.187	.187	.497	∞	"
7.00	.036	.101	.226	.236	.583	8.060	"
8.00	.047	.138	.312	.468	.775	5.860	"
10.00	.074	.257	.465	.912	1.480	7.270	"
12.00	.135	.522	1.215	1.850	2.820	10.090	"
14.00	.268	1.100	2.600	3.900	6.000	24.000	"
16.00	.521	2.340	5.550	8.340	12.700	44.200	"
18.00	.937	4.946	11.600	17.800	27.200	93.000	"
20.00	1.900	10.500	22.600	39.000	57.800	180.000	"
30.00	65.000	510.000	1170.000	1790.000	2900.000	8550.000	"

Suppose β=0.5. Then, the values given in table 1 show that for r(|η|; β=0.05)>21.40 there are two values of |η| satisfying eq. (4). For instance, if r=47, the first value is about $|\eta_1|$=0.0285 V and the second one about $|\eta_2|$=0.08 V. For r very great, $|\eta_1|$ tends to 0.025 V and $|\eta_2|$ to infinity, while for $r=r_m$=21.40 (the minimum permitted value) the values of the two

overtensions become equal to $|\eta_1|=|\eta_2|=0.04$ V. The values in the other five columns must be interpreted in the same manner. One must not forget that eq. (3) refers to the cathodic voltammograms. For the anodic voltammograms it has been shown that suffice to change in eq. (3) β in 1-β, r in 1/r, and to write |I(t)| and d|I(t)|/dt instead of I(t) and dI(t)/dt (because in our convention the anodic current is negative) [7]. Of course, the same changes must be made in condition (4) and table 1, for becoming valid for the anodic voltammograms, but, for sake of simplicity, we don't give these transcriptions. However, the principal conclusions that may be drawn from the table 1 (and its transcription) concern the inequalities that the value r(β) must satisfy in order to exist (for the values β given in the table) pairs of overtensions ($|\eta_1|$, $|\eta_2|$) satisfying eq. (4) (and its transcription), and they are given in table 2.

Table 2.

Domains of r(β) values for which eq. (4), respective its anodic transcription, have solutions (i.e., each equation a pair of values $|\eta|$ satisfying it).

β	Domains of r(β) values	
	Cathodic voltammograms	Anodic voltammograms
0.0	r>2.22	-
0.2	r>5.15	r<1/586.00
0.4	r>12.20	r<1/42.20
0.5	r>22.17	r<1/22.17
0.6	r>42.20	r<1/12.20
0.8	r>586.00	r<1/5.15
1.0	-	r<1/2.22
By "-" one indicates that there is no such a domain		

As one sees, if, for a given β, the necessary condition holds true for the cathodic voltammograms, it doesn't hold for the anodic voltammograms, and inversely. As we shall see in the next paragraph, this conclusion is very important from the point of view of the possible shapes of the voltammograms.

Let's pass now to eq. (5) which gives an other situation when the *second* member of eq. (3) cancels and, consequently, the *first* member of eq. (3) cancels too. Let's observe that for reversible electrode reactions, when $i^0 \rightarrow \infty$, the first member of eq. (3) is equal to zero, *whatever the value* $|\eta|$ *would be*. But this means that also the second member of eq. (3) must be equal to zero, *whatever* $|\eta|$ *would be*, condition that is fulfilled only if eq. (5) holds true. In other words, eq. (5) describes the experimental voltammograms when the electrode redox reactions $0 + e \leftrightarrow R$ have a reversible kinetic behaviour [7]. It thus results that it is possible to exist also

other overtensions for which the first member of eq. (3) cancels, namely that corresponding to certain intersection points of the *real experimental* voltammogram with the *theoretic* voltammogram described by eq. (5) (valid for reversible electrode reactions). Denoting by $|\eta_3|$ the magnitude of such an overtension, it must be less than $|\eta_P|$ (corresponding to the cathodic peak current on the real voltammogram, I_P), because the first member of eq. (3) may cancel only if both I and dI/dt are positive; generally, such an overtension, either doesn't exist, or there is only one.

Concerning the values $|\eta_1|$, $|\eta_2|$, as we have seen, they may be equal (if $r=r_m$), when, generally, $|\eta_1|=|\eta_2|<|\eta_P|$, but for sufficient great values of the ratio r/r_m, $|\eta_1|$ is less than $|\eta_P|$, while $|\eta_2|>|\eta_P|$ (because $|\eta_1|$ gets smaller, and $|\eta_2|$ tends to infinity, when $r/r_m\to\infty$).

POSSIBLE SHAPES OF THE EXPERIMENTAL VOLTAMMOGRAMS IN THE CASE OF QUASIREVERSIBLE ELECTRODE REDOX REACTIONS

Let's analyse the sign of the first member of eq. (3). It is easy to observe that for very small values of t, the great bracket in the first member of eq. (3) tends to the function dI(t)/dt-I(t)/t, whose sign depends on the shape of the curve I vs t very close to t=0. In our recent papers [11, 12] the experimental cathodic voltammograms, obtained by applying the voltammetry with linear scanning of the potential to the redox unielectrodes $Pt/[Fe(CN)_6]^{3-}$, $[Fe(CN)_6]^{4-}$, KCl(1M), using for r the values 10, 20 and 100, had a convex shape (i.e., a negative second derivative) immediately after t=0, followed (after a change of concavity) by a linear increase of I with t and, afterwards, by a nonlinear increase of I towards the peak value I_P. This is the type of voltammograms which we are interested in, because, as we shall see, they may have an unusual shape.

In the first interval, where I(t) is convex, the derivative dI(t)/dt is smaller than I(t)/t and, therefore, the difference dI(t)/dt-I(t)/t being negative, so is also the first member of eq. (3). In the interval, where I increases linearly with t, it has been shown [11] that the great bracket of the first member of eq. (3) gets the expression:

$$\left[\frac{1}{1-\exp\left(-fvt_0\right)}-\beta\right]f|v|I_0$$

where $I_0=I(t_0)$, t_0 being a time within this interval. It is obvious that this expression is positive, and thus the first member of eq. (3) passes from a negative sign to a positive one, existing an intermediate time τ_1, in-between the two intervals, when the first member of eq. (3) cancels. Of course,

because both dI/dt and I must be positive, the point $P_1(\tau_1, I(\tau_1))$ must be before the point where begins the linear increase of I with t, but where I already increases with t. It follows that before the point $P_1(\tau_1, I(\tau_1))$, the curve I(t) presents, if not a veritable "hump" (i.e., local maximum, followed by a local minimum), at least a "shoulder". Of course, the overtension corresponding to the time τ_1 is that denoted in the preceding paragraph by η_1, and its magnitude $|\eta_1|=|v|\tau_1$ satisfies eq. (4). But, in the same paragraph it has been shown that, if eq. (4) (which refers to cathodic voltammograms) has solutions for a given voltammogram (i.e., given r and β), then it has two solutions, η_1 and η_2, satisfying the inequalities $|\eta_1|<|\eta_P|<|\eta_2|$.

On such a voltammogram there is a second point $P_2(\tau_2,I(\tau_2))$; $|\eta_2|=|v|\tau_2$ situated on an other increasing part of the voltammogram (because of the necessary conditions dI/dt>0, I>0). Consequently, it results that the curve I vs t decreases after the cathodic peak up to a moment $\tau<\tau_2$, and afterwards it starts to increase again. Of course, the voltammetry being made without stirring the solution, the thickness of the diffusion layer increases in time and, the electrode reaction getting more and more a reversible kinetic behaviour, the curve I vs t approaches more and more the curve described by eq. (5). Therefore, there is a time $t>\tau_2$ when the curve I vs. t passes through an other local maximum and afterwards it decreases monotonously towards I=0 (for $t \to \infty$).

Of course, similar conclusions apply to anodic voltammograms, for which the role of eq. (4) is played by the equation:

$$1+2\left[1-\beta-\frac{\exp\left(-f|\eta|\right)}{r+\exp\left(-f|\eta|\right)}\right]f|\eta| = 0 \qquad (6)$$

representing the transcription of eq. (4) by making the changes $\beta \to 1-\beta$; $r \to 1/r$. Therefore, if eq. (6) has solutions for a given anodic voltammogram, then, in fact it has two solutions satisfying the inequalities $\eta_1<\eta_P<\eta_2$, and on the curve I vs. t appears a "hump", or at least a "shoulder", followed by the anodic peak and afterwards, by a local maximum which precedes the monotonously decrease of I towards I=0 (for $t \to \infty$). The important difference consists in the fact that, now, the values r(β) must be smaller than certain upper limits (given in table 2) and, consequently there are three possibilities: both voltammograms have usual shapes (i.e., only with a cathodic, (respective anodic), peak), the cathodic voltammogram has an unusual shape (when the anodic one is normal), respective inversely, the shape of the cathodic voltammogram is normal (when the anodic one has an unusual shape).

The two unusual possibilities concerning the shapes of the experimental voltammograms in the case of quasireversible electrode redox reactions are shown in fig. 1, considering that in the vicinity of the first

solution (i.e., overtension) of eq. (4) (respective of its anodic transcription) appears a “shoulder”, while in that of the second solution appears a local minimum followed by a local maximum.

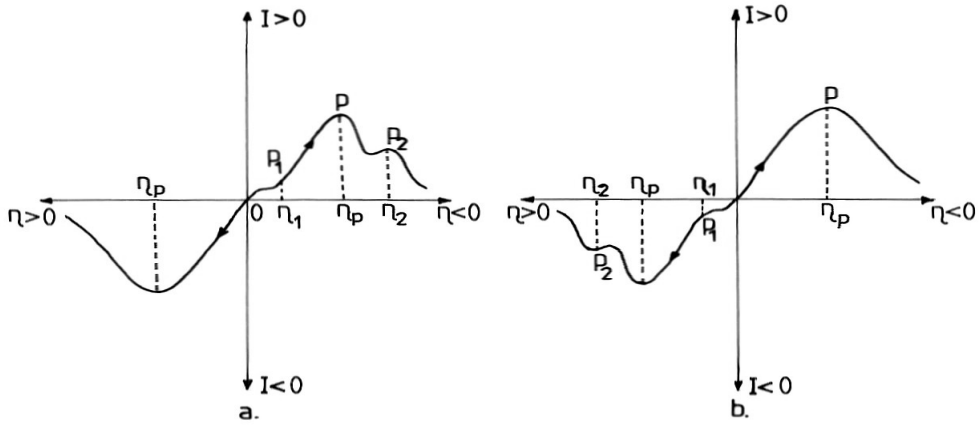

Figure 1. Unusual shapes that the experimental voltammograms may have, although at the interface takes place only one electrode redox reaction (which, of course, must have a quasireversible kinetic behaviour); a. if the shape of the cathodic voltammogram is unusual, then, that of the anodic one is normal; b. if the shape of the anodic voltammogram is unusual, then, that of the cathodic one is normal. The arrows indicate that the voltammograms must be obtained separately.

CONCLUDING REMARKS

The theoretical developments made in this paper demonstrate that in the case of quasireversible electrode redox reactions the voltammetry with linear scanning of the potential, either in a cathodic, or in an anodic, sense, may led to experimental voltammograms which present, excepting the usual cathodic (or anodic) peak (i.e., that corresponding to an overtension of magnitude $|\eta_P|$), a preceding peak, or at least a “shoulder”, for $|\eta_1|<|\eta_P|$, and a succeeding peak for $|\eta_2|>|\eta_P|$, although at the interface occurs only one redox reaction, which, in addition, takes place in a single step (e.g., $O + e \leftrightarrow R$). Of course, such unusual shapes of the experimental voltammograms may appear only if some restrictive conditions regarding the values of the symmetry factor β and of the ratio $r=(D_O/D_R)^{1/2}(a_O/a_R)$ are fulfilled (given in table 2).

Therefore, an important conclusion comes out from the theoretical analysis made in this paper: if on an experimental voltammogram obtained by direct voltammetry appears a succeeding peak after the normal one, it

doesn't mean that at interface occurs a second electrode reaction, or that the electrode redox reaction occurs in two steps; it is possible that the shape of the voltammogram to be the consequence of the quasireversible kinetic behaviour of the redox reaction and of the values of β and r. To give an answer, a possibility would be the changing of the values $|v|$, c_O, c_R (making them smaller) and of the value r (to be sure that the conditions given in table 2 don't hold). In this way, the kinetic behaviour of the electrode reaction approaches that of a reversible electrode reaction, and on the experimental voltammogram must appear only the normal cathodic (or anodic) peak.

Finally, such unusual voltammograms, obtained by direct voltammetry, may have electroanalytical applications, for instance in estimating the value of r from the values $|\eta_1|$, or $|\eta_2|$, where appear the additional peaks.

REFERENCES

1. N. Bonciocat, S. Borca and St. Moldovan, *Bulg. Acad. Sci., Comun. Dept. Chem*., 1990, 23, 289-301
2. N. Bonciocat, *Electrokhimiya*, 1993, 29, 97-102
3. N. Bonciocat, *Electrochimie şi aplicaţii*, Ed. Dacia Europa-Nova, Timişoara, 1996, p. 262-267
4. Adina Cotârță, *Ph. D. Thesis*, Chemical Researches Institute, Bucharest, 1992
5. N. Bonciocat and A. Cotârță, *Rev. Roum. Chim*., 1998, 43, 925-933
6. N. Bonciocat and A. Cotârță, *Rev. Roum. Chim*., 1998, 43, 1027-1035
7. N. Bonciocat, E. Papadopol, S. Borca and I. O. Marian, *Rev. Roum. Chim*., 1999, accepted for publication
8. N. Bonciocat, E. Papadopol, S. Borca and I.O. Marian, *Rev. Roum. Chim*., 1999, accepted for publication
9. N. Bonciocat, E. Papadopol, S. Borca and I.O. Marian, *Rev. Roum. Chim*., 1999, accepted for publication
10. I. O. Marian, R. Săndulescu and N. Bonciocat, *Journal of pharmaceutical and Biochemical Analysis*, 2000, accepted for publication
11. N. Bonciocat, E. Papadopol, S. Borca and I.O. Marian, submitted to *Rev. Roum. Chim*., 1999
12. N. Bonciocat, E. Papadopol, S. Borca and I.O. Marian, submitted to *Rev. Roum. Chim.*, 2000
13. I. O. Marian, E. Papadopol, S. Borca and N. Bonciocat, *Studia Universitatis Babeş-Bolyai. Chemia*, 1998, 43, 57-62
14. I. O. Marian, *Ph. D. Thesis*, "Babeş-Bolyai" University, Cluj-Napoca, 1999

STUDIA UNIVERSITATIS BABEŞ-BOLYAI, CHEMIA, XLIV, 1-2, 1999

SYSTEM NON-LINEARITY COMPENSATION BY MEANS OF NON-LINEAR ELECTROCHEMICAL IMPEDANCE SPECTROSCOPY

ADRIAN NICOARA and LIVIU ONICIU

"Babes-Bolyai" University, Faculty of Chemistry and Chemical Engineering, Department of Physical Chemistry, 11 Arany Janos, 3400 Cluj-Napoca, Romania

ABSTRACT. Generally, for the evaluation of thermodynamic and kinetic parameters of an electrochemical system, an impedance spectroscopy method uses perturbation of small amplitude, in order to assures a linear behavior of the investigated process. When the experiment is strongly influenced by noise, a simple possibility to improve measurement quality is to increase the perturbation amplitude. Unfortunately, this easy way to increase the signal to noise ratio can generate non-linearity distortion impeding on the result quality. In this paper, a new procedure for non-linearity correction using different harmonics parameters was proposed and tested for a reversible electrochemical system.

INTRODUCTION

The investigation of an electrochemical system by dynamic methods can be performed using perturbation of large or small amplitude. The methods using large amplitude perturbation, steps or sweeps of potential or current, generally drive the electrode far from equilibrium where its response is usually a transient signal. The other approach consists in the use of a small amplitude step or, in the case discussed below, a sinusoidal perturbation, which brings the system in steady-state [1].

The main advantages of small amplitude methods are as follows:

- The experimental opportunity of carrying out high precision measurements, primary due to the steady-state regime, which allows the noise minimizing by mediation of successive measurements;
- Simpler mathematical treatment of electrode kinetics and mass transport due to low amplitude perturbation, typically under 5 mV applied voltage, when system response is linear;
- Easier separation of each elementary step contribution to the system response, due to experimental possibility to use perturbation within a large range of frequencies, usually between 0.001 and 100,000 Hz;

- The obtained information can be correlated with the imposed d.c. potential, which is an important feature when the investigated parameters are influenced by the applied potential, as is the case for the electrode reaction, double layer capacitance and, sometimes, even for ohmic resistance [2];
- The compensation of non-ideal behavior of the potentiostat and/or others electronic instrumentation included in the measurement network by means of Laplace plane analysis, facilitated by the system linearity [3].

The disadvantages of small amplitude techniques are mainly generated by the low value of the signal perturbation, determining a small amplitude response of the electrochemical system, which is highly susceptibility to be influenced by noise. Consequently, a sophisticated and expensive instrumentation becomes necessary.

Special alternatives of the electrochemical impedance spectroscopy were proposed to exploit the electrochemical system non-linearity in order to obtain information about its behavior. The most important are: rectification, second order techniques, intermodulation, demodulation and superior order harmonic analysis [1, 4].

Faradaic rectification uses the asymmetry between anodic and cathodic behavior of the electrochemical system in current controlled conditions, causing a modification of the continuous potential component and allowing the straightforward obtaining of the charge transfer coefficient, parameter otherwise difficult to obtain. Second order techniques examine the sinusoidal response signal, generated by systems asymmetry, and having the frequency twice higher as the perturbing one. The appearance of the second harmonic and the rectification component is illustrated by the following equation:

$$\sin(\omega t)^2 = \frac{1-\cos(2\omega t)}{2} \tag{1}$$

with the mention that, for a controlled potential technique, due to the electrochemical system particularity, in the resulting current intensity equation a quadrate of the perturbation term will appear.

Intermodulation techniques use a perturbation obtained by addition of two sinusoidal signals, with different pulsation, ω_M and ω_m. The system response is processed in order to obtain information about different pulsation signals, $\omega_M+\omega_m$ or $\omega_M-\omega_m$, their appearance being illustrated by the trigonometric equality:

$$\sin(\omega_M t)^2 - \sin(\omega_m t)^2 = \sin((\omega_M + \omega_m)t)\sin((\omega_M - \omega_m)t) \tag{2}$$

Demodulation techniques use also a perturbation containing two sinusoidal signals, with high and low pulsation values, and due to the non-

linear behavior of the electrochemical system, the response signal will contain only the low pulsation component [5].

An other non-classical impedance spectroscopy method involves non-stationary impedance concept [6], where the components of the response signal change in time, demanding sophisticated equipment and mathematical processing, as for ex. the rotational Fourier transform [7].

The above mentioned impedance spectroscopy methods are used especially for kinetic measurements in electrocatalysis, corrosion, electrosorption, and also for analytical purposes [8]. The main disadvantage of these techniques consists of sophisticated, and therefore even expensive, instrumentation because in addition to the that necessary for linear impedance measurements, supplementary, a transfer function analyzer and high performance narrow band analogical filters are requested for each investigated harmonic.

Nevertheless, the presence of the non-linear distortion is not always desired for the electrochemical system investigation. A usual possibility to avoid it is the use of low amplitude-perturbing signal (lower than 5 mV/n, where n is the number of electrons involved in the electrochemical process). Unfortunately, a low amplitude value of perturbing signal is somehow in contradiction with the requirement of a large signal to noise ratio. Therefore, instead of improving the measurement quality due to amelioration of the system linearity, a too low perturbation will have a contrary effect because the response will be dominated by noise, basically a random signal.

The aim of the present paper is to find an algorithm to compensate the effect of non-linearity distortion on the system response components, in order to calculate those values as in the case of linear behavior, but using a much larger amplitude perturbation.

Non-linearity induced distortion

A steady-state theoretical voltammogram for a reversible electrochemical system is presented in figure 1, illustrating the influence of the d.c. component of the applied potential, E_{cc}, on the time dependence of the current intensity, when a sinusoidal perturbation is imposed. More important, is suggesting the influence of applied d.c. component on the occurred distortion for symmetrical transport condition (equal limiting currents). It can be seen that, for a d.c. potential closed to the half wave potential ($E_{1/2}$), due to the linearity of the electrochemical system, a slight distortion can be evidenced, containing just odd harmonics. At a different d.c. potential value, the response signal is highly distorted, containing both odd and paired harmonic frequencies.

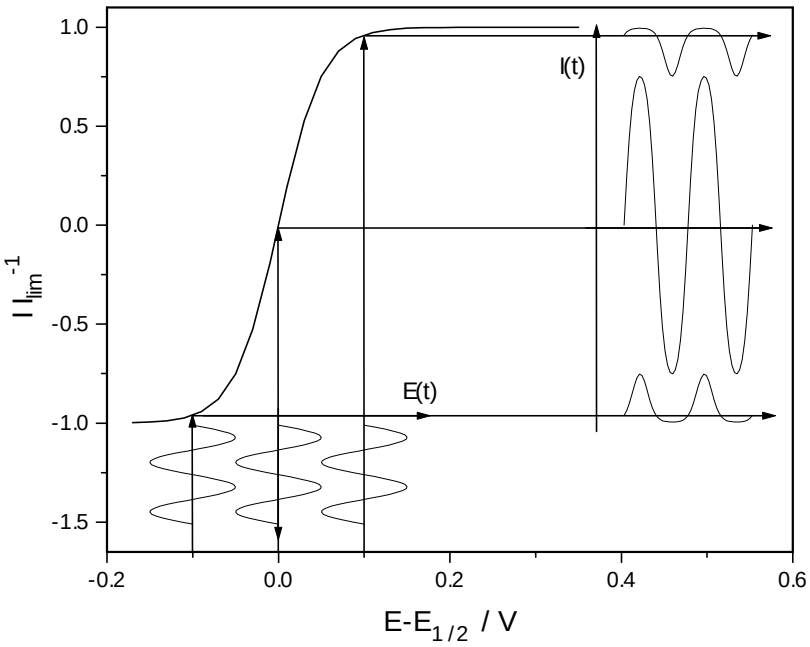

Figure 1. Dependence of the ratio between current intensity and its limiting value on the d.c. component of the applied signal.

Two types of sinusoidal signal distortion can be revealed. If the transfer function of the electrochemical system is linear the output signal is undistorted, containing therefore just the fundamental (first) harmonic frequency. Unlike this situation, if the transfer function in the investigated domain is non-linear, only paired harmonics will be generated. In addition, if the transfer function is asymmetric the odd harmonics will be present, modifying the d.c. current component.

The linearity of an electrochemical system is established if, in potential controlled conditions, for any arbitrary potential, E, the equality:

$$I(E+\Delta E) = I(E) + I(\Delta E) \tag{3}$$

is verified for any potential perturbation, ΔE. In similar situation, the symmetry condition is:

$$I(E+\Delta E) = -I(\Delta E - E) \tag{4}$$

As revealed by figure 1, the linearity condition is difficult to be fulfilled, unless the small amplitude perturbation is applied, whereas the symmetry condition is even harder to be respected, unless d.c. potential near half-wave potential and low perturbation are used.

So, if a large enough sinusoidal perturbation is used, the harmonics measurement can provide an alternative method for obtaining information about thermodynamic and, especially, kinetic parameters of the electrochemical system, using a suitable mathematical model. Unfortunately, an other important effect of the non-linear behavior of the electrochemical system is the alteration of the information carried by the fundamental harmonic, both impedance absolute value and delay being affected.

Harmonic parameter evaluation

Considering that the electrochemical system is perturbed in potential controlled conditions, when the time dependence of the potential is given by:

$$E(t) = E_{cc} + \Delta E \sin(\omega t) \quad (5)$$

where E_{cc} is the d.c. component and ΔE the amplitude of perturbing potential signal, and ω is the pulsation. The resulting current intensity is given by:

$$I(t) = I_{cc} + \Delta I_{ca1} \sin(\omega t + \phi_1) \quad (6)$$

for low amplitude perturbation, or:

$$I(t) = I_{cc} + \Delta I_{ca1} \sin(\omega t + \phi_1) + \Delta I_{ca2} \sin(2\omega t + \phi_2) + ... + \Delta I_{can} \sin(n\omega t + \phi_n) \quad (7)$$

if the perturbation is large enough to consider the electrochemical system outside the linearity domain. In above-mentioned equations, I_{cc} is the d.c. and $\Delta I_{ca\,n}$ the amplitude of n-th harmonic components of the current intensity, ϕ_1 is the phase of the first harmonic current intensity referenced to potential phase and $\Delta\phi_n=\phi_n-\phi_1$ is the delay between the n-th and the first harmonics components of current intensity.

For the determination of various harmonics parameters two approaches can be considered: analogical signal processing, i.e. using several phase lock amplifiers in order to obtain the component of given phase and frequency [9]; digital processing, when a data array representing the current and potential values are used for evaluation of the impedance parameters. The increasing use of the later solution is caused by flexibility, accuracy and, not at least, to lower prices of that solution caused especially by the huge progress of personal computers industry. Digital treatment can be performed in various ways, but more frequent the Fourier transform procedure is used.

The use of the Fourier transform is based on the idea that any periodic signal, like above I(t) function, can by presented as a superposition of sinusoidal signals, with different frequency in arithmetic progression. Using the fundamental frequency, the smallest, adding the harmonic frequencies, both odd and paired, any arbitrary periodic signal can be reconstructed, so information contained by the amplitudes and phases of the different

harmonics can be used for quantitative evaluation [10]. The Fourier transform definition is:

$$F(I(t)) = I(\omega) = \int_0^{\infty} I(t)\exp(-j\omega t)dt \tag{8}$$

where ω is the pulsation of transformed signal, I(ω) and j is the complex operator.

It can be mentioned that non-linear fitting procedures, e.g. Levenberg-Marquardt analysis, or even a multidimensional linear fitting procedures, subsequent to the fitting model's linearization, can be used successfully for the evaluation of various harmonics parameters and the estimation of system's non-linearity.

RESULTS AND DISCUSSIONS

The case of a reversible electrochemical system under potential controlled steady-state conditions will be considered. Therefore, the comparison between the calculated results and the experimental ones must be done just for low frequency measurements. Also will be examined just the case of symmetric mass transport when anodic and cathodic currents have the same limiting values. The simulation of the system behavior was performed using LabVIEW™ graphic programming media due to the important data analysis facilities offered.

In these conditions for the electrode process:

$$O + n\,e^- \leftrightarrow R$$

the equilibrium potential is given by:

$$E(t) = E_{1/2} + \frac{RT}{nF}\ln\left(\frac{1+\dfrac{I(t)}{I_{\lim}}}{1-\dfrac{I(t)}{I_{\lim}}}\right) \tag{9}$$

where: I_{lim} is the limiting current intensity, $E_{1/2}$ is the half-wave potential and R,T and F have theirs usual meanings. From that, the theoretical steady-state transfer function can be derived:

$$\frac{I(t)}{I_{\lim}} = \frac{\exp\left(\dfrac{nF}{RT}\left(E(t)-E_{1/2}\right)\right)-1}{\exp\left(\dfrac{nF}{RT}\left(E(t)-E_{1/2}\right)\right)+1} \tag{10}$$

and was presented in figure 1 for one electron transfer and 25^o C.

Using the non-linear Levenberg-Marquardt fitting procedure, with a multi-sinusoidal regression model, as in equation 7, up to 20 harmonics amplitude and delay can be obtained. This is equivalent with the solve of the next integral equations for the continuous component of the current intensity:

$$I_{CC} = I_{\lim} f_o \int_0^{\frac{1}{fo}} \frac{\exp\left(\frac{nF}{RT}\left(E(t) - E_{1/2}\right)\right) - 1}{\exp\left(\frac{nF}{RT}\left(E(t) - E_{1/2}\right)\right) + 1} dt \quad (11)$$

and for complex harmonic current intensity:

$$I_{can} = I_{\lim} \int_0^{\frac{1}{fo}} \frac{\exp\left(\frac{nF}{RT}\left(E(t) - E_{1/2}\right)\right) - 1}{\exp\left(\frac{nF}{RT}\left(E(t) - E_{1/2}\right)\right) + 1} \exp\left(-j(2\pi f_o n)t\right) dt \quad (12)$$

that allows calculation for each individual harmonic of the amplitude, ΔI_{can}, and the phase, ϕ_n, with:

$$\Delta I_{can} = \sqrt{\mathrm{Re}\left\{I_{can}\right\}^2 + \mathrm{Im}\left\{I_{can}\right\}^2} \quad (13)$$

$$\phi_n = \tan^{-1}\left(\frac{\mathrm{Im}\left\{I_{can}\right\}}{\mathrm{Re}\left\{I_{can}\right\}}\right) \quad (14)$$

The used symbols are: f_o the fundamental frequency, and functions Re and Im denotes the real and imaginary components of the harmonic current intensity.

In figure 2 are presented the influence of the sinusoidal potential amplitude (the values are presented in the legend) on the estimated continuous current component, on the left, and on the absolute value of impedance, on the right. The presented data are simulated in the above-mentioned conditions, considering also that I_{lim}=100 mA. For the numerical integration of equations 11 and 12, an array of 2^{12} = 4096 points in a single period sinusoidal signals was used. In the figures are presented the relative potentials, refered to the half-wave potential, $E_{1/2}$, for a one electron transfer process.

It can be remarked that for low amplitude values, slightly exceeding the linearity limit, the electrochemical system response denotes moderate differences from the linear behavior. Whereas, for large amplitude perturbation the occurred errors can be very important, as in the case of the impedance even impeding on the correct magnitude order determination [11].

These differences, attributed to the harmonic component formation, can be quantified by the harmonic parameter values.

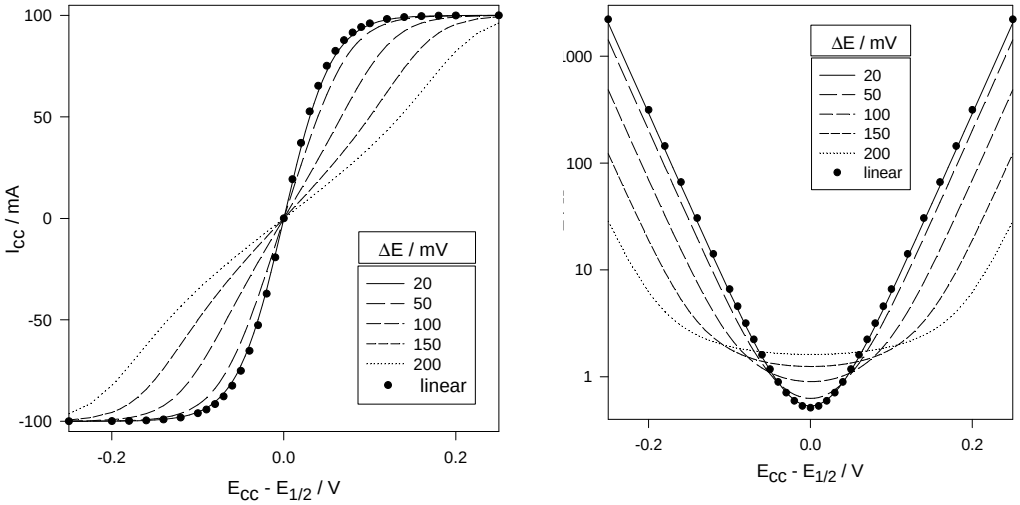

Figure 2. Influence of sinusoidal potential amplitude on the estimated continuous current component (on the left), and on the impedance absolute value (on the right).

For exemplification, in figure 3 are presented the amplitude of odd and paired harmonics for ΔE=0.1 V amplitude perturbation. In order to reveal the sign information, given by the trigonometric function subsequent to the amplitude, in figure 4 are presented the first five harmonics. It should be mentioned that the F function denotes sine for paired and cosine for odd harmonics.

It can be mentioned that amplitudes of a high order harmonic rapidly decline under the measurement limits, that can not exceed four orders of magnitude, especially for continuous component far from half-wave potential. Also, the numbers of the potential where the harmonic amplitude fall to zero, are depending on the harmonic order and could be easily calculated by simple decrementation of the harmonic order.

The amplitude and delay of an arbitrary order current equations, found by means of simulated data analysis, as a function of applied continuous and sinusoidal potential components was previously reported [12].

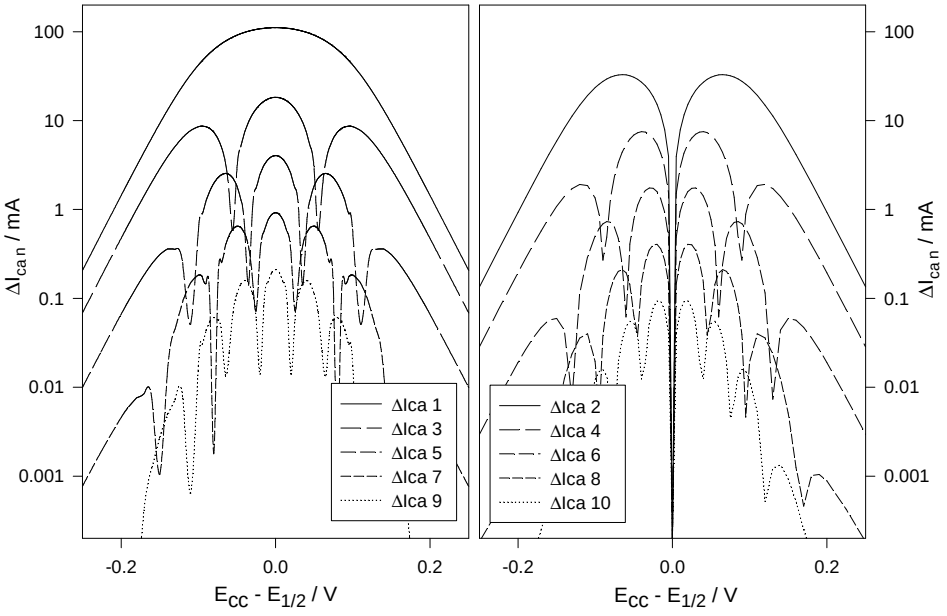

Figure 3. Influence of the applied continuous potential component on the estimated amplitude of sinusoidal current, for odd (on the left), and paired (on the right) harmonics (see the legend.

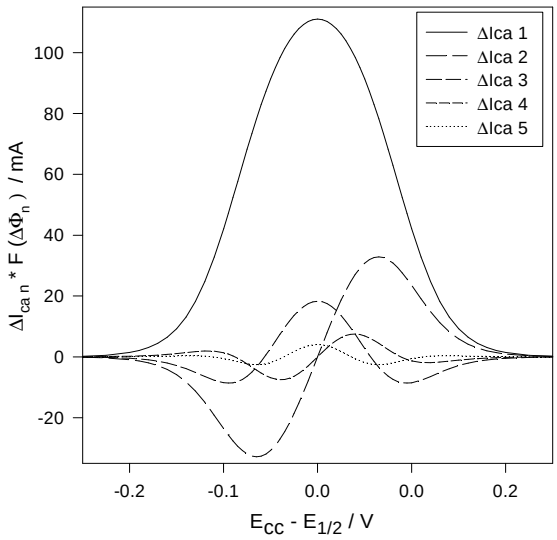

Figure 4. Influence of applied continuous potential component on the estimated amplitude of sinusoidal current harmonics (see the legend).

Inspired by that and using a multidimensional fitting procedure based on “trial and error” principle, the following equations were found, allowing the calculation of the continuous and sinusoidal current intensity components:

$$I_{cc,lin} = I_{cc} + \Delta I_{ca2}\sin(\Delta\phi_2) + \Delta I_{ca4}\sin(\Delta\phi_4) + ... + \Delta I_{ca2n}\sin(\Delta\phi_{2n}) \quad (15)$$

$$\Delta I_{ca1,lin} = \Delta I_{ca1} + 3\Delta I_{ca3}\cos(\Delta\phi_3) + ... + (2n+1)\Delta I_{ca2n+1}\cos(\Delta\phi_{2n+1}) \quad (16)$$

From these equations the absolute value of impedance could be calculated as:

$$Z = \frac{\Delta E}{\Delta I_{ca1,lin}} \quad (17)$$

where “lin” index from subscript of $I_{cc,lin}$ and $\Delta I_{ca1,lin}$ terms, denotes the corrected value, as their determination was performed using a small amplitude perturbation, when the linear behavior condition is fulfilled.

For the validation of equation (15) and (16), relative errors of continuous component and absolute impedance were calculated and presented in figure 5. It must be mentioned that, even if only the first twenty harmonics were used the results for impedance correction are very good, with errors not exceeding 1% in any situation, even for larger amplitude perturbation of 0.2 V. In the absence of the non-linearity correction the errors

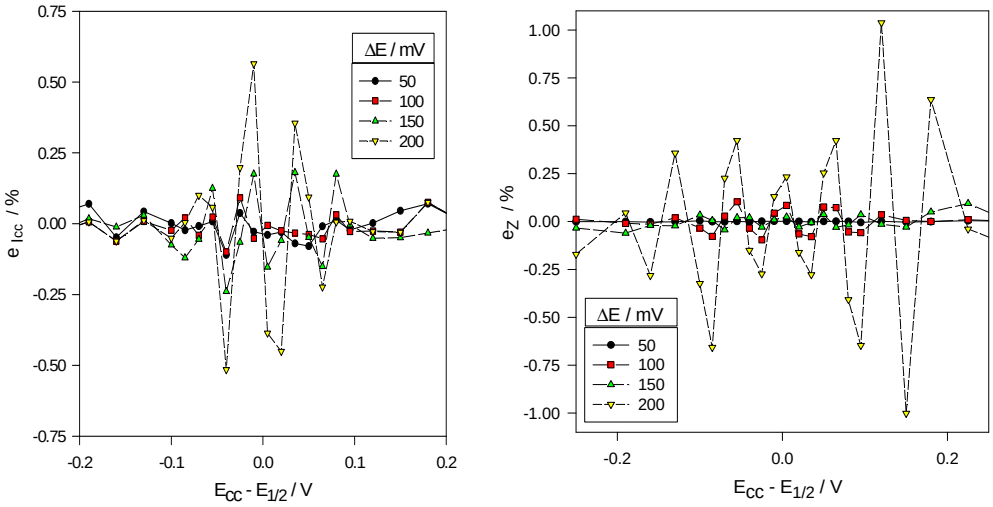

Figure 5. Determined relative error for continuous current component (on the left) and absolute impedance values (on the right) for different values of the applied continuous potential component.

can exceed 6000 %. In the case of continuous component correction the results are even better, partly due to a less important effect of non-linearity on the continuous current component, as revealed by figure 2.

Despite the spectacular results, the practical application of equation (15) and (16) is limited by experimental possibility of obtaining information about the harmonics generated by the system non-linearity. The use of digital instrumentation, based on "Laboratory Virtual Instrumentation" concept launched by National Instruments, and a wide range of data acquisition, processing and analysis functions, seems to be the optimum solution for impedance spectroscopy measurements, especially if the information about the system's non-linearity is required.

REFERENCES

1. M. Sluyters-Rehbach and J. H. Sluyters, in *Electrode Kinetics: Principles and Methodology* (Edited by C. H. Bamford and R. G. Compton), Vol. 26, Elsevier, Amsterdam, 1986.
2. D. D. Macdonald, *Transients Techniques in Electrochemistry*, Plenum Press, New-York, 1977.
3. M. Sluyters-Rehbach and J. H. Sluyters, in *Comprehensive Treatise of Electrochemistry* (Edited by E. Yeager, J. O. M. Bockris, B. E. Conway, and S. Sarangapani), Vol. 9, Plenum Press, New York, 1984.
4. M. Sluyters-Rehbach, *Pure & Appl. Chem.*, 1994, **66**, 1831.
5. C. M. A. Brett and A. M. Oliveira Brett, *Electrochemistry. Principles, Methods, and Applications*, Oxford University Press, Oxford, 1993.
6. B. Savova-Stoynov and Z. B. Stoynov, *Electrochim. Acta*, 1992, **37**, 2353.
7. Z. B. Stoynov, *Electrochim. Acta*, 1992, **37**, 2357.
8. K. Darowicki, *Electrochim. Acta*, 1994, **39**, 2757.
9. C. Gabrielli*, Identification of Electrochemical Processes by Frequency Repose Analysis,* Solartron-Schlumberger, 1981.
10. A. J. Bard and L. R. Faulkner, *Electrochemical Methods. Fundamentals and Applications*, John Wiley and Sons, New-York, 1980.
11. J.-P. Diart, B. Le Gorrec and C. Montella, *Electrochim. Acta*, 1994, **39**, 539.
12. A. Nicoara, S. Dorneanu and L. Oniciu, *Analele Univ. Oradea*, 1997, 29.

STUDIA UNIVERSITATIS BABEŞ-BOLYAI, CHEMIA, XLIV, 1-2, 1999

PARTICULATE BED CATHODE FOR COPPER ION REMOVAL FROM WASTE WATERS
Part I: An optimization study of operational parameters

ANCA MIHAELA MIHAI[1], LIVIU ONICIU[2]

[1] *Department of Chemistry, North University of Baia Mare, 4800, Baia Mare, Romania*
[2] *Department of Physical Chemistry, University "Babes-Bolyai", 3400 Cluj-Napoca, Romania*

ABSTRACT. The electrode parameters of a cell equipped with a particulate electrode for the recovery of copper ions at low level concentrations from waste waters are described. The influence of current feeder type, electrolysis time, current intensity, sulphuric acid on the recovery efficiency in order to set the optimal working parameters, were studied.

INTRODUCTION

The direct discharge of metal-contaminated waters from industrial plants and mining sites rises a serious environmental threat, especially in industrial area. In 1986 Amendments of the Clean Water Act (CWA) and Safe Drinking Water Act (SDWA) [1] specified 13 metals including copper, lead, cadmium and mercury, as main pollutants and established the maximum discharge level for the most of these metals to ppm range. That is why, the safe-release level and the costs for treatments of waste waters, involve growing burden to nearly all metals processing industries. Efficient removal and recovery of heavy metals from industrial waste waters prior to discharge are major challenges.

Commonly, the large-scale treatment of waste waters has been carried out by chemical methods: precipitation of metal ions and processing the sludge for metal recovery [2-4]. It is clear that, these procedures are not a final solution of contamination problems because of difficulties of methods: specific reagents for sludges processing, large quantities of residues.

Also, chemical methods are inefficient in treatment of waste waters with low levels of metallic ions.

One strategy for a long-term and economical clean-up of waste waters is based on the use of electrochemical methods. Electrochemical treatment of waste waters satisfies two major requirements: pollutants can be selectively and quantitatively removed. Moreover, it offers the advantage to be used as final process at sites of continuous waste waters treatment.

The classical electrochemical methods use planar electrodes that have the disadvantages of a low active area per unit of volume and low mass transfer rate at small ions concentrations. Consequently, the residual concentrations will be reached only in long time operations with prohibitive electricity costs.

Therefore, it was necessary to consider an alternative option, namely increasing the electrodes active area per unit of volume. In that purpose, were used extended area electrodes [5-7] with different shapes: plates, rods or gauzes. However, despite of their ingenious design, these electrodes have a rather low active area. A way of overcoming this limitation is the use of three-dimensional electrodes, which are represented by [8]:

- continuous electron-conducting porous structure, with electrolyte flowing through the pores (porous electrodes);
- individual conducting particles in the form of a fixed or fluidized bed, flow through by the electrolyte (particulate electrode);
- individual electron conducting particles circulated as a slurry (circulating electrodes).

In this paper the electrochemical behavior of particulate electrodes, used for copper recovery from waste waters was studied.

EXPERIMENTAL

To investigate the electrochemical behavior of cathodic particulate bed, as electrolytes were used waste waters from S.C. Phoenix S.A., one of the greatest copper ores processing plant from Baia Mare. The electrolyte flows from the bottom to the top of a three electrodes cell, made of a glass tube with 6 cm inner diameter and 25 cm length. Was processing 1.5 l electrolyte with basic composition presented in Table 1:

Table 1.

Composition of the used waste waters

Symbol of electrolyte	Concentration of metallic ions g/l			Concentration of sulphuric acid, g/l
	Cu^{2+}	Zn^{2+}	Pb^{2+}	
I	0.2	0.12	traces	-
II	0.2	0.12	traces	25

It passes the cathodic bed which consists of a package of copper particles and powder. The bed was supported by a steel sieve at the bottom of the cell. In Table 2 are presented the specific parameters of cathodic bed. For a clearly representation, we express the dimensions of particles and powders colligate with sieves apertures, not in mesh as usually.

Table 2.

Physical properties of cathodic bed

Size range	Cooper particles			Copper powder		
	0.6-0.4 cm	0.2-0.125 cm	0.125-0.016 cm	0.6-0.4 cm	0.2-0.125 cm	0.125-0.016 cm
Specific area cm^2/g	105	218	412	625	1305	1427
Physical aspect	plate	wire	wire	crust	granular	dust

Copper particles and powders were pretreated by cleaning in dilute nitric acid, rinsing in water and drying in an oven. Before use they were rinsed in dilute sulphuric acid to remove any oxide coating.

The electrolytes flow rate measured by of rotameter, was adjusted with a pump for every dimenssion range to bring the bed at the desired level of expansion.

Cathodic polarization of bed was performed using two types of current feeder, described in Table 3.

The anode, placed at the upper part of the cell was a stainless steel circular plate of 3 cm diameter.

A calomel electrode, functioning as reference electrode, was placed above the bed. A potentiostat HA 320 from Hokuto Penko Ltd. was used to supply electric power and to control potential difference between working and reference electrode.

Table 3.

Characteristics of current feeder:

Symbol of current feeder	Aspect
A	copper wire placed in the center of the cathodic bed
B	copper sieve placed at the bottom of the cathodic bed

In all experiments, metallic ions concentrations were periodically monitored by a AAS Perkin-Elmer Spectrometer, model 3300/5100 PC.

The experiments were repeated in the same conditions by three times. Was observed changed in all tests carried out between 0-2% and the final results represent an average of particular results.

RESULTS AND DISCUSSIONS

Influence of specific area:

High specific area is an important condition in the choice of a particulate electrode. Considering data from Table 2, the first choice for experiments was a copper powder of 0.125-0.016 cm size range, with specific area 1427 cm^2/g. Preliminary experiments have been affected by two aspects:

- at low electrolyte velocity (< 0.5 cm/s), the powder particles turn off into sludge who agglomerates the surface of the current feeder and the cell becomes hard to operate;

- at high electrolyte velocity (> 0.5 cm/s), the powder particles easily flow-by, reach the anode and are dissolved, increasing the copper concentration of the electrolyte (Figure 1).

Thus, because of inappropriate behavior of range copper powders 0.125-0.016 cm size range, for the other experiments, have been chosen the next size range with high specific area. According to Table 2, this one belongs to copper powder 0.2-0.125 cm (specific area1305 cm^2/g).

As expected, the experiences performed with the others size ranges both particles and powders, presented in Table 2, having specific areas lower that of 0.2-0.125 cm size, give us unsatisfactory results.

Preliminary experiments with copper powder by 0.2-0.125 cm size, have been made with different bed weights in range 2-12 g. The most significant results of copper recovery efficiency was obtained at bed weights in range 8-12g.

The electrolyte flow rate was adjusted in limits 1.5 - 2.3 cm/s to get both packed and fluidized bed.

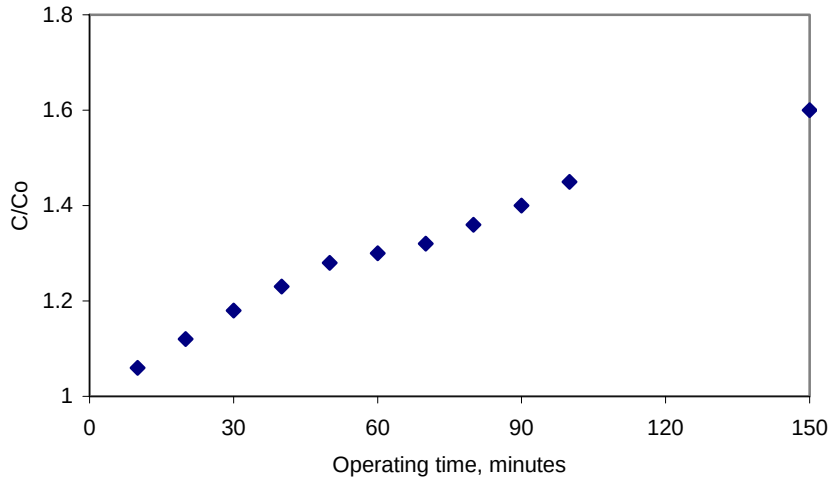

Figure 1. The increase of copper concentration with operating time; copper powder of 0.125-0.016 cm size range (Table 2); bed weight = 8g; current intensity = 2A; current feeder type A (Table 3); electrolyte I (Table 2); C_0 – initial concentration of Cu^{2+} (0.2 g/l); C – [Cu^{2+}] at the considered moment; fluidized bed at electrolyte flow rate 0.8 cm/s

Influence of current intensity on the copper recovery efficiency

In all cases, copper recovery increase with current intensity but not in an uniform way, as can be observed in Figure 2. Comparing the percentage of Cu recovery for each current intensity, it can be observed

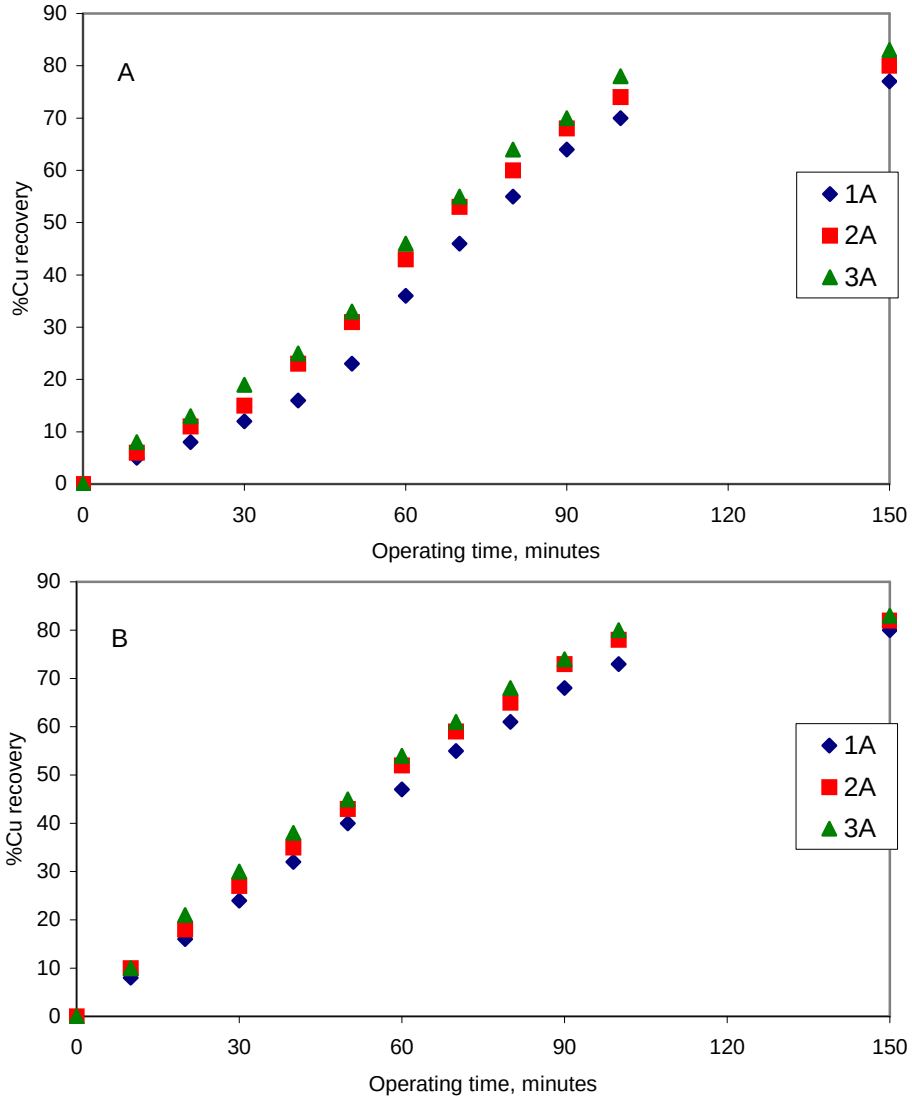

Figure 2. The influence of current intensity and operating time on efficiency of copper recovery at two bed weights; electrolyte I (Table 1); copper powder at 0.2-0.125 cm size range (Table 2); current feeder type A (Table 3); packed bed at 1.5 cm/s electrolyte flow rate; A - 8 g bed weight; B - 10 g bed weight

that the optimal behavior is at 2A. For example, for a 10g bed weight and 100 minutes operating time, an intensity increase from 1A to 2 A determines an recovery efficiency gain of 5% (from 73% to 78%). At the same time of electrolysis, passing from 2A to 3A, the gain is only 2% (from 78% to 80%). Experimental data showed that optimal current intensity, is 2A.

Influence of the bed weight

High specific area of powders at 0.2-0.125 cm size range (Table 2), allows us to conclude, at first sight, that a higher bed weight, equivalent with a higher electrochemical active area, improve the copper recovery efficiency. The experiments made with different bed weights led to the results presented in the Table 4.The Cu recovery efficiency increases with bed weight being higher at 12g bed weight.

A detailed analysis of data from Table 4 shows that %Cu recovery enhances are more clearly when bed weight increases from 8g to 10g rather from 10g to 12g.

Table 4.

The influence of bed weight and operating time on %Cu recovery; copper powder at 0.2-0.125 cm size range (Table 2); packed bed at 1.5 cm/s electrolyte flow rate; I=2A; current feeder type A (Table 3); electrolyte I (Table 1);

Operating time minutes	%Cu recovery		
	8 g	10g	12g
0	0	0	0
10	6	10	12
20	11	18	20
30	15	27	28
40	23	35	36
50	31	43	43
60	43	52	54
70	53	59	60
80	60	65	66
90	68	73	73
100	74	78	79
150	80	82	83

For example, after:

- 10 minutes of electrolysis can be noticed a gain of 4% (from 6% to 10%) when bed weigh increases from 8g to 10 g, comparing with 2% (from 10% to 12%) when bed weight become 12g.

- 50 minutes, the increase is 12%, from 31% at 8g to 43% at 10g, comparing with 0% (43% at both 10g and 12g).

- 100 minutes, the gain is 4%, from 74% at 8g to 78% at 10g and only 1% when bed weight increases with 2g (from 78% at 10g to 79% at 12g).

The small gains of recovered copper obtained at bed weight increase from 10g to 12g, comparing with those from 8g to 12g, allow us to conclude that 10g is the optimal bed weight.

Influence of current feeder

The key point of the electrochemical behavior of particulate bed is the effective solid conductivity. It has been found that in the normal direction the current feeder, the most active regions are near the current collector. As long as the contact between current collector and particulate bed is better, the charge transfer is enhanced.

In case of copper recovery experiments, the shape of the current feeder was an important parameter. A large contact area between current feeder and copper powder and an uniform current distribution determine a higher efficiency for feeder B than A (Table 3). This conclusion is supported by experimental data presented in Figure 3.

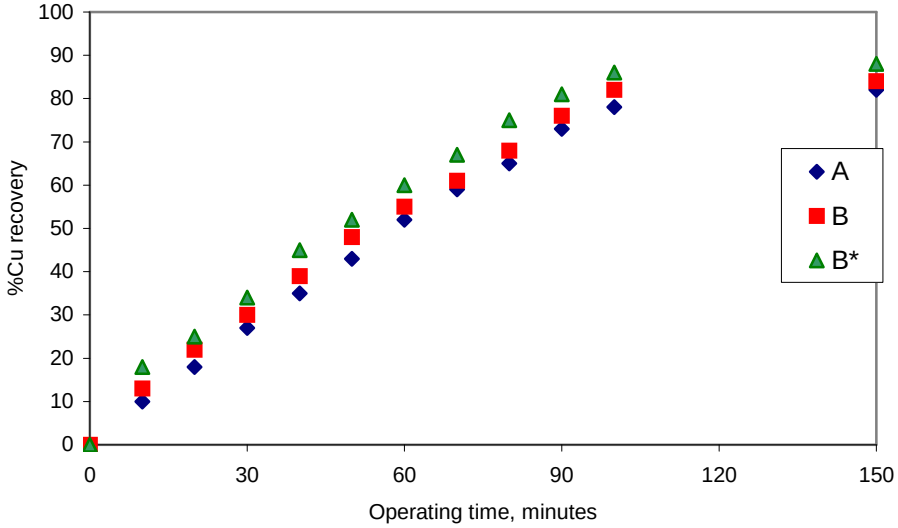

Figure 3. The variation of %Cu recovery with operating time; copper powder at 0.2-0.125 cm size range (Table 2); I = 2A; packed bed at 1.5 cm/s electrolyte flow rate; bed weight = 10g; A, B – current feeders A, B (Table 3), electrolyte I (Table 1); B* - current feeder B (Table 3), electrolyte II (Table 1);

Also, an improvement of charge transfer can be obtained using an acidified electrolyte (Figure 3). The quantity of sulfuric acid added to electrolyte should be not too high, in order to avoid the formation of a cuprous oxide layer on the surface of the electrode which will passivate the

metal [9] (also, hydrogen evolution on particulate bed surface will be observed, in detriment of copper deposition).

Resuming the partial conclusions, we can say that for the packed bed cathode, the optimal operating parameters are the following:

bed weight 10g; current intensity 2A; type of current feeder B (Table 3); acidified electrolyte (Table 1).

Influence of fluidization

Mass transfer of active species plays an important role in the electrodeposition of metals, especially when the concentration of active species is low.

As we observed in previous experiments, low mass transfer rate can be only partially compensated by enhancing the other technical parameters of the process, as current intensity, bed weight, current feeder type, etc.The obtaining of high values of Cu recovery is conditioned by longer operation time at a low current efficiency. Therefore, the necessity to improve the mass transfer by increase of electrolyte flow rate is evident (Figure 4). As can be seen from Figure 4, the effect of electrolyte rate is opposite for the two cases. The rise of electrolyte velocity up to 2 cm/s, increases the copper recovery efficiency. Over this value, at 2.3 cm/s for example, the efficiency of the electrolysis decreases.

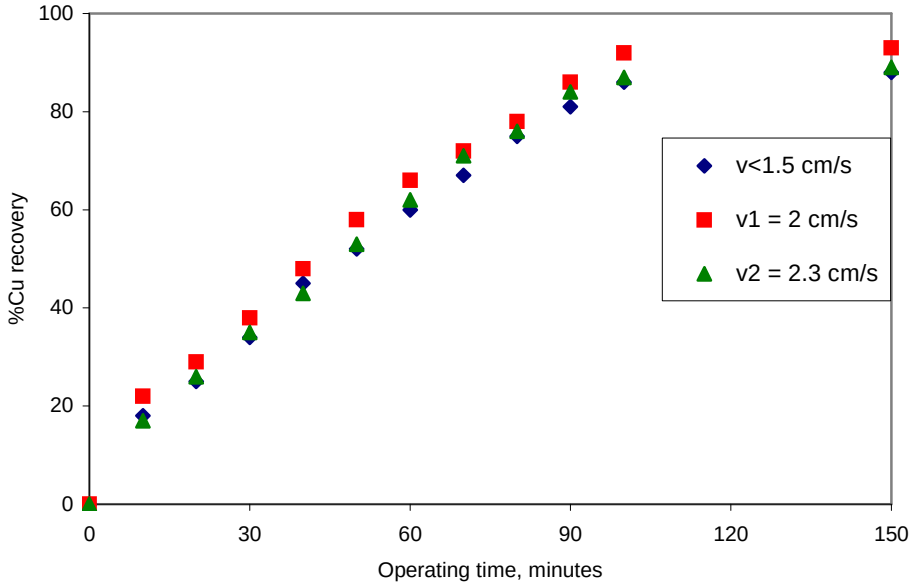

Figure 4. The influence of operating time and electrolyte flow rate on %Cu recovery; copper powder at 0.2-0.125 cm size range (Table 2); bed weight = 10g; electrolyte II (Table 1); current feeder type B (Table 3); I = 2A; v < 1.5 cm/s - packed bed; v > 1.5 cm/s - fluidized bed;

This behavior can be explained considering both the collision and conductive mechanisms proposed to explain the electrodeposition on particulate bed [10]. The particles of the bed are charged while contacted with current feeder or with others charged particles and are discharged because of electrochemical reactions. The slightly increasing of bed expansion by faster circulation of electrolyte, from 1.5 cm/s to 2.0 cm/s, develops the current feeder-particles and particles-particles collisions with enhanced charge transfer and copper recovery efficiency.

The raise of electrolyte rate, from 2 cm/s to 2.3 cm/s, determines of high degree of expansion in the bed. Each particle of the bed becomes free to move about in a random manner, losing touch with one to another and reducing the area in contact with the current feeder.

As the possibility of contacts between particles and current feeder is lower, the ratio of bipolar particles [10] in the fluidized bed will be increased and the %Cu recovery will be decreased.

The aspects presented above are supported by Figure 5. As shown, the current intensities in bed increases as electrolyte flow rate from 1.5 cm/s to 2.0 cm/s. At the lowest bed expansions, a large fraction of the current is carried by particulate phase, so-called “electronic transport”, and used for copper electrodeposition. At high bed expansions are very few conducting particles within the bed and most of the current is carried by the electrolyte -“ionic transport”. At circulation rates of electrolyte higher

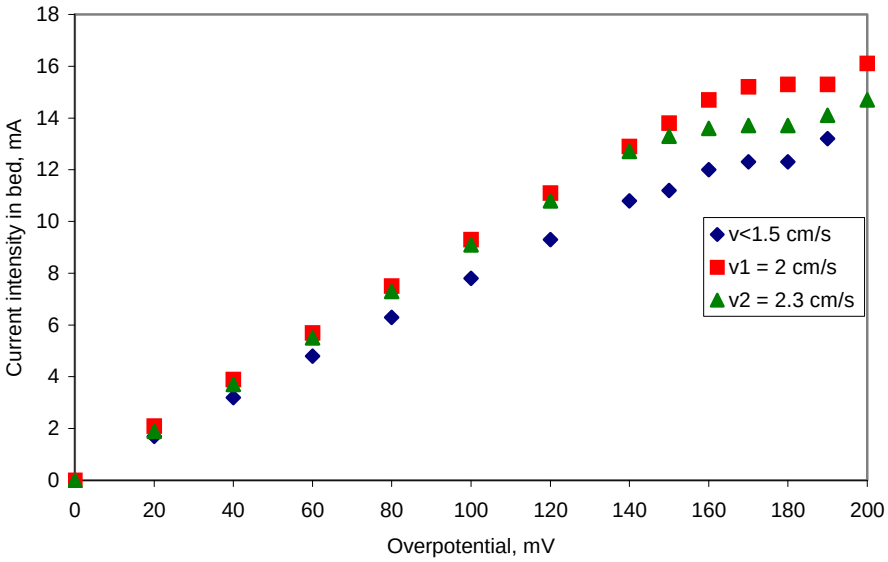

Figure 5. Current intensity in bed against the applied overpotential at different electrolyte flow rates; copper powder 0.2-0.125 cm size range (Table 2) ; bed weight = 10g; electrolyte II (Table 1); current feeder type B (Table 3); current intensity 2A; v < 1.5 cm/s- packed bed; v > 1.5 cm/s - fluidized bed;

than 2.0 cm/s, ionic transport of electric charges becomes more important than electronic transport. Thus, only a small part of the total current is used for electrochemical reaction, and the copper recovery efficiency decreases.

CONCLUSIONS

Particulate bed cathode considered in this paper showed some good performance for the recovery of copper ions from waste waters. A high efficiency is conditioned by :

- high specific area, satisfied by powders with low size (-0.2 + 0.125 cm size range);
- improved mass transfer rate, realized by fluidization of particulate bed (optimal circulation rate of electrolyte 2 cm/s);
- improve of charge transfer by using a large active area current feeder and a acidulate electrolyte;

Correlation of these requirements allows, after 100 minutes of electrolysis, a 93% Cu recovery efficiency.

REFERENCES

1. D. T. Reed, I. R. Tasker, J. C. Cunnane and G. F. Vandergrift, *Environmental Remediation. Removing Organic and Metal Ions Pollutants*, ACS Symposium Series, American Chemical Society, Washington, 1992, 1.
2. M. F. Popea, D. G. Cismaru and L. Paruta, *Procedeu de îndepartare a cuprului din apele reziduale cu continut de sulfat de cupru si amoniu*; Roumanian Patent at No. 63126, 1987.
3. Gh. Volcovinschi and M. Keseru*, Procedeu de recuperare a compusilor metalici din apele reziduale si din namoluri oxidice*, Roumanian Patent No. 67417, 1987.
4. E. Jude, *Procedeu de purificare a apelor reziduale continând ioni de uraniu, cupru, zinc si molibden*, Roumanian Patent No. 71647, 1980.
5. S. Mizumoto, H. Nawafune and M. Kawasaki*, Electrolytic Recovery of Metals from Sludges*, Memoirs of the Konan University, Science Series, No. 23, art. 145, p 35-44, 1979.
6. G. I. Edson, *Electrolytic reactor*, US Patent No. 4,585,539, 29.04.1986.
7. E. N. Balko, *Method for the Recovery of Mercury and Other Heavy Metal Ions from a Liquid Stream*, US Patent No. 4,208,258, 17. 06. 1980.
8. F. Goodridge and A. R. Wright, *Porous Flow-Through and Fluidized Bed Electrodes, în. E. Budevski, Deposition and Dissolution of Metals and Alloys. Part A: Electrocrystallization: Kinetic and Mechanism of Electrode Processes*, B.E. Conway, J. O'M Bockris, Ernest Yeager, SUM Khan and R.E. White (eds.), Plenum Press, New York 1983, vol. 7, p. 399.
9. A. H. Moreira, A.V. Benedetti, P.L. Cabot and P.T.A. Sumodjo, Electrochim. Acta, **38**, 1993, 981-987.
10. Shi-Chern Yen and Ching-Yih Yao, J. Electrochem. Soc., **138**, (1991) 2344-2348, 1991.

STUDIA UNIVERSITATIS BABEŞ-BOLYAI, CHEMIA, XLIV, 1-2, 1999

PARTICULATE BED CATHODE FOR COPPER ION REMOVAL FROM WASTEWATERS.
Part II: A correlation between copper recovery, current efficiency and energy consumption

ANCA MIHAELA MIHAI[1], LIVIU ONICIU[2]

[1] *Department of Chemistry, North University of Baia Mare, 4800, Baia Mare, Romania*
[2] *Department of Physical Chemistry, University "Babes-Bolyai", 3400 Cluj-Napoca, Romania*

ABSTRACT. An analysis based on current efficiency and energy consumption for Cu^{2+} recovery from wastewater, using a copper particulate bed cathode, was attempted. The influence of current intensity on the Cu^{2+} recovery and current efficiency was comparatively examined in order to establish the optimal value of electrolysis current. Additionally, the optimal value of electrolysis time was established based on an economic evaluation.

The investigated method was proved to be efficient for Cu^{2+} removal from wastewater. Thus, after 140 minutes of galvanostatic electrolysis (at 0.25 A) the Cu^{2+} level (10^{-2} M) of 1.5 L of wastewater was reduced with 80%, with a 34.7 % current efficiency. The optimal experimental configuration for the process was attained using a copper powder cathode (10 g, in 0.2 - 0.125 cm size range), a stainless steel sieve as current feeder, and an electrolyte circulation speed of 2 cm/s.

INTRODUCTION

The electrochemical treatment of industrial wastewaters can be considered an efficient method if high efficiency of extraction and current are ensured simultaneously.

It has been shown that fluidized bed of conducting particles in a stream of electrolyte has good performances in metallic ions recovery from dilute solutions [1-5].

In the first part of the study [6], the influence of technological parameters (cathode weight, range size of copper powder used for cathode construction, intensity of the electrolysis current, type of current feeder and electrolyte flow rate) on the extraction efficiency of Cu^{2+} from a wastewater from a metallurgical plant in Baia Mare, has been examined. The analysis of the experimental results indicated the following values as being the

optimal ones: current intensity, 2 A; current feeder with the shape of a sieve placed at the bottom of the electrolysis cell and supporting a cathode made of copper powder from the 0.2-0.125 cm size range; cathode weight of 10 g; electrolyte flow rate of 2 cm s^{-1}. The correlation of these parameters led, after 100 minutes of galvanostatic electrolysis, to an extraction efficiency of 92%.

The present paper aims to analyze the copper recovery process from wastewaters, from the point of view of current efficiency.

EXPERIMENTAL

The composition of the studied wastewater is indicated in table 1. The experimental set-up was identical to that used in the first part of this study [6]. Basically, it has the following construction: the electrolyte flows from the bottom to the top of a three electrode cell, made of a glass with an internal diameter of 6 cm and a length of 25 cm. For an optimum bed expansion, the electrolyte flow rate, measured by a rotameter, was adjusted at 2 cm/s.

Table 1.

Composition of the used wastewater.

Volume of processed electrolyte	Concentration of metallic ions (g/l)			Concentration of sulfuric acid, (g/l)
	Cu^{2+}	Zn^{2+}	Pb^{2+}	
1,5 L	0.2	0.12	Traces	25

The cathode, made of 10g copper powder from 0.2-0.125 cm size range, has been placed at the bottom of the cell on a stainless steel sieve, which represented both the support of the cathode and the current feeder. Copper powder was pretreated by cleaning in dilute nitric acid, rinsing in water and drying in an oven. Before use, it was rinsed in dilute sulfuric acid to remove any oxide coating.

The anode, placed at the upper part of the cell was a stainless steel circular plate of 3-cm diameter. A calomel electrode, functioning as reference electrode, was placed above the bed. A potentiostat (HA 320, Hokuto Penko Ltd.) was used to supply electric power and to monitor the potential difference between working and reference electrode.

In all experiments, an atom absorption spectrophotometer (AAS PERKIN-ELMER Spectrometer, model 3300/5100 PC) was used to monitor periodically the Cu^{2+} concentrations.

The experiments were repeated in the same conditions by three times. In all tests, the final results represent an average of the three experimental results.

For an accurate evaluation of the electrolysis global efficiency, the values of extracted copper used for current efficiency calculation were the same as those used for extraction efficiency calculation.

Current efficiency was calculated using the following relation:

$$r(\%) = \frac{Q_t}{Q_p} 100 \quad (1)$$

where:

Q_t – the charge consumption to extract a certain copper quantity, [C]; it was estimated from the Faraday's law.

Q_p – the practical charge consumption to extract a certain quantity of copper, [C]; it was calculated as the product between the current intensity and the electrolysis time.

RESULTS AND DISCUSSIONS

As previous results indicated [6], the increase of the electrolysis current intensity determined the increase of the extraction efficiency of copper ions (Figure 1). A significant increasing of the copper recovery occurred when the electrolysis current intensity was changed from 1 A to 2 A. Consequently, in the following discussion we will consider only these values for the electrolysis current intensity.

Values of Q_t and Q_p, calculated from the Faraday's law and as the product between the current intensity and the electrolysis time, respectively, were substituted in relation (1) in order to obtain the variation of the current efficiency with electrolysis time (Figure 2).

From Figure 2, it can be noticed that the electrolysis efficiency varies inversely proportional with the electrolysis time and the current intensity. Contrarily, the extraction efficiency increased with the electrolysis current increasing. The maximum value of current efficiency was obtained during the first 10 minutes of electrolysis: 22.8 % at 1 A and 16.7 % at 2 A.

After 100 minutes of electrolysis the current efficiency decreased to 12.4 % at 1 A and 6.9 % at 2 A.

The small values of current efficiency showed that the energy consumption for copper extraction is higher than the gain developed by the recovered copper. A plausible explanation could be formulated if the side process (hydrogen discharge) is taken into consideration.

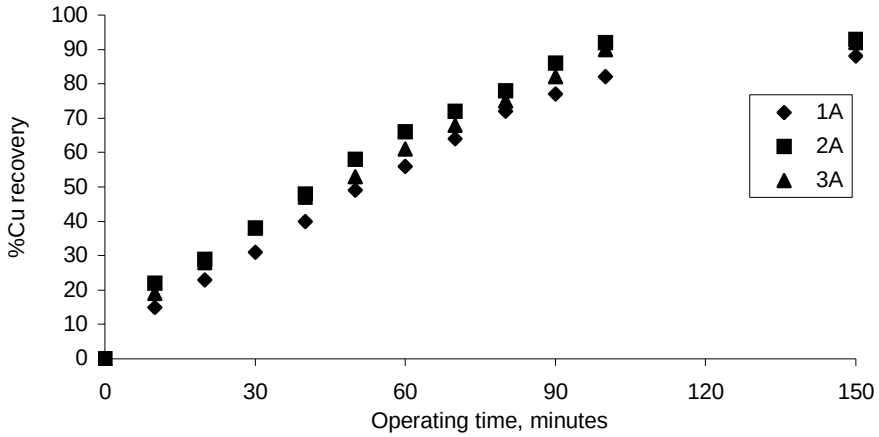

Figure 1. The variation of copper recovery with the electrolysis time for various intensities of the electrolysis current. Experimental conditions: acidified electrolyte (Table 1); cathode made of powder copper in 0.2-0.125 cm size range; cathode weight, 10 g; electrolyte circulation speed 2 cm/s (optimal fluidization); current feeder, stainless steel sieve.

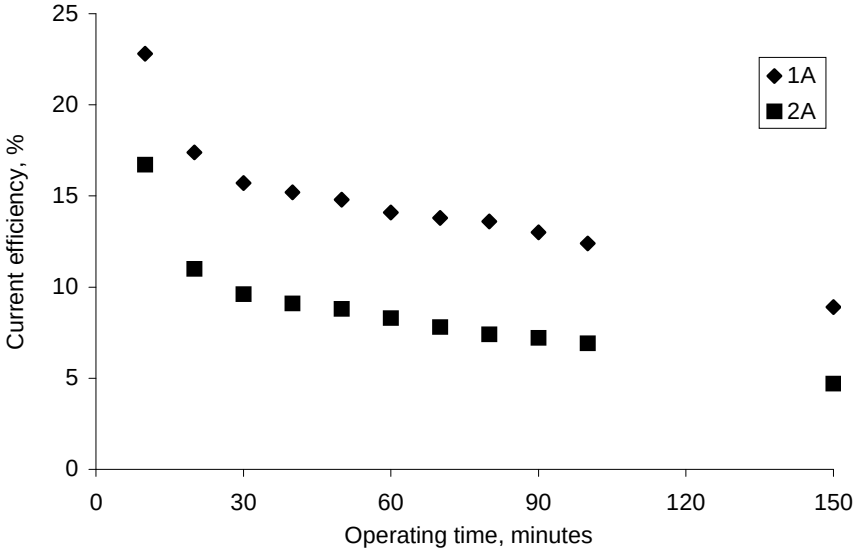

Figure 2. The variation of current efficiency with the electrolysis time for various intensities of electrolysis current. Experimental conditions, as mentioned in figure 1.

Therefore, considering the contrary effects on the copper extraction and current efficiency, induced by the increase of current intensity and time of electrolysis, it was necessary to find values of these parameters to ensure simultaneously high copper recovery and current efficiency. Thus, further it was examined the influence of lower values of current intensity on copper recovery efficiency (Figure 3) and current efficiency (Figure 4).

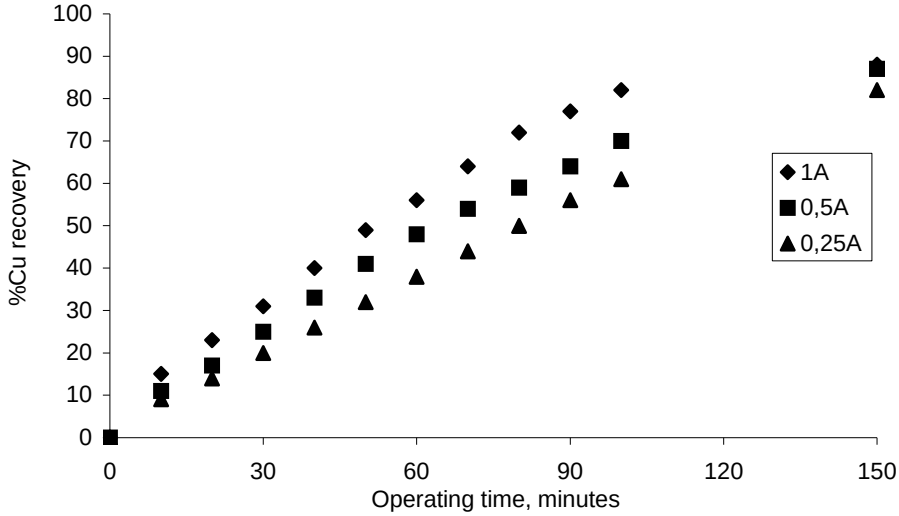

Figure 3. The variation of copper recovery efficiency with the electrolysis time for various intensities of electrolysis current. Experimental conditions, as mentioned in figure 1.

Based on the above-presented results, several conclusions can be stated:

(i) Along with the decrease of electrolysis current intensity, the extraction efficiency also decreased. For example, after 100 minute of electrolysis, a four-time current intensity decrease (from 1 A to 0.25 A) led to a decrease of extraction efficiency by 1.34 times, from 82 % to 61 %.

(ii) The decrease of electrolysis current determines the increase of the necessary operating time to obtain the same extraction efficiency. For example, to obtain a copper extraction percentage of 80 %, the four time current intensity decrease (from 1 A to 0.25 A) required a prolongation of 1.4 times of the electrolysis time (from 100 minutes to 140 minutes).

(iii) The decrease of electrolysis current intensity determines the increase of current efficiency. For example, after 100 minute electrolysis, the four time decrease in electrolysis current intensity (from 1 A to 0.25 A) led to 2.98 times increase of current efficiency (from 12.4 % to 37 %). Simultaneously, the maximum current efficiency corresponding to the first 10 minutes of electrolysis increased 2.39 times (from 22.8% to 54.7%).

Correlating all experimental data, it can estimate that, in order to decrease the energy consumption related to the process, it is more convenient to choose an operating intensity of 0.25 A (instead of 2 A), concomitantly with the prolongation of electrolysis time.

To ensure simultaneously high copper extraction and current efficiency, the following values ot the experimental parameters were considered optimal: current intensity of 0.25 A; current feeder, stainless steel sieve; cathode made of copper powder in 0.2-0.125 cm range size; cathode weight, 10 g, acidified electrolyte (Table 1); electrolyte circulation speed of 2 cm/s.

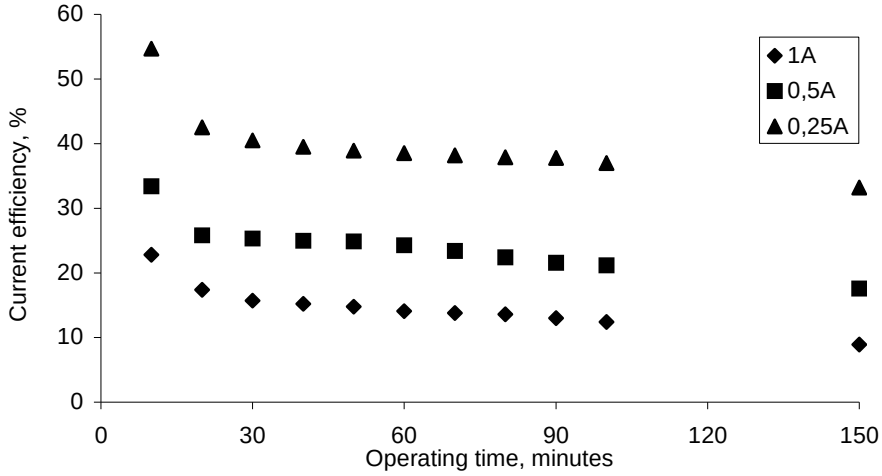

Figure 4. The variation of current efficiency with the electrolysis time for various intensities of electrolysis current. Experimental conditions, as mentioned in figure 1.

The optimal electrolysis time and, implicitly, the copper recovery percentage could be done on the basis of an economic analysis, taking into account the concomitant fulfillment of the following requirements:

- a high extraction and current efficiency;
- a maximum profit, mainly determined by the worth of the extracted copper.

An estimation of the profit requires preliminary calculations of income and expenses, involved by the electrolysis process performed under the optimal experimental conditions, already established.

I. *The income* was calculated on the basis of the following relation:

$$\text{Whole income} = \frac{v \cdot C_o \cdot \%Cu \cdot 10^{-3} \cdot 1.578}{100} \quad (2)$$

where:

Whole income – the income obtained by the processing 1 L of electrolyte, [$/l];

v - volume of processed electrolyte, [1 L];

C_0 - initial copper concentration in the electrolyte, [g/l];

%Cu - copper extraction efficiency;

1.578 - price of electrolytic copper in March 2000, [$/Kg]

II. *Expenses* were calculated taking into account the materials consumed at a laboratory scale:

- The electrolyte is wastewater and does not require any processing expense,
- The copper powder used for the cathode can be obtained as waste material from the copper powder-processing department from the same metallurgical plant;
- The electrolyte circulation pump;
- The power source used for electrolysis;

Observing that solely expenses related to the energy consumption of the pump and electrolysis power source occur, these were calculated according to the relation (3):

$$\text{Whole expenses} = \frac{0.044(W_p + W_e)}{v} = \frac{0.044(P_p t + \eta_e I t 10^{-3})}{v} \quad (3)$$

where:

Whole expenses – expenses for the processing of 1 L electrolyte, [$/l];

W_p – pump energy consumption to ensure electrolyte circulation with a speed of 2 cm/s (optimal fluidization), [KWh];

W_e – energy consumption of electrolysis power source, [KWh];

0.044 – cost of 1KWh, value applied to industrial consumers in March 2000, [$/KWh];

v – volume of processed electrolyte, [1.5 L];

P_t – pump electric power, [kW]; $P_p = 10^{-3}$ kW;

t –pump operating time equal to electrolysis time, [h].

I – electrolysis current intensity, [0,25 A];

η_e – the necessary overpotential for copper ions discharge at the cathode, [V]; it was determined in the following manner: in a cell filled with the investigated electrolyte were placed a copper and a calomel electrode. From the value of potential difference measured by a voltmeter (0.55 V) the

potential value of the calomel electrode (0.244 V) was subtracted, and the value of 0.256 V was obtained. To compensate the possible loss occurring in the system, we preferred the value 0.3 V for η_e.

The values of Profit, correlated with current efficiency, copper extraction efficiency and electrolysis time, are presented in Table 2.

Table 2.

The variation of Cu extraction efficiency, current efficiency and profit with the electrolysis time. Experimental conditions: intensity of electrolysis current 0.25 A; for other experimental conditions see figure 1.

Electrolysis time (minutes)	Cu extraction efficiency (%)	Current efficiency (%)	Profit (10^5 \$/L)
0	0	0	0
10	9	54.7	2.3
20	14	42.5	3.3
30	20	40.5	4.7
40	26	39.5	6
50	32	38.9	7.4
60	38	38.5	8.7
70	44	38.2	10.1
80	50	37.9	11.5
90	56	37.8	12.8
100	61	37	13.9
110	66	36.4	14.9
120	71	35.9	16
130	75	35	16.7
140	80	34.7	17.8
150	82	33.2	17.8
160	84	31.9	17.9
180	87	29.3	17.8
200	88	26.7	17.1
220	88	24.3	16

In order to choose the optimum electrolysis time, on the same plot it was represented the variation of Cu extraction efficiency (%Cu recovery), current efficiency (r,%) and profit (Profit, \$/L) with the electrolysis time (Figure 5).

The choice of a 60-minute electrolysis time, obtained by the intersection of curve r (%) and %Cu, would lead to a current efficiency of 38.5 %, a Cu extraction efficiency of 38 % and a profit of $8.7 \cdot 10^{-5}$ \$/L. Although the condition to achieve a high current efficiency is fulfilled, after the recovery of only 38 % of the initial copper, the Cu^{2+} concentration in wastewater remains 124 mg/l.

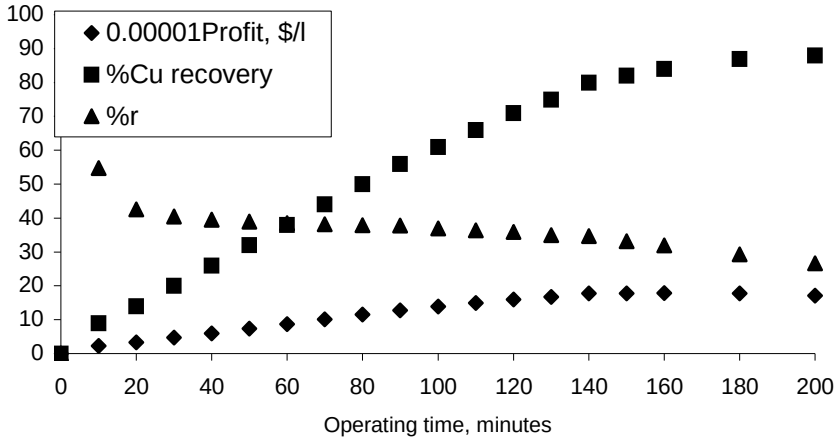

Figure 5. The variation of Cu extraction efficiency (%Cu recovery), current efficiency (r, %) and profit ($/L) with the electrolysis time. Experimental conditions: intensity of electrolytic current 0.25 A; for other experimental conditions see figure 1.

This value is higher than the value admitted by the Romanian reglementation (10 mg/L) [7]. An increase of Cu extraction efficiencappears necessary, even this will involve a decrease of the current efficiency.

More appropriate seems to be an electrolysis time of 140-minutes, which assures a Cu recovery efficiency of 80 %, a current efficiency of 34.7 % and a profit of $17.8 \cdot 10^{-5}$ $/L. To attain the level of Cu^{2+} concentration corresponding to the maximum admitted imposed by the Romanian reglementation (10 mg/l), a 95% Cu extraction efficiency should be achieved. It results that a single electrolysis stage, being limited by technological and economical reasons (long processing time and high- consumption of energy), appears to be unsatisfactory. To further lower the Cu^{2+} concentration, a second electrolysis stage will be necessary, either the use of a different Cu^{2+} extraction method should be considered.

Summarizing, it can be stated that after 140 minutes of galvanostatic electrolysis (0.25 A), using a 10 g fluidized cathode (made of copper powder in 0.2 - 0.125 cm range size), a Cu extraction efficiency of 80 % with a 34.7 % current efficiency can be attained, when 1.5 L of wastewater (containing 0.2 g Cu^{2+}/L) were processed with an electrolyte circulating speed of 2 cm s^{-1}. In the same time, a $17.8 \cdot 10^{-5}$ $/L profit was estimated.

REFERENCES

1. F. Coeuret and M. Paulin, J. Appl. Electrochem., 1987, **18**, 161-165.
2. P. Deverneuil and G. Lacoste, J. Appl. Electrochem., 1988, **4**, 394-400.
3. V.D. Stankovic and S. Stankovic, J. Appl. Electrochem., 1990, **21**, 124-129.
4. J.M. Bisang, J. Appl. Electrochem., 1995, **26**, 135-142.
5. B.M. Dweik, C.C. Liu and R.F. Savinell, J. Appl. Electrochem., 1996, **26**, 1093-1102.
6. A.M. Mihai, L. Oniciu, Studia Univ. "Babes-Bolyai", Chem., in press.
7. Monitorul Oficial al României, partea I-a, 327, 25X 1997, "*Normativ privind stabilirea limitelor de încarcare cu poluanti a apelor uzate evacuate in resursele de apa"* NTPA-001.

STUDIA UNIVERSITATIS BABEŞ-BOLYAI, CHEMIA, XLIV, 1-2, 1999

ELECTROCHEMICAL AND STRUCTURAL CHARACTERISTICS OF CADMIUM ELECTRODE ACTIVE MATERIAL

DELIA MARIA CONSTANTIN, ELEONORA MARIA RUS, L. ONICIU

"Babeş-Bolyai" University, Faculty of Chemistry and Chemical Engineering, Department of Physical Chemistry, 3400 Cluj-Napoca, Roumania

ABSTRACT. Cadmium electrodes were prepared by cathodical polarization, in 25% KOH electrolyte, of sintered nickel supports impregnated with $Cd(NO_3)_2.4H_2O$.The electrochemical characteristics of sintered cadmium electrodes were investigated in a half-cell, by charge-discharge curves in galvanostatic regime, in 6N KOH electrolyte and 6N KOH with 35 g/l LiOH additive, respectively.

The structural characteristics of active material in uncycled, charged and discharged forms were investigated by X-ray diffraction and scanning electron microscopy.

INTRODUCTION

The cadmium electrode has been the object of many studies because of its utilization as anode in nickel-cadmium and silver-cadmium alkaline batteries [1-8].

The processes that take place during charge-discharge of the cadmium electrode are represented by equation:

$$Cd + 2OH^- \underset{\text{charge}}{\overset{\text{discharge}}{\rightleftharpoons}} Cd(OH)_2 + 2\bar{e} \qquad (1)$$

$$\varepsilon^0 = -0.809V/NHE$$

For the best conditions of charge-discharge processes, it is necessary an easy diffusion of electrolyte inside electrodes. From this point of view, the sintered type electrodes are extremely efficient. Sintered supports are prepared by pressing and sintering the nickel powder on a current collector. Activation is performed by precipitation of active material in the pores of supports by a chemical, electrochemical or thermal method. They have high specific capacities and energies and good mechanical properties.

Despite the long technological history of cadmium electrode, its

electrochemistry is not yet fully understood. This is due to the participation of different modifications of discharged active material: α, β and γ $Cd(OH)_2$, CdO and CdO_2 in the potential-determining reactions [9-12]. The existence of these species is related to the preparing method of active material, charge-discharge cycling conditions, electrolyte concentration and composition [13].

In this paper the results of the electrochemical and structural investigations of the sintered cadmium electrode prepared by an original method are presented.

EXPERIMENTAL

Cadmium electrodes were prepared by electrochemical activation of the sintered nickel supports impregnated with $Cd(NO_3)_2 .4H_2O$ [14]. The sintered nickel plates were realized from nickel powder obtained by thermolysis of $Ni(NO_3)_2.6H_2O$ [15].

The sintered supports were immersed in a saturated solution of $Cd(NO_3)_2.4H_2O$ for 24 h, at room temperature, and then were dried at 80^0C. After impregnation with the cadmium nitrate, the supports were cathodically polarized between two cadmium plates (99.99 wt% Cd) in 25 wt% KOH electrolyte.

The electrochemical behaviour of these electrodes has been investigated by charge-discharge curves in galvanostatic regime, at room temperature. The charge-discharge curves were performed in a half-cell consisting of the sintered cadmium electrode as working electrode, a nickel plate as counter electrode and SCE as reference. All the potentials given in this paper are refered to SCE. The electrolyte was 6N KOH and 6N KOH containing 35 g/l LiOH additive, respectively.

The different forms of active material (uncycled, charged and discharged) were characterized by X-ray diffraction (XRD) and scanning electron microscopy (SEM). X-ray diffractograms were obtained with a Dron 3 powder diffractometer, using CuK_α radiation. SEM photographs were taken using a BS 340/1990 Tesla-Brno microscope.

RESULTS AND DISCUSSION

Preparation of Sintered Cadmium Electrodes

The processes that occur in the electrochemical activation step, are:

- At the cathode, NO_3^- ions are reduced to NH_3:

$$NO_3^- + 6H_2O + 8e^- \rightarrow NH_3 + 9OH^- \quad (2)$$

The active material, $Cd(OH)_2$, is deposited inside the pores of the sintered support by a chemical precipitation reaction:

$$Cd^{2+} + 2OH^- \rightarrow Cd(OH)_2 \quad (3)$$

- At the anode, the oxygen evolution reaction takes place:

$$4OH^- \rightarrow O_2 + 2H_2O + 4e^- \quad (4)$$

Electrochemical Characteristics

The sintered cadmium electrodes (70x35x1 mm) were charged and discharged in galvanostatic regime. It is known that, in Ni-Cd battery, the addition of LiOH in KOH electrolyte enhances the discharge capacities and the coulombic efficiencies of nickel electrodes [16,17]. In order to study the influence of LiOH addition on Cd electrode behaviour, the performance curves were performed in 6N KOH electrolyte and in 6N KOH+35 g/l LiOH, at I = 300 mA (Fig. 1).

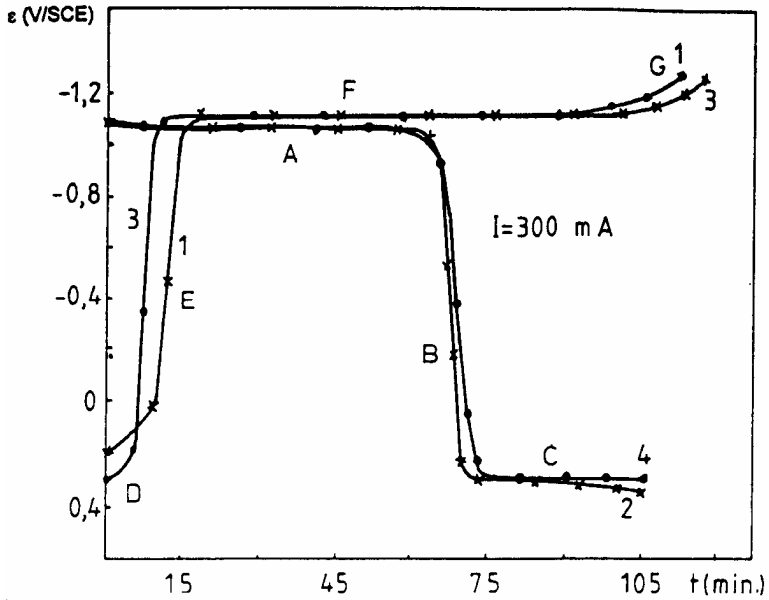

Fig. 1. Charge-discharge curves of sintered cadmium electrode, for I = 300 mA, in 6N KOH + 35 g/l LiOH electrolyte(1-2) and in 6N KOH electrolyte (3-4).

It is evident that the presence of LiOH in electrolyte does not influence the processes, that occur in active material, in negative potentials range.

Thus, the plateau A (curves 2 and 4) corresponding to oxidation of Cd to $Cd(OH)_2$ (discharge process) and respectively, the plateau F (curves 1 and 3) corresponding to reduction of $Cd(OH)_2$ to Cd (charge process) are at the same potentials for both electrolytes.

The LiOH addition influences only the processes that occur in positive potentials range, regarded to the transformations of NiOOH and $Ni(OH)_2$ from sintered nickel support (regions C and D).

The reversible potential (ε_r) values of cadmium electrode, evaluated from ε vs. lg t data by intersecting the anodic and cathodic recovery lines, in 6N KOH (Fig. 2) and in 6N KOH + 35 g/l LiOH (Fig. 3) were found being identical.

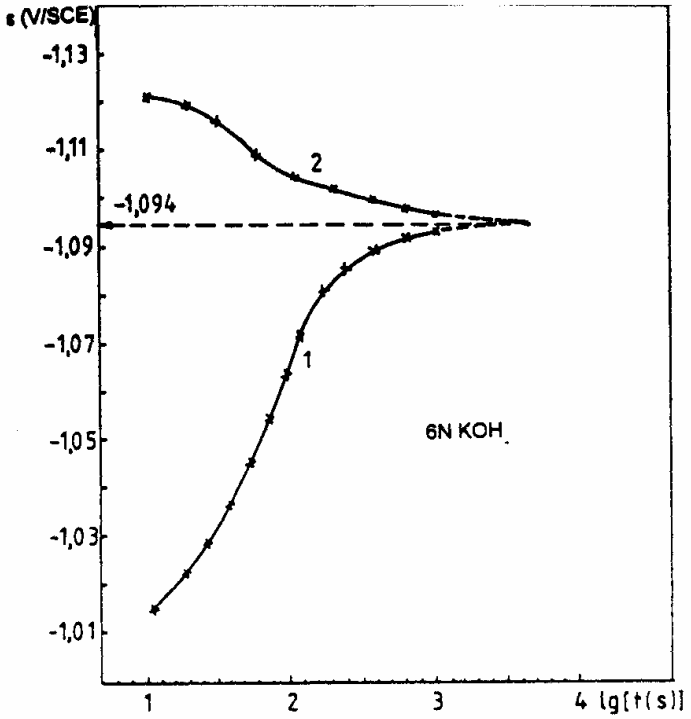

Fig. 2. Evaluation of reversible potential of sintered cadmium electrode in 6N KOH electrolyte.

This fact confirms that the presence of LiOH in electrolyte does not influence the electrochemical behaviour of cadmium electrode in alkaline batteries.

For 6N KOH electrolyte, the experimental value, ε_r = -1.094 V/SCE, is comparable with the theoretical value, $\varepsilon_{r,t}$ = -1.088 V/SCE, calculated for t = 20^0 C [18].

From galvanostatic charge-discharge curves (I = 100, 400, and 500 mA) were determined the discharge capacities and the coulombic efficiencies of the sintered cadmium electrodes in 6N KOH + 35 g/l LiOH electrolyte (Table 1).

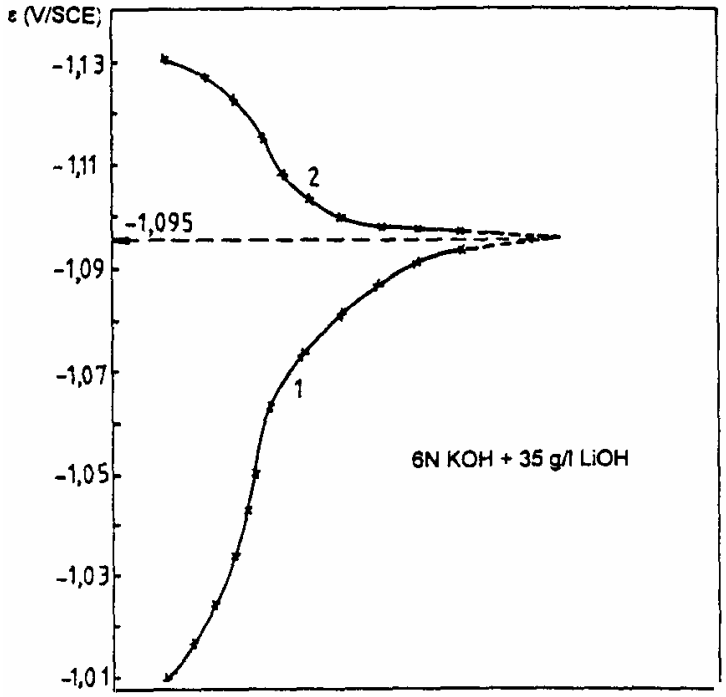

Fig. 3. Evaluation of reversible potential of sintered Cd electrode in 6N KOH + 35 g/l LiOH electrolyte.

Table 1.

Coulombic efficiencies of sintered cadmium electrodes.

I_{charge} (mA)	t_{charge} (h)	C_{charge} (mAh)	$I_{discharge}$ (mA)	$t_{discharge}$ (h)	$C_{discharge}$ (mAh)	Coulombic efficiency (%)
100	6	600	100	5	500	83.33
400	1.46	584	400	1.16	464	79.45
500	1.08	540	500	0.80	400	74.07

Structural Characteristics

For uncycled electrode, the electron micrograph reveals a microcrystalline structure with porous texture (Fig. 4).

The compounds deposited on sintered nickel support consist largely of $Cd(OH)_2$ and a small amount of $CdCO_3$. Unreacted or partly changed $Cd(NO)_3$ crystals remained, here and there.

Fig. 4. SEM photograph of uncycled sintered cadmium electrode.

The X-ray diffraction patterns in the $2\theta = 4 - 63^0$ range, obtained on the powder scraped from the electrode surface, show two characteristic lines, (111) and (200), for nickel of the sintered support, appreciable amounts of $Cd(OH)_2$ and some lines of small intensity corresponding to $CdCO_3$ (Fig. 5, curve a).

It should be pointed out that, by cathodical polarization, the active material was impregnated in sintered support in discharged form.

The charged active material consists largely of microcrystalline structure of metallic cadmium, containing a small amount of CdO octahedral crystals (Fig. 6).

The XRD patterns evidenced also a small number of lines corresponding to $Cd(OH)_2$ remained in discharged form (Fig. 5, curve b).

In the discharged active material $Cd(OH)_2$, there are undischarged Cd and a small amount of $CdCO_3$ (Fig. 5, curve c and Fig. 7).

The presence of unreduced $Cd(OH)_2$ in charged active material and of unoxidized Cd in discharged active material can be explained by the higher capacity of sintered cadmium electrode than of nickel plate electrode, used as counter electrode.

The presence of $CdCO_3$ in active material is a result of the action of CO_2 from air on KOH electrolyte solution and of the pronounced tendency of substitution of NO_3^- ions, remained from the preparation step, by CO_3^{2-} ions.

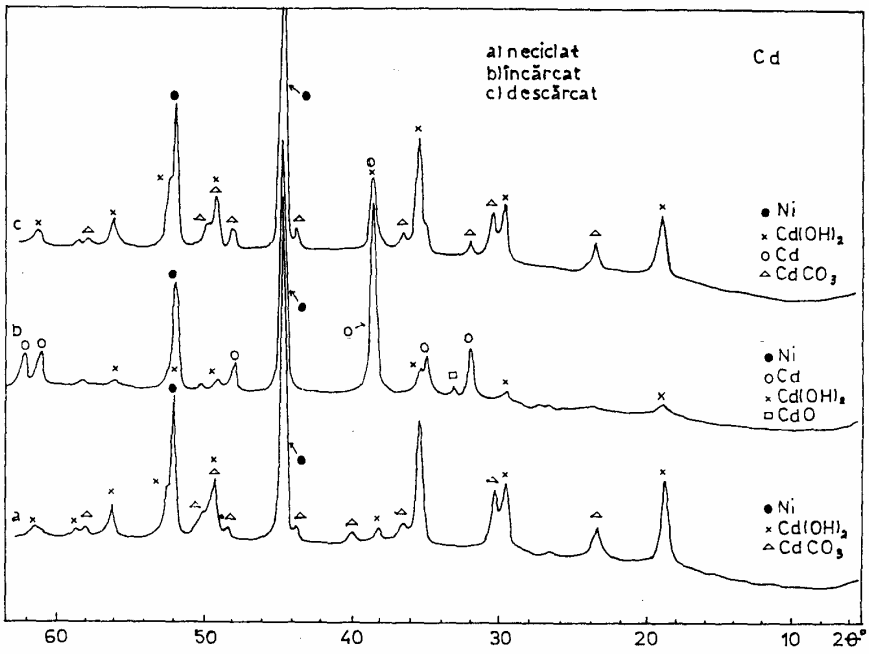

Fig. 5. X-ray diffractograms of sintered cadmium electrode:
a) uncycled, b) charged, and c) discharged.

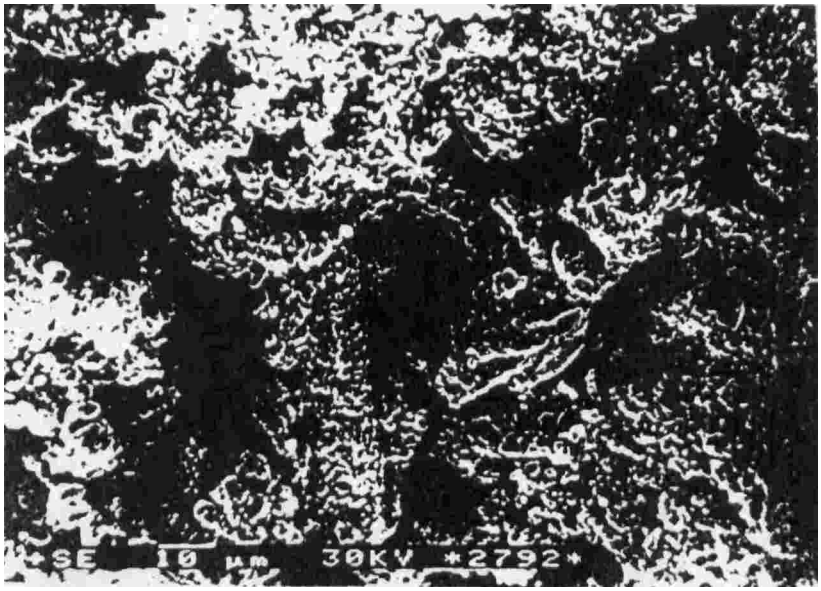

Fig. 6. SEM photograph of charged sintered cadmium electrode.

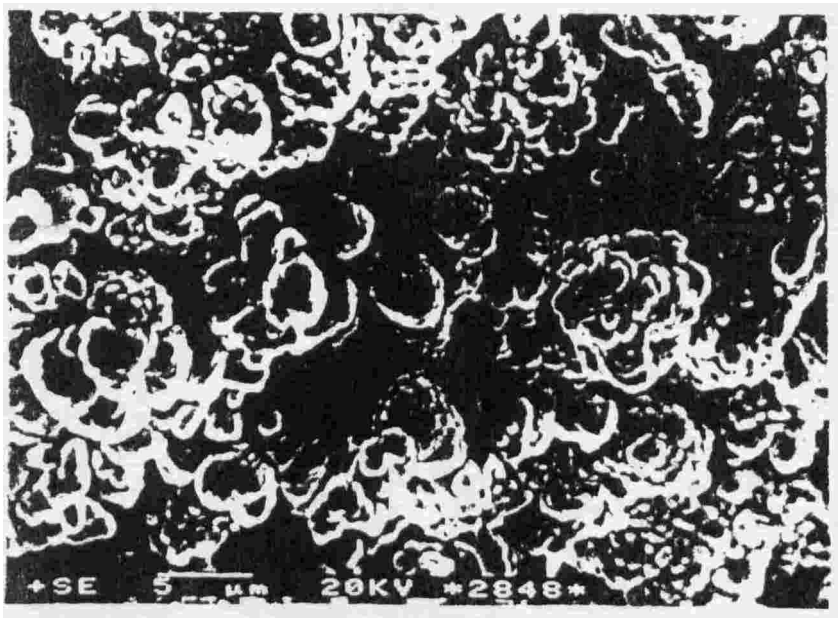

Fig. 7. SEM photograph of discharged sintered cadmium electrode.

CONCLUSIONS

From the investigation of structural and electrochemical characteristics of sintered cadmium electrodes, prepared by us, the following conclusions can be drawn:

a) The uncycled active material, impregnated in sintered support by cathodical polarization, is in discharged form, $Cd(OH)_2$;
b) The charged active material consists largely of microcristalline structure of Cd, containing small amounts of CdO crystals and $Cd(OH)_2$ remained in discharged form;
c) The discharged active material consists of $Cd(OH)_2$, containing a small amount of Cd remained in charged form;
d) The presence of $CdCO_3$ in active material is a result of the action of CO_2 from air on KOH electrolyte solution and of the pronounced tendency of substitution of NO_3^- ions, remained from the preparation step, by CO_3^{2-} ions;
e) The addition of 35 g/l LiOH in 6N KOH electrolyte didn't influence the electrochemical behaviour of cadmium electrode;
f) The characteristics and the performance of our sintered cadmium

electrodes, prepared by electrochemical activation of sintered nickel supports impregnated with cadmium nitrate, point to the possibility of their successful utilization as anodes in alkaline batteries.

REFERENCES

1. L. Oniciu, Eleonora Maria Rus, *Surse electrochimice de putere*, Ed. Dacia, Cluj-Napoca, 1987, chapter 7.
2. R. Dragon, S. Wacke, T. Gorecki, *J. Appl. Electrochem.*, **25**, 699 (1995).
3. J. F. Koenig, A. Sehili, M. Hamdani, P. Chartier, *J. Appl. Electrochem.*, **14**, 241 (1984).
4. H. W. Breiter, *Electrochim. Acta*, **22**, 1219 (1977).
5. R. Barnard, K. Edmondson, J. A. Lee, F. L. Tye, *J. Appl. Electrochem.*, **6**, 107 (1976).
6. M. A. V. Devanathan, S. Lakshmanan, *Electrochim. Acta*, **13**, 667 (1968).
7. I. Sanghi, S. Visuanathan, S. Ananthanarayanan, *Electrochim. Acta*, **3**, 65 (1960).
8. M. W. Breiter, W. Vedder, *Electrochim. Acta*, **13**, 1405 (1968).
9. M. Hamdan, J. F. Kornig, P. Chartier, *J. Appl. Electrochem.*, **14**, 247 (1984).
10. Y. Okinaka, C. M. Whitehurst, *J. Electrochem. Soc.*, **117**, 583 (1970).
11. E. J. Casey, C. L. Gardner, *J. Electrochem. Soc.*, **122**, 851 (1975).
12. K. Apelt, *Electrochim. Acta*, **13**, 1727 (1968).
13. S. T. Selvan, N. Venkatakrishnan, *J. Appl. Electrochem.*, **21**, 646 (1991).
14. L. Oniciu, Eleonora Maria Rus, Delia Constantin, Florentina Ciomo¿, Revista de Chimie, **37**, 44 (1986).
15. L. Oniciu, Eleonora Maria Rus, P.Ilea, Violeta Voina, Delia Constantin, Revista de Chimie, **36**, 340 (l985).
16. Delia Maria Constantin, Eleonora Maria Rus, L. Oniciu, L. Gherghari, *J. Power Sources,* **74**, 188 (1998).
17. Eleonora Maria Rus, Delia Maria Constantin, L.Oniciu, L.Ghergari, *Croatica Chemica Acta,* **72** (1), 25-41 (1999).
18. G. Halpert, *J. Power Sources*, **12**, 177 (1984).

STUDIA UNIVERSITATIS BABEŞ-BOLYAI, CHEMIA, XLIV, 1-2, 1999

ELECTROCHEMICAL AND STRUCTURAL CHARACTERISTICS OF NICKEL ELECTRODE ACTIVE MATERIAL

DELIA MARIA CONSTANTIN, ELEONORA MARIA RUS, L. ONICIU

"Babeş-Bolyai" University, Faculty of Chemistry and Chemical Engineering, Department of Physical Chemistry, 3400 Cluj-Napoca, Roumania

ABSTRACT. Ternary electrodes Ni+Co+Cd, consisting of nickel hydroxide as cathode active material, and with Co and Cd hydroxides as additives were prepared by anodic polarization, in KOH electrolyte, of sintered nickel supports impregnated with mixed metal nitrate solutions. The electrochemical and structural characteristics of these electrodes were investigated by charge-discharge curves in galvanostatic regime, and by X-ray diffraction and scanning electron microscopy, respectively. The coulombic efficiencies determined from charge-discharge curves demonstrated the beneficial effects of LiOH addition to the electrolyte and of Co and Cd hydroxides presence in the active cathode material.

INTRODUCTION

The electrochemical and structural characteristics of nickel hydroxide have been the object of many studies, because its utilization as cathode active material in various alkaline batteries: nickel-cadmium, nickel-iron, nickel-zinc, nickel-hydrogen, and most recently, in nickel-metal hydride systems [1].

The processes that take place during charge-discharge of the nickel electrode are represented by equation:

$$NiOOH + H_2O + e^- \Leftrightarrow Ni(OH)_2 + HO^- ; \quad \varepsilon^0 = 0.490 \text{ V/NHE} \quad (1)$$

The active material of the nickel electrode consists of Ni(II) hydroxide, in discharged state and Ni(III) oxihydroxide in charged state. Two distinct couples, β-$Ni(OH)_2$/β-NiOOH and α-$Ni(OH)_2$/γ-NiOOH, can participate in the charge-discharge reactions of the nickel electrode [2-8]. The charge process of nickel electrode occurs usually in competition with oxygen evolution reaction (OER):

$$4OH^- \rightarrow O_2\uparrow + 2H_2O + 4e^- \quad (2)$$

For an efficient charge of nickel cathode, the oxygen evolution must be minimized.

The addition of foreign metal ions (Co, Cd, Zn, Mg ions) to the nickel electrodes in alkaline batteries improves the utilization of the active material, increases the polarization of OER and depresses the capacity loss during long charge-discharge cycles [9 -16].

In recent years, high energy density nickel electrodes, were produced on sintered supports. The active material is precipitated in pores of these supports by chemical, electrochemical or thermal methods [17-21].

In this paper, the results of the electrochemical and structural investigations of the sintered nickel electrodes containing cobalt and cadmium hydroxides as additives in active material are presented.

EXPERIMENTAL

The sintered nickel supports (70 x 35 x 1 mm), having about 70% porosity, were prepared from nickel powder. Nickel powder was obtained by thermolysis of $Ni(NO_3)_2 \cdot 6H_2O$. Sintered supports were obtained by pressing a mixture of nickel powder (80 wt%) and $(NH_4)_2CO_3$ (20 wt%) on a current collector (a nickel plated iron screen), followed by a heat treatment at 800^0C.

For activation, the sintered supports, impregnated with nickel nitrate, were anodicaly polarized between two nickel cathodes in 42 wt% KOH solution, at a current density of aprox. 30 mA/cm^2. After polarization, the electrodes were washed with distilled water and dried at 80^0C [22].

A ternary electrode, Ni+Co+Cd, containing 5 wt% $Co(OH)_2$ and 5 wt% $Cd(OH)_2$ as additives in active material, was prepared by the same method. Thus, the sintered nickel support was immersed in a mixed metal nitrate solution: $Ni(NO_3)_2 \cdot 6H_2O$, $Co(NO_3)_2 \cdot 6H_2O$, and $Cd(NO_3)_2 \cdot 6H_2O$ before anodic polarization.

The electrochemical behaviour of these electrodes has been investigated by charge-discharge curves in galvanostatic regime. The charge-discharge curves were performed in a half-cell consisting of the sintered nickel electrode as working electrode, a nickel plate as counter electrode and a SCE as reference electrode. All the potentials given in this paper are referred to SCE. The electrolytes are 6N KOH and 6N KOH containing 35 g/l LiOH as additive, respectively.

The crystal morphology of the electrodes was examined by scanning electron microscopy (SEM). The electron micrographs were obtained on a Tesla-Brno BS 340-1990 scanning electron microscope.

Phase compositions of electrodes in different states (uncycled, charged and discharged) were analyzed by X-ray diffraction (XRD) with a DRON-3 type diffractometer with a Cu-cathode, using k_α radiation (λ =1.57051Å).

RESULTS AND DISCUSSION

Electrochemical Characteristics

The charge-discharge curves of sintered nickel electrode containing cobalt and cadmium additives in active material, compared with the charge-discharge curves of nickel electrode without additives, in 6N KOH and in 6N KOH + 35 g/l LiOH electrolyte are shown in Fig. 1 and Fig. 2.

The coulombic efficiencies, determined from charge-discharge curves, demonstrate the beneficial effects of LiOH addition into electrolyte and of cadmium and cobalt hydroxides addition in active material (Table 1).

Table 1.

Coulombic efficiencies of nickel electrodes.

Electrode	Electrolyte	Q^{*}_{charge} (mAh)	$Q^{**}_{discharge}$ (mAh)	r_F (%)
Ni	6N KOH	550	350	63.63
	6N KOH+35 g/l LiOH	550	383	69.64
Ni+Co+Cd	6N KOH	550	425	77.27
	6N KOH+35 g/l LiOH	550	450	81.81

* corresponds to charging for 5.5 h at I = 100 mA;
** calculated from the plateau of the discharge curves at I = 100 mA.

The decrease of plateaus corresponding to OER from charge curves of Figs. 1 and 2, induced by Co and Cd addition, also demonstrates the increase of the charge efficiency and hence, the improvement of the discharge characteristics of Ni+Co+Cd electrode.

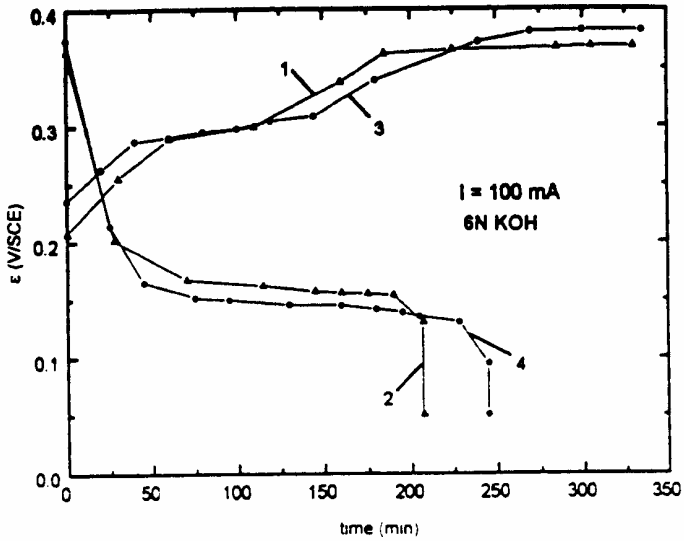

Fig. 1. Charge-discharge curves of Ni (1-2), Ni+Co+Cd (3-4), at I = 100 mA, in 6N KOH.

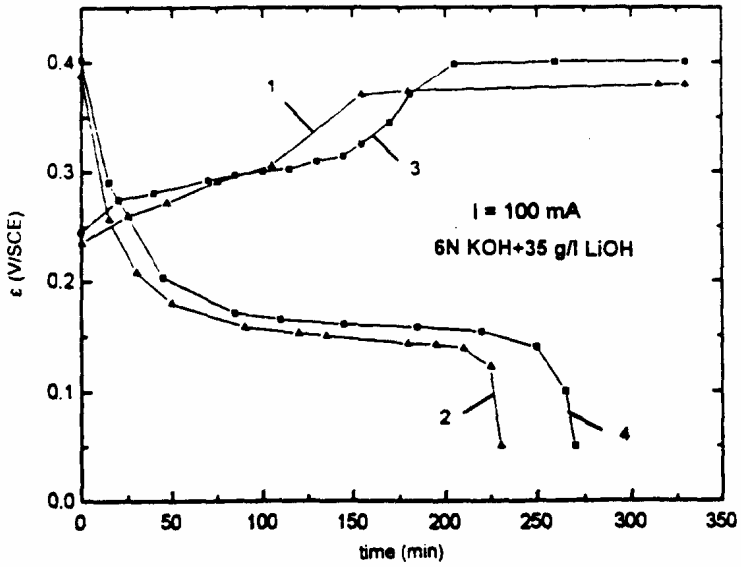

Fig. 2. Charge-discharge curves of Ni (1-2), Ni+Co+Cd (3-4), at I = 100 mA, in 6N KOH+35 g/l LiOH.

The reversible potentials ε_r of the electrodes, were evaluated from ε vs. lg t data, by intersecting the anodic and cathodic recovery lines (Fig. 3 and Fig. 4).

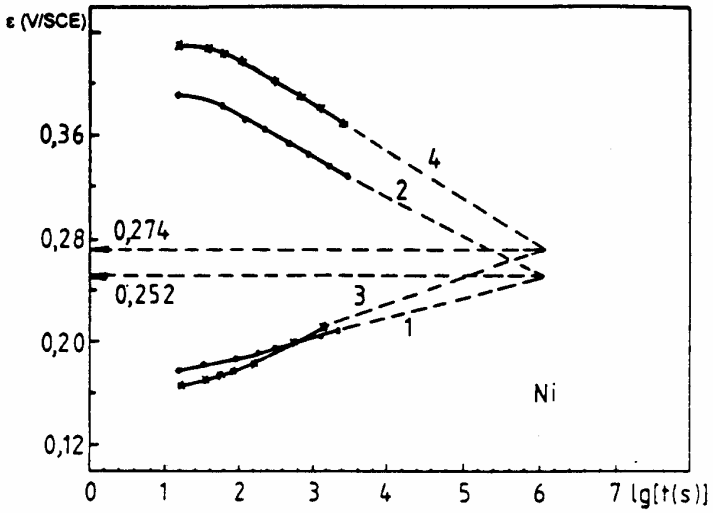

Fig. 3. Evaluation of reversible potentials of Ni electrode in 6N KOH (1-2) and in 6N KOH+35 g/l LiOH (3-4).

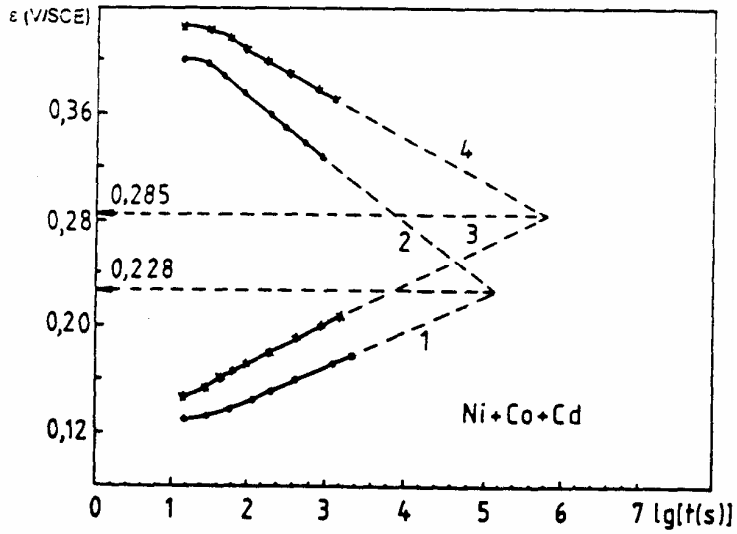

Fig. 4. Evaluation of reversible potentials of Ni+Co+Cd electrode in 6N KOH (1-2) and in 6N KOH+35 g/l LiOH (3-4).

The ascending recovery lines were obtained after a discharge of the electrodes with I = 100 mA, to 0.05 V.

The descending recovery lines were obtained after a charge of the electrodes with I = 100 mA for 5.5 h. The obtained values of ε_r are shown in Table 2.

Table 2.

Reversible potentials of nickel electrodes.

Electrode	Electrolyte	ε_r (V/SCE)
Ni	6N KOH	0.252
	6N KOH+35 g/l LiOH	0.274
Ni+Co+Cd	6N KOH	0.228
	6N KOH+35 g/l LiOH	0.285

In 6N KOH electrolyte, because the shift of ε_r to more cathodic value by addition of Co and Cd, the charge takes place at less positive potentials and it is more complete, minimizing the OER.

In the presence of LiOH in electrolyte, the charge efficiency was improved, because increasing the overpotential of oxygen evolution on electrodes [22].

Structural Characteristics

Our previous structural investigations of the nickel electrode without additives, by XRD and SEM, demonstrated the presence of α and β-$Ni(OH)_2$ in the discharged electrode, and of γ and β-NiOOH in the charged electrode [23].

The X-ray diffraction pattern in the $2\theta = 4 - 63^0$ range, obtained on the powder scraped from the surface of uncycled Ni+Co+Cd electrode, shows the well expressed (111) and (200) lines, corresponding to nickel and some lines of small intensity corresponding to $Ni(OH)_2$ (theofrasit), a nonstoechiometric Co and Cd compound, and to KNO_3, remained from the preparation step (Fig. 5, curve a).

The electron micrograph of the uncycled electrode reveals a microcrystalline-amorphous structure with porous texture (Fig. 6).

In the charged electrode, the XRD reveals an appreciable amount of γ-NiOOH and smaller amounts of $CoCO_3$ and $CdCO_3$ (Fig. 5, curve b). γ-NiOOH form of active material confers to electrode a more reduced self-discharge than β-NiOOH [24].

The SEM of the charged electrode shows a microcrystalline structure with porous texture, and two kinds of crystals: hexagonal crystals with lamellar habitus, of 1-4 μm, attributed to γ-NiOOH and smaller isometric crystals of 0.5 -1 μm attributed to $CoCO_3$ and $CdCO_3$ (Fig. 7).

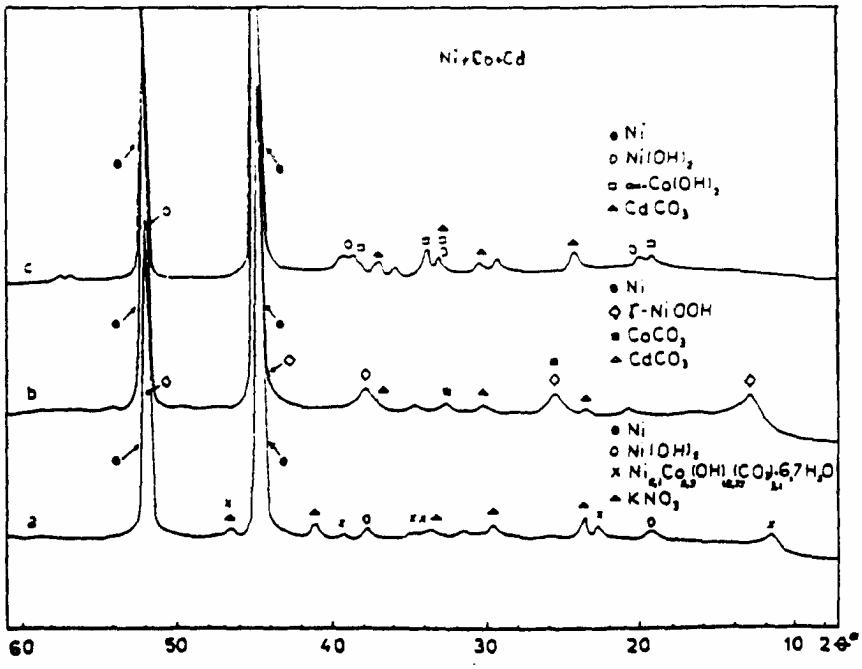

Fig. 5. X-ray diffractograms of Ni+Co+Cd electrode:
a) uncycled, b) charged, c) discharged.

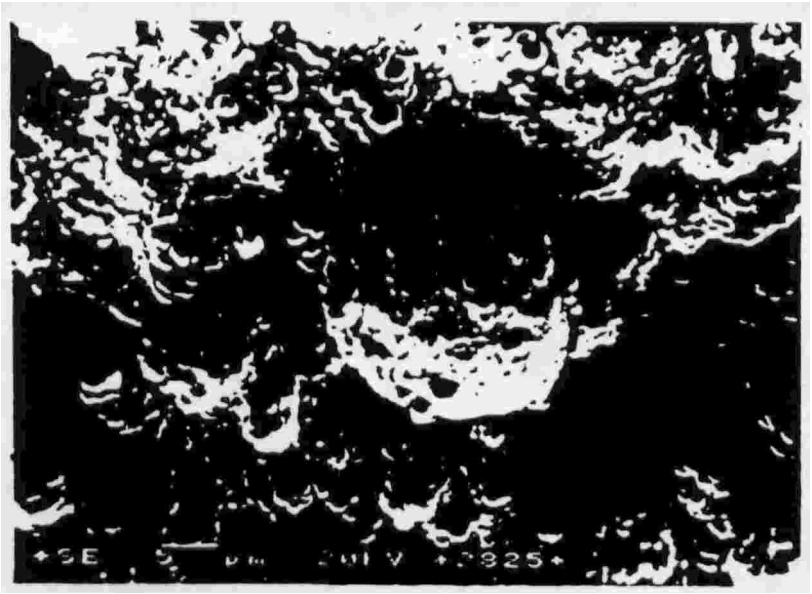

Fig. 6. SEM photograph of uncycled Ni+Co+Cd electrode.

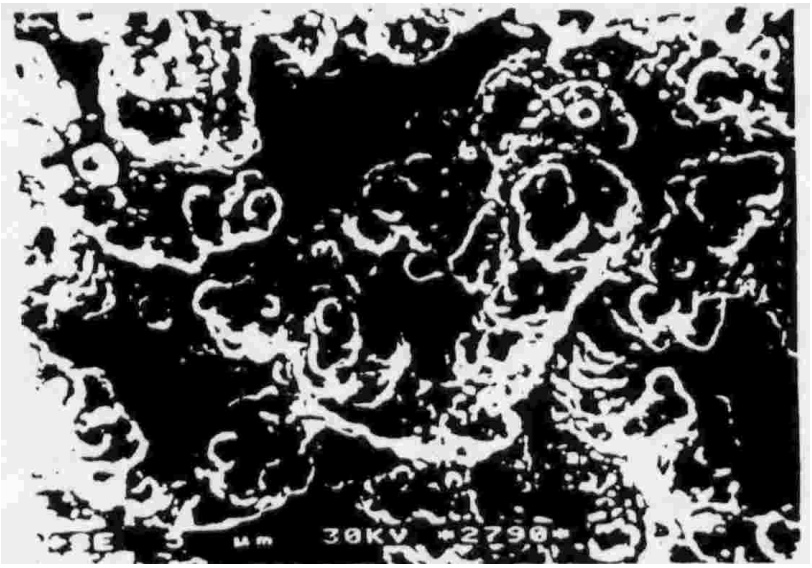

Fig. 7. SEM photograph of charged Ni+Co+Cd electrode.

In the discharged electrode, the active material is α-$Ni(OH)_2$ [22]. Cd compound remains as rhombohedral $CdCO_3$, while Co compound appears as trigonal crystals of α-$Co(OH)_2$ (Fig. 5, curve c and Fig. 8).

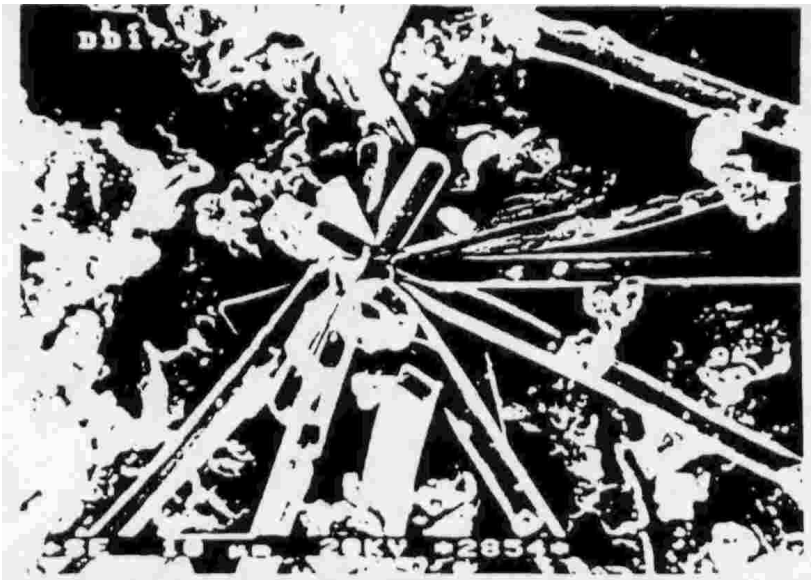

Fig. 8. SEM photograph of discharged Ni+Co+Cd electrode.

CONCLUSIONS

a) A ternary electrode, Ni+Co+Cd, containing nickel hydroxide active material, with 5 wt.% $Co(OH)_2$ and 5 wt.% $Cd(OH)_2$ as additives was prepared by electrochemical activation of sintered nickel support.
b) The coulombic efficiencies determined from charge-discharge curves, demonstrated the beneficial effects of LiOH addition into electrolyte and of Co and Cd hydroxides addition in active material;
c) The uncycled active material, impregnated in sintered support by anodical polarization, was in discharged form, $Ni(OH)_2$;
d) The charged form of active material was γ-NiOOH and the corresponding discharged form was α-$Ni(OH)_2$;
e) The electrochemical and structural characteristics of Ni+Co+Cd electrodes point to the possibility of their successful utilization as cathodes in alkaline batteries.

REFERENCES

1. L. Oniciu, E.M. Rus, *Surse electrochimice de putere,* Ed. Dacia, Cluj-Napoca, 1987.
2. J. Desilvestro, O. Haas, *J. Electrochem Soc.,* 1990, **137***,* 5c.
3. R. Barnard, C.F. Randell, F.Y. Tye, *J. Appl. Electrochem.,* 1980, **10***,* 109.
4. H. Bode, K. Dehmelt, J. Witte, *Electrochim. Acta,* 1966, **11***,* 1079.
5. D.A. Corrigan, S.L. Knight, *J. Electrochem. Soc.,* 1989, **136***,* 613.
6. G.W.D. Briggs, P.R. Snodin, *Electrochim. Acta,* 1982, **27***,* 565.
7. P. Oliva, J. Leonardi, J.F. Laurent, C. Delmas, J.J. Braconnier, M. Figlarz, F. Fievet, A. de Guibert, *J. Power Sources,* 1982, **8***,* 229.
8. B.C. Cornilsen, X. Shan, P.L. Loyselle, *J. Power Sources,* 1990, **29***,* 453.
9. L. Oniciu, Eleonora Maria Rus, P. Ilea, Violeta Voina, Delia Constantin, *Rev. Chim.,* 1985, **36***,* 340.
10. D.A. Corrigan, R.M. Bendert, *J. Electrochem. Soc.,* 1989, **136***,* 723.
11. P.V. Kamath, M.F. Ahmed, *J. Appl. Electrochem.,* 1993, **23***,* 225.
12. L.Demourgues-Guerlou, C. Delmas, *J. Electrochem. Soc.,* 1994, **141***,* 713.
13. L. Oniciu, Delia Constantin, Eleonora Maria Rus, Violeta Voina, Cristina Corăbian, *Studia Univ. "Babes-Bolyai", Ser. Chem.,* 1994, **39***,* 218.
14. C.A. Gervasi, J.R. Vilche, P.E. Alvarez, *Electrochim. Acta,* 1996, **41***,* 455.
15. S.K. Tiwari, P. Chartier, R.N. Singh, *J. Electrochem. Soc.,* 1995, **142***,* 148.
16. B.B. Ezhov, O.G. Malandin, *J. Electrochem. Soc.,* 1991, **138***,* 885.
17. M. Paszkiewicz, *J. Appl. Electrochem.,* 1981, **11***,* 135.
18. B. Lafage, M. Comtat, R. Routie, *J. Appl. Electrochem.,* 1988, **18***,* 363.
19. M. Oshitani, Y. Sasaki, K. Takashima, *J. Power Sources,* 1984, **12***,* 219.
20. M. Wales, *Electrochim. Acta,* 1979, **24***,* 629.
21. K. Ho, J. Jorne, *J. Electrochem. Soc.,* 1990, **137***,* 149.
22. Delia Maria Constantin, Ph.D. Thesis, "Babeş-Bolyai" Univ., Cluj-Napoca, Romania, 1996.
23. Eleonora Maria Rus, Delia Maria Constantin, L. Oniciu, L. Ghergari, *Croatica Chem. Acta*, 1999, **72**, 25.
24. B.B. Ezhov, O.G. Malandin, *J. Electrochem. Soc.,* 1991, **138***,* 885.

STUDIA UNIVERSITATIS BABEŞ-BOLYAI, CHEMIA, XLIV, 1-2, 1999

INFLUENCE OF Pb^{2+} IONS ON ZINC ELECTROWINNING FROM SULFATE SOLUTIONS

LIANA MUREŞAN, OLIMPIA ONAC

"Babeş-Bolyai" University, Faculty of Chemistry and Chemical Engineering, Department of Physical Chemistry, 3400 Cluj-Napoca, Romania

ABSTRACT. The effect of trace lead on zinc electrodeposition from sulfate electrolyte has been investigated in terms of cathodic deposit morphology and cyclic voltammetry.

The results indicated that Pb^{2+} ion has a deleterious effect on zinc electrodeposition from sulfate electrolyte. In presence of increasing Pb^{2+} concentrations, the morphology of zinc deposits was observed to change from smooth to dendritic, less adherent and the color changed from silver to a dark gray, proving a grain refining related to an inhibition effect. Pb^{2+} also affects the zinc deposition cyclic voltammograms. It increases the nucleation overpotential and diminishes the area of cathodic and anodic peaks, proving the inhibition of both the cathodic and anodic reactions.

The addition of horse chestnut extract (HCE) to the Pb^{2+} containing electrolyte counteracts the detrimental effect of these ions, leading to cathodic deposits with acceptable morphology, while increasing concentrations of animal glue, at the same Pb^{2+} concentration ($3.18\ 10^{-4}$ g/l) do not improve the cathodic morphology.

INTRODUCTION

The effects of metal impurities on zinc electrowinning from acid sulfate electrolytes have been extensively analyzed in terms of current efficiency, deposit morphology, crystal orientation and cyclic voltammetry [1-7]. Impurities behavior is not well understood and many questions remain regarding the acceptable limits of impurities for an efficient operation of zinc electrodeposition.

Unfortunately, not only the absolute magnitudes of the various impurities, but also the synergistic interactions among them ultimately determine the quality of deposit [3]. The presence of trace lead in zinc tankhouse solutions is inevitable because the zinc ore contains lead and either silver-lead or pure lead anodes are employed in the electrowinning step. Estimates of lead solubility in acid zinc sulfate solutions range from 4 to 10 mg/l [4].

The effects of trace lead and the corrosion behavior of Zn-Pb alloys have been investigated with respect to applications in alkaline zinc batteries. Trace lead (~20 mg/l) suppresses the onset of zinc dendrites [2,8] and Zn-Pb compositions (Pb ≤ 1% weight percent) exhibit superior corrosion resistance compared to pure zinc [9].

In acid media, lead has been reported as having either a small positive [5] or a small negative [10] effect on current efficiency, depending on the electrolysis conditions, solution purity, form of lead added and method of current efficiency measurement. On the other hand, lead is an impurity able to impede hydrogen evolution on zinc; at the same time, adsorbed lead strongly inhibits most of the reactions taking place on the zinc electrode [2].

Since is little agreement in the existing literature on the effects of lead, particularly with regard to its influence in the presence of organic additives, the present work was undertaken to help clarify the matter.

EXPERIMENTAL

Solution preparation

A stock solution of 1M zinc sulfate was prepared by using pure reagents (Merck) and distilled water. Electrolytes with various Pb^{2+} content ($1.59 \cdot 10^{-4}$ g/l – $1.9 \cdot 10^{-3}$ g/l) were prepared using this solution and a saturated solution of $PbNO_3$, by adding appropriate volumes into a known volume of stock solution. The horse chestnut extract was prepared by an original method [11] from the seeds of Aesculus Hyppocastanum.

Electrolysis

Small-scale electrolysis was performed in the absence and in the presence of various amounts of Pb^{2+} and/or organic additives, employing a 250 dm^3 plexiglass cell equipped with one central aluminum cathode and two symmetrical lead anodes. Zinc deposited on both sides of the cathode. The current density was held constant at 500 mA cm^{-2} and the deposition time was 60 min. Morphological examination of the copper deposits was made by visual inspection.

Cyclic voltammetry

The cyclic voltammetry experiments were conducted in a glass cell with separate compartments, using an Al disk working electrode (area 0.9 cm^2), a Pt counter electrode and a saturated calomel reference electrode. The working electrode was prepared by wet polishing on 600 grit paper and then rinsing with distilled water before each experiment. The cyclic voltammograms were recorded under potentiostatic conditions using a PS 3 potentiostat (Meinsberg, Germany), a signal generator (LP 7e Praha, Czech Republic) and a X-Y recorder (Endim 620.02, Germany). The potential range was between 0.5 V vs. SCE and –1.6 V vs SCE and the scan rate was 0.75 V/min.

RESULTS AND DISCUSSIONS

Influence of Pb^{2+} in absence of organic additives

A typical voltammogram obtained for zinc electrodeposition from an additive-free electrolyte is shown in Figure 1a. A cycle starting from point A goes through a region of low current until point C where the cathodic process begins. The current increases to point D where the scan is reversed. At the point B the current becomes anodic, corresponding to zinc dissolution. The anodic peak reaches a maximum at point E and dissolution is complete on return to A.

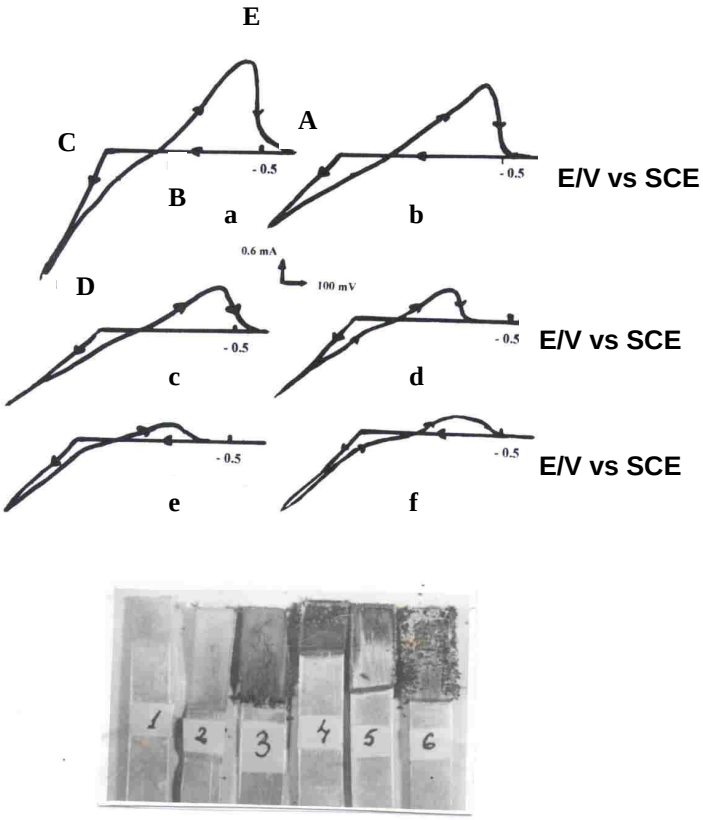

Figure 1. Cyclic voltammograms and cathodic deposits obtained in 1 M $ZnSO_4$ with increasing Pb^{2+} concentrations: a) without Pb^{2+} (electrode 1); b) 1,59. 10^{-4} g/l Pb^{2+} (electrode 2); c) 3.18.10^{-4} g/l Pb^{2+} (electrode 3); d) 6.37.10^{-4} g/l Pb^{2+} (electrode 4); e) 1.27. 10^{-3} g/l Pb^{2+} (electrode 5); f) 1.91. 10^{-3} g/l Pb^{2+} (electrode 6) Experimental conditions for voltammetry: scan rate 0.75 V/min; Experimental conditions for small-scale electrolysis: current density 500 mA/cm^2; Al cathode; Pb anodes.

The region BCD is called nucleation hysteresis loop. The point C has been used to define a nucleation overpotential [6]. The position of C shifts when certain impurities and/or additives are present in the electrolyte. The crossover potential, corresponding to B point is at or close to the reversible potential of the system.

Curves from Figure 1b until 1f represent the voltammograms recorded in presence of different Pb^{2+} concentrations. It can be observed that Pb^{2+} inhibits both cathodic and anodic reactions. The BEA region of the voltammogram, i.e. the anodic dissolution of zinc, is considerably reduced in the presence of increasing Pb^{2+} concentrations, the hight of the anodic peak (I_a) decreasing as well (Figure 2).

At the same time, the nucleation overpotential, (section BC in figure 1a) increases and the slope of CD section decreases, proving the inhibition of the cathodic process by adsorbed lead. These results are in accordance with those already reported in the literature [2], which admit that Pb^{2+} ions adsorb on the electrode, reducing the electrode coverage by ZnH_{ads}, Zn^{+}_{ads}, and active sites Zn*, species involved in the multi-step process of zinc deposition, and thus generate an inhibiting effect.

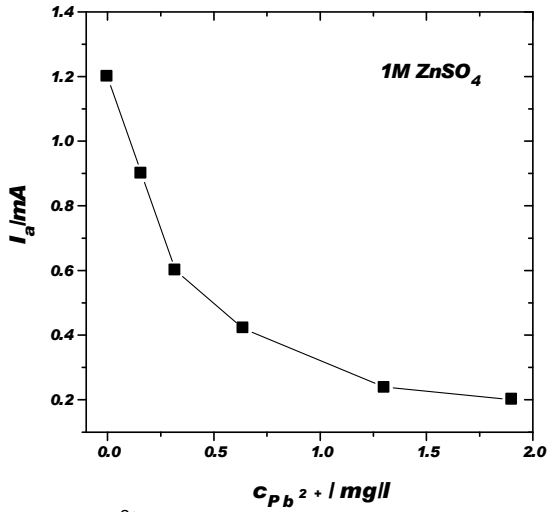

Figure 2. Influence of Pb^{2+} concentration on anodic peak current from the cyclic voltammograms recorded in 1M $ZnSO_4$ solutions; experimental conditions as in figure 1.

Moreover, hydrogen evolution on Pb_{ads} differs from hydrogen evolution on zinc, taking place with a higher overpotential. The morphology of zinc deposits was observed to be changed from smooth to dendritic, less adherent and the colour changed from silver to a dark grey, proving a grain refining

related to the inhibition effect. At the same time, the deposit quality changes from acceptable to unacceptable, suggesting that Pb may be partially incorporated into the zinc lattice, as reported in the literature [4].

Influence of Pb^{2+} in presence of organic additives

Organic additives are usually added to the zinc electrolyte because they counteract the effect of impurities and thus maintain a high current efficiency [7]. They refine the deposit grain size and this results in smooth and compact deposits.

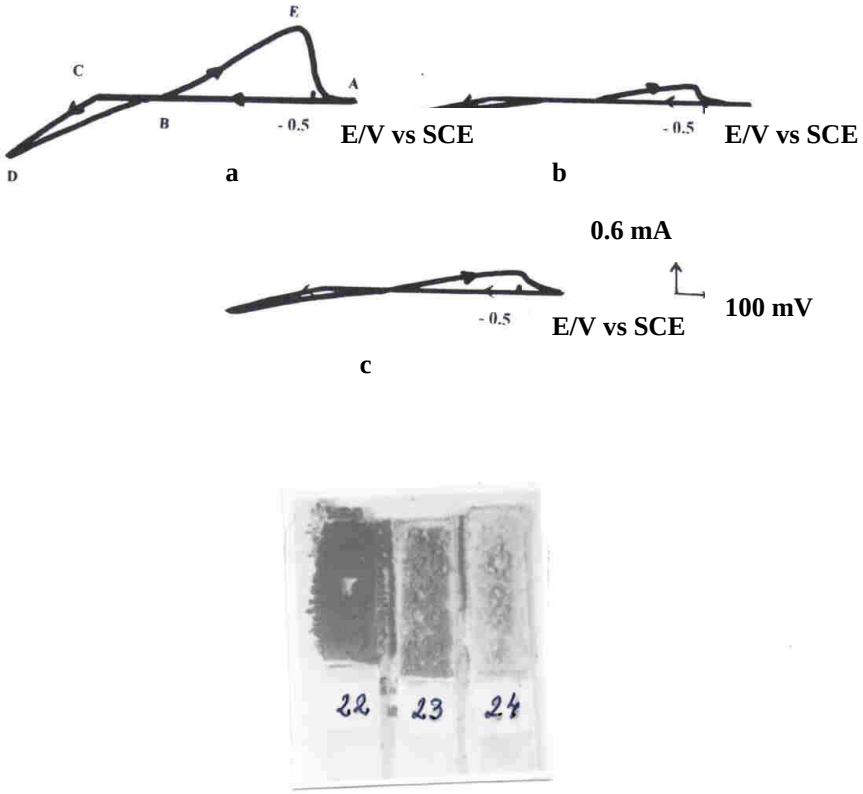

Figure 3. Cyclic voltammograms and cathodic deposits obtained in 1 M $ZnSO_4$ with fixed Pb^{2+} concentration ($3.18 \cdot 10^{-4}$ g/l) aznd increasing concentration of HCE: a) 15 mg/l HCE (electrode 22); b) 45 mg/l HCE (electrode 23); 90 mg/l HCE (electrode 24). Experimental conditions as in figure 1.

Figure 3 shows the effect of increasing HCE concentration on deposit morphology and cyclic voltammograms for electrolytes containing a fixed concentration of lead (3.18. 10^{-4} g/l). As it can be seen, increasing concentration of the organic additive has a beneficial influence on cathodic morphology. At higher HCE concentrations (Figure 3, electrode 24) the deposits become levelled and any negative influence of Pb^{2+} seems to be counteracted.

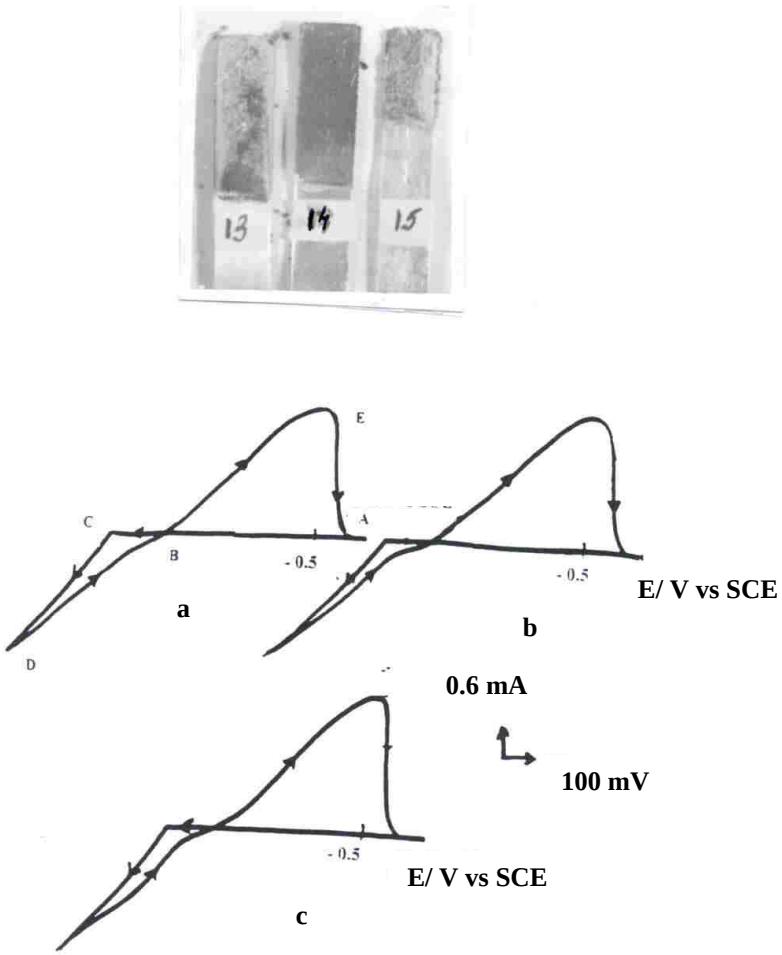

Figure 4. Cyclic voltammograms and cathodic deposits obtained in 1 M $ZnSO_4$ with fixed Pb^{2+} concentration (3.18 10^{-4} g/l) and increasing concentration of animal glue: a) 15 mg/l glue (electrode 13); b) 45 mg/l glue (electrode 14); 90 mg/l glue (electrode 15). Experimental conditions as in figure 1.

The aspect of cyclic voltammograms suffers some changes. At higher HCE concentration, they exhibit smaller anodic and cathodic peaks as in the absence of HCE, at the same Pb^{2+} concentration (Figure 1c). In all cases, the slopes of CD and BE portions decrease dramatically, showing a diminution of zinc deposition, hydrogen evolution rate and zinc corrosion, respectively. The 3D-hysteresis loop BCD diminishes its area proving a controlled nucleation.

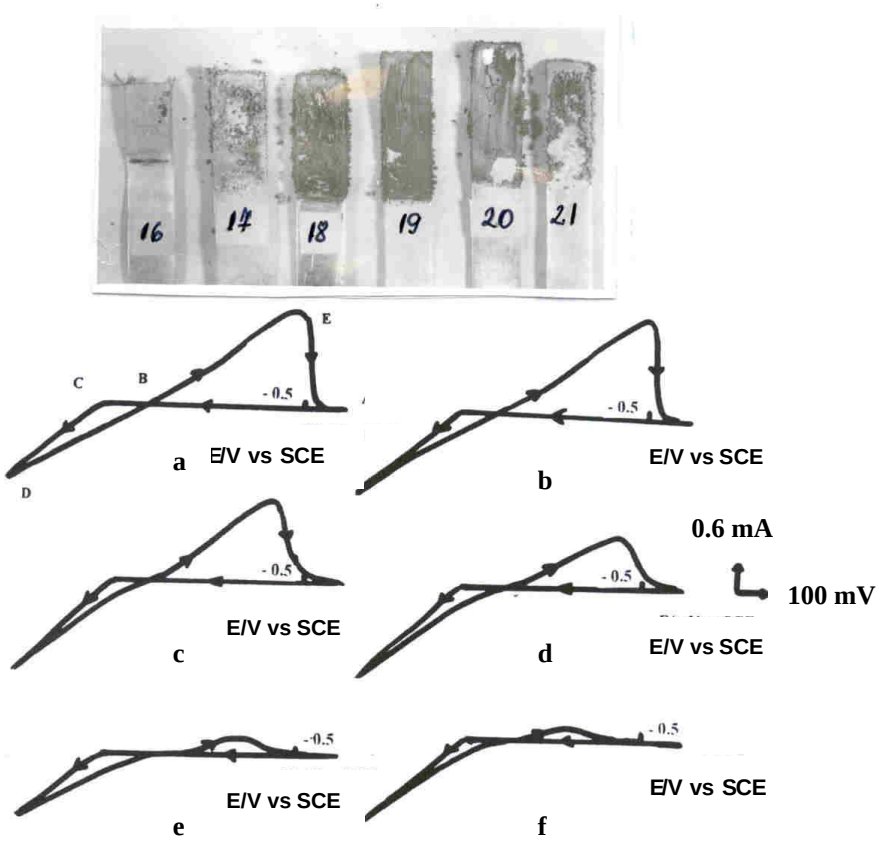

Figure 5. Cyclic voltammograms and cathodic deposits obtained in 1 M $ZnSO_4$ with fixed HCE concentration (30 mg/l) and increasing concentrations of Pb^{2+}: a) 0 g/l Pb^{2+} (electrode 16); b) 1,59. 10^{-4} g/l Pb^{2+} (electrode 17); c) 3.18.10^{-4} g/l Pb^{2+} (electrode 18); d) 6.37. 10^{-4} g/l Pb^{2+} (electrode 19); e) 1.27.10^{-3} g/l Pb^{2+} (electrode 20); f) 1.91. 10^{-3} g/l Pb^{2+} (electrode 21). Experimental conditions as in figure 1.

A different effect is put on evidence in the presence of animal glue. Increasing concentration of glue, at the same Pb^{2+} concentration (3.18 10^{-4} g/l) do not improve the cathodic morphology (Figure 4). An increase of anodic and cathodic peak area is observed and the slopes of CD and BD portions are almost unaffected. Thus, it can be concluded that the animal glue does not counteract the effect of Pb^{2+} ions.

This difference in the behavior of the two additives could be attributed to the formation of an adsorbed complex species $[Pb\ (HCE)]_{ads}$ when HCE is used, complex which exerts a beneficial inhibiting effect upon zinc electrodeposition. The above-mentioned complex species was put on evidence during lead electrodeposition and its formation is diffusion-controlled [11]. A similar complex does not appear in the case of animal glue.

The beneficial effect of HCE vanishes by increasing Pb^{2+} concentration at constant HCE (Figure 5). This leads to the idea that, as both additives act at the interface, a competition between them is possible, and Pb^{2+} adsorption prevails at higher concentration of this ion and, consequently, the result is a decrease of cathodic leveling degree.

CONCLUSIONS

The results indicated that Pb^{2+} ion has a deleterious effect on zinc electrodeposition from sulfate electrolyte. In presence of increasing Pb^{2+} concentrations, the morphology of zinc deposits was observed to change from smooth to dendritic, less adherent and the color changed from silver to a dark gray, proving a grain refining related to an inhibition effect. Pb^{2+} also affects the zinc deposition cyclic voltammograms. It increases the nucleation overpotential and diminishes the area of cathodic and anodic peaks, proving the inhibition of both the anodic and cathodic reactions.

The addition of horse chestnut extract (HCE) to the electrolyte counteracts this detrimental effect, leading to cathodic deposits with acceptable morphology, while same amount of animal glue doesn't have a similar beneficial effect. Increasing concentrations of glue, at the same Pb^{2+} concentration (3.18 10^{-4} g/l) do not improve very much the cathodic morphology.

REFERENCES

[1] R. Ichino, C. Cachet, R. Wiart, *J. Appl. Electrochem* 1995, **25**, 556

[2] C. Cachet, R. Ichino, R. Wiart, *Proc. 4th Internat. Symp. in Mineral and Metal Processing, Eds. P.E. Richardson, R. Woods & F.M.Doyle, The Electrochem. Soc.* 1996, 391

[3] D.R. Fosnacht, T.J.O. Keefe, *J. Appl. Electrochem*. 1980, **10**, 495

[4] E.J. Frazer, *J. Electrochem. Soc*. 1988, **135** (10), 2465
[5] A. R. Ault, E. J. Frazer, *J. Appl. Electrochem*. 1988, **18,** 583
[6] D. J. Mackinon, J. M. Brannen, P. L. Fenn, *J. Appl. Electrochem*. 1987, **17**,1129
[7] L. Mureşan, G. Maurin, L. Oniciu, D. Gaga, *Hydrometall.* 1996, **43** 345
[8] J. Bressan, R. Wiart, *J. Appl. Electrochem.* 1977, **7**, 505
[9] H. Krug, H. Borchers, *Electrochim. Acta* 1968, **13**, 2203
[10]. D. J. Mackinon, J. M. Brannen, R. C. Kerby, *J. Appl. Electrochem*. 1979, **9** 55
[11] L. Oniciu, L. M. Mureşan, V. A. Topan, D. Ghertoiu, *Rom. Pat*. 104,946, 1991
[12] L. Mureşan, R. Wiart, L. Oniciu, *J. Appl. Electrochem*. 1994, **24**, 332.

STUDIA UNIVERSITATIS BABEŞ-BOLYAI, CHEMIA, XLIV, 1-2, 1999

FLAME ATOMIC EMISSION SPECTROMETRIC DETERMINATION OF BARIUM USING THE METHANE - AIR FLAME. OPTIMIZATION OF THE FLAME AND INSTRUMENTAL PARAMETERS

LADISLAU KÉKEDY-NAGY and EMIL A. CORDOŞ

Universitatea "Babeş-Bolyai" Facultatea de Chimie şi Inginerie Chimică
3400 Cluj-Napoca, Arany J. 11, România

ABSTRACT. The effect of the flame composition, the observation height in the flame and the bandpass of the monochromator on the emission of barium in the methane-air flame were studied. The effect of Na, K, Mg, Sr, SO_4^{2-}, and PO_4^{3-} on the emission of barium was studied too. The best results were obtained with the barium line of 553.5 nm at the observation height of 5 mm, with the fuel rich flame and the slitwidth of 1.5 mm. The detection limit of 0.2 ± 0.1 mg/L was obtained at a significance level of 0.05, using the two step Neyman-Pearson criterion.

INTRODUCTION

Barium, as an alkali-earth metal, exhibits a low excitation and ionization energy (2.23 eV and 5.21eV, respectively), which makes suitable its determination by atomic emission spectrometry. Flame atomic emission spectrometry (FAES) is a simple, sensitive method for the determination of barium in low concentrations. As excitation source usually the high temperature C_2H_2-air, C_2H_2-O_2, C_2H_2–N_2O, H_2-air flames are used. The optimal conditions for the determination of barium in these flames were established, the detection limits are of order of 10^{-1}-10^{-3} mg/L [1-8].

The low temperature flames (~ 2000 K), as propane-butane-air (PB-A) are used in low performance commercial flame-photometers, designated for routine analysis. The methane-air (M-A) flame has similar properties (temperature, burning velocity etc) with the PB-A flame [9]. To our best knowledge the behaviour of barium in the M-A flame was not studied, and the detection limits are not known. The aim of this work is to study the behaviour of barium in the M-A flame, to optimize the flame and instrumental parameters in order to obtain the highest signal-to-noise ratio (S/N) and the lowest detection limit.

EXPERIMENTAL

Instrumentation

The experimental setup used was the same as described earlier [10,11].

Chemicals

The stock standard solution of barium (1000 mg/L) was prepared by dissolving 1.436 g of $BaCO_3$ (Specpure, Johnson Matthey Chemicals Limited, England) in 10 mL HCl 1:1 (analytical grade, Merck, Darmstadt, Germany) and diluted with double distilled water to 1 L. The other stock standard solutions (1000 mg/L) were prepared by dissolving the appropriate amounts of metals (Mg (Specpure, Johson Matthey Chemicals Limited, England)) and compounds ($SrCO_3$ (Specpure, Johnson Matthey Chemicals Limited, England) in corresponding acid. KCl, NaCl (analytical grade, Reactivul, Bucuresti, Romania), HCl, H_2SO_4 and H_3PO_4 (analytical grade, Merck, Darmstadt, Germany)) were dissolved and diluted in double distilled water, respectively. For further dilutions double distilled water was used in all cases.

Procedure

The behaviour of barium in the M-A flame was observed in the flame up to h = 18 mm over the burner head (in1mm steps), at three different flame compositions: 0.88; 1.00; 1.12 expressed in relative stoichiometric units (RSU). Four replicate measurements were made in each case. The mean, the standard deviation, the S/N and the signal-to-background ratio (S/B) were calculated for each h and flame composition investigated. The homogeneity of the means was tested by the F test at a significance level of 0.05. The burner was held parallel with the optical axis of the spectrophotometer. The slit width of the monochromator was of 0.1 mm, the sensitivity of the strip chart recorder was different in different spectral domains in function of the intensity of the emission lines and the background observed. For a given set of determinations the sensitivity was kept constant.

RESULTS AND DISCUSSION

The emission spectrum of barium

The emission spectrum of barium in the M-A flame was determined in the 200 – 800 nm spectral domain. The spectrum of the flame alone was recorded first, then that of the flame in the presence of 1000 mg/L barium solution in the flame. Using spectral tables only the resonance atomic line with λ = 553.5 nm was identified. Barium emits a broad molecular spectrum too, in the spectral domain of 450.0 – 580.0 nm. The molecular emission band belongs to BaO with the band-heads at λ = 496.5 nm, 503.0 nm, 508.6 nm, 549.2 nm, 571.8 nm and to BaOH with the band-heads at λ = 487.0 nm, 512.0 nm, 520.3 nm, respectively [12]. Intensive band-heads lines are those of 487.0 nm, 508.6 nm, 520.3 nm, 549.2 nm in the M-A

flame. The emission atomic line is superimposed on the molecular band spectrum, which make difficult the precise quantitative determination of barium.

Optimization of the flame and instrumental parameters,

determination of the Analytical emission line

The aim is to obtain those values for the flame composition and observation height h for whose the S/N ratio is maximal. The composition of the flame was kept constant, at 1.12 RSU. The concentration of the calibration solution was of 100 mg/L. The analytical signal, intensity (I), was measured for the most intensive lines selected, at 487.0 nm, 520.3 nm and 553.5 nm, respectively. The variation of the line intensities versus observation height over the burner head is represented in Fig.1.

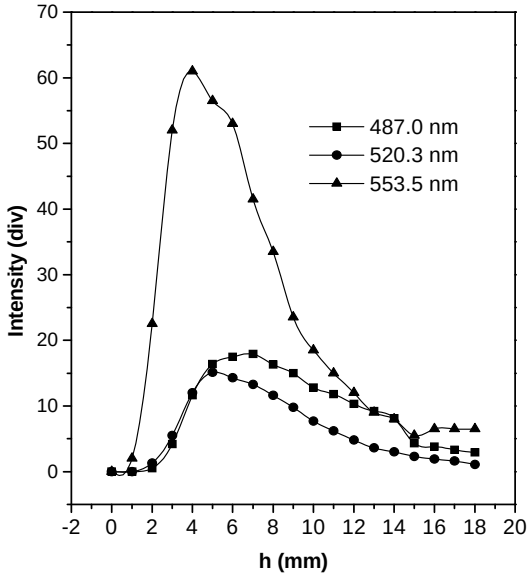

Figure 1**.** The intensity of different barium lines versus observation height (h)

For the quantitative estimation of the results at different wavelengths only the maximal value of the analytical signal (I_{max}) for each line was selected. In order to get comparable data the corrected intensity (I_{cor}) and the relative intensity (I_{rel}) for each line were calculated, considering the sensitivity of the chart recorder. The reference sensitivity of 1.10^{-9} A/div and the reference line was the weakest one. The S/B ratio was determined in the same way. The results are summarized in Table I.

Table I

The relative intensities of the emission lines of barium in the M-A flame

Wavelength (nm)	Emittent	h(mm)	I_{max} (div)	$I_{Corr.}$ (div)	I_{rel}	S / B
487.0	BaOH	6-7	17.9	17.9	1.18	1.72
520.3	BaOH	5	15.1	15.1	1.00	1.98
553.5	Ba I	4-5	12.2	122.0	8.07	17.40

The intensity of the molecular emission lines is the same order of magnitude, the most intensive being the resonance atomic emission line at 553.5 nm. This line is excited in the primary reaction zone in the flame, at 4-5 mm over the burner head. The molecular species, BaOH, is excited in the interconal zone in the flame, where the OH radicals reach its maximum concentration. This fact suggests that the formation and the excitation of BaOH take place *via* these radicals [13]. The S/B ratio is low, due to the high value of the flame background in relation to the line intensity.

The influence of the flame composition and of the observation height on the analytical signal for the most sensitive line was investigated using three flame compositions (0.88, 1.00, 1.12 RSU) and at the concentration level of 100 mg/L barium. The data were processed by using the MicroCal Origin™ Software package, version 5.0 (MicroCal Software Inc., MA, USA) and plotted as 2D contour map (Fig.2).

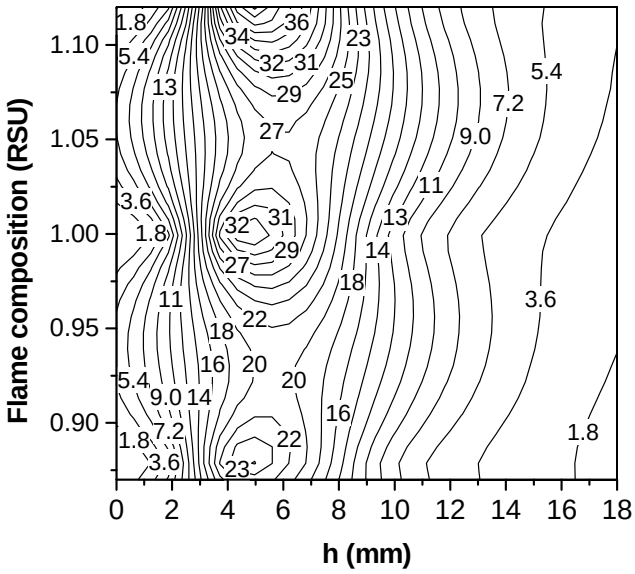

Figure 2. The 2D contour map of the emission of the 553.5 nm barium-line vs. observation height and flame composition. The labels on the plot indicate the grid matrix values.

The analytical signal depends both on observation height and flame composition. The emission increases slowly with the increase of the methane content of the flame, being the highest in fuel-rich conditions. The maximum emission intensity was observed at the same height of 5 mm over the burner head, regardless of flame composition. The standard deviation of all means was homogeneous, the magnitude of the S/N ratio being decided by the magnitude of the mean. In conclusion, the optimal conditions for the quantitative determination of barium in the M-A flame are λ = 553.5 nm, h = 5 mm and flame composition 1.12 RSU.

The influence of the spectral bandpass of the monochromator on the analytical signal, S/N and S/B ratio

The spectral bandpass of the monochromator, determined by its slitwidth (SW), influences in different manner the amplitude and the fluctuations of the emission signal. Therefore the optimal value of SW can be determined for which the S/N ratio is maximum. The flame and instrumental parameters used were the optimal ones, determined earlier. The influence of the slitwidth on I, the S/N and S/B ratio was studied in the 0.1 – 1.5 mm domain, in steps of 0.1 mm, using a 100 mg/L barium solution. The results show that the emission signal increases linearly with the spectral bandpass of the monochromator (I = -2.798 + 18.664SW, r = 0.9930). The standard deviation of the means increases slowly with the increase of SW but remains homogeneous in the entire SW domain. The maximum value of S/N was of 187.5 at the SW of 1.4 mm. The S/N ratio decreases uniformly, its variation could be approximated with a third order polinomial function ($S/B = 2.348 - 2.130SW + 0.931SW^2 - 0.140SW^3$, r = 0.9949). This is the consequence of the fact that the 553.5 nm barium line is superimposed on the BaOH emission molecular band and the flame background.

In conclusion, the slitwidth could be increased up to 1.5 mm without a significant decay of the S/N ratio, but the broader SW diminishes seriously the S/B ratio.

Interferences

The effect of Na, K, Mg, Sr, SO_4^{2-} and PO_4^{3-} on the emission signal of barium of 10 mg/L was investigated. The experimental conditions were the optimal ones, determined previously. In the presence of Na, K, Mg and Sr the background signal was measured at 552.0 nm. The variation of the barium emission signal versus the concentration of the interferents are represented in Fig 3.

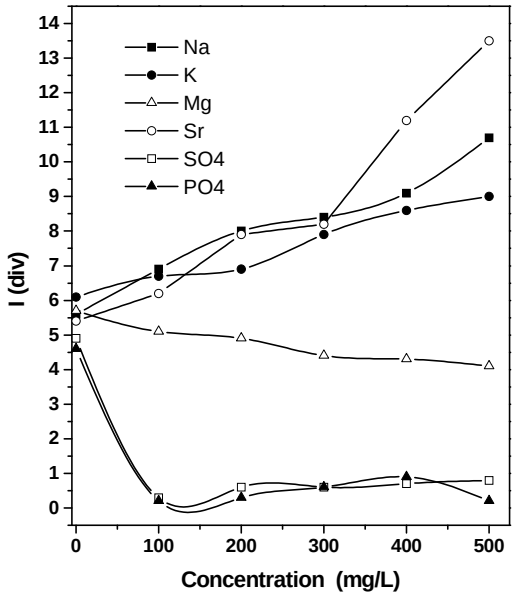

Figure 3. Influence of Na, K, Mg, Sr, SO_4^{2-}, and PO_4^{3-} on the emission signal of barium of 10 mg/L.

The barium emission signal increases in the presence of Na, K and Sr as the result of the flame background signal enhancement. Sr and K over the concentration of 300 mg/L exhibit a releasing effect, increasing efficiently the net barium emission signal too. Mg, SO_4^{2-} and PO_4^{3-} ions decrease the barium emission signal, due to formation of stable, refractory compounds in the flame.

Calibration, determination of the detection limit

For the determination of the detection limit the variation of the analytical signal versus concentration was studied in the 1-1000 mg/L barium concentration range. Four calibration curves were plotted; one curve covered only one order of magnitude of concentration. Each calibration curve was established by using six standard solutions. Six replicate measurements were made at each concentration level. The measurements were carried out at two wavelengths: at 553.5 nm and, for background correction, at 552.0 nm. The homogeneity of the means and the linearity of the calibration curve were tested. The equation of the regression line, the confidence limits and the coefficient of correlation (r) were calculated with the least squares method. The detection limit was calculated using the two step Neyman-Pearson model [14,15], for the fixed values of $(P_{10})_0 = 0.025$ and $(P_{11})_d = 0.975$. The results are summarized in Table II.

Table II

Calibration data of barium determination in the M-A flame

Concentration range (mg/L)	Sensitivity (A/div)	Slit width (mm)	Equation of the calibration curve	Detection limit (ppm)
1000 - 100	$20*10^{-9}$	0.1	I = -0.0032 + 0.0679*C r = 0.9999	7 ± 3
100 – 10	$5*10^{-9}$	0.1	I = -0.385 + 0.316*C r = 0.9998	2 ± 1
10 – 1	$1*10^{-9}$	0.1	I = -0.348 + 1.267*C r = 0.9992	0.2 ± 0.1
10 – 1	$50*10^{-9}$	1.5	I = -0.456 + 0.969*C r = 0.9993	0.2 ± 0.1

The concentration-intensity relationship is linear over three orders of concentration domain (1 – 1000 mg/L), regardless of the barium concentration. The sensitivity of the determinations can be enhanced, by using a broader slitwidth. The detection limits obtained for each concentration range are also summarized in Table II. These values are low but they are about one order of magnitude higher than those obtained with acetylene flames. The broader slit width does not allow attaining a lower the detection limit.

CONCLUSIONS

In the M-A flame barium exhibits an atomic and molecular spectrum. The most intensive line (the analytical line) is the atomic line at 553.5 nm. The intensity of the barium lines vary with the composition of the flame and observation height over the burner head. In the fuel rich flame the optimal excitation zone is at 5 mm over the burner head. The observation height for the maximum intensity is independent of the flame composition. In order to increase the S/N ratio the slitwidth of the monochromator could be increased till 1.5 mm without decay of the S/N ratio and attaining a lower detection limit. Mg, SO_4^{2-} and PO_4^{3-} ions decrease the barium emission signal. The calibration curves (in optimal experimental conditions) are linear in the 1 - 1000 mg/L concentration range, the detection limit obtained being of 0.2 ± 0.1 mg/L.

REFERENCES

[1] J.D. Winefordner, *Spectrochemical methods of analysis*, New York., Wiley Interscience, 1971, p.130.
[2] H. Matusiewicz, *Spectroscopy (Springfield,-Oreg)*, 1986, **1**, 32.
[3] B. M.Fidel'man, N.V. Bondareva, *Zh.Anal.Khim.*, 1988, **43**, 1959.
[4] A.M. Ervin, R. Panayappan, J.C. Cooper, *Anal.Lett.*, 1988, **21**, 2117.
[5] G. Schwedt, *LaborPraxis*, 1990, **14**, 620.
[6] M. Jerrow, I.L. Marr, M.S. Cresser, *Anal.Proc. (London)*, 1991, **28**, 40.
[7] M. Billah, T. Honjo, K. Terada, *Fresenius' J.Anal.Chem.*, 1993, **347**, 107.
[8] Y.Q Cai, Q.F Ni, *Lihua.Jianyan, Huaxue.Fence.*, 1994, **30**, 227.
[9] A.G. Gaydon, H.G. Wolfhardt, *Flames, their Structure, Radiation and Temperature*, Chapman and Hill, New York, 1970.
[10] L. Kékedy Nagy, *Studia*, 1992, **37**, 109.
[11] L.Kékedy-Nagy, E.A.Cordos*, ACH Models In Chemistry*, 1999, **136**, 237.
[12] R. Mavrodineanu, H. Boiteux, *Flame spectroscopy*, John Wiley, New York, 1965, p.371.
[13] E. Cordoş, L. Kékedy-Nagy, *Studia*, 1992, **37**, 61.
[14] C. LIteanu, I. Rîcă, *Statistical Theory and Methodology of Trace Analysis,* John Wiley, New York, 1980.
[15] D.L. Massart, B.G.M. Vandeginste, S.N. Deming, Y. Michotte, L. Kaufman, *Chemometrics: a textbook,* Elsevier, New York, 1988.

STUDIA UNIVERSITATIS BABEŞ-BOLYAI, CHEMIA, XLIV, 1-2, 1999

VAPOR-PHASE OXIDATION OF CYCLOHEXANE

FLORIN PĂTCAŞ

"Babeş-Bolyai" University of Cluj-Napoca, Department of Chemical Technology, M. Kogalniceanu 1, RO-3400 Cluj-Napoca, Romania

ABSTRACT. In this review the reported literature data for the gas phase oxidation of cyclohexane are systematically presented and discussed. The production of oxygen-containing organic products by direct gas phase oxidation of cyclohexane is practically imposible, although it is allowed thermodynamically. Possibilities for the functionalization of cyclohexane towards valuable products such as cyclohexene or cyclohexadiene by gas phase oxidation over solid catalysts are emphasized.

CONTENS

1. INTRODUCTION

The basis of raw materials for the petrochemical industry changed decisively in the eighties. The use of previously disregarded paraffins and even of synthesis gas for the production of valuable chemical products is more and more envisaged as an alternative to the reactive but expensive and scarce olefins which were extensively used by now. In order to employ paraffins in the manufacture of chemicals, their activation or functionalization is necessary. With this respect the catalytic oxidation to oxygen-containing

products or the oxidehydrogenation of the paraffin leading to the homologous olefins are applicable, arising both the economic and the scientific interest [1-7]. Cyclohexane is an important basic material for many valuable intermediate products [8-10], whereby alone the production of cyclohexanol and cyclohexanone for the caprolactam production is for instance $1.6 \cdot 10^6$ to/year and that for adipic acid is $1.2 \cdot 10^6$ to/year [11].

Cyclohexanol and cyclohexanone were formerly manufactured from phenol but today the main raw material is cyclohexane. The oxidation is performed in the liquid phase with air by using homogeneous catalysts (H_3PO_4 or organic salts of Co^{2+} or Mn^{2+}). To avoid the further conversion of the desired products cyclohexanol/cyclohexanone to higher oxidized products, the reaction is driven at small conversion degrees (3-10 %). The necessity of recycling the unreacted cyclohexane, as well as the difficult separation of the products cause thereby high energy and capital outlays. The production of cyclohexanol/cyclohexanone from cyclohexene, although a very attractive process, has itself so far only little established [11, 12]. Reason for it is the difficult production of cyclohexene.

The production of cyclohexene from butadiene and ethylene is technically hardly realizable [13]. The cyclohexene selectivity achieved by partial hydrogenation of benzene is so far merely larger than 30 % [11]. The main product formed thereby is cyclohexane, which must be recycled to a new processing. By using another reaction route cyclohexene can be manufactured industrially by dehydration of the cyclohexanol both in liquid phase using sulfuric acid, and in the gas phase over alumina or alumosilicates after a cost-intensive technology [14]. Data regarding the direct functionalization of cyclohexane to cyclohexanol and cyclohexanone by a catalytic vapor-phase oxidation are not available within the present level of knowledge. On the basis of the literature data some new possibilities for the functionalization of cyclohexane can be envisaged, e.g. the oxidative dehydrogenation to cyclohexene and/or to 1,3-cyclohexadiene after the reaction (1):

(1)

The production of cyclohexene by the heterogeneously catalyzed oxidehydrogenation of cyclohexane could be thereby a new reaction way for the technical cyclohexanol/cyclohexanone production. At the same time new possibilities for the production of other technically interesting products arise, e.g. adipic acid, cyclohexene oxide, 1,2-cyclohexandiol, cyclohexyl aldehyde, cyclohexyl benzene etc. The oxidative dehydrogenation of cyclohexane to cyclohexene and cyclohexadiene is also scientifically very interesting. With this respect some promising research results were recently reported [15-17].

2. THERMODYNAMIC FEATURES OF CYCLOHEXANE OXIDATION AND OXIDEHYDROGENATION

In the gas phase system consisting of cyclohexane and air the following reactions become possible, which can be divided in cyclohexane oxidehydrogenation (2-4), oxidation (5-8) and dehydrogenation (9-11), as well as the reactions of the intermediate products (12-20).

Reactions of cyclohexane:

		$\Delta_r H^o_{298}$/kJ·mol^{-1} [18, 19]	
$C_6H_{12} + 1/2\ O_2 \longrightarrow C_6H_{10} + H_2O$		–124	(2)
$C_6H_{12} + O_2 \longrightarrow C_6H_8 + 2\ H_2O$		–255	(3)
$C_6H_{12} + 3/2\ O_2 \longrightarrow C_6H_6 + 3\ H_2O$		–520	(4)
$C_6H_{12} + 1/2\ O_2 \longrightarrow C_6H_{11}OH$		–172	(5)
$C_6H_{12} + O_2 \longrightarrow C_6H_{10}O + H_2O$		–349	(6)
$C_6H_{12} + 6\ O_2 \longrightarrow 6\ CO + 6\ H_2O$		–1992	(7)
$C_6H_{12} + 9\ O_2 \longrightarrow 6\ CO_2 + 6\ H_2O$		–3690	(8)
$C_6H_{12} \longrightarrow C_6H_{10} + H_2$		+118	(9)
$C_6H_{12} \longrightarrow C_6H_8 + 2\ H_2$		+229	(10)
$C_6H_{12} \longrightarrow C_6H_6 + 3\ H_2$		+206	(11)

Reactions of the intermediary formed organic products:

$C_6H_{10} + 1/2\ O_2 \longrightarrow C_6H_8 + H_2O$	–13	(12)
$C_6H_{10} + O_2 \longrightarrow C_6H_6 + 2\ H_2O$	–396	(13)
$C_6H_{10} + 11/2\ O_2 \longrightarrow 6\ CO + 5\ H_2O$	–1868	(14)
$C_6H_{10} + 17/2\ O_2 \longrightarrow 6\ CO_2 + 5\ H_2O$	–3565	(15)
$C_6H_8 + 1/2\ O_2 \longrightarrow C_6H_6 + H_2O$	–265	(16)
$C_6H_8 + 5\ O_2 \longrightarrow 6\ CO + 4\ H_2O$	–1737	(17)
$C_6H_8 + 8\ O_2 \longrightarrow 6\ CO_2 + 4\ H_2O$	–3435	(18)
$C_6H_6 + 9/2\ O_2 \longrightarrow 6\ CO + 3\ H_2O$	–1472	(19)
$C_6H_6 + 15/2\ O_2 \longrightarrow 6\ CO_2 + 3\ H_2O$	–3170	(20)

It would be desirable to bind oxygen atom in the cyclohexane molecule in such a way that the valuable products such as cyclohexanol or cyclohexanone develop according to the reactions (5) or (6). As shown by the reaction free-enthalpy as a function of temperature represented in Fig. 1 a, b after [16], the formation of cyclohexanol (5) and cyclohexanone (6) are thermodynamically possible by gas phase oxidation of cyclohexane in the

range of practice-usual temperatures. The formation of cyclohexanone (6) is even more favorable than the formation of cyclohexene (2) or cyclohexadiene (3) being exceeded only by the formation of benzene (4) (s. Fig. 1 a).

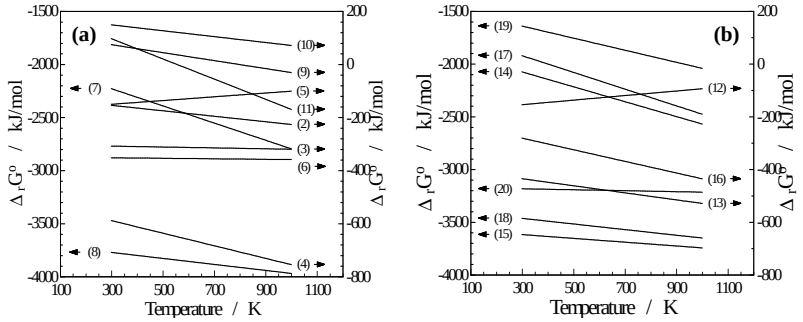

Fig. 1. Reaction free-enthalpy as a function of temperature for the reactions of oxidation, oxidehydrogenation and dehydrogenation in accordance with equations (2-20)

Despite the favorable thermodynamics, no results regarding the formation of cyclohexanol/cyclohexanone by gas-phase oxidation of cyclohexane are known so far. This fact could be explained by the much faster conversion of the formed intermediate products in the kinetically controlled cyclohexane activation, to the thermodynamically stable inorganic products. Here it must be noticed that the reaction free-enthalpy for the formation of the inorganic products is an order of magnitude higher than that for the formation of organic products.

In order to suppress the formation of benzene and the inorganic products, the kinetic control of the reaction is necessary. This is enabled by the use of suitable catalysts and of defined short retention times. The oxidative dehydrogenation of cyclohexane (2-3) is thermodynamically more favorable in comparison to the pure dehydrogenation of cyclohexane (s. Fig. 1 a). The formation of cyclohexadiene both by benzene hydrogenation and by cyclohexane dehydrogenation is thermodynamically unfavorable [18, 19]. However at higher temperatures the stability of the formed organic products is questionable. Within the oxidative dehydrogenation the thermodynamic driving force is increased and the conversion of cyclohexane to cyclohexene and/or cyclohexadiene is favored [18]. While the pure dehydrogenation is an endothermic process, in the presence of oxygen there is energy that is set free. Therefore, there are several processes known in the industrial practice where an endothermic reaction is coupled with an exothermic one, which supplies the necessary energy for the former. An example is the oxidehydrogenation of the methanol to formaldehyde over silver catalysts. Similar technologies were also developed for the dehydrogenation of

ethylbenzene to styrene. The oxidative dehydrogenation of cyclohexane is until now less known. For this reason systematic investigations regarding cyclohexane oxidation or oxidehydrogenation are interesting.

3. VAPOR-PHASE HOMOGENEOUS OXIDATION OF CYCLOHEXANE

3.1. Noncatalytic vapor-phase oxidation

On the search for improving the possibilities of manufacturing oxygen-containing organic compounds from oil products, cyclohexane already drew the attention of specialists. Estradare reported in 1933 [20] about the non-catalysed vapor-phase oxidation of a gas mixture consisting of cyclohexane and oxygen in a mole ratio of 1/4 in a glass tube filled with 3 mm glass rods. The lowest temperature of oxidation was 340 ℃. Per oxides were observed to form below that temperature but disappeared when the temperature was raised with 10-15 ℃ above it. Carbon monoxide and dioxide were both formed at 340 ℃, the maximum yield being at 400 ℃ of about 65 % CO and 18 % CO_2. By using a gas mixture of cyclohexane/air of 1/8 molar ratio in a quartz vessel of 24 mm diameter at 316 ℃ Ivan ov [21] has isolated a peroxide in the non-volatile liquid product. The waste gases contained 10.8 % O_2, 1.2 % CO, 5.6 % CO_2 and 0.7 % hydrocarbon. Hoot et al. [22] studied the kinetics of the gas phase oxidation of cyclohexane in a flow reactor, on a mixture of cyclohexane/air of 1/3 mol/mol with a contact time of 1.4 sec. The effluent gas was analyzed for CO, CO_2, O_2, water and aldehydes (determined as formaldehyde). Additionally cyclohexanone, pentanal, acrolein and acetaldehyde were detected in the condensed product mixture. The tests indicated the presence of acids, unsaturated hydrocarbons, peroxides, and cyclohexane oxide. The amount of oxygen containing organic products is very low and exceeds barely ca. 25 meq. per 100 g cyclohexane reacted. The presence of cyclohexene oxide was also suspected. By investigating the influence of reaction temperature on the product formation, the yield of CO, CO_2 and water achieved a maximum at approx. 380-400 ℃ . The effect of the residence time showed that an induction period was necessary for the reaction. This shows the accumulation of products, which causes the chain to branch (degenerate branching). The time for the induction decreases with increasing reaction temperature.

The formation of hydroperoxides during the gas-phase oxidation of cyclohexane [23] indicated the occurrence of the elementary reactions:

$$ROO\cdot + RH \longrightarrow ROOH + R\cdot \qquad (21a)$$

$$R\cdot + O_2 \longrightarrow ROO\cdot \qquad (21b)$$

. . .

An aldehyde or peroxide intermediate in this temperature region could play an autocatalytical role. It is known that the oxidation stability of aldehydes decreases with increasing temperature above 350 ℃. Increased temperatures would decrease the aldehyde concentration, which in turn decrease its autocatalytic effect. This can account for the decrease of total reaction rate in the temperature range 450 ℃ to 53 0 ℃. The test results have shown that during the gas phase oxidation of cyclohexane firstly aldehydes, among other formaldehyde, are formed, which are transformed in a subsequent reaction to CO and CO_2. At 410 ℃ benzene was also identified in a propor tion of 3 %, related to the reacted cyclohexane. Other oxygen-containing compounds occurred only when the reaction time was higher than 0.8 s. This shows the existence of an induction period. Furthermore a proportional dependence between the yield of oxidation products and the oxygen concentration in the gas mixture was determined. The increase of the ratio between the reactor surface and the reactor volume (A/V) of approx. 2 to 12 cm^2/cm^3 led to a clear inhibition of the cyclohexane oxidation. A further increase of the A/V ratio on approx. 28 cm^2/cm^3 did not influence the conversion rate. The investigations carried in order to clear up the reaction mechanism still permit, irrespective of its representation from today's view, the following conclusions:

- a number of single and consecutive reactions are possible in the vaporphase oxidation of cyclohexane;
- the reactions begin to accelerate after an induction period;
- the oxygen-containing organic products result from the autocatalytic oxidation on the basis of some peroxides formed in the incipient phase of the process;
- the yields of oxygen-containing products depend on the temperature, reaction time and feed composition.

3.2. Oxidation of cyclohexane by addition of gaseous additives

During the oxidation of n-alcanes having secondary C-atoms (propane, butane) in the presence of gaseous HBr as an activator, Bell et al. [24], Rust et al. [25] and Nawrocki et al. [26] achieved yields of carbonyl compounds up to 75 %. On the contrary in the case of cycloalcanes (cyclopentane, methylcyclopentane, cyclohexane) much smaller yields of carbonyl compounds were achieved, which is accounted for by the formation of condensation products under the effect of HBr. On the other hand the formed carbonyl compounds and other oxygen-containing intermediate products are less stable than the hydrocarbons. Nawrocki et al. [26] fed 15 ml/min HBr to a gas mixture of 30 ml/min gaseous cyclohexane, N_2 and O_2. These reactants were brought in a 450 cm^3 large glass bulb at 220 ℃. The following results were obtained:

- the reaction consumed 40 % of the oxygen but only 8 % of this was accounted for as CO, CO_2 and H_2O;
- the oxidized mixture contained cyclohexanone and small amounts of diketones.

Hoot et al. [22] examined the effect of other activators in the gas-phase, like I_2 (0.3 wt. %), N_2O_4 (1.1 wt. %), $Pb(C_2H_5)_4$ (0.2 wt. %), aniline (1.0 vol. %), cyclohexylamine (1.0 vol. %), isoamyl nitrite (1.0 vol. %) and diethyl ether (1.0 vol. %) in the oxidation of cyclohexane. The composition of the product stream or the condensed products hardly differs from those without additives.

4. HETEROGENEOUS VAPOR-PHASE CATALYZED OXIDATION AND OXIDEHYDROGENATION OF CYCLOHEXANE

Few data were reported in the literature so far on the oxidation and oxidative dehydrogenation of cyclohexane over solid catalysts in the gas phase. The reason could be the failure of the attempts to insert oxygen atoms in the cyclohexane molecule and in particular the preservation of the 6-carbon ring against further oxidation. Although the formation of valuable products such as cyclohexanol, cyclohexanone and adipic acid by gas phase oxidation of cyclohexane is thermodynamically possible, no one has reported so far the formation of such products by the catalytic gas phase oxidation of cyclohexane. Berezin et al. [23] explained that the formation of valuable products by the gas phase oxidation of cyclohexane is improbable, in opposition with liquid phase oxidation, because of the completely different mechanisms. While the oxidation reaction in the liquid phase takes place at 120-140 ℃, a higher temperature of around 200 ℃ i s necessary in order to start the reaction in the gas phase. This causes a more intense C–C bond rupture so that the products of the gas phase oxidation contain less than 6 carbon atoms. The major products are therefore formaldehyde, CO, CO_2 and H_2O. However the authors do not deal with the important role of the catalyst.

The gas phase oxidation of cyclohexane can lead to organic products of oxidehydrogenation (CH), oxygen containing organic compounds (CHO) and inorganic products (CO_x) according to the reaction scheme (22).

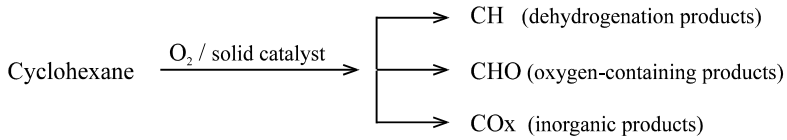

(22)

In order to understand the possibilities and limits of the gas phase oxidation of cyclohexane and the factors controlling this process, the results reported in the literature will be discussed from the point of view of the oxidation products as presented in the above reaction scheme, but divided according to the main catalyst types.

4.1. Oxide supported metal catalysts

The oxidehydrogenation of cyclohexane over catalysts consisting on metals deposited on oxide carriers such as Pt/Al_2O_3 or Pd/Al_2O_3 is always accompanied by the deep oxidation to CO_2 [27, 28]. A small part of cyclohexane is dehydrogenated to cyclohexene and benzene. The selectivity to benzene decreases and the selectivity to CO_2 increase with increasing the partial pressure of O_2. In experimentally identical conditions the Pd/Al_2O_3 catalyst favors the total oxidation at variance to Pt/Al_2O_3, but the addition of CCl_4 to the reaction mixture leads to a decreasing activity and to an increasing selectivity to benzene [27]. The carbon balance and the appearance of the used catalysts showed the formation of coke as a result of cracking and molecular growth of the hydrocarbon species present [28]. No oxygenated organic compounds were identified.

4.2. Metal oxides

The oxidation of cyclohexane over unsupported metal oxides catalysts leads to the formation of inorganic products (CO, CO_2, H_2O) and dehydrogenation products (cyclohexene, benzene) in almost all works [22, 23, 30, 31]. Only a few authors reported the formation of small amounts of oxygen-containing organic compounds, usually maleic acid [23], and/or maleic acid anhydride [7, 23, 32]. Most of the results presented in the literature regarding cyclohexane oxidation on metal oxides [22, 23, 30-34] showed that the dehydrogenation reactions are always accompanied by the deep oxidation to inorganic compounds. For this reason these parallel reaction pathways will be discussed together, the control of the catalytic process towards one or another direction being considered as particular cases of a more general picture.

The unsupported metallic oxides catalysts, displayed in the Table 1, were examined by Hoot et al. [22] who found only CO_2 and H_2O as oxidation products of cyclohexane. As a measure for activity the lowest temperature of incipient reaction for the gas-phase oxidation of cyclohexane was indicated.

In another activity test, where the temperature to achieve a conversion grade of 80 % was determined during the cyclohexane total oxidation, Stein et al. [35] set up the following activity series for a set of metallic oxide catalysts:

$Co_3O_4 > Mn_2O_3 > Cr_2O_3 > NiO > TiO_2 > ThO_2 > \alpha\text{-}Fe_2O_3 > CeO_2 > CuO > \gamma\text{-}Al_2O_3 > MgO > Pb_3O_4 > BeO > SiO_2 > WO_3 > V_2O_5 > ZnO > CaO > ZrO_2$

The different surface areas of the catalysts were however not considered.

Table 1

Catalysts and lowest temperature of incipient reaction for gas-phase oxidation of cyclohexane after Hoot et al. [22]

Catalyst	Lowest temperature of incipient reaction, ℃	Catalyst	Lowest temperature of incipient reaction, ℃
V_2O_5	240	V-Zeolite	336
Ag_2O	292[a)]	CoO	207
$CuCr_2O_4$	170 [b)]	MnO_2	342
$PbMoO_4$	297	ZrO_2	444
UVO_4	294	$Sn_3(VO_4)_2$	348
MoO_3	330	Shell 105 [c)]	340
Fe_2O_3	288		

Reaction conditions: Temperature T = 150-550 ℃, re tention time t = 0.2-12 s; $R_{cyclohexane/air}$ = 0.1-2 or 0.2-1.25 for Ag_2O and V_2O_5. [a)]Using water as a dilutant, lowest temperature of incipient reaction began at 503 ℃; use of 1 % cyclohexanone in cyclohexane feed lowered temperature to 198 ℃. [b)]1 % cyclohexanone was added to cyclohexane feed to act as reaction initiator. [c)]Dehydrogenation catalyst: $Fe_2O_3 \cong 70$ %, $Cr_2O_3 \cong 30$ %, $CuSO_4 = 1$ %, $KNO_3 = 0.5$ %;

By analysing the results obtained by Stein et al. [35, 36], Golodets [37] presented a correlation between the activity of oxide catalysts expressed as the temperature to achieve a conversion grade of 80 % (T_{80}) with the bonding energy of lattice oxygen of the oxide (q_s) (Fig. 2).

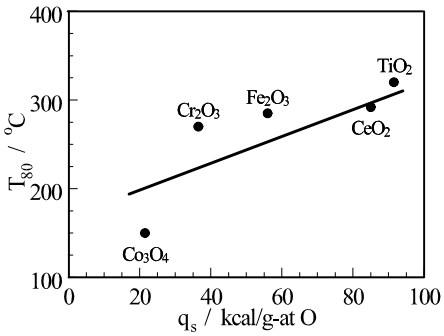

Fig. 2. A correlation of the catalytic activity for the oxidation of cyclohexane (T_{80} is the reaction temperature for 80 % conversion) with the bonding energy of lattice oxygen of the oxide, q_s [37]

After Margolis et al. [38] the catalyzed total oxidation of cyclohexane follows a second-order reaction rate. An activation energy of 158 kJ/mol was determined over a $MgCr_2O_4$ catalyst while over a $CuCr_2O_4$ catalyst it was 73.6 kJ/mol. The reaction order higher than 1 was not reproduced in the later experiments [30, 31].

Recent researches regarding the kinetics and mechanism of the total cyclohexane oxidation yielded a formal reaction order of cyclohexane of 0.8÷1.0 over $CuMn_2O_4$ and 0.65÷0.8 over $LaMnO_3$ in an oxidant reaction mixture (cyclohexane concentration between 0.01-0.40 vol. %) [31]. The apparent activation energy was of about 58 kJ/mol ($CuMnO_4$) and 56 kJ/mol ($LaMnO_3$). The partial pressure of oxygen has a slight influence only at lower temperatures (below 270 °C), at higher temperatures the reaction order of oxygen being close to zero. It was shown that the total oxidation was controlled at low temperatures by the surface reaction between electrophilic oxygen and adsorbed cyclohexane (a Langmuir-Hinshelwood mechanism) while at higher temperatures the rate controlling step was the reactive interaction of gas-phase cyclohexane with the surface oxygen species (Eley-Rideal mechanism).

At the same time, the experimental results suggest that the global oxidation process occurs by consecutive transformation reactions of cyclohexane (1) to cyclohexene (2) and benzene (3) and also by parallel oxidation reactions to CO (4) and CO_2 (5) after the network in Fig. 3.

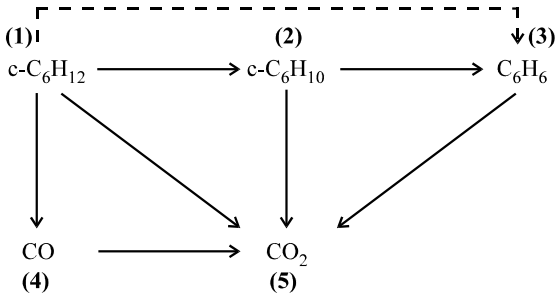

Fig. 3. The reaction network for the gas phase cyclohexane oxidation over $CuMn_2O_4$ after [31].

Under similar experimental conditions apparent activation energies of about 51 kJ/mole for Cr_2O_3 and 90 kJ/mole for ZnO were obtained [30]. The association of zinc and chromium cations inside the same oxide frame apparently led to no synergistic effect; thus, zinc chromite obeyed the rule of Boreskov [39]. The activation energy of about 83 kJ/mole indicated the predominance of the redox mechanism through lattice surface oxygen, although the electronic properties of $ZnCr_2O_4$ (p-type semiconductor, very

close to Cr_2O_3) should allow it to chemisorb easily oxygen. It is possible that the spinel lattice exposes less free chromium cations able to bound molecular oxygen than Cr_2O_3. A difference between $ZnCr_2O_4$ and Cr_2O_3 is the greater selectivity of the former towards organic products, especially benzene (Fig. 4, after [30]). Since as shown by electric measurements the electronic properties of the chromium-based catalysts are actually close it may be suggested that there are not the bulk properties, but the chemical nature of the oxide surface that decides the selectivity features of the catalyst.

As Kung et al. [5] have shown, the insertion of hard reducible cations in the lattice of an oxide catalyst (as for example, MgO in V_2O_5) led to an increase in selectivity towards dehydrogenation products. This fact is attributed to the oxygen atoms being bounded both to the reducible and to the hard-reducible cation, thus rendering them less disposable for an insertion in the organic molecule which is the first step towards total oxidation. This may be the source for the higher yield of dehydrogenation products in the case of zinc chromite. The low activation energy over chromium oxide indicated also an important share of the associative mechanism by electrophilic oxygen in the total oxidation rate [39]. The electronic properties of Cr_2O_3 as a p-type semiconductor allow the activation of a larger amount of electrophilic oxygen by adsorption of gas-phase molecular oxygen than over ZnO. The increase of the electrical conductivity value in air on going from the ZnO catalyst to the chromium based catalysts [30] may parallel their catalytic activity. The features of Cr_2O_3 and $ZnCr_2O_4$ are almost similar and very different from ZnO.

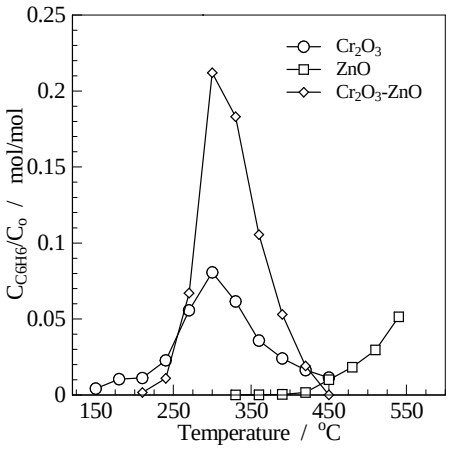

Fig. 4. The distribution of benzene (as organic product) as a function of reaction temperature (after [30]): m_{cat} = 0.5 g; d_p = 0.4-0.63 mm; $\dot{V}$ = 15.9 l · h^{-1}(NTP); C_o = 0.2 vol. % cyclohexane in air.

Michalakos et al. [40] and Kung et al. [41] found as appropriate catalysts for the oxidehydrogenation of cyclohexane to cyclohexene the magnesium vanadate, vanadium-magnesium mixed oxides and neodymium- and samarium vanadates. The reaction orders are very dependent on the nature of the catalyst. The order with respect to cyclohexane is first, and with respect to oxygen is zero on a Mg-V-O catalyst. The corresponding orders over $NdVO_4$ catalysts were 0.82 and 0.63. At low conversion degrees cyclohexene was the main product. The selectivity of cyclohexene was higher than 60 %, however only at conversion grades less than 5 % and sank immediately with increasing cyclohexane conversion. Benzene and carbon oxides were the other reaction products. Depending on the catalyst the selectivities amounted ca. 20-55 % for benzene and ca. 10-20 % for CO_x, whereby CO_2 was the main product of destructive oxidation. The examination of the oxidation behavior of cyclohexane and butane as compared with propane and isobutane [6, 34, 40-43] led to the following conclusions:

- the first product of the oxidehydrogenation process of a paraffin is the homologue olefin.
- the ability of the formed olefins towards further delivery of an allylic hydrogen atom determines the selectivity for the oxidehydrogenation product. The more difficult is the abstraction of allylic hydrogen or the formation of allyl species from the olefin over the catalyst surface (as in the case of propene and iso-butene), the larger is the desorption ability of the olefine, so that the intrinsic catalyst selectivity becomes larger. When the abstraction of allylic hydrogen is facile (butene, cyclohexene), the intermediary formed allyl complexes are easily transformed to further dehydrogenated products (dienes, benzene) and the selectivity towards olefines is lower.
- the selection of one or another reaction path (formation of dehydrogenated or oxygen-containing organic products or carbon oxides) depends on the topology of the catalyst surface or its active centers as well as on the type of the oxygen species (nucleophilic, electrophilic).

There are many catalysts known for their ability to insert oxygen or nitrogen into the molecules of lower chain paraffins C_3-C_5. Thus, acroleine [44-50], acrylonitrile [45, 48] and acrylic acid [51, 52] are produced from propane in two step processes. The maleic anhydride is obtained with high selectivities by oxidizing linear C_4 and C_5 paraffins over VPO [7, 32, 40, 53] and VMgO [40] catalysts. Unlike those, in the oxidation of C_6-C_7 alkanes significant amounts of cracking products are detected. The selectivity of maleic anhidride passes through a maximum. These observations suggest that the maleic anhidride formation observed in the oxidation of C_6 and C_7 alcanes does not derive from the primary oxidation of these hydrocarbons, but probably from the oxidation of the hydrocarbons (*i. e.* benzene) formed in the cracking of the C_6 and C_7 alcanes [7].

4.3. Supported metal oxides

Milas et al. [54] achieved for the first time in the 1930s an yield of maleic acid of approx. 20 % over a V_2O_5/pumice stone catalyst. The maleic acid was analyzed by titration and it can be assumed that the maleic anhydride formed in the reaction was hydrolyzed and determined as maleic acid. Formaldehyde, CO_2, H_2O as well as a small proportion benzene and benzochinone were also identified.

A systematic investigation of V_2O_5/TiO_2 supported catalysts by the oxidation of cyclohexane [32] showed that the modification of the carrier (anatase or rutile) as well as the number of the theoretical V_2O_5 layers on the carrier surface play an important role, both for the activity of the catalyst and for the product distribution [55]. The yield of maleic anhydride amounts up to approx. 50 % [32]. Phthalic anhydride, benzene and C_3-C_4 cracking products were also identified, but no oxygen-containing hydrocarbons with 6 carbon atoms.

In a recent publication Alyea et al. [15] reported on the oxidative dehydrogenation of cyclohexane using an oxygen/helium mixture over MoO_3 and MoO_3/γ-Al_2O_3 catalysts. The reaction products were cyclohexene, benzene, CO, CO_2 and H_2O. The ratio $C_6H_{12} : O_2 = 1 : 2.7$ was kept constant. By using cyclohexene as a reactant, benzene and the mentioned inorganic products were identified. Cyclohexadiene or oxygen-containing products were not found. Similarly to the oxidehydrogenation of other hydrocarbons over V_2O_5 [43, 56-58] the reaction occurs via a hydrogen atom abstraction from cyclohexane as the first step, which takes place on the Mo=O groups and leads selectively to cyclohexene [15].

It is generally accepted that nucleophilic oxygen species on the surface of oxide catalysts promote the partial oxidation reactions, whereas electrophilic oxygen adsorbed at the catalyst surface is responsible for the destructive oxidation, *i. e.* the formation of carbon oxides and water [59-64]. There are however situations where catalysts known for their capability to generate electrophilic oxygen are used for partial oxidation, in which case the limitation of the total oxidation is realized by kinetic control.

Chu et al. reported in a new publication [65] on the partial oxidation of methane to synthesis gas over NiO/γ-Al_2O_3 and NiO-La_2O_3/γ-Al_2O_3-catalysts. The increase of the NiO content from 10 %(wt.) to 17.5 %(wt.) caused a proportional increase in the yield of synthesis gas. A further increase of the NiO content to 20 %(wt.) led on the contrary to a reduction of the yield. The doping of the NiO with La_2O_3 (to 5 %(wt.)) did not bring clear modifications in the catalytic behavior. The formation of CO/H_2 is directly connected with the space velocity. At lower space velocity the oxidation of methane runs a successive reaction pathway, the CO/H_2 formed as an intermediate product being further oxidized to CO_2/H_2O. As

parallel reactions, the direct total oxidation of CH_4 and its conversion reaction (reformation) with water also take place. At higher space velocity the reformation reactions are suppressed and CO/H_2 and CO_2/H_2O are the products of the direct oxidation of methane in parallel reactions.

The results presented above and the interpretation from a new perspective of those reported by Mochida et al. [66, 67] led to the re-evaluation of the supported NiO catalysts, known earlier as total oxidation catalysts, as potential contacts for the selective oxidation of cyclohexane to cyclohexene [16, 17]. It has been shown that for the dissociation of the strong C–H bonding of the paraffinic cyclohexane molecule, the highly reactive electrophilic oxygen species on the surface of nickel oxide are of a great importance.

P-type semiconductors such as NiO are suitable for the generation of electrophilic oxygen species [62]. Their electron acceptor characteristics cause however the "emptying" of the adsorbed hydrocarbons of electrons. The consequence is a strong oxidation potential, which leads to the formation of total oxidation products, as it happens when nickel oxide is used as a catalyst for the destruction of volatile organic compounds. The presence of electrophilic oxygen species facilitates this oxidation. Therefore those catalysts have to be selected and manufactured that posses the ability to generate electrophilic oxygen species, but their electron acceptor characteristics or their bulk are nevertheless limited. A possibility to fulfill this demand consists of immobilizing a thin, if possible monomolecular layer of metallic oxide at the surface of an isolating carrier. Thus each NiO unit keeps its electron acceptor characteristic in detail, but these cannot however be extended over the lattice of the p-semiconductor oxide, which is missing, so that the electron acceptor ability is limited but the generation of electrophilic oxygen is still possible.

Within our preliminary investigations [16] on the oxidation of cyclohexane over a series of supported transition metal oxides, the NiO/γ-Al_2O_3 catalyst showed a unusual and so far unknown efficiency. Whereas over pure, carrier-free NiO (Merck) carbon monoxide and dioxide were the oxidation products as expected, an industrial nickel oxide/aluminum oxide catalyst (Harshaw, 0.2 % NiO/γ-Al_2O_3) yielded 3-17 % benzene. Additionally cyclohexene was also obtained with a selectivity of 5 %.

The analysis of the factors determining the catalytic properties of the supported nickel oxide and the possibility to control them, yielded the following conclusions:

- the catalytic characteristics of the NiO supported catalysts depend on the distribution and on the type of the NiO species formed on the carrier

- the formation and distribution of the NiO species of the active component as well as the strength of their interaction with the carrier are influenced by the following factors: the chemical nature and phase composition of the carrier, the pore morphology of the carrier, i.e. porosity and the internal geometrical structure of the pore system, the loading of the carrier with the active component; the thermal treatment of the green catalyst
- the working conditions during the oxidation process, the composition of the reactant mixture determines the oxidation state of the surface whereas the reaction temperature determines the type of reaction mechanism which the catalytic reaction follows.

We attempted to study the influence of the acidity of different carriers on the catalytic behavior of supported nickel oxide in cyclohexane oxidation [16, 68]. Two acid carrier, i.e. γ-Al_2O_3 and SiO_2, having different acid strength and MgO as strongly basic carrier were selected and examined systematically. Additionally SnO_2 as an oxygen acceptor was also tested as a carrier. The aim here was to check to what extent the catalytic oxidehydrogenation of cyclohexane can be controlled by oxygen mobility, by supposing NiO as an oxygen donor to SnO_2 as an oxygen acceptor.

A doubtless correlation between the activity of the examined catalysts and the specific surface or the Ni-content could not be determined. This fact is close to the assumption that the structure of the NiO species formed on the carrier surface as well as their interaction with the carrier play the crucial role for the conversion of the substrate and not the carrier surface. The formation and structural interaction of the NiO species with the carrier are related by all means to the carrier characteristics. The high activity of the NiO/SnO_2 catalysts having smaller surface area (Fig. 5 (a)) is surprising. This can be explained through to an oxygen-donor/oxygen acceptor synergy, which occurs at the boundary of the available NiO and SnO_2 phases. As a p-type semiconductor NiO possesses the ability to activate by adsorption gaseous oxygen [62, 69] thus behaving like an oxidation catalyst. The presence of an oxygen acceptor such as SnO_2 in the direct proximity of NiO enables the transfer of such very mobile oxygen species, which are responsible for the total oxidation of cyclohexane suppressing the desired partial oxidation. Thereby the presence of the oxygen acceptor improves the oxidehydrogenation reaction. A positive synergism of such mixed oxides having oxygen donor/acceptor interaction is exploited also in the selective oxidation of olefins [70] as well as in the oxidation of hydrogen or carbon monoxide [31].

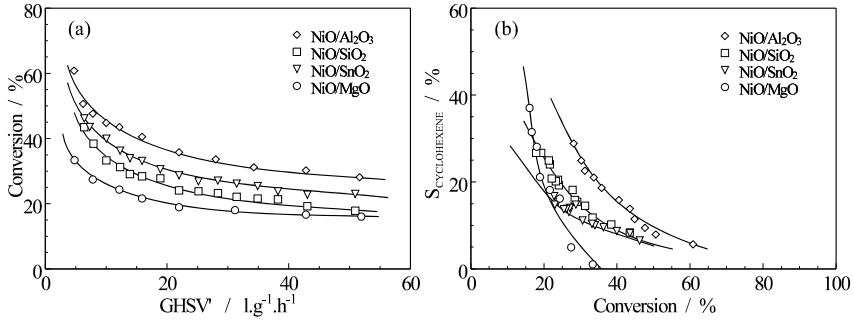

Fig. 5. Conversion (a) and cyclohexene selectivity (b) as a function of the space velocity in the oxidative dehydrogenation of cyclohexane over NiO supported catalysts, after [16]: NiO/γ-Al_2O_3 (91 m^2/g), NiO/SiO_2 (205 m^2/g), NiO/SnO_2 (5 m^2/g), NiO/MgO (29 m^2/g). Reaction conditions: feed concentration C_o = 0.2 vol. % cyclohexane in air; reactor temperature T = 390 ℃; catalyst grain size d_p = 0.4-0.63 mm.

Systematic investigations of the catalytic system NiO/γ-Al_2O_3 revealed a connection between the catalytic characteristics (activity, selectivity) and the structure of the NiO species formed on the catalyst surface. On the basis of the TPR, XRD, FTIR and Laser-Raman spectroscopy a new model was developed for the formation and structure of the NiO species over NiO/γ-Al_2O_3 catalysts, which allowed the understanding of their role in the cyclohexane oxidation. The following possible NiO species can be thereby regarded [16]:

- *bulk-NiO* crystallites
- *isolated NiO units* (oxidized single Ni atoms) on the surface of the carrier
- *bidimensionally NiO monolayer* developed on the top of the alumina carrier
- *surface nickel oxide species* incorporated in the surface of the carrier and having $NiAl_2O_4$ character
- *bulk-$NiAl_2O_4$* consisting of nickel cations which migrated deeply under the surface of the alumina carrier.

By comparing the catalytic results and the structural characterization of the catalysts it seems that the bi-dimensional NiO monolayer is responsible for both the activity (s. Fig. 6 (a)) and the conversion to cyclohexene (s. Fig. 6 (b)). The bulk $NiAl_2O_4$ caused a small activity or a small selectivity to dehydrogenation products. The presence of the bulk NiO species led to the complete oxidation.

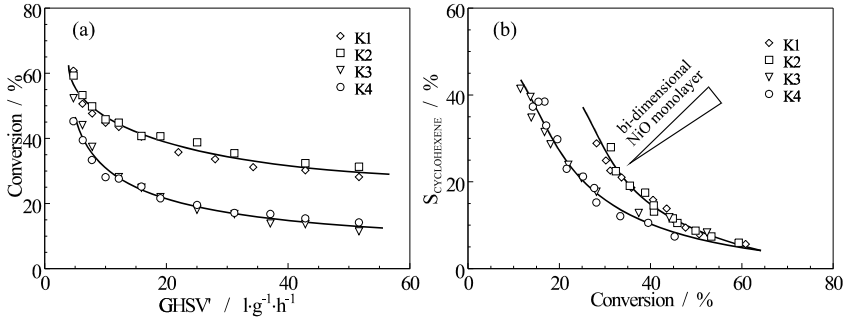

Fig. 6. Conversion as a function of the space velocity (a) and the selectivity in cyclohexene as a function of the conversion grade (b) during the oxide-hydrogenation of cyclohexane over the NiO/γ-Al_2O_3-catalysts after [16] (for description of K1-K4 catalysts s. text). Reaction conditions: inlet concentration C_o = 0.2 vol. % cyclohexane in air; reactor temperature T = 390 ℃; catalyst grain size d_p = 0.4-0.63 mm.

The distribution of the nickel species on the surface of the NiO/γ-Al_2O_3 carrying 2.54 wt.% NiO was changed during preparation by using different thermal treatments of the crude catalyst. As proved by TPR/TPO, XRD, FTIR- and Laser-Raman spectroscopy, the catalysts labeled as K1 and K2 on the one side, and K3 and K4 on the other displayed approximately the same surface structure. The increase of the calcination temperature from 600 ℃ (K1) to 750 ℃ (K2) caused firstly the dispe rsion of the NiO from the bulky phase on the carrier surface and its transformation into bi-dimensionally interlaced NiO species. This was also observed by Wachs *et al.* [71] in the case of other metallic oxide/carrier catalyst systems. A further increase of the calcination temperature to 900 ℃ (K3) or the p rolongation of the heating duration from 6h (K1, K2, K3) to 24h at 750 ℃ (K4) is accompanied by the formation of the crystalline $NiAl_2O_4$. At higher temperatures nickel from the upper layer of the carrier migrates inside the carrier.

The experimental results showed that the oxidation of cyclohexane over NiO/γ-Al_2O_3 catalysts is a structure-sensitive reaction. The positive effect of the bi-dimensionally interlaced NiO species is obvious. On the non-porous and highly crystalline γ-Al_2O_3 carrier (Degussa type C) the bi-dimensional NiO monolayer species were preferably formed and the catalyst showed the highest activity and selectivity to cyclohexene. Oppositely, the migration of the Ni-cations in the structure of the carrier and the formation of $NiAl_2O_4$ were facilitated by a porous and weakly crystallized structure of the γ-Al_2O_3 carrier, with a higher number of structural defects.

The analysis of the selectivity-conversion patterns after the method developed by Riekert [72] and Kotter et al. [73] allowed the determination of the reaction pathways for the conversion of the chemical species present

during the oxidation of cyclohexane. A strong decrease of the cyclohexene selectivity with increasing conversion was determined, which points out to a stability parameter [72] of cyclohexene smaller than one. This is explained by large conversion rates to 1,3-cyclohexadiene, benzene or carbon oxides. The clear tendency of the initial benzene selectivity towards zero, as well as the shape of the selectivity curve of 1,3-cyclohexadiene with a maximum, is a strong hint of the indirect formation of benzene over cyclohexene or 1,3-cyclohexadiene. The relatively low level of the cyclohexadiene concentration in the gas phase could arise from its small desorption rate that leads to its further oxidehydrogenation. With the increase of the cyclohexane conversion over 75 % (low space velocity) the condition are created for the oxidation of benzene to CO_2, so that the benzene selectivity decreases. The formation of CO from the 1,3-cyclohexadiene can be neglected on the basis of the low concentration of this intermediate in the gas phase. The carbon monoxide already existed in the reaction system (probably by the conversion of cyclohexane and cyclohexene) before the formation of 1,3-cyclohexadiene occurred. On the basis of experimental results the reaction network represented in Fig. 7 could be settled [16] for the oxidation of cyclohexane over a $NiO/\gamma\text{-}Al_2O_3$ catalyst. The conversion of cyclohexane (1) begins as a process with three parallel reactions to the products cyclohexene (2), CO (5) and CO_2 (6) and develops to one with parallel and successive reactions towards carbon oxides with 1,3-cyclohexadiene (3) and benzene (4) as intermediary products.

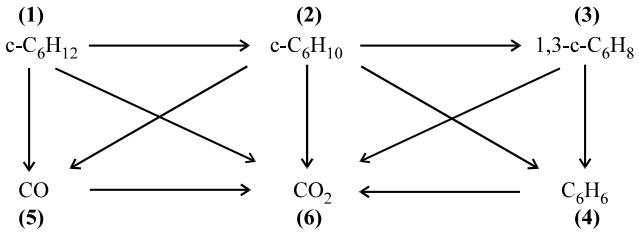

Fig. 7. The reaction network by cyclohexane oxidation over $NiO/\gamma\text{-}Al_2O_3$

4.4. Egg-shell oxide catalysts

The selectivity towards partial oxidized [74-76] or hydrogenated [77] products can be improved when using egg-shell-type catalysts with regular pore system, that is having pores with defined dimensions [78, 79]. In order to increase the selectivity to the desired target product cyclohexene, the possibilities for the production of egg-shell-type catalysts with as high surface area as possible and at the same time short and wide far pores were explored, in order to suppress the influence of the pore diffusion of the components and thus its influence on the product selectivity. In the classical manufacturing processes of egg-shell-type catalysts by the anodic oxidation from wire

sticks or metal plate pieces in the Faraday range, followed by impregnation [75-77, 81] the formation of the active component in the oxide egg-shell is a crucial process for the catalytic effectiveness of the catalyst. Because of the small stability of the oxide matrix formed by anodic oxidation towards acid or basic solutions [80, 81], the selection of the precursor of the active component is a difficult point. Here it must also be taken into account the fact that the catalyst manufacture processes involving many steps are critical from the point of view of the reproducibility.

A new procedure, the anodic oxidation under spark discharge (ANOF) [82], proved itself suitable to avoid these disadvantages. It was developed for the production of oxide coatings on barrier layer-forming metals, like aluminum, titanium, tantalum, niobium, zircon, magnesium etc. and it was successfully applied [17, 82-84]. Due to the particular art of shell formation, the pore sizes, the layer growth and the active component doping, reproducible layer systems can be produced in one single process step. By appropriate selection of the aqueous electrolytes and the coating parameters the egg-shell-type catalysts can thus be manufactured having desired layer composition, and continuous pore system. In Fig. 8 a SEM picture of the surface texture of the catalyst is $NiO/Al_2O_3/Al$ is shown as an example.

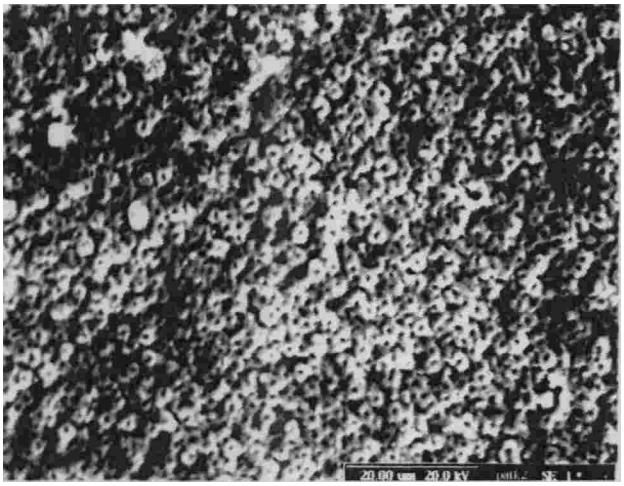

Fig. 8/ SEM photography of the surface structure of the catalyst $NiO/Al_2O_3/Al$ [85].

Such egg-shell-type catalysts on metallic wire sticks such as $NiO/Al_2O_3/Al$, $NiO/TiO_2/Ti$ or lithium doped $NiO\text{-}Li_2O/Al_2O_3/Al$, manufactured by ANOF, have proven themselves as suitable in the oxidative dehydrogenation of cyclohexane to cyclohexene [85]. In Fig. 9 the conversion grade of cyclohexane and the product selectivities as a function of temperature on a $NiO/Al_2O_3/Al$ are represented.

The special feature of the ANOF manufactured $NiO/Al_2O_3/Al$ catalysts consists of the fact that the NiO active component on the catalyst surface is distributed as a bi-dimensional layer, without the formation of "bulk NiO". Thus the prerequisites for the selective attack of the electrophilic oxygen species formed on the oxide catalyst surface are realized and the cyclohexene formation is favored. The doping of the $NiO/Al_2O_3/Al$ catalyst with low valence Li supports the formation of electrophilic oxygen species, so that the activation of cyclohexane is facilitated [85].

The decrease of the cyclohexene selectivity with increasing temperature (Fig. 9) is probably due to its oxidation with formation of 1,3-cyclohexadiene or benzene as products of the successive oxidehydrogenation. The formation of 1,3-cyclohexadiene with a selectivity of up to 3-5 % is remarcable. The CO selectivity is situated within the range of 0-4 % and does not change substantially with the temperature. The shape of the CO_2 selectivity curve as a function of the temperature is unusual. On the $NiO/Al_2O_3/Al$ catalyst the conversion amounts approx. 30 % at 330 ℃, than sinks to approx. 24-25 % in the temperature range of 390-450 ℃ and then rises continuously with the temperature up to approx. 32 % at 530 ℃.

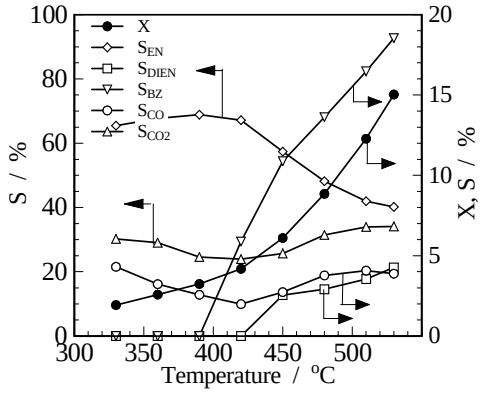

Fig. 9. Cyclohexane conversion and distribution of reaction products as a function of temperature on the $NiO/Al_2O_3/Al$ catalyst; m_{cat} = 0.5 g; $l_{cat}x\phi_{cat}$ = 4.0x1.0 mm; $\dot{V}$ = 15.9 $l \cdot h^{-1}$(NTP); C_o = 0.2 % (vol.) cyclohexane.

The experimental findings for the CO_2 selectivity on the catalysts $NiO/Al_2O_3/Al$ and $NiO\text{-}Li_2O/Al_2O_3/Al$ suggest a change of the oxidation mechanism at temperatures between 330-400 ℃. In the low temperature range a mechanism involving electrophilic oxygen species is probably occurring, while in the higher temperature range a redox mechanism of the Mars-van Krevelen type takes place, assisted by the nucleophilic oxygen species, similar to the model proposed by Bielanski and Haber [62]. The

temperature range for the change of the oxidation mechanism is connected to the magnetic properties of NiO as revealed by the work of Cimino et al. [89] and Bielanski et al. [90]. Thus, in the Néel temperature domain the magnetic transition of the nickel oxide containing catalysts and the disappearance of the rhombohedral deformation of the cubic lattice of NiO takes place [86-88].

4.5. Ion-exchanged zeolites

There are some few work dealing with the oxidation of cyclohexane over ion-exchanged zeolites [66, 67, 91-93]. Mochida et al. [66] examined the oxidation of cyclohexane over transition metal oxides ion-exchanged NaY zeolites. Up to 350 ℃, benzene and carbon mono xide were the main products, and also a small amount of cyclohexene. Above 350 ℃ other products were also observed, as acetic acid and propionic acid. The Cu(II)-Y was found to be the most selective catalyst for benzene formation among Cr(III), Ni(II) and Ag(I) exchanged Y zeolites. Pd(II)-Y had the largest activity for the formation of carbon dioxide.

The kinetic study of cyclohexane oxidation over Cu(II)-NaY-catalyst [67] showed a low dependence of the formation rate of benzene and CO_2 on cyclohexan partial pressure, in a reactant mixture containing 0.05 to 0.95 atm oxygen and 0.01 to 0.18 atm cyclohexane. The reaction order of oxygen was 1 for the formation of benzene and 0.5 for the formation of carbon dioxide. The determined apparent activation energies over the Cu(II)-NaY catalyst amounted to approx. 113 kJ/mol for the formation of benzene and approx. 122 kJ/mol for the formation of CO_2. For the other exchanged zeolites the corresponding values ranged 40-113 kJ/mol and 52-149 kJ/mol, respectively. The reaction occurred at small conversion grade in the form of a parallel reaction (formation of CO_2 and benzene), but with increasing conversion other parallel and successive reactions took place.

To clear-up the influence of the metal loading of the zeolites on the possible reaction pathways, the oxidation of cyclohexane over Cu(II)-NaY was firstly examined [67]. Upon the increase of the loading with Cu^{2+} cations, a higher conversion rate of cyclohexane was found. The selectivity to cyclohexene decreased however very strongly and became almost zero by over 20% (wt.) copper loading. That means that while Cu^{2+} cations represent the active sites for oxidation, the presence of not-exchanged Na^{+} cations may be beneficial for the selective formation of cyclohexene. The formation of benzene occurs both through cyclohexene (at small conversion grades) and directly from cyclohexane, in each case in competition with the formation of CO_2. The rate of CO_2 formation is independent of the exchange degree of the zeolite. That means that the responsible oxygen species are connected with the zeolite itself and not with the exchanged cations. This

findings are conform with the results of Minachev et al. [92, 93], who have shown that the oxidative dehydrogenation of cyclohexane can occur in the presence of alkaline cation-exchanged zeolites of type A, L, chabazite, erionite and mordenite containing no transition metals with cyclohexene as the major product.

In order to investigate the role of the reactants in the oxidation process [67], the Cu(II)-NaY catalyst was firstly saturated at 320 ℃ either with cyclohexane, or with oxygen, or with both. Then the corresponding second reactant, oxygen or cyclohexane or helium as a flushing gas was admitted in form of pulses. Based on the observed results it was concluded that the chemisorption of the less reactive cyclohexane blocked the copper active centers and the O_2 adsorption became thus the rate-determining step. On the catalyst surface cyclohexane formed weakly and strongly adsorbed species. While the reaction of weakly adsorbed cyclohexane with associatively adsorbed oxygen species led to benzene, the strongly adsorbed cyclohexane yielded together with dissociatively adsorbed oxygen mainly CO_2. Associative as well as dissociative oxygen may be present on Cu(II)-Y, however, it is plausible to assume associative oxygen as the reactive species for benzene formation in this oxidative dehydrogenation.

These conclusions are partially in contradiction to the theory of Haber [59-61] over the role of the electrophilic or nucleophilic oxygen species in determining the reaction pathway in oxidation reactions. His works pointed to the electrophilic O_2^- and O^- as responsible for splitting the C–C bond and causing a further oxidation. The nucleophilic O^{2-} bound at the transition metal cations was taken as responsible for the partial oxidation with or without oxygen insertion.

On the basis of the present level of knowledge, the experimental results published by Mochida et al. [67] can also be differently interpreted: The independence of the CO_2 rate of formation on the Cu loading can be due to the presence of the O_2^- and O^- species at the surface of the Cu(II)–NaY catalyst. The existence of such oxygen species on a copper free zeolite surface was already proven by Wang and Lunsford [94] by the ESR technique. This explains the independence of the CO_2 rate of formation on the degree of loading of NaY zeolites with Cu^{2+}. The existence of the Cu^{2+} ions in the zeolite lattice enables the dissociative chemisorption of oxygen and the formation of O^{2-}, which is responsible for the oxidehydrogenation of cyclohexane to benzene. The formation of cyclohexene is favored by the strongly basic centers, which are likely to take a proton off from cyclohexane. The second hydrogen atom from the carbocation could be delivered under the influence of, for example, an electrophilic oxygen species (O_2^-, O^-) in a second step as H^-. That could explain the formation of cyclohexene already over zeolites having only a small exchange degree of sodium with copper

cations. The participation of electrophilic oxygen species to the selective oxidehydrogenation was stated also by Tagawa et al. [95, 96] during the oxidative dehydrogenation of ethylbenzene to styrene.

The experimental findings of Minachev et al. [92] during the investigations of cyclohexane oxidehydrogenation over alkaline cation-exchanged zeolites suggested that a surface reaction between adsorbed cyclohexane and only slightly adsorbed molecular oxygen was the limiting process step. The reaction rate was directly proportional to oxygen partial pressure while the order of cyclohexane reaction was below unity and was described by the equation:

$$r = \frac{k \cdot P_{O_2} \cdot P_{C_6H_{12}}}{1 + a_{C_6H_{12}} \cdot P_{C_6H_{12}}} \qquad (23)$$

The determined apparent activation energy was 23 kJ/mole and the heat of adsorption of cyclohexane 12.5 kJ/mole. The catalytic runs were performed at 300-500 ℃ and at cyclohexane partial pressure of 0.05 to 0.3 atm and oxygen partial pressure of 0.05 to 0.18 atm.

Alimardanov [91, 97] reported results on cyclohexane oxidation over H–Mordenite (degree of decationization ca 75 %) modified with Fe_2O_3 und Gd_2O_3 in a quantity of 50% (wt.). The condensed liquid product contained cyclohexane, cyclohexene, benzene and methylcyclopentene isomers. Carbon dioxide and C2-C3 hydrocarbons were found in the gaseous product. Hydrogen and carbon monoxide were detected too, but their concentration were insufficient for their accurate determination. After distilling at 90 ℃ the liquid reaction product, in the condensed water layer the following oxygen-containing compounds were found: epoxycyclohexane, epoxymethylcyclopentane, cyclohexanol, methylcyclopentanols, cyclohexenol, cyclohexanone, cyclohexenone. Their amount did not exceed 0.5-0.7 % of the total weight. No other publication reported by now the formation of oxygen containing C_6 products upon gas phase oxidation of cyclohexane. The interpretation of the results yielded a reaction scheme composed of parallel and successive reactions. The formation of cyclohexene is described by a first order kinetics reported to cyclohexane and 0.5 with respect to oxygen, while for the formation of benzene the orders were both 1. A reaction mechanism for the oxidehydrogenation of cyclohexane by means of nucleophilic oxygen species O^{2-} was suggested. For the formation of oxygen-containing organic compounds a reaction mechanism was postulated, which contained both catalytic and homogeneous reaction steps.

5. GENERAL REMARKS

The technical purpose of gas phase cyclohexane oxidation may be either the partial oxidation for the manufacture of functional derivatives of cyclohexane by preserving the six atom ring, or the total oxidation yielding selectively CO_2 and H_2O as products when the removal of cyclohexane vapor from residual gases is desired. Although thermodinamically possible, gas phase oxidation of cyclohexane yields no oxygen containing organic compounds, both in the presence and in the absence of catalysts and/or additives. This fact can be attributed to the much higher rate of destruction of the oxygen containing compounds than the rate of their generation. At the present state of the art in the field, the formation of cyclohexene and casually of cyclohexadiene remains the only possibility of oxidative gas phase functionalization of cyclohexane. This transformation occurs by means of electrophilic or nucleophilic oxygen species generated by oxide, supported oxide or modified zeolite type catalysts.

If one admits that the process of catalytic oxidation involves the continuous switch of the oxidation state of the active center, we may consider that whatever the type of oxygen species that are involved in the oxidation (electrophilic or nucleophilic) is, the catalytic reaction is mirrored by the redox cycles of the active site. The rate of the catalytic reaction may thus be expressed as the turnover frequency of the reduction/reoxidation of the catalyst.

While the re-oxidation of the reduced active centers of the catalyst takes place only by the gas phase oxygen, the reduction of the active centers takes place both via cyclohexane and via all formed intermediate products. If the chemisorption of cyclohexane is the rate-determining step and the concentration of other components is very small [6, 16, 40-42, 57, 64, 100-102], the reduction rate of the catalyst under participation of other components may be neglected in comparison to that of cyclohexane. The reduction rate r_{Red} and re-oxidation rate r_{Ox} are then described by the equations (24) and (25), respectively:

$$\mathrm{r_{Red}} = \mathrm{k_{Red}} \cdot \mathrm{P_{C_6H_{12}}} \cdot \Theta_{\mathrm{Ox}} \tag{24}$$

$$\mathrm{r_{Ox}} = \mathrm{k_{Ox}} \cdot \mathrm{P_{O_2}} \cdot \Theta_{\mathrm{Red}} \tag{25}$$

where: k_{Red}, k_{Ox} are the rate constants of the reduction or the re-oxidation; $P_{C_6H_{12}}$, P_{O_2} are the partial pressures of cyclohexane and oxygen; Θ_{Ox}, Θ_{Red} are the proportions of oxidized or reduced active centers.

In the stationary state:

$$r_{Red} = r_{Ox} \tag{26}$$

and the total reaction rate *r* becomes:

$$r = \frac{1}{\frac{1}{k_{Red} \cdot P_{C_6H_{12}}} + \frac{1}{k_{Ox} \cdot P_{O_2}}} \tag{27}$$

For the eq. (27) two limit situation may occur:

Case I

$$k_{Red} \cdot P_{C_6H_{12}} >> k_{Ox} \cdot P_{O_2} \tag{28}$$

The eq. (27) can then be simplified as eq. (27a). The oxidation rate of the reduced catalyst becomes the rate-determining step with kinetics of first order concerning oxygen and zero-order concerning cyclohexane.

$$r = k_{Ox} \cdot P_{O_2} \tag{27a}$$

The situation corresponds to the oxidation over a difficult oxidizable catalyst or an oxygen-poor gas mixture. The catalyst operates in the predominantly reduced status.

Case II

$$k_{Ox} \cdot P_{O_2} >> k_{Red} \cdot P_{C_6H_{12}} \tag{29}$$

The reduction rate is determining for the kinetics of the whole process and eq. (27) becomes (27b).

$$r = k_{Red} \cdot P_{C_6H_{12}} \tag{27b}$$

The reaction is first-order regarding cyclohexane and zero-order order regarding oxygen. The catalyst works in a highly oxidized state.

As a matter of fact, during the catalytic process the catalyst changes its oxidation state within some limits [34, 55, 103-106] and the experimental determined values are in much cases temporary ones which lay between those limits.

To understand the role of the catalyst as a key factor of the oxidation process we shall describe on the basis of the simplified scheme in Fig. 10 its transformation to cyclohexene in a first stage. The further transformation of cyclohexene occurs then similarly.

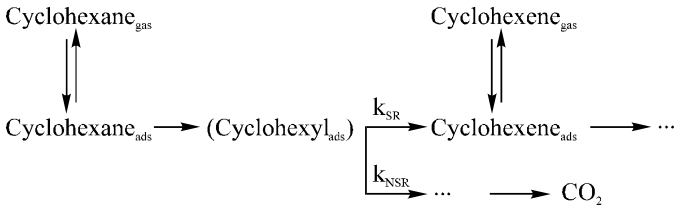

Fig. 10 Reaction scheme of cyclohexane oxidation

The cyclohexane oxidehydrogenation begins by the adsorption of cyclohexane molecule at an active center. According to the mechanism for the oxidehydrogenation of paraffins and cycloparaffins suggested in [40, 41, 98, 99], the attack of the oxygen at a C–H bond and the abstraction of an hydrogen atom is the first step of the surface reaction. Investigations for the oxidehydrogenation of paraffins showed that the dissociative chemisorption with splitting the C–H bond is the rate-determining step [6, 16, 40-42, 57, 64, 100-102]. In the case of cyclohexane oxidation under co-operation of nucleophilic lattice oxygen after a redox mechanism of the type Mars and van Krevelen [108], in conformity with literature data [6, 41, 91, 107], where the formation of carbo-ions as surface intermediate products occurs, the catalyst undergo a redox process, which is not discussed here. For the oxidehydrogenation of cyclohexane over a series of metal vanadates, Chaar et al. [42] and Patel et al. [34, 100] suggested a homolytic C–H splitting, which shall be considered here. This process yields a cyclohexyl radical, which is stabilized by the capture of the available electron to the incompletely filled d–d orbital of the metal (coordinative bonding) or by fixation in a neighbouring oxygen vacancy. The cyclohexyl radical has two possibilities to interact with oxygen species:

1) the attack of the oxygen at the C_β–H bonding and formation of cyclohexene, which remains adsorbed by its p-electrons at the oxygen vacancy;
2) attack of the oxygen at the carbon skeleton (C–C bond) and formation of carbon oxides.

The catalyst is in both ways reduced. The formation of dehydrogenation products is called selective reduction of the catalyst and has the rate constant k_{SR}. Similarly the formation of inorganic products (CO_x, H_2O) by the non-selective reduction of the catalyst has the rate constant k_{NSR}. The cyclohexene formed has to be desorbed as fast as possible, in order to avoid the further conversion, according to a rake model [60]. The rate of the further oxidehydrogenation of adsorbed olefins depends on their ability to build allylic alkyl species and is thereby greater for cyclohexene then for linear

C3-C6 olefins [40, 41]. With the increase of the dehydrogenation degree, the adsorption tendency of the intermediates formed also rises. In this way the oxidehydrogenation of cyclohexane (under co-operation of two oxygen atoms) will probably lead merely to benzene (with ist stable aromatic structure) than to cyclohexene [98].

By taking into account the reaction network in Fig. 10, the maximal cyclohexene selectivity of the catalyst (intrinsic selectivity) S_{EN} can be expressed as the ratio between the rate of selective reduction of the catalyst and that of the non-selective reduction:

$$S_{EN} = \frac{r_{SR}}{r_{SR} + r_{NSR}} \tag{30}$$

The catalyst selectivity for cyclohexene formation is always superior to the selectivity of the reactor as yielded by experiments [72]. The cyclohexene selectivity expressed by eq. (30) is the maximum value that the catalyst could achieve in the absence of successive transformation of cyclohexene or of mass or heat transfer limitations.

In order to obtain high selectivity of cyclohexene, the non-selective reduction of the catalyst should be avoided. This requires to maintain the catalyst at a low oxidation degree as shown by Andersen et al. [103]. This poses problems regarding the on-stream stability of the catalyst [99]. Practically, the only remaining possibilities remain either the appropriate combination of active components, which encompasses eventually most of the present researches, or the control of the oxidation state of the catalyst by optimizing the ratio between cyclohexane and oxygen in the gas phase.

6. CONCLUSION

The data discussed in this review show that the functionalization of cyclohexane by gas phase oxidation can be achieved with satisfactory results only in the presence of catalysts. The most interesting products are cyclohexene and 1,3-cyclohexadiene. The other possible oxidation products are benzene and carbon oxides. No oxygen containing products were reported except for ref. [91], but there were also to low amounts obtained to be quantified.

A wide range of catalysts encompassing supported metals, metal oxides and modified zeolites exchanged with transition or alkali-earth metals were tested for cyclohexane oxidation. The magnesium vanadate, vanadium-magnesium mixed oxides and neodymium- and samarium vanadate catalysts were found as appropriate catalysts for the oxidehydrogenation of cyclohexane to cyclohexene. Remarcable results were obtained recently by using nickel supported catalysts on non porous microparticulate alumina, or over egg-

shell catalysts manufactured by anodic oxidation where the active component was again nickel oxide. The activity and selectivity of these catalysts was attributed to the formation on the carrier surface of a bi-dimensionally interlaced nickel oxide monolayer, a species that preserves the oxidative characteristics of the p-type semiconductors but prevents their amplification due to the presence of the bulk phase.

The mechanism of the oxidative generation of cyclohexane to cyclohexene depends on the catalyst nature and on the temperature, the extraction of the hydrogen atoms being achieved either by electrophilic (at lower temperatures) or by nucleophilic (at higher temperatures) oxygen species. The kinetics of cyclohexane oxidation depends here on the nature of the catalyst and the reaction conditions, but is generally accepted that the rate-determining step is the the heterolytic or homolytic dissociation of the first C–H bond. The catalytic oxidation of cyclohexane begins as a parallel reaction network from cyclohexane to cyclohexene and carbon oxides, and continues with successive transformation of cyclohexene to cyclohexadiene and benzene. To achieve high cyclohexene selectivity catalysts are needed, which are able to suppress the non-selective transformation of cyclohexane to inorganic products and to desorb cyclohexene rapidly. Further researches in these directions are still required.

REFERENCES

[1] K. Weissermel und H. -J. Arpe, in: *Industrielle Organische Chemie* 3. Auflage, Verlag Chemie, Weinheim, 1988, p. 117.

[2] H. A. Wittcoff, *Chem. Techn.*, **20(1)** (1990) 48.

[3] J. F. Roth, *Chem. Techn.*, **21(6)** (1991) 357.

[4] P. Ruiz, B. Delmon (Eds.), *Stud. Surf. Sci. Cat.*, Vol. 72 “New Developments in Selective Oxidation by Heterogeneous Catalysis”, Elsevier, Amsterdam, 1992.

[5] H. H. Kung (Ed.), *Stud. Surf. Sci. Cat.*, Vol. 45, “Transition Metal Oxides: Surface Chemistry and Catalysis”, Elsevier, Amsterdam, 1989.

[6] E. A. Mamedov, V. C. Corberan, *Appl. Catal. A*, **127** (1995) 1.

[7] G. Centi, F. Trifiró, *Catal. Today*, **3** (1988) 151.

[8] G. P-J. Hareau, M. Koiwa, S. Hikichi, F. Sato, *J. Amer. Chem. Soc*., **121(15)**, (1999) 3640.

[9] D. Lednicer, *US Patent* 4,115,589/19.09.1978.

[10] L. Burak, *PCI Magazine*, June, (1999) 68.

[11] M. L. Campbell in: *Ullmann’s Encyclopedia of Industrial Chemistry*, Fifth Completely and Revised Edition, Verlag Chemie, Weinheim, 1987, Vol. A8, p. 209.

[12] K. Yamashita, *Kagaku Kogaku*, **59(8)** (1995) 29.

[13] H. M. Weitz, J. Hartig in: *Ullmann’s Enzyclopädie der technischen Chemie*, 4. Auflage, Bd. 9, Verlag Chemie, Weinheim 1975, p. 6.

[14] C. Bezouhanova, Y. Kalvachev, H. Lechert in: *Catalysis of Organic Reactions*, E. W. Pascoe (Ed.), Chemical Industries Serie, Vol. 47, Eastman Kodak

Company, Rochester, New York 1991, p. 185.
[15] E. C. Alyea, M. A. Keane, *J. Catal.*, **164** (1996) 28.
[16] F. Patcas, in: *Heterogen katalysierte Gasphasen-Oxidehydrierung von Cyclohexan an Nickeloxid-Trägerkatalysatoren*, Verlag für Wissenschaft und Forschung, Berlin, 1998.
[17] W. Krysmann, D. Hönicke, F. Patcas, *DE Patent* 198 52 150 A1/18.05.2000
[18] I. Barin, in: *Thermochemical Data of Pure Substances*, 3rd ed., Verlag Chemie, Weinheim, 1995.
[19] T. E. Daubert, R. P. Danner, H. M. Sibul, C. C. Stebbins, in: *Physical and Thermodynamic Properties of Pure Chemicals: Data Compilation*, Taylor & Francis, Washington, 1996.
[20] S. Estradare, *Compt. Rend.*, **196** (1933) 674.
[21] K. I. Ivanov, *Zhur. Obshchei Khim.*, **196** (1936) 470, cit. in [23].
[22] W. F. Hoot, K. A. Kobe, *Ind. Eng. Chem.*, **47(1)** (1955) 776.
[23] I. V. Berezin, E. T. Denisov, N. M. Emmanuel, in: *The Oxidation of Cyclohexane*, Pergamon Press Ltd., Oxford-London, 1966, p. 241.
[24] E. R. Bell, F. M. Dickey, J. N. Raley, F. F. Rust, W. E. Waughan, *Ind. Eng. Chem.*, **41** (1949) 2597.
[25] F. F. Rust, W. E. Waughan, *Ind. Eng. Chem.*, **41** (1949) 2595.
[26] P. J. Nawrocki, J. N. Raley, F. F. Rust, W. E. Waughan, *Ind. Eng. Chem*., **41** (1949) 2604.
[27] M. Young, J. C. Balaceanu in: *Actes du 2me Congr. Int. Catal*., Vol. I, Ed. Technip, Paris, 1961, p. 645.
[28] F. Patcas, F. C. Buciuman, publication in preparation.
[29] F. Patcas, F. C. Buciuman, N. Maxim, *"Oxidehydrogenation of Cyclohexane in Heterogeneous Catalysis"*, Proceeding of the fifth National Simposium on Catalysis, Bucharest, July, 9-11, 1997, Abs. p. 36.
[30] F. Patcas, N. Maxim, M. Alifanti, F. C. Buciuman, *Progr. in Catal*., **8(2)** (1999) 54.
[31] F. C. Buciuman, *PhD Thesis*, Babes-Bolyai University of Cluj-Napoca, 1999.
[32] V. Duma, *Diploma Thesis*, Babes-Bolyai University of Cluj-Napoca, 1994.
[33] M. Chaar, D. Patel, H. H. Kung, *J. Catal*., **109** (1988) 463.
[34] D. Patel, P. Anderson, H. H. Kung, *J. Catal.*, **125** (1990) 132.
[35] K. C. Stein, J. J. Feenan, G. P. Thompson, J. F. Schultz, L. J. E. Hofer, R. B. Anderson, *Ind. Eng. Chem.*, **52** (1960) 671.
[36] K. C. Stein, J. J. Feenan, L. J. E. Hofer, R. B. Anderson, *Bull. Bur. Mines*, US Dept. Inter., 1962, p. 4.
[37] G. I. Golodets, in: *Stud. Surf. Sci. Cat.*, Vol. 15, "Heterogeneous Catalytic Reactions Involving Molecular Oxygen", G. I. Golodets (Ed.), Elsevier, Amsterdam, 1983, p. 646.
[38] Ya L. Margolis, O. M. Todes, in: *Problems of Kinetic and Catalysis*, Vol. VI, Izdat. Nauk SSSR, Moskow, 1949, p. 281.
[39] K. G. Boreskov, in: *Catalysis, Science and Technology*, J. R. Anderson, M. Boudart, (Eds.), Springer Verlag Berlin, 1982, Vol. 3, p. 87.
[40] P. M. Michalakos, M. C. Kung, I. Jahan, H. H. Kung, *J. Catal.*, **140** (1993) 226.
[41] M. C. Kung, H. H. Kung, *J. Catal.*, **128** (1991) 287.
[42] M. Chaar, D. Patel, M. C. Kung, H. H. Kung, *J. Catal.*, **105** (1987) 483.
[43] D. Siew Hew Sam, D. Soeden, J. Volta, *J. Catal.*, **123** (1990) 417.

[44] C. R. Adams, T. J. Jennings, *J. Catal.*, **3** (1964) 549.
[45] J. L. Callahan, R. K. Grasseli, E. C. Milberger, N. A. Strecter*, Ind. Eng. Chem. Prod. Dev.*, **9** (1970) 134.
[46] R. K. Grasseli, D. D. Suresh, *J. Catal.*, **25** (1972) 273.
[47] W. Ueda, Y. Moro-Oka, T. Ikawa, *J. Catal.*, **70** (1981) 409.
[48] R. K. Grasseli, J. D. Burrington, *Adv. Catal.*, **30** (1981) 133.
[49] M. Allen, R. Betteley, M. Bowker, G. J. Hutchings, *Catal. Today*, **9** (1991) 97.
[50] K. H. Schultz, D. F. Cox, *J. Catal.*, **143** (1993) 464.
[51] C. Mazzocchia, F. Direnzo, P. Centola, A. del Rosso, in: H. F. Barry, P. C. H. Mitchel (Eds.), *Proc. 4th Int. Conf. on Chemistry and Uses of Molybdenun*, Climax Molybdenum, Golden, CO, 1982, p. 406.
[52] E. Serwicka, J. B. Black, J. Goodenough, *J. Catal*., **106** (1987) 23.
[53] G. Centi, G. Fornasari, F. Trifiro, *Ind. Eng. Chem. Prod. Res. Dev.*, **24** (1985) 32.
[54] N. A. Milas, W. L. Walsh, *J. Amer. Chem. Soc.*, **61** (1939) 633.
[55] H. Mitzel, *Dissertation*, Technische Universität Chemnitz, 1997.
[56] S. T. Oyama, *J. Catal.*, **128** (1991) 210.
[57] A. Corma, J. M. Lopez Nieto, N. Paredes, *J. Catal.*, **144** (1993) 425.
[58] A. Corma, J. M. Lopez Nieto N. Paredes, M. Perez, Y. Shen, H. Cao, S. L. Suib, in: *Stud. Surf. Sci. Cat.*, P. Ruiz, B. Delmon (Eds.), Vol. 72, "New Developments in Selective Oxidation by Heterogeneous Catalysis", Elsevier, Amsterdam, 1992, p. 213.
[59] J. Haber, in: *Proc. 8th Int. Congr. on Catal*., Berlin, 1984, Vol. 1, p. 85.
[60] J. Haber, *Z. Chem.* **13(7)** (1973) 241.
[61] J. Haber in: *ACS Symposium Series*, "Solid State Chemistry in Catalysis", R. K. Grasselli and J. F. Bradzil (Eds.), Vol. **279** (1985) 3.
[62] A. Bielanski, J. Haber in: *Oxygen in Catalysis*, Marcel Dekker Inc., New York, 1991, p. 132.
[63] V. D. Sokolovskii, *Catal. Rev.-Sci. Eng.*, **32(1-2)** (1990) 1.
[64] E. Bordes in: *Elementary Reactions Steps in Heterogeneous Catalysis, NATO-Series*, R. W. Joyner, R. A. Santen (Eds.), Kluwer Academic Publishers, Amsterdam, 1993, p. 137.
[65] Y. Chu, S. Li, J. Lin, J. Gu, Y. Yang, *Appl. Catal. A*, **134** (1996) 67.
[66] I. Mochida, T. Jitsumatsu, A. Kato, T. Seiyama, *Bull. Chem. Soc. Japan*, **44** (1971) 2595.
[67] I. Mochida, T. Jitsumatsu, A. Kato, T. Seiyama, *J. Catal.*, **36** (1975) 361.
[68] F. Patcas, A. Akbas, F. C. Buciuman, D. Hönicke, *Chem. Technik*, (in press, 2000).
[69] E.-G. Schlosser, W. Herzog, *Ber. Bunsenges. Phys. Chem.*, **71(4)** (1967) 358.
[70] L. T. Weng, P. Ruiz, B. Delmon, in: *Stud. Surf. Sci. Cat.*, P. Ruiz, B. Delmon (Eds.), Vol. 72, "New Developments in Selective Oxidation by Heterogeneous Catalysis", Elsevier, Amsterdam, 1992, p. 406.
[71] I. Wachs, F. D. Hardcaltle, in: *Catalysis. A Periodical Report*, Vol. 10, Royal Society of Chemistry, Cambridge, 1993, p. 132.
[72] L. Riekert, *Appl. Catal. A*, **15** (1985) 89.

[73] M. Kotter, L. Riekert, F. Weyland in: *Stud. Surf. Sci. Cat.*, Vol.16, “Preparation of Catalysts III”, G. Poncelet, P. Grange, P. A. Jacobs (Eds.), Elsevier, Amsterdam, 1983, p. 521.
[74] D. Hönicke, *J. Catal.*, **105** (1987) 19.
[75] D. Scholl, *Dissertation*, Universität Karlsruhe (TH), 1988.
[76] B. Woldeyes, *Dissertation*, Universität Karlsruhe (TH), 1993.
[77] G. Wieţmeier, *Dissertation*, Universität Karlsruhe (TH), 1996.
[78] A. Wheeler, in: *Adv. in Catal. Vol. III*, Academic Press, New York, 1951, p. 313.
[79] C. N. Satterfield, in: *Heterogeneous Catalysis in Industrial Practice*, Second Edition, McGraw-Hill Inc., New York, 1991, p. 117.
[80] J. W. Diggle, T. C. Downie, C. W. Goulding, *Chem. Rew*., **69** (1969) 365.
[81] D. Hönicke, S. Ludwig, *Chem.-Ing.-Tech.*, **64(7)** (1992) 639.
[82] W. Krysmann, P. Kurze, K.-H. Dittrich, H. G. Schneider, *Crystal Res. & Technol*., **19(7)** (1984) 973.
[83] W. Krysmann, *Ingenieur-Werkstoffe*, **4(11)** (1992) 61.
[84] W. Krysmann, in: *Korrosionsschutz durch Beschichtungen und Überzüge auf Metallen*, Teil 8, WEKA Technik-Verlag, Augsburg, 1996, p. 1.
[85] F. Patcas, W. Krysmann, D. Hönicke, *Chem.-Ing.-Tech.*, **72(4)** (2000) 405.
[86] K. Rooksby, *Acta Cryst*., **1** (1948) 226.
[87] L. D. Brownlee, E. W. J. Mitchell, *Proc. Phys. Soc. B*, **65** (1953) 710.
[88] J. S. Smart, S. Greenwald, *Nature*, **166** (1950) 523.
[89] A. Cimino, E. Molinari, G. Romeo, *Zeitschrift für phys. Chem. N. F.*, **16(1-2)** (1958) 100.
[90] A. Bielanski, J. Deren, J. Haber, J. Sloezynski, *Zeitschrift für phys. Chem. N. F.*, **24** (1960) 345.
[91] K. M. Alimardanov, *Petrol. Chem*., **31(1)** (1991) 22.
[92] Kh. M. Minachev, D. B. Tagiyev, Z. G. Zulfugarov, V. V. Kharlamov, N. D. Zelinsky, in*: "Proceeding of the International Conferences of Zeolites"*, *5th*, London, 1980, p. 625.
[93] Kh. M. Minachev, D. B. Tagiyev, V. V. Kharlamov, *Izv. Aakd. Nauk SSSR, Ser. Chem.*, (1977) 1931.
[94] K. M. Wang, J. H. Lundsford, *J. Phys. Chem*., **73** (1969) 2046.
[95] T. Tagawa, T. Hattori, Y. Murakami, *J. Catal.*, 75 (1982) 56.
[96] T. Tagawa, T. Hattori, Y. Murakami, *J. Catal.*, 75 (1982) 66.
[97] K. M. Alimardanov, E. T. Suleimanova, S. A. Magerramov, *Naftekhimiya*., **26(5)** (1988) 628.
[98] H. H. Kung, *Adv. Catal.*, **40** (1994) 1.
[99] H. H. Kung, P. Michalakos, L. Owens, M. Kung, P. Andersen, O. Owen, I. Jansen, in: *Catalysis Selective Oxidation*, ACS Symp. Series, Vol. 523, Washington, 1993, p. 389.
[100] D. Patel, M. C. Kung, H. H. Kung, in: *Proc.9th Int. Congr. on Catalysis*, Calgary 1988, M. J. Phillips, M. Ternan (Eds.), Ottawa 1988, p. 1553.
[101] R. M. Martin-Aranda, M. F. Portela, L. M. Madeira, F. Freire, M. Oliveira, *Appl. Catal. A*, **127** (1995) 201.
[102] O. S. Owen, H. H. Kung, *J. Mol. Catal*., **79** (1993) 265.

[103] P. J. Andersen, H. H. Kung, in: *Stud. Surf. Sci. Cat.*, Vol. 75, "New Frontiers in Catalysis", L. Guczi, F. Solymosi, P. Tetenyi (Eds.), Elsevier, Amsterdam, 1993, p. 206.
[104] A. J. van Hengdtum, J. G. van Ommen, H. Bosch, P. J. Gellings, in*: Proc. 8th Int. Congress on Catal.*, Berlin, Vol. 4 (1984) p. 297.
[105] A. Kadkhodayan, A. Brenner, *J. Catal*., **117** (1989) 311.
[106] H.-H. Hildenbrand, *Dissertation*, Universität Karlsruhe (TH), 1991.
[107] L. M. Madeira, F. J. Maldonado-Hódar, M. F. Portela, F. Freire, R. M. Martin-Aranda, M. Oliveira, *Appl. Catal. A*, **135** (1996) 137.
[108] P. Mars, D. W. van Krevelen, *Chem. Eng. Sci. Suppl*., **3** (1954) 41.

STUDIA UNIVERSITATIS BABEŞ-BOLYAI, CHEMIA, XLIV, 1-2, 1999

POLYMETHINE DYES. PART II*. THE PHOTOCHROMIC BEHAVIOUR OF SOME CATIONIC DIMETHINE DYES

IOAN BALDEA, IOAN PANEA and ADRIAN CONSTANTIN APETRI

Babes-Bolyai Univ. of Cluj, Faculty of Chemistry and Chemical Engineering
Cluj-Napoca 3400, 11 Arany Janos Str., Romania. E-mail: ibaldea@chem.ubbcluj.ro

ABSTRACT. The photochromic behaviour of some 1-H-indazolo-3–dimethine dyes (1-3) in dimethylformamide and 5-chloro-1,3,3.trimethyl-2-[2-(4-oxo-4-H-1-benzopyran-3-yl)ethenyl]-3-H-indolium perchlorate (4) in 1,2 dichloroethane, acetone and acetic acid has been studied. The reason for the photochromism consists of the Z/E or *cis/trans* isomerisation reaction. The formation of Z configuration at light exposure and thermal re-formation of E configuration at dark is supported by spectroscopic data (UV-VIS, IR and ^{1}H- NMR) and kinetic data. Activation parameters for the *cis-trans* isomerisation have been determined.

INTRODUCTION

The *cis- trans* isomerisation of various unsaturated organic molecules induced by light has been extensively studied because of their involvement in the eyesight and photosynthetic bacteria [1], the photochemical degradation of various stilbenic and polymethine dyes [2] mechanism by which part of the harmful energy of U.V. radiation is dissipated by the body [3]. Many of the applications of cyanine dyes (cationic polymethines) have been explained by their photochromic behaviour [2, 4-6], which has been largely examined [4-7]. Panea [5] has proved unambiguously that the photochromism of 1-H-indazolo-3-dimethine dyes is based on the E - Z or *trans – cis* isomerisation, the direct transformation being induced by light and the reverse transformation taking part thermally, in the dark.

The present work supplements the data on photochromic behaviour of 1-H-indazolo-3-dimethine dyes making use of dimethylformamide as solvent, along with the examination the photochromism of a dye from the class of 4-oxo-4-H-1-benzopyran-3-dimethines in dichloroethane, acetone and acetic acid.

EXPERIMENTAL SECTION

Synthesis of the dyes. Cationic 1-H-indazolo-3-dimethine dyes ***(1-3)*** as perchlorate [5,8.] and 1,3,3-trimethyl-5-chloro-2-[2-(4-oxo-4-H-1-benzopyran-3-yl)ethenyl]-3-H-indolium perchlorate [9] were synthesised and purified according quoted references.

UV-VIS, IR and NMR spectra. Electronic spectra were recorded for all the dyes synthetised in various solvents. We recorded the spectra of more stable *trans*-isomers by using a Specord-UV-VIS Zeiss spectrophotometer or a Jasco V-530 spectrophotometer with the solutions of appropriate concentrations, kept in the dark for a long time. The spectra of the photo-generated isomer (*cis*) were recorded after photoexcitation for a known period of time using either a UV lamp, a tungsten lamp or a blue filter (λ = 450 mn). IR spectra were registered as KBr pellets by using a Zeiss Jena UR-20 spectrophotometer. The ^{1}H-NMR spectra were obtained by means of a Varian Gemini 300 (300 MHz) NMR spectrometer.

Kinetic measurements were performed by spectrophotometrical means, recording the absorbance increase for the thermodynamically stable isomer (*trans*-isomer) in the dark, after the *cis- trans* equilibrium has been shifted to the left and the solution has became practically colourless under irradiation. The photostationary state has been attained. The formation of the more stable and more intense coloured species has been recorded as a function of time at the wavelength corresponding to the peak absorption of each dye. The effect of solvents and temperature has been investigated. Either a Zeiss Spekol or a Jasco V-530 spectrophotometer was used. Both of them were provided with thermostated cell holders. A thermostat has been connected to cell-holder. Three to six replicate runs were performed for each set of experimental conditions. Some of them consisted of several consecutive irradiation and dark reaction of the same dye solution, and some used different solutions with the cell irradiated with light for the same period of time and dark process was monitored. Rate constant determined did not vary to more than 3-4 % for the same experimental conditions. Four ways of irradiation were used: a UV lamp, a tungsten lamp, a tungsten lamp with a blue filter, and a prolonged exposure to daily diffuse light. Reproducible results were obtained with the last two ways of exposure to light. When UV source of light, or repeated irradiation using a ultraviolet or a visible tungsten lamp was used, the systems did not revert to the same value of final absorbance at dark, some irreversible processes took place.

RESULTS AND DISCUSSION

Photochromism of 1,3,3-trimethyl-2-[2-(1-H-indazol-3-yl)-ethenyl]-5-X-3-H-indolium perchlorate with X = methoxy ***(1),*** hydrogen ***(2)*** and nitro ***(3)*** groups has been studied in dimethylformamide (DMF).

Figure 1 presents the visible absorption spectrum of *trans* isomer and the spectrum after an exposure to blue light for 45 sec. The points A, B and C represent the absorbance values reached in the dark after a period of 50, 115 and 210 sec, respectively.

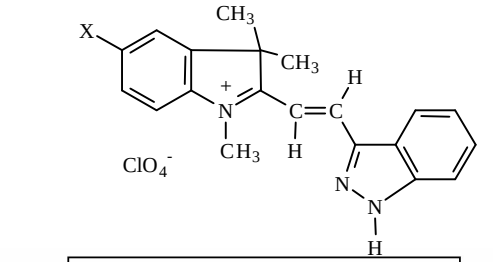

(**1 – 3**)

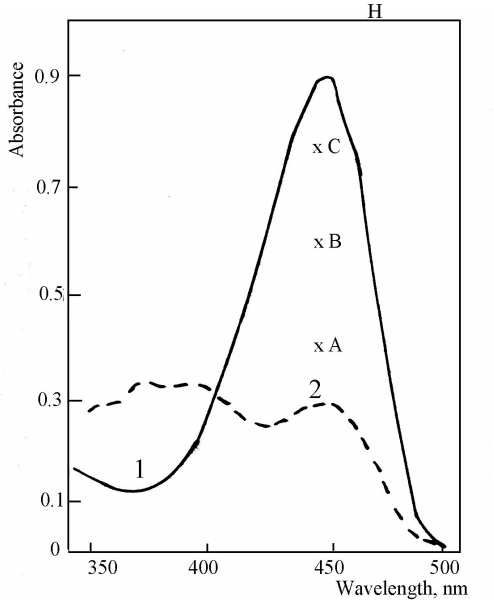

Fig. 1. Absorption spectra for **3** at 20°C in DMF having the concentration of 3.22×10^{-5} M 1- *trans* –isomer, 2- after irradiation.

The shift of the *cis-trans* equilibrium towards the thermodinamically stable isomer at dark follows a first-order kinetics over all experimental conditions employed, even in the cases when some degradation of more coloured species has taken place. The semilogarithmic plots

$$\ln(A_\infty - A) = \ln(A_\infty - A_0) - kt \qquad (1)$$

gave straight lines up to 85 – 90 % of reaction, with correlation coefficients of 0.9930 – 0.9990. The value A_∞, A_0 and A stands for the absorbance at the end, at the beginning and at various time intervals from the interruption

of light exposure. When repeated irradiation was used, or the reaction time is too long, A_∞ is difficult to obtain. Under such conditions, Guggenheim's method has been used [10] to determine first-order rate constant.

$$\ln(A_{t+\Delta} - A_t) = \ln(e^{-k\Delta} - 1)(A_\infty - A_0) - kt \quad (2)$$

Δ represents a period of time, always the same, having a value of 2 – 3 times larger than the half-life. It is recommended for the first-order reactions when final readings are unknown. Very good correlation coefficients were obtained using the linear equation (2). Table 1 contains the data obtained with the three dyes ***(1-3)***.

Table 1

Kinetic data on the dark reconversion to *trans* isomer

Substrate	T(K)	10^3k (s^{-1})	Ea ($kJ.mol^{-1}$)	$\Delta H^{\neq}$ ($kJ.mol^{-1}$)	$\Delta S^{\neq}$ ($J.mol^{-1}.K^{-1}$)
1	302.8 312 321.5	0.258 1.03 3.03	106.4±4.4	104.0±4.3	+30.1±4.5
2	297.7 302.8 311.6 316.5 319.0	0.88 0.89 0.90 1.65 1.64 1.57 1.63 4.96 4.98 4.98 6.92 7.06 6.88 13,5 13.7 13.9	94.3±.6.0	91.8±6.0	+5.0±11
3	293.2 298 303.3 312.3	6.60 9.60 20.1 42.5	76.1±.4.0	73.6±.4.0	-35.6±.6.0

If $\Delta G^{\neq}$ at 298 K were calculated, the following values were obtained for the three compounds: 95.0 ± 5.5, 90.3±4.0 and 84.2± 6.0 $kJ.mole^{-1}$ respectively.

Photochromism of 5-chloro-1,3,3-trimethyl-2-[2-94-oxo-4-H-1-benzo-pyran-3-yl) ethenyl]-3-H-indolium perchlorate ***(4)***. The E(*trans*) configuration relative to ethenylic bridge of ***(4),*** obtained by sinthesys [8], was established based on spectral analysis.

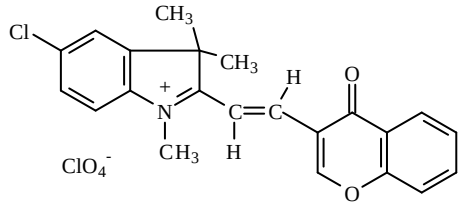

(**4**)

Thus, the relative narrow and intense peak in the visible range (see fig. 2) in dichloroethane (λ_{max} = 410 nm, ε_{max} = 80.000 $M^{-1}cm^{-1}$) is characteristic to E(*trans*) isomer [4,5]. The absorption peak at 983 cm^{-1} on IR spectrum for ν –HC=CH- (ethenylic bridge) or coupling constant of 16 Hz from the corresponding doublets of the bridge hydrohen atoms [5] on NMR spectrum proves the same thing. By exposure to light (blue or U.V.) of ***(4)*** the absorption peak at the in the visible range becomes more extended and little intense (ε_{max} = 40.000 $M^{-1}cm^{-1}$) and slightly hypsochromically shifted by about 15 nm as compared to the one characteristic to *trans* isomer. This is in agreement with the *trans – cis* transformation [4,5]. The photo-product is unstable and changes back to *trans* isomer thermally at dark. Therefore the compound ***(4)*** exhibits photochromic behaviour. The re-conversion to *trans* isomer in the dark has been monitored using 1,2 –dichloroethane, acetone and acetic acid for various temperature values and various ways of irradiation. Figure 2 presents the spectra at several periods after the irradiation with blue light was interrupted in 1,2 –dichloroethane. Two isosbestic points are obvious indicating that only two coloured species are present in the mixture.

To be sure the absorbance values at various concentration obey Lambert-Beer relationship, measurements were made, covering a quite large concentration interval. The linearity was very good up to concentration range of $1.8x10^{-3}$ M. Above that, the Lambert-Beer relationship did not hold, due to some associations of dye molecules. Kinetic measurements were carried out at concentration range far below this limit.

By using 1,2-dichloroetane as solvent and an UV lamp and consecutive exposure to light, to shift the *cis – trans* equilibrium to the left, irreproducible results were obtained, concerning the rate constant and the final value of absorbance. We noticed that the solvent itself undergone some decomposition, which induced irreversible transformation with the dye. It has been revealed by spectrophotometrical means. Several spectra present increasing peaks in the ultraviolet region at successive exposure to ultraviolet light from a Hg-lamp. The spectra are presented in figure 3.

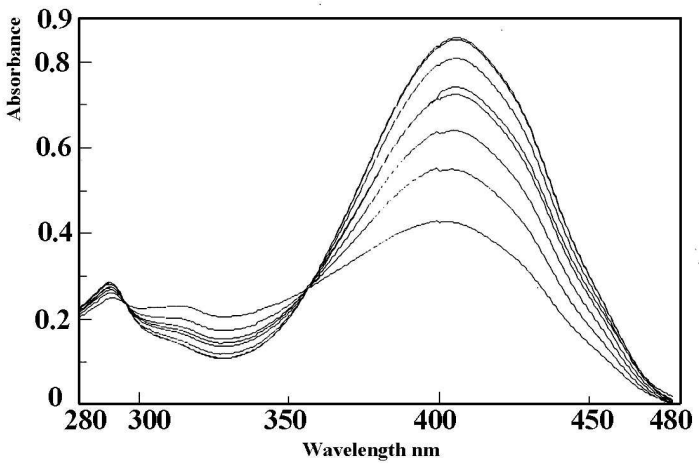

Fig. 2. Electronic spectra of ***4*** at a concentration of 1.07×10^{-5} M in 1,2 dichloroethane at various periods of time after irradiation.

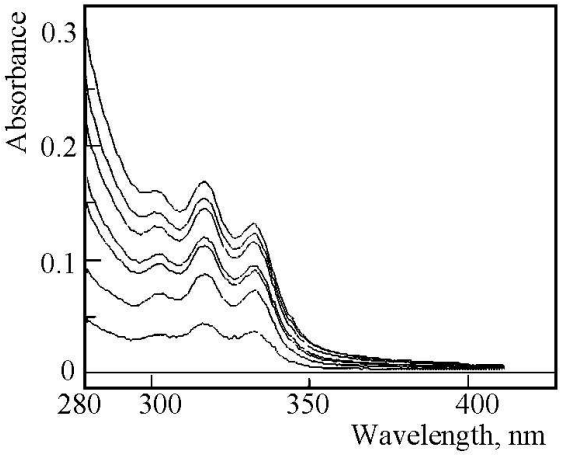

Fig. 3. Absorption spectra of successive irradiated cell of 1,2,dichloroetane. The reference contains unirradiated 1,2,dichloroethane.

With the blue filter or exposure to diffuse daylight, reproducible results were obtained even when 4 – 5 successive irradiation - dark periods were used. With acetone or acetic acid as solvents, only these ways of exposure to light were used. Figure 4 presents the automatically recorded values of absorbance versus time for the re-conversion to *trans* configuration, illustrating an exponential shape.

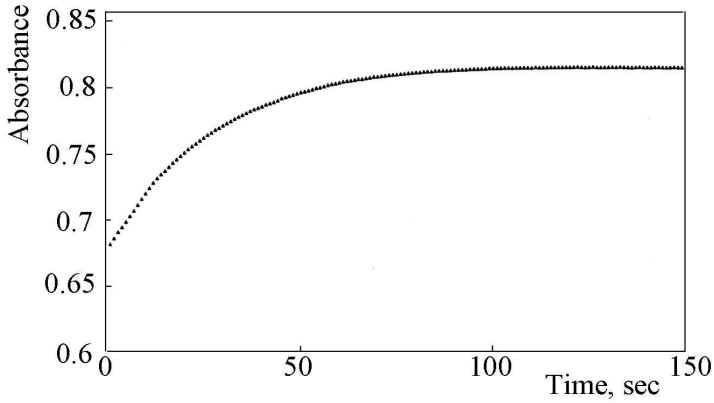

Fig. 4. The evolution of absorbance after irradiation in acetone as solvent.

All kinetic measurements lead to first-order dependence. The linear dependence described by equation (1) was obtained in all the experiments undertaken, correlation coefficients between 0.9960 and 0.9990 were obtained. The results are collected in table 2. Activation parameters were calculated by means of Arrhenius and Eyring equations. Different values were obtained for the solvents employed. It is clear that acetone, a polar solvent, interacts more strongly with activated state, the ionic twisted state of the dye, which is better solvated as compared to a non-polar solvent. This is responsible for unfavourable entropy change, and causes some decrease in activation energy. In the case of acetic acid, a more polar and protic solvent, with possibilities of hydrogen bonding, the mentioned effects are still increased. An important decrease of activation energy as compared to the others has been found. If one calculates the Gibbs free energy of activation, quite close values are obtained for the isomerisation in the three solvents.

Table 2.

First-order rate constants (10^2 k sec^{-1}) for *cis–trans* thermal isomerisation in different solvents and different temperature values and activation parameters.

Temp. (K)/ Solvent	1,2 Dichloroethane	Acetone	Acetic acid
293	0.95	2.16	2.89
294	1.03		
295		2.70	3.11
296	1.30		3.50
297			3.85
298	1.72	2.88	3.90

Temp. (K)/ Solvent	1,2 Dichloroethane	Acetone	Acetic acid
299			3.96
300	2.11	2.96	
301	2.40		
302			
303	3.00	4.86	
304			
305.5		5.3	
308		7.87	
Ea kJ.mole^{-1}	87.8±4.0	6o.2±3.0	29.3±2.8
Δ H$^{\neq}$ kJ.mole^{-1}	85.4±4.0	57.8±3.0	27.7±2.7
ΔS$^{\neq}$ J.mole^{-1}K^{-1}	2±3	-79±4	-182±13
ΔG$^{\neq}$kJ.mole^{-1} at 298 K	84.8±5.0	81.3±3.6	81.9±7.6

CONCLUSIONS

The present study evidentiates the photochromic behaviour of dimethine dyes, having only one stereogenic double bond between the two heterocyclic parts of dye molecule.

The reaction at dark is quite slow to be followed by means of classical spectrophotometrical methods. The spectroscopic measurements (^{1}H-NMR, UV-VIS and IR) of starting material kept in the dark for a long time indicate a E(*trans)* configuration. On the other hand, on the electronic spectra two isosbestic points apear, indicating the involvement of two species in the photochemical-thermal equilibrium.

The broader absorption band and the smaller molar absorptivity for the photo-product as compared to the starting configuration, is in agreement to the fact that the photo-produced isomer is in Z(*cis*) configuration [4].

Kinetic parameters determined here are in accordance with the isomerisation reaction Z(*cis*) – E(*trans*) [4] and the previous conclusions obtained by Panea [5] for other solvents.

Acknowledgement The financial support of the study by the Romanian National University Research Council (CNCSIS Grant A) is greatefully acknowledged.

REFERENCES

*) Part I. I. P a n e a, I. C r i s t e a, *Studia Univ. Babes-Bolyai, Chem.,***1996,** *41*, 9.

1. R. R. B i r g e, L. M. H u b b a r d, *J. Amer. Chem. Soc.,* **1986**, *102,* 2195; T. Y e, N. F r l e d m a n, Y. G a t, G. H. A t k I n s o n, M. S h e v e s, M. O t t o l e n g h i, S. R u h m a n, *J. Phys. Chem. B,* **1999**, 103, 5122.
2. H. M e i e r, in *The chemistry of Synthetic Dyes* Ed. K. Venkataraman, Vol. IV, Acad. Press London 1971, Chap. 7, pp. 420, 425-428, 490.
3. H. P. B a d e n, M. A. P a t h a k, D. Butler, *Nature,* **1966,** *210,* 732.
4. G. B r o w n, *Photochromism,* Wiley-Interscience, New York, 1971, pp 366- 375, 538-543, 796.
5. I. P a n e a, *Diss.* Univ. Basel, 1977.
6. G. E. F I c k e n, in "*The Chemistry of Synthetic dyes*" Ed. K. Venkataraman, Vol. IV, Acad. Press London, 1971, Chap. 7, pp. 334-335; J. H e l s s, K. F e l d m a n n, *Angew. Chem.,* **1965**, *77,* 546; P. J. M c Ca r t i n, *J. Chem. Phys.***1965**, *42,* 2980.
7. D i e t z, S. K. R e n t s c h, *Chem. Phys.,* **1985**, 96, 145; G. P o n t e r i n i, F. M o m i c c h i o l i, *Chem. Phys.,* **1991**, *151,* 111; K. K a s a t a n i A U e n a, T. O g a t a, M. K a t s u k k i, *Fukuoka Joshi daigaku Kiyo* **1994,** *25*, 43 (cf *CA* **1994,** *121,* 156906 c); A. S. T a t i a k o v, Kh. S. D z h u l l b e k o v, Z h. A. K u z m i n, *Izv. Akad. Nauk. Ser. Khim.,* **1993,** 719; W. W e m k e, M. P f e i f e r, T. J o h r, A. L a u, W. F r y e r, *Springer Proc. Physi.,* **1994**, *74,* 100*;* S. G h e l l i, G. P o n t e r i n i, *J. Mol. Struct.,* **1995,** *335,* 193; M. I k e g a n i, T. A r a i, *Kokagaka,* **1997**, *26,* 42 (cf. CA **1998**, *128,* 49428 w); E. N. K a l i e v s k a y a, T. K. R a z u m o v a, A. N. T a r n o v s h i i, *Opt. Spektrosk.* **1999**, *86,* 139 (cf . CA. **1999**, *131*, 186213 y).
8. I. P a n e a, *Rom. Pat*. 75.012, 1980.
9. I. P a n e a. V. C h i o r e a n, *Rom. Pat*. 75.092, 1980.
10. E. A. G u g g e n h e i m, *Philos. Mag.,* **1926**, 2, 588; E. S. S w i n b o u r n e, *J. Chem. Soc.,* **1960**, 237.

STUDIA UNIVERSITATIS BABEŞ-BOLYAI, CHEMIA, XLIV, 1-2, 1999

POLYMETINE DYES. PART III*. THE CATIONIC 1-H-INDOLO-3-DIMETHINE DYES

IOAN PANEA and IOAN BALDEA

Faculty of Chemistry and Chemical Engineering, Babes-Bolyai University.
11 Arany Jnos Str. 3400, Cluj-Napoca. Romania

ABSTRACT. By means of elemental and spectral (I.R., UV-VIS and ^{1}H-NMR) analysis data, the structure of cationic 1-H-indolo-3-dimethine dyes (3) of the products resulted by condensation of unsubstituted 1-H-indolo-3-carbaldehyde (4) with different 2- or 4-methylcycloimmonium perchlorates (5) has been proved. The synthesised cationic 1-H-indolo-3-dimethine dyes (3) have an E (*trans*)- configuration relative to the C=C double bond in ethenylic bridge. The obtained compounds exhibit bacteriostatic activity against Grampositive bacteria and good applicability as dyes.

INTRODUCTION

The cationic 1-H-indolo-3-dimethine dye structure is present in some Astrazon dyes (**1**)[1-3]. In these Astrazon type cationic 1-H-indolo-3-dimethine dyes (**1**), the 1-H-indole moiety is substituted. Some drugs with cationic polymethine dye structure are known. Among these, there is one with the name pirvinium [4], a pyrolo-4-dimethine (**2**).

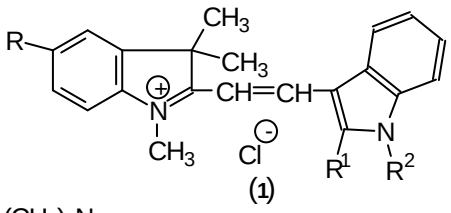

(**1**)

a: R=R^1=H; R^2=CH$_3$

b: R=H; R^1=CH$_3$; R^2=C$_6$H$_5$

c: R=OCH$_3$; R^1=CH$_3$; R^2=C$_6$H$_5$

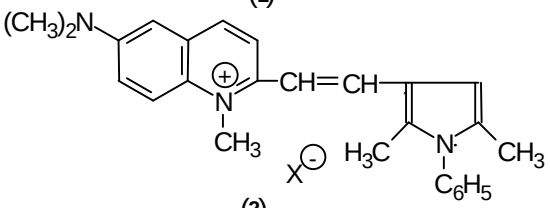

(**2**)

X$^{\ominus}$: pamoate

*) Part II, This Journal, this issue

Because 1-H-indolo-3-dimethines are analogues of benzologue at the pyrole ring in pirvinium, they are also expected to present biological activity.

Taking into account the two areas of interest concerning the compounds with a cationic 1-H-indolo-3-dimethine structure we were stimulated to undertake a study of such new dyes, unsubstituted at the 1-H-indolium moiety ***(3)***. It should be mentioned that only a few representatives of this last type of dyes are known [2,5].

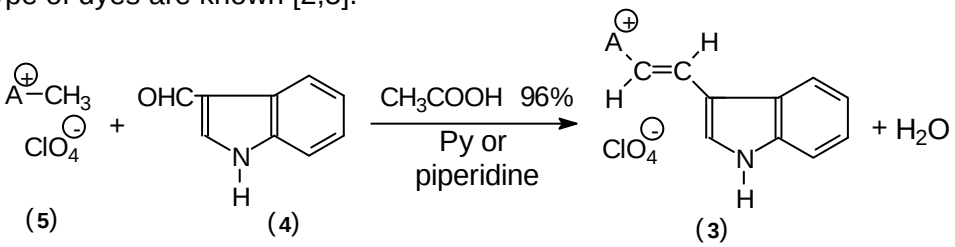

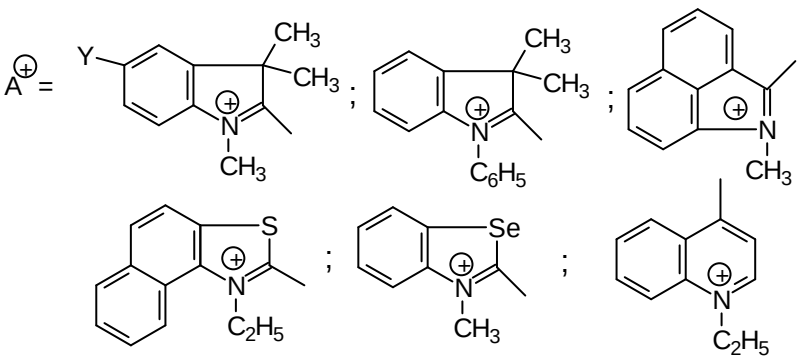

Y= Cl, NO_2, CH_3O

This work aims to confirm the cationic 1-H-indolo-3-dimethine dyes structure ***3*** of the products obtained by condensation of 1-H-indolo-3-carbaldehyde ***(4)*** with different 2- or 4- methylcycloimmonium perchlorates ***(5)*** in glacial acetic acid as solvent, in the presence of catalytic amounts of pyridine or piperidine.

EXPERIMENTAL

The condensation product between 1-H-indolo-3-carbaldehyde ***(4)*** and different 2- or 4- methylcycloimmonium perchlorates ***(5)*** in glacial acetic acid as solvent were obtained and purified as previously described [7]. The elemental analysis has been performed at Raluca Ripan Institute of Chemistry in Cluj. I.R. spectra were registered by means of a Karl Zeiss Jena spectro-

photometer, model UR-20, with solid powders in KBr pellets. The ^{1}H-NMR spectra were registered using a Varian Gemini 300 (300MHz) or a Tesla BS 487 (80 MHz) spectrometer. Hexadeuterodimethylsulfoxide has been used as solvent. Electronic spectra were recorded by means of a Karl Zeiss Jena UVVIS Specord spectrophotometer using methanol-water (64 %) solutions.

RESULTS AND DISCUSSION

The main method to synthesise dimethine cationic dyes is the condensation of cycloimmonium salts having an alkyl or alkylene active group [1,2,5,6] with heterocyclic aldehydes having the aldehyde group conjugated with the heteroatom of the cycle. 1-H-indolo-3 -carbaldehyde ***(4)*** fulfills this condition. Consequently, it was expected that its condensation with 2- or 4- methylcycloimmonium perchlorates ***(5)*** yields the desired cationic 1-H-indolo-3-dimethine dyes ***(3)***.

When condensation reaction has been performed in acetic acid (96%) in the presence of small amounts of pyridine or piperidine [7], some orange to blue coloured products were obtained from colourless starting materials. These products exhibit dyestuff properties. They easily dye polyacrylonitrile fibres, having a medium lightfastness [7]. It has been proved that the obtained dyes present bacteriostatic action, comparable to antibiotics used for therapy against Baccilus subtilis or Staphylococcus aureus (Oxford variant) [7]. The cationic 1-H-indolo-3-dimethine dyes structure ***(3)*** of the condensation products obtained has been confirmed by means of elemental analysis, as well as by spectral (UVVIS, IR, and ^{1}H-NMR) measurements.

The structure assignement is discussed in detail for the condensation product obtained between 1-H-indolo-3-carbaldehyde ***(4)*** and 5-chloro-1,2,3,3-tetramethyl-3-H-indolium perchlorate ***(6)***. The elemental analysis data, contained in table 1 are in agreement with the molar ratio 1:1 condensation product. This may be a dimolecular, crotonic type condensation yielding ***(7)*** or a polymolecular condensation product. The data in table 1 rule out a trimolecular condensation between an aldehyde molecule ***(4)*** and two perchlorate molecules ***(6).*** On the other hand, if a polycondensation product were obtained, it should have formed a polymethinic saturated chain, which is in contrast with the formation of a coloured product. Moreover, the UVVIS spectrum of the product exhibits an intense and quite narow peak in the visible range, as presented in table 2. This behaviour is characteristic to cyanine [8]. Hence, the electronic spectrum of examined condensation product is compatible only with the form of cationic dimethine ***(7)*** or of pentamethine dye [9].

Table 1

The composition of the condensation product between 1-H-indolo-3-carbaldehyde (**4**) and 5-chloro-1,2,3,3-tetramethyl-3-H-indolium perchlorate ***(6)***

Composition	% C	% H	%N
Calculated for 1:1molar ratio	58.0	4.6	6.4
Calculated for 1:2 molar ratio	53.3	4.7	5.65
Found experimentally	57.8	4.9	6.3

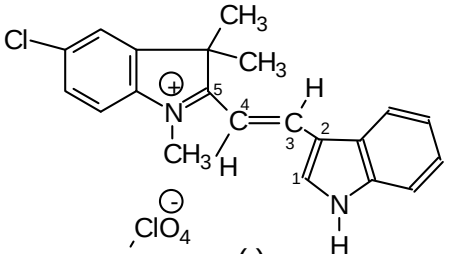

(7)

The formation of a polycondensation product is ruled out also by ^{1}H-NMR spectrum. The chemical shifts of hydrogen atom nuclei in methine group have values greater than 7 ppm, being in accord with an olefine structure of dimethine ***(7)*** [10] but in contrast to a saturated structure that should have δ smaller than 3 ppm [10]. Moreover the values obtained for chemical shifts of hydrogen nuclei in examined condensation product obey the alternation rule which is characteristic to cationic polymetine with delocalised charge [11]. In accordance with this rule, the chemical shifts of hydrogen atom nuclei in position 1 (δ = 8.68 ppm) and 3 (δ = 8.70 ppm) should be approximately the same and greater than that of hydrogen in position 4 (δ = 7.14 ppm). The experimental confirmation of this is presented in table 2.

A undoubted proof for the cationic dimethine structure ***(7)*** of the condensation product between ***(4)*** and ***(6)*** comes from the value of 15.65 Hz for the coupling constant of methine hydrogen nuclei, which is characteristic [10] to an ethenylic bridge having an E (*trans*) configuration. Such a configuration is also supported by the peak located at 950 cm^{-1} in IR spectrum, corresponding to an out of plane deformation of trans –HC=CH- group [12]

The involvement of 2-methyl group of cycloimmonium perchlorate ***(6)*** in the condensation process has been established on the base of ^{1}H-NMR spectra of the condensation product and those of starting materials, as presented in figure 1. NMR spectrum of the dye exhibits the signal characteristic to N-CH_3 and not for the gropup 2-CH_3.

The signal corresponding to the group 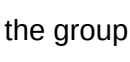 ($\delta < 3.3$ ppm for .C-CH_3) [13] is not found in ^{1}H-NMR spectrum of the condensation product while the signal corresponding to the quaternised 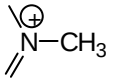 group ($\delta \geq 3.9$ ppm for 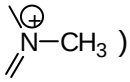)[14]. appears on this spectrum (see fig. 1 and table 2).

Table 2

Some properties of the condensation product between 1-H-indolo-3-carbaldehyde ***(4)*** and 5-chloro-1,2,3,3-tetramethyl-3-H-indolium perchlorate ***(6)***

Property	Values
Melting point (^{o}C)	306-307 with decomposition
Visible range spectrum in MeOH :H_2O, λ_{max} (nm) ε_{max} ($M^{-1}cm^{-1}$)	485 55000
IR spectrum (KBr pellet) (cm^{-1}) for: CH=CH out of plane deformation ν Cl-O from ClO_4^- ν N-H	950 625,1000 3260
^{1}H-NMR spectrum in DMS-d_6 Chemical shift in ppm for $C(CH_3)_2$ + N-CH_3 C_4-H C_3-H C_1-H N-H Coupling constant J H_3-H_4 (Hz)	 1.81(s)*; 6H** 3.97 (s) ;3H 7.14 (d);1H 8.70 (d);1H 8.68 (s);1H 12.85 (b);1H 15.65

*) multiplicity: (s)-singlet, (d)-doublet, (b) broad; **) number of hydrogen atoms. Spectrarecorded with Varian Gemini 300 spectrometer.

The conclusion of the above presented data is that the condensation product between 1-H-indolo-3-carbaldehyde and 5-chloro-1,2,3,3-tetramethyl-3-H- indolium prechlorate has a cationic dimethine dye structure, namely that of 5-chloro-1,3,3-trimethyl-2-[2-(1-H-indol-3-yl)ethenyl]-3-H-indolium perchlorate ***(7)***. As convincing evidence to assign the cationic dimethine day structure for ***(7)*** we used ^{1}H-NMR data (especially the vicinal coupling constant $J_{1,3}$ = 16 Hz, characteristic to a *trans* configuration ethenylic group). We have used such parameters to assign the structure ***(3)*** with an E (*trans*) configuration relative to ethenylic bridge to several other dyes obtained. The results are presented in table 3.

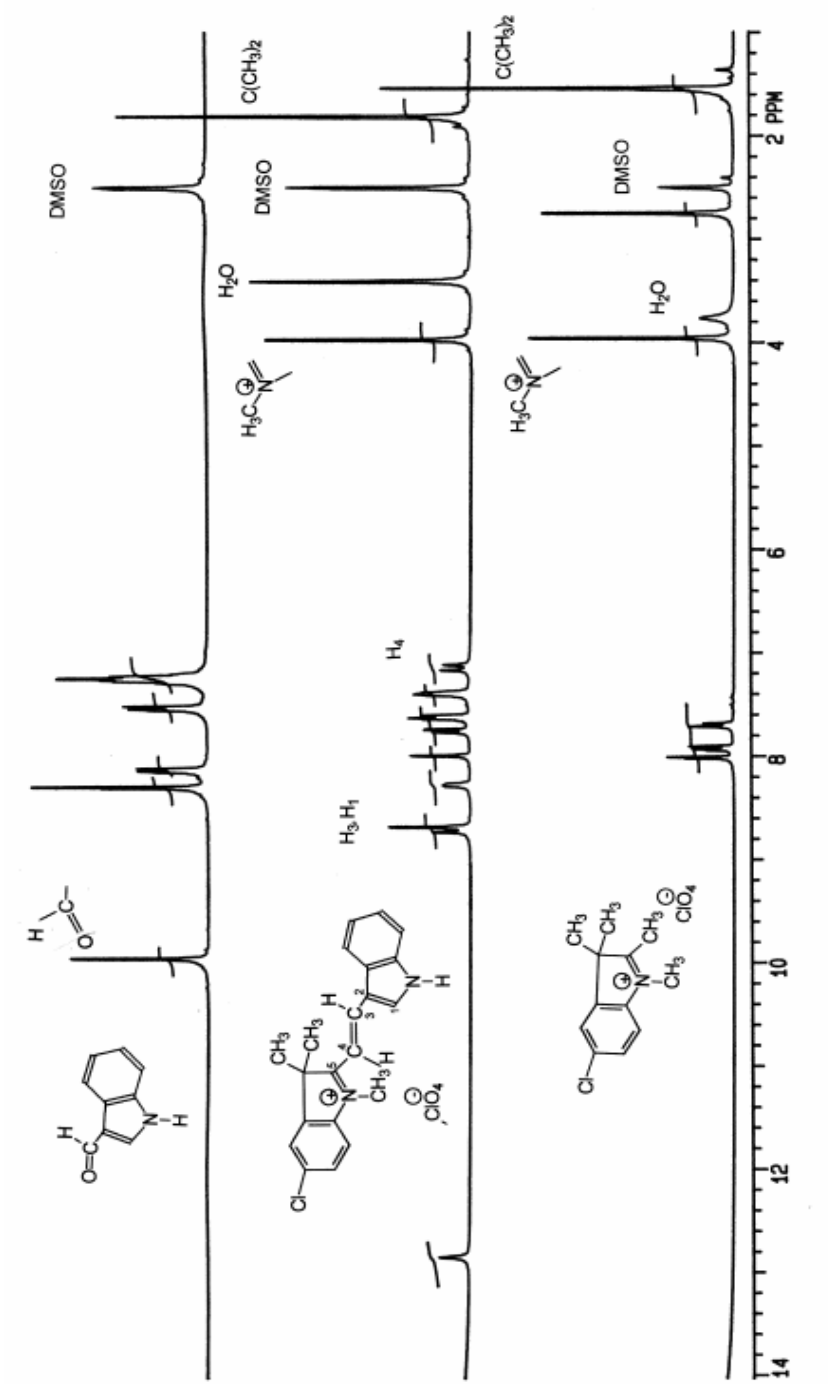

Fig. 1. NMR spectra of 1-H-indolo-3-carbaldehyde, 5-chloro-1,2,3,3-tetrametthyl-3-H-indolium perchlorate (***6***) and of 5-chloro-1,3,3-trimethyl-2-[2-(1-H-indol-3-yl)ethenyl]-3-H-indolium perchlorate in Hexadeutero-dimethylsulfoxide, registered with Varian Gemini 300 spectrometer.

Table 3

^{1}H-NMR data (chemical shift δ in ppm, multiplicity*, number of hydrogen atoms and coupling constant J in Hz) for some condensation products of 1-H-indolo-3-carbaldehyde ***(4)*** with 2- or 4-methyl-cycloimmonium perchlorate ***(5)***.

Assigned structure:

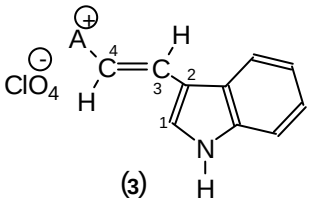

(3)

Compound **3** A^+ =		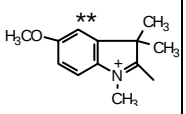	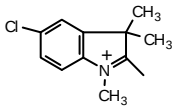	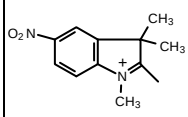	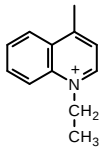
Hydrogen atoms of the group	$C(CH_3)_2$	1.95 (s) 6H	1.98 (s) 6H	2.02 (s) 6H	
	$+NCH_2R$	δ NCH_3 4.12 (s) 3H	δ NCH_3 4.12 (s) 3H	δ NCH_3 4.12 (s) 3H	δ NCH_2- 4.05 (q) 2H 7 Hz δ NCH_2-CH_3 1.75 (t) 3H 7 Hz
	CH aromatic	7.2-8.5 (m) 7H	7.45-8.5 (m) 7H	7.4-8.9 (m) 7H	7.3-9.3 (m) 10H
	C_4-H	7.07 (d) 1H 16 Hz	7.27 (d) 1H 16 Hz	7.27 (d) 1H 16 Hz	8.1 (d) 1H 16 Hz
	C_3-H	8.73 (d) 1H 16 Hz	8.83 (d) 1H 16 Hz	8.95 (d) 1H 16 Hz	8.70 (d) 1H 16 Hz
	C_2-H	8.70 (s) 1H	8.80 (s) 1H	8.90 (s) 1H	8.60 (s) 1H
	N-H	12.84 (b) 1H	13.00 (b) 1H	14.29 (b) 1H	13.20 (b) 1H

*) multiplicity: (s)-singlet, (d)-doublet, (t)-triplet, (q)-quartet, (b)-broad, (m)-complex multiplet
**) δ O-CH_3 = 4.0(s), 3H. Spectra recorded with Tesla BS 487 spectrometer.

Acknowledgement. The support of this research by the Romanian National University Research Council (CNCSIS Grant A) is greatefully acknowledged.

REFERENCES

1. D. R. B a e r in *The Chemistry of Synthetic Dyes,* Ed. K. Venkataraman, Academic Press, London, **1971**, Vol 4**,** p.184-185; R. R a u e, O. R i e s t e r in *Ullmanns Encyclopaedia der Technische Chemie, 4-th Ed.,*Verlagchemie*,* Weinheim, **1978**, Vol 16, p. 652-653; D. M. S t u r m e r, D. R. D i e h l in *Kirk-Othmer Encyclopedia of Chemical Technology, 3-rd Ed.,* John Wiley, New York, **1982**, Vol. 18, pp. 848-850, 870.
2. J. B. C a l d w e l l, N. A. E v a n s, D. J. G a l e, I. W. S t o p l e t o n, J. F. K. W i l s h i r e, *J.Soc. Dyers Colour.* **1973**, *89,* 94.
3. V. P a r a m e s v a r a n, A. V. R a m a, K. V e n k a t a m a r a n, *Indian J. Chem.,* **1974**, *12,* 785.
4. G. E. F i c k e n in *The Chemistry of Synthetic Dyes,* Ed. K. Venkataraman, Academic Press, London, **1971,** Vol. 4**,** p.337-339.
5. F. M. H a m e r, I. M. H e i l b r o n, J. H. R e a d e, H. N. W a l l s, *J. Chem. Soc.,* **1932,** 251; J. F i n k e l s t e i n, J. L e e, *U.S. Pat.,* 2695290, **1954**; A. M. A c k e r m a n, H. V e l d s t r a, *Rec. trav. Chim.,* **1954,***73,* 629; R. N. C a s t l e, C h. W. W h i t t l e, *J Org. Chem.,* **1959**, *24,* 1189; I. P a n e a, *Diss. Univ. Basel,* **1977**; P. M o e c k li, *Ger.Offen. 2711521,* **1977**; T. V. S t u p n I k o v a , V. N. K a l a f a t, N. A. K l y u e v, V. P. M a r s h t u p a, R. S. S a g i t u l l i n, *Khim. Geterotsikl. Soedin.,* **1980**, 1360; R. R a u e, H. P. K u e h l t h a u, *Ger. Offen., D.E. 3136583,* **1983**; R. R a u e, H. P. K u e h l t h a u , K. F. L e h m e n t, *Ger. Offen., D.E .*3210596 **1983**; K. S a t o , K. K a n o, T. Y a f u n e, M. H i d a, S. A r a i, T. Y a m a g i s h i, *Heterocycles,* **1994**, *37*, 955.
6. F. M. H a m e r, *The Cyanine dyes and Related Compounds,* Intersci. Publ., London, **1964,** pp.132-136, 316-317, 353-355; E. S c h m i d t, *Ger.***Pat***.,* 2060615; 2064881, 2064 882*,* **1972**; G. A. R e y n o l d s, J. A. V a n A l l a n, *Fr. Pat.,* 2055690, **1972;** N. M. O m a r, *J. Pharm.Sci.,***1973**,*14*, 183; A. M. O s m a n, M. S. K. Y o u s s e f, *Z. H Kahalil. Appl. Chem. Biotechnol.,* **1976**, *26*, 762; R. D. H a u g w i t z, B. V. M a u r e r, *U.S. Pat*.4006137, **1977**; I. P a n e a, *Rom. Pat.*, 75012 **1980**; I. P a n e a, V. C h i o r e a n, *Rom.Pat.* 75092, **1980**; I. P a n e a, V. F a r c a s a n, F. P a i u, V. C h i o r e a n, *Rom*. *Pat*.,77770, **1981**; Z. L i, Z. Z h a n g, J. G u o, *Huaxue Tangbao,* **1985***,*13 cf. CA **1986**,*104*, 150779r.
7. I. P a n e a, S. S a i d a c, E. B a r b a c a r u, V. A m a r i u t e i, V. C h i o r e a n, *Rom. Pat.* 84458, **1984.**
8. E. S. E m e r s o n, M. A. C o n l i n, A. E. R o s a n o f f, K. S. N o r l a n d, H. R o d r i g u e z, D. C h i u, G. R. B i r d, *J. Phys. Chem.,* **1967**,*71,* 2396; A. I. K i p r i a n o v, G. G. D y a d y u s h a, F. A. Mikailenko, *Russian Chem. Rev.* **1966**, *35*, 361.
9. U. M a y e r, *Textilverdlung,* **1972,** *7*, 492.
10. L. M. J a c k m a n, S. S t e r n h e l l, *Application of NMR Spectroscopy in Organic Chemistry,* 2-nd Ed. Pergamon Press, London, **1969**,pp.163, 185-185, 302.
11. S. D a h n e, J. R a n f t, *Z. physik. Chem.,* **1963,** *224,* 65; R. R a d e g l i a, E. G e y, K. D. N o l t e, S. D a h n e, *J. prakt. Chem.,***1970**, *312*, 877.

12. L. J. B e l l a m y, *The I.R. Spectra of Complex Molecules*, 2-nd Ed. London, Methuen, **1965,** p.34**.**
13. E. K l e i n p e t e r, R. B o r s d o r f, F. D i e t z, *J. prakt. Chem.,* **1973,** *315,* 600; D. N. K r a m e r, L. P. B i s a u t a, R. B a t o, B. L. M u r r jr., *J. Org. Chem.,***1974,** *39,* 3132.
14. J. K i s t e r, A. B l a n c, F. D a v i n, J. Metzger, *Bull. Soc. Chim. Fr.,* **1975,** 2297.

STUDIA UNIVERSITATIS BABEŞ-BOLYAI, CHEMIA, XLIV, 1-2, 1999

OPTIMIZATION OF THE FLAME ATOMIC EMISSION DETERMINATION OF MAGNESIUM IN THE METHANE - AIR FLAME

LADISLAU KÉKEDY-NAGY and EMIL A. CORDOŞ

Universitatea "Babeş-Bolyai" Facultatea de Chimie şi Inginerie Chimică
3400 Cluj-Napoca, Arany J. 11, România

ABSTRACT. The effect of the flame composition, the observation height in the flame and the bandpass of the monochromator on the emission of magnesium in the methane-air flame were studied. These parameters were optimized in order to achieve the highest signal-to-noise ratio and the lowest detection limit. The best results were obtained with the magnesium line of 371.9 nm at the observation height of 6 mm over the burner head, with the stoichiometric flame and the slitwidth of 0.34 mm. The detection limit of 0.3 ± 0.1 mg/L was obtained at a significance level of 0.05, using the two step Neyman-Pearson criterion.

INTRODUCTION

Magnesium ranks eighth among the elements in order of abundance and is a common constituent of different samples. Flame atomic emission spectrometry (FAES) is a simple, precise method for the determination of magnesium in low concentrations. As excitation source usually the high temperature C_2H_2-air, C_2H_2-O_2, C_2H_2–N_2O, H_2-air flames are used. The optimal conditions for the determination of magnesium in these flames were established, the detection limits are of order of 10^{-1}-10^{-2} mg/L [1-6].

The low temperature flames (~ 2000 K), as propane-butane-air (PB-A), are used in low performance commercial flame-photometers, designated for routine analysis. The methane-air (M-A) flame has similar properties (temperature, burning velocity etc) with the PB-A flame [7]. To our best knowledge the behaviour of magnesium in the M-A flame was not studied, and the detection limits are not known. The aim of this work is to study the behaviour of magnesium in the M-A flame, to optimize the flame and instrumental parameters in order to obtain the highest signal-to-noise ratio (S/N) and the lowest detection limit.

EXPERIMENTAL

Instrumentation

The measurements were carried out with a HEATH-701 (Heath Co., Benton Harbor, MI, USA) spectrophotometer, a HEATH EU-700 scanning monochromator, a HEATH EU-700-30 type photomultiplier module and a 1P28A (RCA, USA) photomultiplier (-700 V). The photomultiplier signal was recorded with a K-201 (Carl Zeiss Jena) strip chart recorder. The pneumatic nebulizer-spray chamber-burner system was used from an AAS -1 (Carl Zeiss Jena) atomic absorption spectrophotometer. The original 100 mm slot type burner head for C_2H_2-air flame was replaced with a similar Mecker type, developed by us, for the M-A flame [8,9]. The burner was held parallel to the optical axis of the spectrophotometer. For higher nebulization efficiency the original 8 mm glass ball impactor was replaced with an 1 mm cylindrical one, placed at optimal distance of 5 mm from nebulizer head [10]. The air flow-rate was kept constant at 500 L/h, the flow rate of the methane being varied as a function of the gas mixture wanted. As CH_4 source the city gas of 99 % purity was used, from the pipe.

Chemicals

Stock standard solution of magnesium (1000 mg/L) was prepared by dissolving 1g of magnesium metal (Specpure, Johnson Matthey Chemicals Limited, England) in 10 mL HCl 1:1 (analytical grade, Merck, Darmstadt, Germany) and diluted with double distilled water to 1 L. The pH of the stock standard solution as well as of the diluted measuring standard solutions was kept constant, at the value of 2 [1]. For further dilutions double distilled water was used in all cases.

Procedure

The behaviour of magnesium in the M-A flame was observed in the flame up to h = 18 mm over the burner head (in1mm steps), at three different flame compositions: 0.88; 1.00; 1.12 (expressed in relative stoichiometric units (RSU)). Four replicate measurements were made. The mean, the standard deviation, the S/N and the signal-to-background (S/B) ratio were calculated for each h and flame composition investigated. The homogeneity of the means was tested by the F test at a significance level of 0.05. The slit width of the monochromator was of 0.1 mm, the sensitivity of the strip chart recorder was different in different spectral domains in function of the intensity of the emission lines and the background observed. For a given set of determinations the sensitivity was kept constant.

RESULTS AND DISCUSSION

The emission spectrum of magnesium

The emission spectrum of magnesium in the M-A flame was determined first by nebulizing a magnesium solution of 1000 mg/L in the flame, recording the spectrum of the flame alone, in the 200 - 800 nm spectral range, then that of the flame in the presence of magnesium. Using spectral tables there were identified atomic lines with λ = 277.98 nm, 285.27 nm, 382.94 nm, 383.23 nm, 383.83 nm, 457.11 nm, 516.73 nm, 517.27 nm and 518.36 nm, respectively. Magnesium emits two ionic lines with λ = 279.55 nm, 280.27 nm and an intense molecular emission band in the spectral domain of 370-400 nm. The molecular band, with the most intensive band-heads at 371.9 nm and 382.2 nm, respectively belongs to MgO and MgOH formed in the flame [11].

Optimization of the flame composition and instrumental parameters, determination of the analytical emission line

The aim is to obtain those values for the flame composition and observation height h for whose the S/N ratio is maximal. The concentration of the calibration solution was 100 mg/L. The analytical signal, intensity (I), was measured for the most intensive lines selected, at 277.98 nm, 279.55 nm, 285.27 nm, 371.9 nm, 382.2 nm, 516.73 nm, 517.27 nm and 518.36 nm, respectively. The composition of the flame in this step was kept constant, at 1.12 RSU. The variation of the line intensities versus observation height over the burner head is represented in Fig.1.

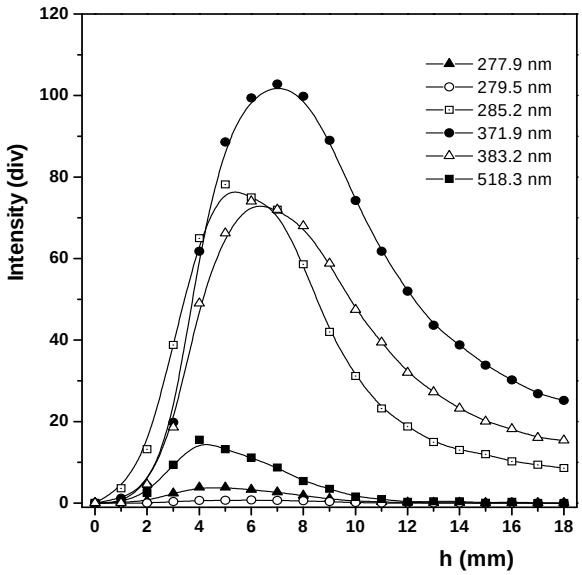

Figure 1**.** The intensity of different magnesium lines versus observation height (h)

For the quantitative estimation of the results at different wavelengths only the maximal value of the analytical signal (I_{max}) for each line was selected. In order to get comparable data the corrected intensity (I_{cor}) and the relative intensity (I_{rel}) for each line was calculated, considering the sensitivity of the chart recorder. The reference sensitivity of 1.10^{-9} A/div and the reference line was the weakest one. The S/B ratio was determined in the same way. The results are summarized in Table I.

Table I

The relative intensities of the emission lines of magnesium in the M-A flame

Wavelength (nm)	Emittent	h (mm)	I_{max} (div)	$I_{Corr.}$ (div)	I_{rel}	S / B
277.98	Mg I	4-5	38.6	38.6	5.21	0.81
279.55	Mg II	6	7.4	7.4	1.00	0.17
285.27	Mg I	5	39.5	790.0	106.75	7.60
371.9	MgO, MgOH	7	51.4	1028.0	138.91	21.80
382.2	MgO, MgOH	6	37.0	740.0	100.00	13.80
516.73	Mg I	7	3.1	62.0	8.37	1.40
517.27	Mg I	3-4	12.6	126.0	17.02	11.60
518.36	Mg I	4	15.5	155.0	20.94	13.80

The most intensive line is the molecular emission band head at 371.9 nm, observed at 7 mm over the burner head, being excited in the interconal reaction zone of the flame. The S/B ratio is low, due to the high value of the background. The atomic lines are less intensive, only the resonance atomic emission line of λ = 285.27 nm has comparable intensity to the molecular band head lines. The intensity of the lines varies in the same manner as the concentration of different radicals in the flame, fact which suggests that the excitation process takes place *via* these radicals [12].

The influence of the flame composition and of the observation height on the emission signal for the most sensitive line was investigated (the analytical line) using three flame compositions (0.88, 1.00, 1.12 RSU) and at the concentration level of 100 mg/L. The data were processed by using the MicroCal Origin™ Software package, version 5.0 (MicroCal Software Inc., MA, USA) and plotted as 2D contour map (Fig.2).

The emission signal depends both on observation height and flame composition. The I-h curves are of Gaussian-shape, with the maximum between h = 5-7 mm. The emission increases with the increase of the methane content in the flame, being the highest in the stoichiometric flame. In the fuel rich flame the emission decreases slowly. The standard deviation of all means was homogeneous, the magnitude of the S/N ratio being decided by the magnitude of the mean. In conclusion, the optimal conditions for the quantitative determination of magnesium in the M-A flame are λ = 371.9 nm (the analytical line), h = 6 mm and flame composition 1.00 RSU.

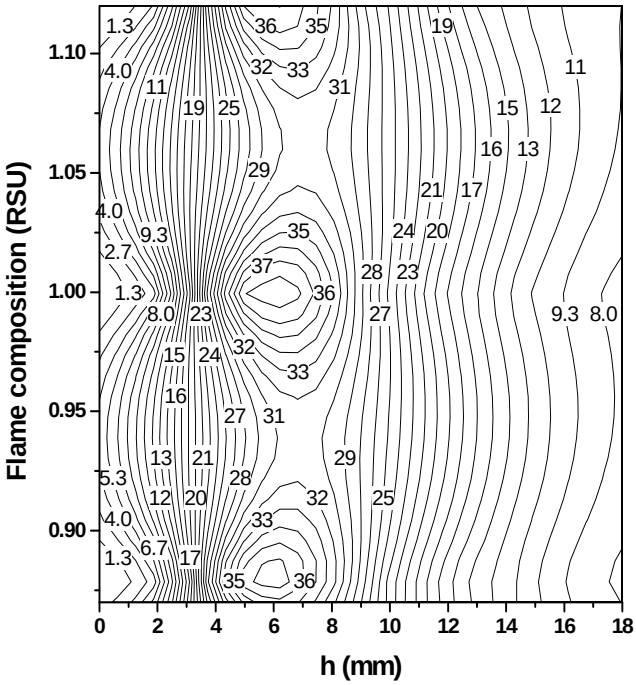

Figure 2. The 2D contour map of the emission of the 371.9 nm magnesium-line vs. observation height and flame composition. The labels on the plot indicate the grid matrix values.

The influence of the spectral bandpass of the monochromator on the Analytical signal, S/N and S/B ratio

The spectral bandpass of the monochromator is determined by its slitwidth (SW). The SW influences both the amplitude and the fluctuations of the emission signal, but not in the same manner. Therefore the optimal slitwidth for which the S/N ratio is maximum can be determined. The flame and instrumental parameters used were the optimal ones, determined earlier. The influence of the slitwidth on I, the S/N and S/B ratio was studied in the 0.1 - 0.7 mm domain in steps of 0.1 mm, using a 100 mg/L magnesium solution.The results are shown in Figure 3.

The results show that the emission signal increases with the spectral bandpass of the monochromator, it varies according to a second order polinomial function ($I = -0.47143-7.42857\ SW+290\ SW^2$, $r = 0.9999$). The S/N ratio increases too, up to a SW of 0.55 mm, then decreases. The standard deviation of the means increases suddenly at SW value of 0.6 mm, but remains homogeneous in the entire SW domain. The S/B ratio is practically constant regardless of the SW value. This is the consequence of the fact that the 371.9 nm magnesium line is a molecular band-head line.

In conclusion, the slitwidth could be increased up to 0.7 mm without a significant decay of the S/N ratio.

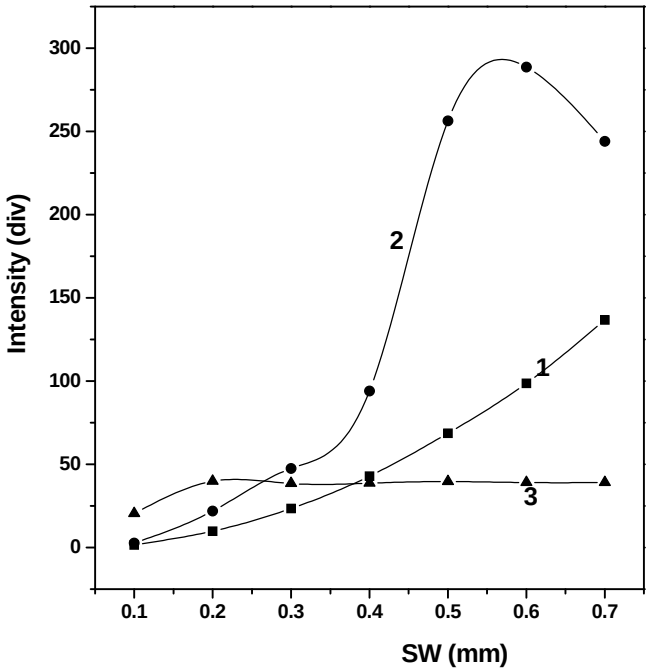

Figure 3. Variation of the intensity of 371.9 nm magnesium line (100 mg/L) versus the slitwidth (SW) of the monochromator: 1 – line intensity, 2 – S/N ratio, 3 – S/B ratio.

Interferences

The effect of Na, K, Mg, Sr, SO_4^{2-} and PO_4^{3-} on the emission signal of magnesium of 10 mg/L was investigated. The experimental conditions were the optimal ones, determined previously. The variation of the magnesium emission signal versus the concentration of the interferents is represented in Fig 4.

Na, K, Ca and Sr influence simultaneously the emission of magnesium and that of the flame. The alkaline metals depletes slowly the magnesium emission, whilst Ca and Sr increase it. These interferents exhibit the greatest influence on emission of the flame, increasing linearly the flame background with the concentration of the interferent. This effect varies for the studied elements in order of Sr > K > Ca > Na. The SO_4^{2-} and PO_4^{3-} ions decrease drastically the magnesium emission signal, due to formation of stable, refractory compounds in the flame.

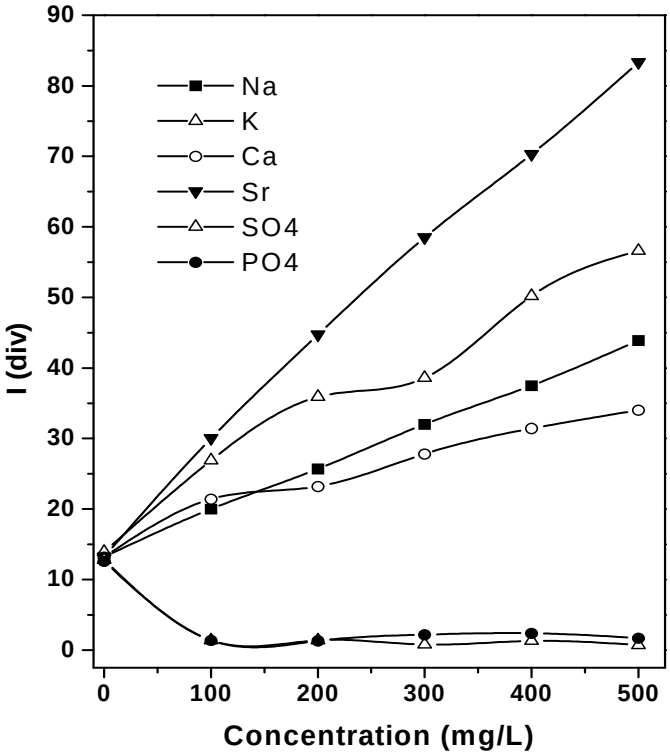

Figure 4. Influence of Na, K, Ca, Sr, SO_4^{2-}, and PO_4^{3-} on the emission signal of magnesium of 10 mg/L.

Calibration, determination of the detection limit

For the determination of the detection limit the variation of the analytical signal versus concentration was studied. The calibration curves were plotted in the 1-100 mg/L magnesium concentration range. One curve covered only one order of magnitude of concentration. Each calibration curve was established by using six standard solutions. Six replicate measurements were made at each concentration level. The homogeneity of the means and the linearity of the calibration curve were tested. The equation of the regression line, the confidence limits and the coefficient of correlation (r) were calculated with the least squares method. The detection limit was calculated using the two step Neyman-Pearson model [13,14], for the fixed values of $(P_{10})_0$ = 0.025 and $(P_{11})_d$ = 0.975. The results are summarized in Table II.

Table II

Calibration data of magnesium determination in the M-A flame

Concentration range (mg/L)	Sensitivity (A/div)	Slit width (mm)	Equation of the calibration curve	Detection limit (ppm)
100 – 10	$2*10^{-9}$	0.10	I = -1.65 + 0.502*C r = 0.9996	0.8 ± 0.6
10 – 1	$1*10^{-9}$	0.10	I = -1.32 + 0.982*C r = 0.9897	0.7 ± 0.5
10 – 1	$5*10^{-9}$	0.34	I = -3.77 + 2.483*C r = 0.9987	0.3 ± 0.1

The concentration-intensity relationship is linear in the 1 – 100 mg/L domain, regardless of the magnesium concentration. The sensitivity of the determinations can be enhanced, by using a broader slitwidth. The slitwidth could be increased only till 0.34 mm because the flame photometer does not afford to compensate the high flame emission background signal, which overlaps the low analytical signal. The detection limits obtained for each concentration range are also summarized in Table II. These values are low being comparable with those obtained with other types of flames. The increased slit width does not improve significantly the detection limit.

CONCLUSIONS

In the M-A flame magnesium exhibits a complex spectrum (atomic, ionic and molecular). The most intensive line (the analytical line) is the molecular band-head line at 371.9 nm. The intensity of the magnesium lines vary with the composition of the flame and observation height over the burner head. In the stoichiometric flame the optimal excitation zone is at 6 mm over the burner head. The observation height for the maximum intensity is independent of the flame composition. In order to increase the S/N ratio, and lower the detection limit, the slitwidth of the monochromator could be increased till 0.7 mm without decay of the S/N ratio. Na, K, Ca and Sr increase significantly the emission of magnesium by a linear increase of the flame background with their concentrations. The calibration curves (in optimal experimental conditions) are linear in the 100 -1 mg/L concentration range, the detection limit obtained is of 0.3 ± 0.1 mg/L.

REFERENCES

[1] J.D. Winefordner, *Spectrochemical methods of analysis*, New York., Wiley Interscience, 1971, p.130.
[2] D.A. Hickman, G. Harbottle, E.V. Sayre, *Forensic.Sci.Int.*, 1983, **23**,189
[3] H. Matusiewicz, *J.Anal.At.Spectrom*., 1989, 4, 265
[4] G.E. Roscoe,R. Miles, C.G. Taylor, *Anal.Chim.Acta*, 1990, **234**, 439
[5] F. Hu, Z. Wang, Q. Liu, *Chin.Sci.Bull*., 1991, **36**, 560
[6] I.B. Razagui, P.J. Barlow, *Food.Chem*., 1992, **44**, 309
[7] A.G. Gaydon, H.G. Wolfhardt, *Flames, their Structure, Radiation and Temperature*, Chapman and Hill, New York, 1970.
[8] E. Cordoş, L.N. Kékedy, R. Hui, Patent RSR, nr. 67867 / 1977.
[9] E. Cordoş, L. Kékedy-Nagy, *Studia*, 1992, **37**, 61.
[10] L. Kékedy-Nagy, *Talanta*, 1997, **44**, 1919.
[11] R. Mavrodineanu, H. Boiteux, *Flame spectroscopy*, John Wiley, New York, 1965, p.326.
[12] L. Kékedy Nagy, *Studia*, 1992, **37**, 109.
[13] C. LIteanu, I. Rîcă, *Statistical Theory and Methodology of Trace Analysis,* John Wiley, New York, 1980.
[14] D.L. Massart, B.G.M. Vandeginste, S.N. Deming, Y. Michotte, L. Kaufman, *Chemometrics: a textbook,* Elsevier, New York, 1988.

STUDIA UNIVERSITATIS BABEŞ-BOLYAI, CHEMIA, XLIV, 1-2, 1999

AMPEROMETRIC STUDY OF THE INHIBITORY EFFECT OF BENZOIC ACID ON A TYROSINASE-MODIFIED PLATINUM ELECTRODE

SARMIZA ELENA STANCA[1], IONEL CATALIN POPESCU[2], LIVIU ONICIU[2]

[1] *Department of Physics, Chemistry and Informatics, Faculty of Environmental Protection, University of Oradea, 3700 Oradea, Romania*
[2] *Department of Physical Chemistry, University "Babes-Bolyai", 3400 Cluj-Napoca, Romania*

ABSTRACT. A new type of tyrosinase (PPO)-modified Pt electrode, based on physical entrapment of the enzyme in agar-agar gel, was constructed and used to investigate the inhibitory effect of benzoic acid on the PPO activity. At an applied potential of -50 mV *vs.* SCE, the bioelectrode develops a fast, steady state response, linearly correlated with the phenol concentration up to 0.1 mM, with a sensitivity of 4.2 $mA.M^{-1}.cm^{-2}$. A kinetic interpretation of the amperometric response to phenol recorded in the absence and in the presence of benzoic acid, allowed identifying the inhibition process as a competitive one. The inhibition constant, $(1.16 \pm 0.01)*10^{-6}$ M, and inhibition coefficient, $(1.24 \pm 0.15)\ 10^{-3}$ M, were found in good agreement with similar data published in the literature.

INTRODUCTION

Tyrosinase (polyphenoloxidase, PPO) [1-3] and laccase [4, 5] are enzymes containing binuclear copper, which catalyzes the hydroxylation of monophenols to o-diphenols (cresolase activity) and the oxidation of o-diphenols to o-quinones (catecholase activity). Based on this catalytic scheme, a wide group of bioelectrodes incorporating PPO [6-26] or laccase [27] was built for amperometric detection of phenolic compounds.

On the other hand, it was showed that amperometric biosensors are also very convenient probes for monitoring the inhibition of enzyme activity [28,30]. In this way, these devices extended theirs applications toward detection of some important analytes, which act as enzyme inhibitors, and provided deeper information about the interaction mechanism between substrate and enzyme.

Based on the value of the stability constant (K_I, M^{-1}), corresponding to the inhibitor-enzyme complex, the organic acid inhibitors of the PPO active site can be divided into two main groups (Table 1) [1]. To the first group belong weak inhibitors, bearing a carboxylic function which is not conjugated into the aromatic system ($K_I < 150\ M^{-1}$). The nature of the chain attached to the carboxylic function does not exert a significant effect on the inhibition activity. Contrarily, the second group is composed of strong inhibitors, where the carboxyl is well conjugated into an aromatic ring ($K_I > 1000\ M^{-1}$).

The effect of both organic and inorganic (CN^-, F^-, Cl^-, Br^-, I^-, PO_4^{3-}, CO_3^{2-}, SO_4^{2-}, $B_4O_7^{2-}$, NO_3^-, NO_2^-, N_3^-) inhibitors on the PPO activity are often investigated in literature [28-38]. Generally, this kind of studies was performed with dissolved enzyme in homogeneous systems, using spectrophotometry as monitoring method [39]. However, recently it was proved that the inhibition type can be established and the inhibition parameters can be quantitatively estimated *via* amperometric measurements, examining the biosensor response to its substrate in the presence of the investigated inhibitor [28-38].

Table 1.

The stability constants (K_I) of the complex tyrosinase-inhibitor for some organic acids in aqueous solution [1].

Strong inhibitors acids K_I (M^{-1})		**Weak inhibitors acids** K_I (M^{-1})	
m-toluic	450	o-toluic	<10
m-brombenzoic	700	o-brombenzoic	40
benzoic	1400	acetic	10
p-toluic	2000	phenylacetic	110
p-brombenzoic	4100	naphthylacetic	90
p-ethylbenzoic	6800	cyclohexane carboxylic	70
picolinic	570	cycloheptane carboxylic	18
terephthalic	1200		

Starting from the Lineaweaver-Burk equation [40]:

$$\frac{1}{I_{ss}} = \frac{1}{I_m} + \frac{K_m}{I_m}\frac{1}{[S]} \qquad \textbf{(1)}$$

adapted for an amperometric biosensor in the case of a competitive inhibition [39], the reciprocal value of the steady-state response ($1/I_{SS}$) observed for a substrate concentration ([S]) and an inhibitor concentration ([I]) is given by the following equation:

$$\frac{1}{I_{ss}} = \frac{1}{I_m} + \frac{K_m}{I_m}\left(1+\frac{[I]}{K_I}\right)\frac{1}{[S]} \qquad \textbf{(2)}$$

Introducing the inhibition coefficient, $\alpha = (K_m/K_I)$ [31], the equation (2) becomes:

$$\frac{1}{I_{ss}} = \frac{1}{I_m} + \frac{K_m + \alpha[I]}{I_m}\frac{1}{[S]} \quad \textbf{(3)}$$

where: I_m is the intensity of the maxim current and K_m is the apparent Michaelis-Menten constant. Based on equations (1) and (3) a kinetic interpretation of the biosensor responses to substrate, recorded in the absence and in the presence of the inhibitor, allow the estimation of the inhibition parameters α or K_I.

In this work a new amperometric biosensor for phenol detection was developed, by entrapping tyrosinase into agar-agar gel followed by its deposition on a Pt electrode. The aplicability of this kind of bioelectrode for the investigation of enzyme inhibition was checked using benzoic acid, a compound known as a strong inhibitor for PPO [1]. In the same context, in order to check the versatility of the enzyme immobilization technique a similar amperometric biosensor based on laccase was constructed and tested under the same experimental conditions, knowing that the benzoic acid acts for laccase as un uninhibitor [4,5].

EXPERIMENTAL

Reagents

Tyrosinase from mushroom (EC 1.14.18.1; 385 Sigma units/mg) was purchased from Sigma. The laccase extract was prepared as follows. Fresly cutted apple slices and $CaCO_3$ powder, in the ratio 3:1(w/w), were thoroughly mixed for 15 minutes, in a mortar. Then, the necessary amount of distilled water was added in order to obtain a 15 % (w/w) mixture. After 1 hour, the filtered solution can be used as stock solution of laccase.

Electrochemical measurements were made using as supporting electrolyte a 0.1 M $LiClO_4$ solution made in 0.1 M phosphate buffer (pH 7). The phosphate buffer was obtained by mixing the corresponding volumes of 0.1 M KH_2PO_4 and 0.1 M K_2HPO_4.

Phenol, $KH_2\ PO_4$, K_2HPO_4 and $LiClO_4$ were obtained from Merck and used as received. The agar-agar powder, $K_4[Fe(CN)_6]$ and $CaCO_3$ were obtained from "Reactivul" Bucharest and were used without any further purification. The apples were purchased from a grocery.

Enzyme electrode preparation

The technique of enzyme entrapment in agar-agar gel [41] consisted in two steps:

(i) 20 mg of agar-agar powder was homogenized with 0.9 mL of 0.1 M $LiClO_4$ in 0.1 M phosphate buffer (pH = 7). The mixture was heated

at 100 ^{o}C and, subsequently, it was cooled at 50 ^{o}C. Then, 1 mL of enzyme solution was added. The concentration of tyrosinase solution was 2.5 mg/mL and it was prepared by dissolving the pure enzyme in distilled water.

(ii) The above-prepared mixture was deposited on a dialysis membrane of 0.3-mm thickness. The so obtained enzyme-modified membrane was stored at 5^{o}C into phosphate buffer (pH 6.5).

In order to investigate the amperometric response of the bioelectrode to substrate (phenol), the enzyme-modified membrane was mechanically attached to a Pt disk electrode (3-mm diameter), taking care to put the enzyme matrix in a close contact with the electrode surface.

Electrochemical measurements

All measurements were performed using a computer-assisted potentiostat (Autolab-PGSTAT-10, Eco Chemie, Utrecht, The Netherlands), connected to a conventional electrochemical cell equipped with three electrodes. The bioelectrode was the working electrode. A saturated calomel electrode (SCE) was used as reference electrode and a Pt-foil as counter electrode in all experiments.

Amperometric measurements were done as follows: the bioelectrode was immersed in 10 ml of testing solution (0.1 M phosphate buffer containing 10^{-6} M $K_4[Fe(CN)_6]$ and 0.1 M $LiClO_4$) at room temperature and poised at the desired value of the applied potential. When the recorded signal attained a stable value, a known volume of standard solution of substrate (phenol) was added under a vigorous stirring. Subsequently, the signal variation corresponding to the reduction of enzymatically produced o-quinone was recorded for 1-2 minutes. Thus, the calibration curve was constructed by mean of successive additions of small volumes of standard aqueous solution of substrate.

Before using the bioelectrode was kept at 5 ^{o}C in a humid atmosphere. The procedure presented above was repeated unchanged in all tests carried out using the amperometric bioelectrode.

RESULTS AND DISCUSSIONS

In order to optimize the behavior of the PPO incorporating bioelectrode, its steady-state amperometric response to phenol was recorded at different enzyme loadings. As it can be seen from figure 1A, an enzyme loading higher than 30 % (w/w) was not productive. Consequently, all further experiments were carried out with bioelectrodes having this enzyme loading.

The temperature dependence of the biosensor response, showed in figure 1B, revealed that the optimum temperature range for enzyme activity was between 20 and 30 ^{0}C. In order to decrease as much as possible the enzyme thermal denaturation for all further investigations, 21 ^{0}C was chosen as working temperature.

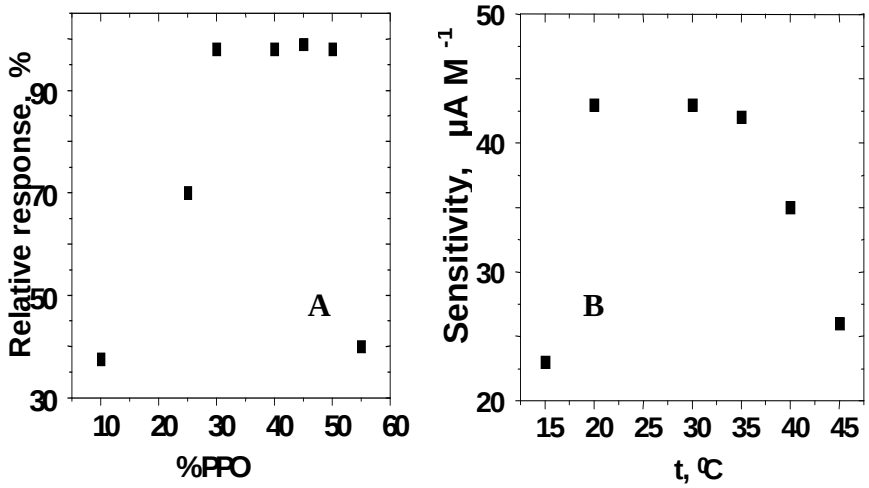

Figure 1. The dependence of the bioelectrode response to phenol on enzyme loading *(**A**)* and on temperature *(**B**).* Experimental conditions: applied potential, -0.18 V *vs.* SCE; phenol concentration, 0.1 mM; supporting electrolyte, 0.1 M phosphate buffer and 0.1 M $LiClO_4$ (pH 7).

As previously reported [6-26], the phenol amperometric detection can be accomplished by applying a potential of -0.2 V *vs.* SCE to detect amperometrically the biocatalytically generated o-quinone. Recently [42], it was proved that using $[Fe(CN)_6]^{4-}$ as mediator it is possible to obtain a significant increase of the bioelectrode selectivity using a lower value of the applied potential (-0.05 V *vs.* SCE), well placed in the optimal domain of the amperometric detection [43]. Operated in this maner, the optimized bioelectrode developed a well-shaped Michaelis-Menten response, proved by the excelent agreement between the experimental data and the calculated curve (Figure 2). The bioelectrode sensitivity to phenol, calculated as the slope of the linear domain, was found (4.2 $mA.M^{-1}.cm^{-2}$) being five times lower than the highest sensitivity reported for PPO containing bioelectrodes [44]. The lower sensitivity and the extended linear domain (up to 0.1 mM) could be attributed to the existance of a diffusion barier, represented by the dialysis membrane used in the bioelectrode construction.

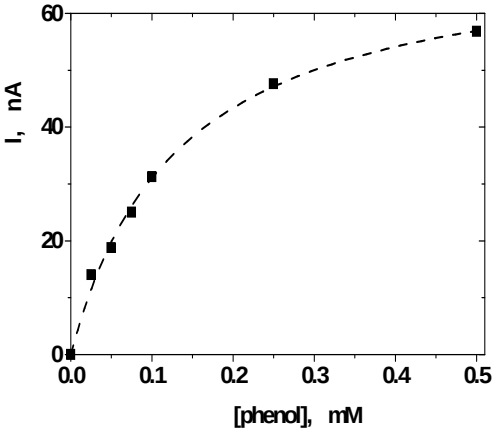

Figure 2. Amperometric response to phenol of the PPO based bioelectrode. Experimental conditions: applied potential, -0.05 V *vs.* SCE; 0.1 M phosphate buffer, pH 7.0, temperature 21^{0}C. The dashed line corresponds to the Michaelis-Menten fitting of the experimental data.

The presence of benzoic acid induced a strong inhibitory effect on the response to phenol of tyrosinase-based bioelectrode (Figure 3A). Contrarily, as it was expected the [4,5], the benzoic acid, in the same domain of concentration, did not exert any influence on the response to phenol for the laccase-based bioelectrode (Figure 3B).

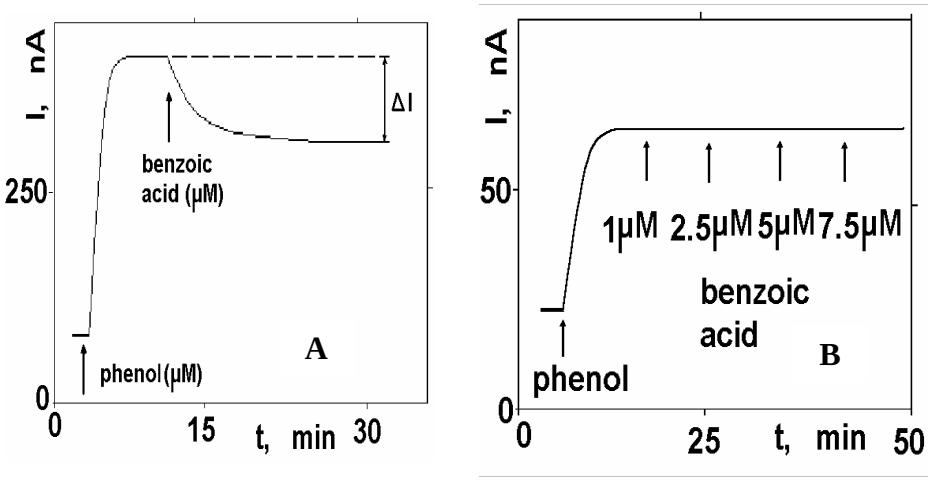

Figure 3A: The amperometric response to phenol of the PPO-based bioelectrode, recorded in the absence and in the presence of 10^{-6} M benzoic acid. Experimental conditions: phenol concentration, 10^{-4} M; applied potential, -0.05 V *vs.* SCE; supporting electrolyte, 0.1 M phosphate buffer and 0.1 M $LiClO_4$ (pH 7); temperature, 21 ^{0}C.

Figure 3B. The amperometric response to phenol of the laccase-based bioelectrode, recorded in the absence and in the presence of the 10^{-6} M benzoic acid. Experimental conditions: as specified for figure 2A.

From the calibration curves to phenol for the PPO-based bioelectrode, recorded in the absence and in the presence of benzoic acid (Figure 4A), and using the equations (2) and (3), in fact from the Linewever-Burk plots (Figure 4B), the characteristic parameters of the inhibition process were estimated (Table 2).

Table 2.

The parameters of the Lineawear-Burk plots for the inhibited and uninhibited response of PPO-based bioelectrode.

Response type	Slope (M/nA)	$1/I_{max}$ (nA^{-1})	Regression coefficient / Number of experimental points
Inhibited	$2.678\ 10^{-6}$	0.0175	0.9965 / 6
Uninhibited	$1.440\ 10^{-6}$	0.0178	0.9908 / 6

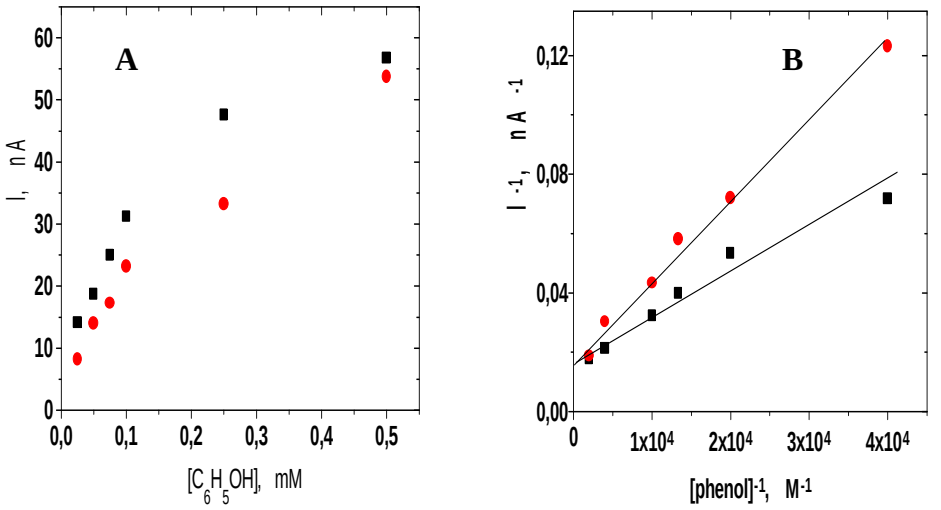

Figure 4. Calibration curves to phenol (**A**) and the corresponding Lineweaver-Burk plots (**B**) for the PPO-based bioelectrode, obtained in the absence (-■-) and in the presence (-●-) of 10^{-6} M benzoic acid. Experimental conditions: applied potential, -0.05 V *vs.* SCE; supporting electrolyte, 0.1 M phosphate buffer and 0.1 M $LiClO_4$ (pH 7); temperature, 21 ^{0}C.

Taking into account that in the both cases (inhibited and uninhibited process) the maximum current intensity had practically the same value (I_{max} ~ 58 nA), it was concluded that the inhibition of the tyrosinase by benzoic acid is competitive with the phenol, at the cresolase active site of the enzyme [39]. The calculated values for the inhibition constant, $(1.16 \pm 0.01)*10^{-6}$ M, and inhibition coefficient, $(1.24 \pm 0.15)\ 10^{-3}$ M, were found in good concordance with that recently published for a PPO-based bioelectrode [45].

CONCLUSIONS

A fast and simple technique for bioelectrode preparation was proposed for the construction of PPO- or laccase- based bioelectrodes. The obtaining procedure of PPO-containing bioelectrode was optimized in respect to the enzyme loading of the enzyme matrix.

A kinetic interpretation of the amperometric response to phenol for the PPO-based bioelectrode, recorded in the absence and in the presence of benzoic acid, allowed identifying the inhibition process as a competitive one. In the same time, no inhibitory effect was noticed for the benzoic acid on the laccase-basaed bioelectrode functioning. In this way it was proved that immobilized in agar-agar gel both enzymes kept their specific bioactivity. Moreover, a comparison with tyrosinase entrapment in amphiphilic polypyrrole [9] showed that the agar-agar gel does not induced a significant loss of enzyme activity.

REFERENCES

1. D.Wilcox, A.G.Porras, Y.T.Hwang, K.Lerch, M.E.Winkler, E.I.Solomon, J. Am. Chem. Soc., 1985, **107**, 4015.
2. H.S.Mason, *Prelyminary Remarks on Polyphenoloxidase*, in *The Biochemistry of Copper*, J.Peisach, P.Aisen and W.E.Blumberg (eds.), Academic Press, New York, 1966, pp. 339-341.
3. D.W.Brooks, C.R.Dawson, *Aspects of Tyrosinase Chemistry*, in *The Biochemistry of Copper*, J.Peisach, P.Aisen and W.E.Blumberg (eds.), Academic Press, New York, 1966, pp. 343-357.
4. T.Nakamura and Y.Ogura, *Characteristics of the State of Copper in Rhus Laccase*, in *The Biochemistry of Copper*, J.Peisach, P.Aisen and W.E.Blumberg (eds.), Academic Press, New York, 1966, pp.389-405.
5. W.G.Levine, *Lacasse. A Review*, in *The Biochemistry of Copper*, J.Peisach, P.Aisen and W.E.Blumberg (eds.), Academic Press, New York, 1966, pp. 371-385.
6. J.G.Schiller, A.K.Chen and C.C.Liu, Anal. Biochem., 1978, **85**, 25.
7. G.F.Hall, D.J.Best and A.P.F.Turner, Anal. Chim. Acta, 1988, **213**, 113.
8. J.Wang and M.S.Lin, Anal. Chem., 1988, **60**, 1545.
9. M.P.Connor and J.Sanchez, Analyst, 1989,**114**, 1427.
10. J.Kulys and R.D. Schmid, Anal. Lett., 1990, **23**, 589.
11. J.Wang and K.Varughese, Anal. Chem., 1990, **62**, 318.
12. P.Skládal, Collect. Czech. Chem. Commun., 1991, **56**, 1427.
13. F.Botrè, F.Mazzai, M.Lanzi, G.Lorenti and C.Botrè, Anal. Chim. Acta, 1991, **255**, 59.
14. F.Ortega and E. Dominguez, J. Biotechnol., 1993, **31**, 289.
15. J.Wang and Y.Lin, Anal. Chim. Acta, 1993, **271**, 53.

16. S. Uchiyama, Y. Hasebe, H.Shimizu and H.Ishihara, Anal. Chim. Acta, 1993, **276**, 341.
17. L.Campanella, A.Fortuney, M.P.Sammartino and M.Tomasseti, Talanta, 1994, **41**, 1397.
18. S.Naish-Byfield, C.J.Cooksey and P.A.Riley, Biochem. J., 1994, **304**, 155.
19. S.Canofeni, S.Di Sario, J.Mela and R.Pilloton, Anal. Lett., 1994, **27**, 1659.
20. J.Wang, F.Lu and D.Lopez, Biosens. Bioelectron., 1994, **9**, 9.
21. M.J.Dennison, J.M.Hall and A.P.F.Turner, Anal. Chem., 1995, **67**, 3922.
22. Q.Deng and S.Dong, Anal. Chem. 1995, **67**, 1357.
23. C.Petit, A.G.Cortes and J.M.Kauffmann, Talanta, 1995, **24**, 1783.
24. G.M.Varga, E.Burestedt, C.J.Svensson, J.Emnéus, L.Gorton and T.Ruzgas, Electroanalysis, 1996, **8**, 1121.
25. D.Puig, T.Ruzgas, J.Emnéus, Lo Gorton, G.M.Varga and D.Barcelo, Electroanalysis, 1996, **8**, 885.
26. E.I.Iwuoha and M.R.Smyth, Biosens. Bioelectron., 1997, **12**, 53.
27. F.Trudeau, F.Daigle and D.Leech, Anal. Chem., 1997, **69**, 882-886.
28. A.M.Donlan, G.J.Moody and J.D.R. Thomas, Anal. Lett., 1989, **22**, 1873.
29. L.Campanella, T.Beone, M.P.Sammartino and M.Tomasseti, Analyst, 1993, **118**, 979.
30. M.H.Smit and G.A. Rechnitz, Anal. Chem., 1993, **65**, 380.
31. M.H.Smit and G.A. Rechnitz, Electroanalysis, 1993, **5**, 747.
32. G.Robinson, D.Leech and M.R.Smyth, Electroanalysis, 1995, **7**, 952.
33. J.Wang and L.Chen, Anal. Chem., 1995, **67**, 3824.
34. L.Stancik, L.Macholán and F.Scheller, Electroanalysis, 1995, **7**, 649.
35. J.Wang, S.A.Kane, J.Liu, M.R.Smyth and K.Rogers, Food Technol. Biotechnol., 1996, **34**, 51.
36. Y.Hasebe, K.Oshima, O.Takise and S.Uchiyama, Talanta, 1995, **42** , 2079.
37. Q.Deng and S.Dong, Analyst, 1996, **121**, 1979.
38. K.Streffer, H.Katz, C.G.Bauer, A.Makower, Th.Schulmeister, F.W.Scheller, M.G.Peter and U.Wollenberger, Anal. Chim. Acta, 1998, **362**, 81.
39. D.V.Roberts,"Enzyme Kinetics", Cambridge University Press, Cambridge, 1977, pp. 1-321.
40. H.Ju, D.Zhou, Yi Xiao and H.Chen, Electroanalysis, 1998, **10**, 541.
41. A.E.Cass, "Biosensors. A Practical Approach", IRL Press-Oxford University Press, 1990, pp. 2-262.
42. S.E.Stanca, I.C.Popescu and L.Oniciu, Studia. Univ. Babes-Bolyai, Chem., 1999, accepted.
43. L.Gorton, Electroanalysis, 1995, **7**, 23.
44. S.Cosnier and I.C.Popescu, Anal. Chim. Acta, 1996, **319**, 345.
45. J.Wang, E.Dempsey and A.Eremenko, Anal. Chim. Acta, 1993, **279**, 203.

STUDIA UNIVERSITATIS BABEŞ-BOLYAI, CHEMIA, XLIV, 1-2, 1999

BIOSENSORS FOR PHENOL DERIVATIVES USING ELECTROCHEMICAL AND BIOCHEMICAL SIGNAL AMPLIFICATION

SARMIZA ELENA STANCA[1], IONEL CATALIN POPESCU[2], LIVIU ONICIU[2]

[1] *Department of Physics, Chemistry and Informatics, Faculty of Environmental Protection, University of Oradea, 3700 Oradea, Romania*
[2] *Department of Physical Chemistry, University "Babes-Bolyai", 3400 Cluj-Napoca, Romania*

ABSTRACT. Three different approaches to enhance the sensitivity of tyrosinase (PPO) based biosensor for the amperometric detection of phenols have been compared. An electrochemical approach, involving ferrocyanide as mediator for the detection of enzymatically produced o-quinone, was tested using a monoenzyme bioelectrode for phenol. In order to investigate the biochemical approach, based on the cooperative functioning of tyrosinase and D-glucose dehydrogenase (GDH) or tyrosinase and horseradish peroxidase (HRP), two bienzyme electrodes were constructed for L-tyrosine detection at -180 mV *vs.* SCE. For monoenzyme bioelectrode, as well as for bienzyme bioelectrodes, the enzymes were immobized in agar-agar gel. The highest signal amplification factor (74), was observed for the PPO-GDH couple, while that recorded for PPO-HRP couple and PPO-ferrocyanide system were 32 and 4, respectively.

INTRODUCTION

There is a continuous increasing demand for selective and sensitive detection of phenol and its derivatives since these toxic compounds are widely used in the manufacture of various industrial products such as pesticides, disinfectants, fumigants, etc.

Owing to their high selectivity and simple use for continuous on site analysis, biosensors constitute powerful tools for environmental monitoring [1]. In particular, several biosensors based on tyrosinase, a polyphenol oxidase (PPO), were elaborated for the determination of phenol. Since PPO catalyses the oxidation of phenol to o-quinone by dioxygen, various kinds of electrochemical detection were involved in these biosensors: (i) the detection of dioxygen consumption [2-4]; (ii) the direct reduction of the generated o-quinone [5-21]; (iii) the mediated reduction of o-quinone by hexacyanoferrate (II) [22-23], tetracianoquinonedimethane [24], 1,2-naphtoquinone-4-sulphonate [25,26] and N-methylphenazonium [27].

For phenol amperometric biosensors working via the electrochemical reduction of the quinone product a partial substrate recycling was suggested, inducing amplification on the biosensor response [7,11,17-20]. This "intrinsic" amplification effect was supposed to be responsible for the very low detection limits reported for phenol and o-diphenols.

Recently, significant response amplification of PPO-based biosensors has been reported involving: a cyclic chemical reaction between the enzyme-generated o-quinone and a deliberately added reducing agent, as ascorbate [28] or NADH [29]; a cooperative functioning of PPO and horseradish peroxidase (HRP) [30].

In this context, we describe here a study aiming to compare three approaches for response amplification of the tyrosinase (PPO) based biosensor, applied for amperometric detection of phenols. For this purpose mono- and bienzyme electrodes were constructed using agar-agar gel as enzyme immobilization matrix. The electrochemical approach (Figure 1), involving ferrocyanide-mediated reduction of enzymatically produced o-quinone, was tested for phenol detection at PPO monoenzyme bioelectrode. The biochemical approaches, consisting of two enzymes cooperative functioning, have been investigated for PPO and D-glucose dehydrogenase (GDH) couple (Figure 2), as well as for PPO and horseradish peroxidase (HRP) couple (Figure 3). Both bienzyme electrodes were tested for L-tyrosine detection.

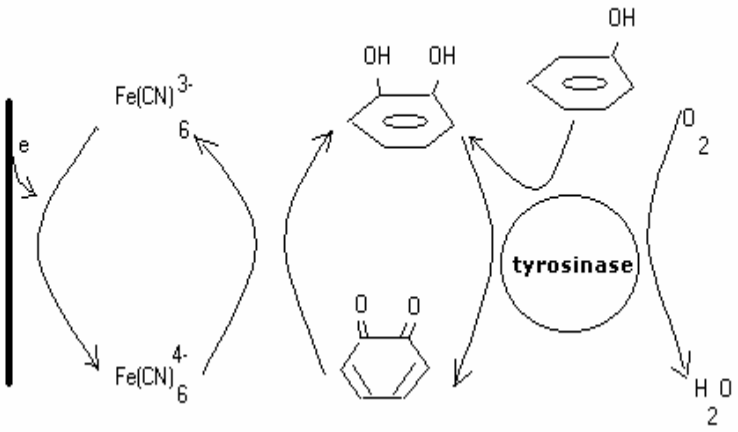

Figure 1. Mediated electro-reduction of o-quinone involved in the signal amplification at PPO-based bioelectrode used for phenol detection [20].

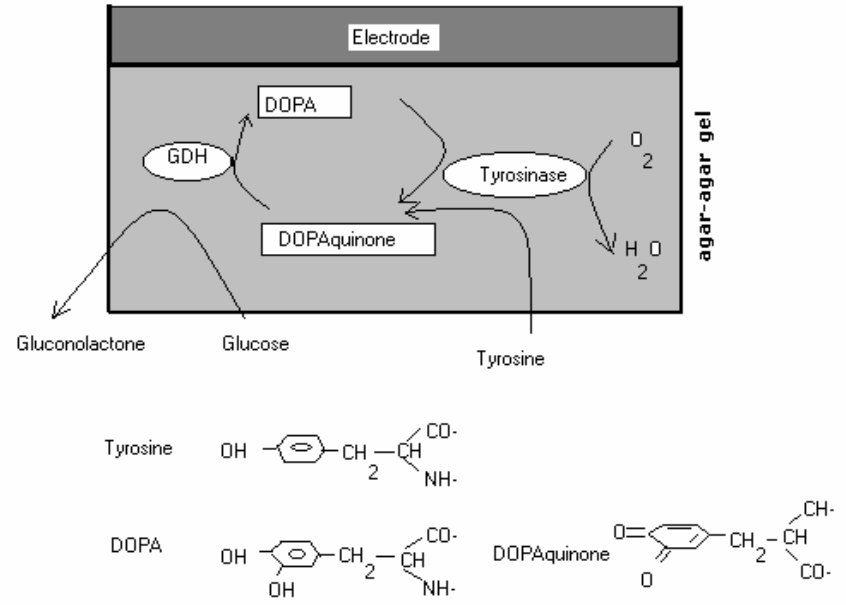

Figure 2. Schematic recycling of DOPA-quinone between tyrosinase and glucose dehydrogenase within a PPO-GDH containing matrix used for L-tyrosine amperometric detection [31].

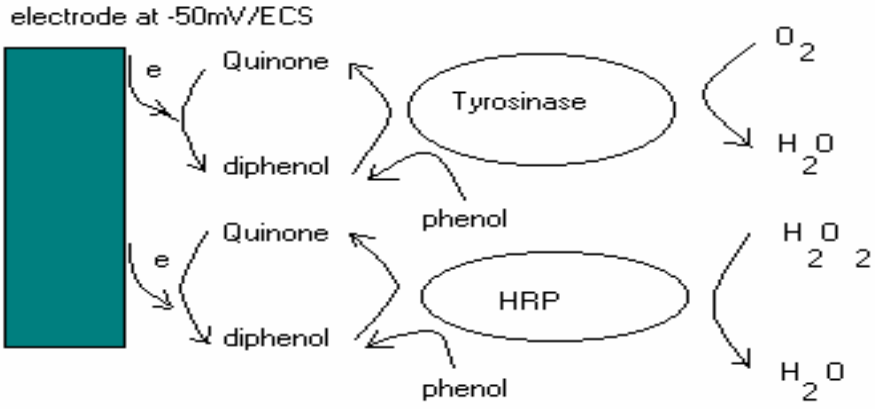

Figure 3. Schematic amplification of the phenol response at PPO-HRP bienzyme bioelectrode [30].

EXPERIMENTAL

Reagents

Tyrosinase from mushroom (EC 1.14.18.1; 385 Sigma units/mg), glucozdehydrogenase (E.C.1.1.1.47; 250 Sigma units/mg) and horseradishperoxidase (EC.1.11.1.7; 250 Sigma units/mg) were purchased from Sigma.

Phenol, L-tirosine, KH_2PO_4, K_2HPO_4 and $LiClO_4$ were obtained from Merck and used as received. The agar-agar powder and $K_4[Fe(CN)_6]$ were obtained from "Reactivul" Bucharest and were used without any further purification.

Electrochemical measurements were made using as supporting electrolyte 0.1 M $LiClO_4$ in 0.1 M phosphate buffer (pH 6,5 and 7), obtained by mixing the corresponding volumes of 0.1 M KH_2PO_4 and 0.1 M K_2HPO_4.

Enzyme electrode preparation

The technique of enzyme entrapment in agar-agar gel [32] consisted in two steps:

(i) 20 mg of agar-agar powder was homogenized with 0.9 mL of 0.1 M $LiClO_4$ in 0.1 M phosphate buffer (pH 7). For biosensors using mediated detection, in the above described mixture, 10^{-4} M $K_4[Fe(CN)_6]$ was added. The obtained mixture was heated at 100 ^oC and, subsequently, it was cooled at 50 ^oC. Then, 1 mL of enzyme/enzymes solution was added. The concentration of each enzyme solution was 2.5 mg/mL, and for bienzyme bioelectrodes the enzyme ratio was 1:1(w/w). All enzyme solutions were prepared by dissolving pure enzyme in distilled water.

(ii) the above described mixture was deposited on a dialysis membrane of 0.3 mm thickness. The so obtained enzyme-modified membrane was stored at 5^oC into phosphate buffer at pH = 6.5.

Electrochemical measurements

All measurements were performed using a computer-assisted potentiostat (Autolab-PGSTAT-10, Eco Chemie, Utrecht, The Netherlands), connected to a conventional electrochemical cell equipped with three electrodes. The bioelectrode was the working electrode. In all experiments a saturated calomel electrode (SCE) was used as reference electrode and a Pt-foil as counter electrode.

Amperometric measurements were done as follows: the bioelectrode was immersed in 10 ml of testing solution (0.1 M phosphate buffer containing 0.1 M $LiClO_4$) at room temperature and poised at the desired value of applied potential. When the recorded signal attained a stable value, a known volume of standard solution of substrate (phenol or L-tyrosine) was added, under a vigorous stirring. Subsequently, the bioelectrode amperometric response was recorded for 1-2 minutes. Thus, the calibration curve was

constructed by mean of successive additions of small volumes of standard aqueous solution of substrate.

Before using the bioelectrode was kept at 5 ^{o}C in a humid atmosphere.

RESULTS AND DISCUSSIONS

A. Mediated amperometric detection

A remarkable difference between the response rate corresponding to mediated and unmediated amperometric detection of phenol was noticed for bioelectrodes using tyrosinase entrapped in agar-agar gel (Figure 4). In the same time, as expected, a much greater sensitivity (400 μA/M) for mediated detection than for unmediated process (98 μA/M) was estimated, as the slope of the linear domain, from the calibration curve shown in figure 5.

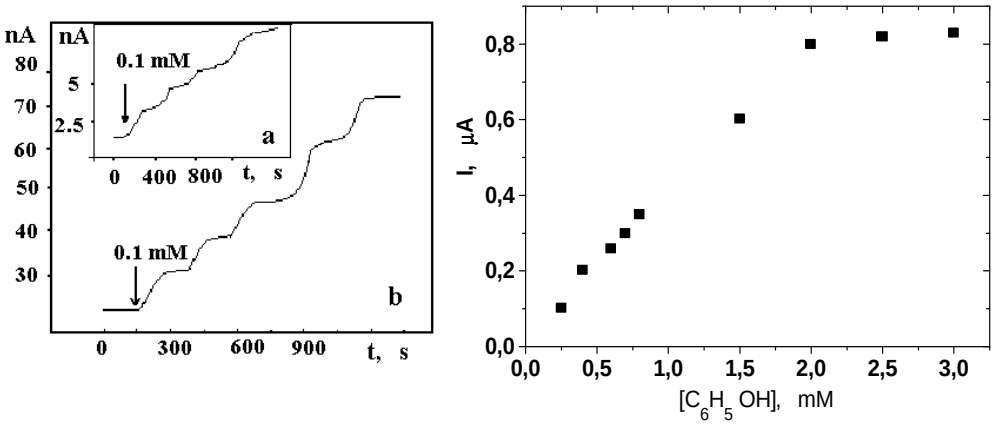

Figure 4. Amperometric response to phenol recorded for the bioelectrode based on tyrosinase entrapped in agar-agar gel: without ***(a)*** and in the presence of $[Fe(CN)_6]^{4-}$ ***(b)***. Experimental conditions: applied potential, -180 mV *vs.* SCE; pH 7, stirred solution; t 21 ^{0}C.

Figure 5. Calibration curve to phenol for tyrosinase-based biolectrode using mediated amperometric detection. Experimental conditions: as indicated for figure 4.

The rate constant (k_{med}) corresponding to the reaction between the redox mediator and the biochemically-produced o-quinone is an important parameter characterizing the intensity of the electrocatalytic effect. A very efficient method for k_{med} evaluation is based on the value of the catalytic limiting current (I_k), described by equation 1 [33]:

$$I_k = nFAC_{med}\sqrt{2D_{med}k_{med}[E]} \quad (1)$$

where: n, represents the number of transfered electrons; A, stands for the electrode surface; C_{med} is the bulk concentration of the mediator; [E] stands for

the total enzyme concentration; D_{med} is the diffusion coefficient of the mediator in solution. Taking n = 1; [E] = 2.5 mg/mL; A = 7.07 mm^2; C_{med} = 4.5 μM; D_{med} = $7.8 \cdot 10^{-6}$ cm^2/s, the k_{med} value was estimated at (1.3 ± 0.04) 10^5 $M^{-1}s^{-1}$, which was found in good agreement with published data [33].

B. Bienzyme cooperative functioning

A comparison of the amperometric responses to L-tyrosine was done between monoenzyme PPO-based bioelectrode and bienzyme bioelectrodes using PPO-GDH and PPO-HRP enzyme couples. The obtained results are presented in figure 7.

In all cases, in order to facilitate the comparison, the enzyme matrix contained the same amount of PPO, and the amperometric detection was performed measuring the current intensity corresponding to o-quinone reduction.

As it can be seen, the highest response was recorded for PPO-GDH couple and the lowest for the PPO-based bioelectrode, using as detection process the mediated o-quinone electro-reduction. This sequence of bioelectrochemical responses is in good agreement with recently published results about the beneficial effect of H_2O_2-HRP couple on the phenol-PPO reaction [30], and about the efficient substrate recycling evidenced for PPO-GDH couple [31].

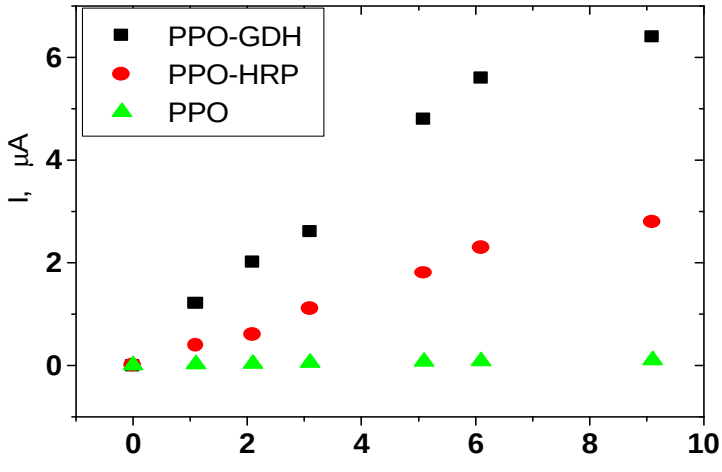

Figure 7. Calibration curves to L-tyrosine for monoenzyme (PPO) bioelectrode and bienzyme bioelectrodes (PPO-GDH and PPO-HRP). Experimental conditions: applied potential, -180 mV *vs.* SCE; supporting electrolyte, 0.1 M fosfat buffer containing $LiClO_4$ 0.1M (pH 6.5); stirred solution; 21 ^{0}C; for PPO-HRP bioelectrode, 1 mM H_2O_2 was added; for PPO-GDH bioelectrode, 2 mM glucose was added.

The bioelectrochemical parameters, I_{max} and K_m, for the three investigated bioelectrodes were estimated using the Lineweaver-Burk linearization of the bioelectrodes response to L-tyrosine, and together with the bioelectrodes sensitivity are presented in table 1.

Table 1.

The bioelectrocemical parameters corresponding to L-tyrosine response of PPO, PPO-GDH and PPO-HRP based bioelectrodes.

Enzyme matrix	Sensitivity (mA/M)	I_{max} (μA)	K_m (mM)
PPO	**0.010**	**0.196**	**10**
PPO-HRP	**0.326**	**19.6**	**55**
PPO-GDH	**0.741**	**16.4**	**14**

It is interesting to remark that comparing the performances of PPO and PPO-GDH bioelectrodes, despite the dramatic sensitivity increase (74 times), the K_m value remained practically unchanged. This behavior confirms the response amplification scheme presented in figure 2. Contrarily, the PPO-HRP bioelectrode, besides an improved sensitivity (32 times) showed a significant higher value for K_m than the specific value for PPO. This K_m increase suggests a decrease of the substrate-enzyme affinity or a supplementary diffusion constraint exisiting in the enzyme matrix, both associated with the increase of enzyme activity, induced by the presence of H_2O_2 [31].

CONCLUSIONS

The mediated scheme for o-quinone detection allowed sensitivity increasing of 4 times compared with a similar biosensor using the direct detection. The phenol biosensor based on ferocianide recycling was found very convenient for aqueous solution using. Simple construction, robustness and a relative long lifetime (more than 3 months) characterized it.

Taking into account the sensitivity and the bioelectrochemical parameters of the investigated bioelectrodes, the biochemical approach for signal amplification based on GDH-PPO couple was found the most suitable for L-tyrosine detection. Moreover, the PPO-GDH bioelectrode showed, besides the highest sensitivity, the shorter response time.

When entrapped in the agar-agar gel all enzymes kept their specific activity, pointing out this matrix as a very convenient one for enzyme immobilization.

ACKNOWLEDGEMENT

The Institute for Instrumental Analysis, Research Center, Karlsruhe (Germany), the Agronomy Faculty from Cluj Napoca (Romania) and the Medicine Faculty from Oradea (Romania) are gratefully acknowledged for their generous supply of enzymes, L-tyrosine and dialysis membrane, respectively.

REFERENCES

1. D. Griffits and G. Hall, TIBTECH, 1993, **11**,122.
2. L. Macholan and L. Schanel, Collect. Czech. Chem. Commun., 1977, **42**, 3667.
3. L. Campanella, M.P. Sammartino, and M. Tomassetti, Sens. Act. **B**, 1992, **7**, 383.
4. S. Canofeni, S. Di Sario, J. Mela and R. Pilloton, Anal. Lett., 1994, **27**, 1659.
5. G.F. Hall, D.J. Best and A.P.F. Turner, Anal. Chim. Acta, 1988, **213**, 113.
6. P. Skladal, Collect. Czech. Chem. Commun., 1991, **56**, 1427.
7. S. Cosnier and C. Innocent, J. Electroanal. Chem., 1992, **328**, 361.
8. J. Wang, N. Naser, H.-S. Kwon and M.Y. Cho, Anal. Chim. Acta, 1992, **264** 7.
9. J. Wang, A.J. Reviejo and S. Mannino, Anal Lett., 1992, **25**, 1399.
10. F. Ortega, E. Dominguez, G. Jönsson-Pettersson and L. Gorton, J. Biotechnol., 1993, **31**, 289.
11. S. Cosnier and C. Innocent, Bioelectrochem. Bioenerg., 1993, **31**, 147.
12. J. Wang, Y. Lin and Q. Chen, Electroanalysis, 1993, **5**, 23.
13. J. Wang, Y. Lin and L. Chen, Analyst, 1993, **118**, 277.
14. J. Wang, L. Fang and D. Lopez, Analyst, 1994, **119**, 455.
15. J.L. Besombes, S. Cosnier, P. Labbé and G. Reverdy, Anal Lett., 1995, **28**, 405.
16. L. Coche-Guérente, S. Cosnier and C. Innocent, Anal. Lett., in press.
17. J. Wang, F. Lu and D. Lopez, Biosens. Bioelectron., 1994, **9**, 9.
18. F. Liu, A. J. Reviejo, J.M. Pingarrón, Talanta, 1994, **41**, 455-459.
19. M. Lutz, E. Burestedt, J. Emnéus, H. Lidén, S. Gobhadi, L. Gorton and G. Marko-Varga, Anal. Chim. Acta, 1995, **305** 8.
20. P. Önnerfjord, J. Emnéus, G. Marko-Varga, L. Gorton, F. Ortega and E. Domínguez, Biosens. Bioelectron., 1995, **10**, 607.
21. C. Nistor, J. Emneus, L. Gorton, L. and A. Ciucu, Anal. Chim. Acta, 1999, **387**, 309.
22. M. Bonakdar, J.L. Vilchez and H.A. Mottola, J. Electroanal. Chem., 1989, **226**, 47.
23. P.I. Ortiz, P.R.A. Nader and H.A. Mottola, Electroanalysis, 1993, **5**, 165.
24. J. Kulys and R. D. Schmid, Anal. Lett., 1990, **23**, 589.
25. M.H. Smit and G.A. Rechnitz, Electroanalysis, 1993, **5**, 747.
26. W.R. Everett and G.A. Rechnitz, Anal.Chem., 1998, **70**, 807.
27. H. Kotte, B. Grundig, K. D. Vorlop, B.Stuhlitz, U. Stottmeister, Anal. Chem., 1995, **67**, 3922.
28. S. Uchiyama, Y. Hasebe, H. Shimizu and H. Ishihara, Anal. Chim. Acta, 1993, **276**, 341.
29. R. S. Brown, K.B. Male and J.H.T. Luong, Anal. Biochem., 1994, **222**, 131.

30. S. Cosnier and I.C. Popescu, Anal. Chim. Acta, 1996, 3**19**, 145.
31. A.V. Eremenko, A. Makower, C.G. Bauer, I.N. Kurochkin, F.W. Scheller, Electroanalysis, 1997, **9**, 288.
32. A.E. Cass, *Biosensors. A practical Approach*, IRL Oxford University Press, 1990, p. 2-262.
33. G. Robinson, D. Leech and M.R. Smyth, Electroanalysis, 1995, **7**, 952.

STUDIA UNIVERSITATIS BABEŞ-BOLYAI, CHEMIA, XLIV, 1-2, 1999

BIOELECTRODE BASED ON TYROSINASE ENTRAPMENT IN ELECTROPOLYMERIZED MATRIX FOR AMPEROMETRIC DETECTION OF PHENOLIC COMPOUNDS

SARMIZA ELENA STANCA[1], IONEL CATALIN POPESCU[2], LIVIU ONICIU[2]

[1] *Department of Physics, Chemistry and Informatics, Faculty of Environmental Protection, University of Oradea, 3700 Oradea, Romania*
[2] *Department of Physical Chemistry, University "Babes-Bolyai", 3400 Cluj-Napoca, Romania*

ABSTRACT. Based on simplicity and low enzyme denaturation, physical methods for enzyme immobilization were extensively used for biosensor construction. In this context, two "*in situ*" obtained polymer matrix, polyaniline and poly-amphiphilic pyrrole, were compared for tyrosinase immobilization on Pt electrodes, in order to construct bioelectrodes for phenol amperometric detection. Mixtures of tyrosinase and the corresponding monomer were electropolymerized, in the presence of a supporting electrolyte (0.1 M $LiClO_4$), at 0.75 and 0.45 V *vs.* SCE for amphiphilic pyrrole derivative and for aniline, respectively. Steady state amperometric measurements, performed at -180 mV *vs.* SCE (aqueous buffer, KCl 0.1 M, phosphate tampon pH=7) and -50 mV *vs.* SCE (0.1 M $C_6H_5CH_2N(CH_2)_3Cl$ in $CHCl_3$), were used to estimate the bioelectrodes electroanalytical parameters. It was established that the polypyrrole matrix has a higher efficiency for enzyme retention resulting in higher bioelectrode sensitivity both in aqueous or chloroform media.

INTRODUCTION

The development of new amperometric biosensors continues to be a rapidly growing research field. When a redox enzyme is used as an active component in such systems, two basic aspects must be considered [1]: (i) the method of assembly of the enzyme electrode; (ii) the electrical contact of the bioelectrocatalyst within this assembly.

One method that offers a high rate of electron transfer between enzyme and electrode is the enzyme entrapment whitin conducting polymers. The most studied conducting polymers have been polyacetylene, polythiophene [2], polypyrrole and its derivative [3], and polyaniline [4].

They are easily to prepare by electrochemically oxidizing of the substrate on the electrode surface. The solvent used, and more particularly the counter anion present in solution, have a major effect on the polymer properties, especially on its conductivity and selectivity.

Phenols and phenol derivatives, due to their high toxicity and environmental persistence, represent a class of compounds of primary interest for water quality monitoring [5]. Recently, it was shown that a widely group of phenols could be detected aqueous media employing amperometric biosensors incorporating tyrosinase (polyphenol oxidase, PPO) [6-18].

The use of PPO for phenol detection in non-aqueous media has been studied intensively due to some advantages of this system [6, 12, 13]. Thus, PPO remains active when, entrapped within a thin aqueous film, is deposited on an electrode surface. Moreover, PPO is not soluble into organic solvents. Hence, there is not necessary a covalent immobilization as in aqueous media, the physical retaining of enzyme on the electrode being successful. On the other hand, the substrate concentration range is more extended because in nonaqueos media the polymerization of o-quinone, the product of the phenol oxidation, is less important than in aqueous solutions. In the same time, the prevention of electrode fouling by such polymerization products increases the biosensor lifetime [3, 18]. Nevertheless, eventually the hydration layer of the enzyme is slowly removed and the enzyme becomes dried and inactivates. Consequently, to avoid the enzyme denaturation the bioelectrode should be stored before using into humid atmosphere.

Summarizing, three kinds of effects should be considered when the influence of the solvent nature on the bioelectrode behavior is examined [19, 20]:

- the general effects due to the solvent hydrophobicity
- the solvent effect on the catalytic activity of the enzyme
- the solvent effect on the solution mass transport properties

This paper presents a comparison of the main electroanalytical parameters for phenol amperometric detection, performed with two different biosensors incorporating tyrosinase. PPO was physically entrapped in two different polymer matrix, obtained by ”*in situ*” electropolymerization of aniline (Figure 1) and an amphiphilic polypyrrole derivative [18] (Figure 2). The influence of a highly hydrophobic nonaqueous solvent (chloroform) on the PPO activity, when the enzyme was entrapped whitin amphiphilic polypyrrole matrix was also investigated.

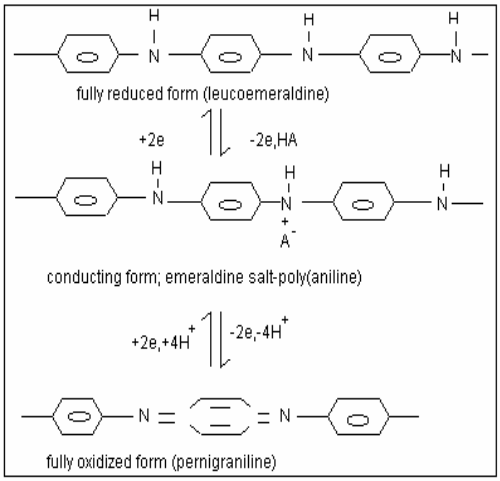

Figure 1. Oxidation of aniline to polyaniline showing switching modes [2].

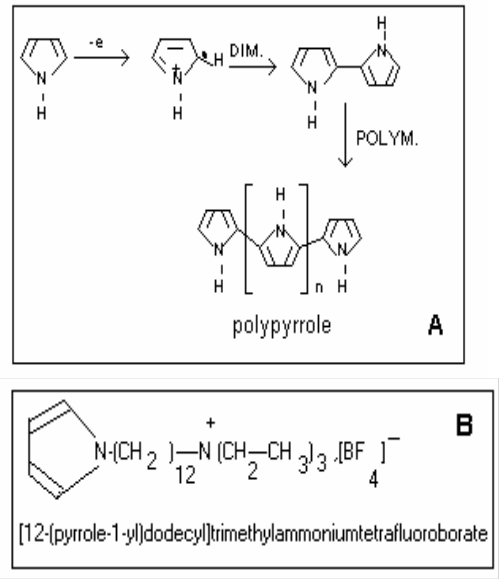

Figure 2. Oxidative polymerization of pyrrole (A) [2] and structure of the amphiphilic pyrrole (B) [18].

EXPERIMENTAL

Reagents

Tyrosinase (EC 1.14.18.1, from mushroom, 4200 Sigma units/mg) was purchased from Sigma. Phenol, chloroform, aniline, KH_2PO_4, K_2HPO_4 and $LiClO_4$ were obtained from Merck and used as received. The amphiphilic pyrrole derivative, [12-(pyrrole-1-yl) dodecyl] trimethylammonium tetrafluoroborate], was generously supplied as a gift by Dr. Serge Cosnier, LEOPR, Grenoble, France.

0.1M $LiClO_4$ and 0.1M phosphate buffer (pH 7, obtained by mixing of the corresponding volumes of 0.1M KH_2PO_4 and 0.1M K_2HPO_4) were used as supporting electrolytes for aqueous solutions for electropolymerisation and for amperometric measurements, respectively. 0.1M $C_6H_5CH_2N(CH_2)_3Cl$, supplied from Aldrich, was employed as supporting electrolyte for voltammetric and amperometric measurements in chloroform solutions.

Electrochemical measurements

All measurements were performed using a computer-assisted potentiostat (Autolab-PGSTAT-10, Eco Chemie, Utrecht, The Netherlands), connected to a conventional electrochemical cell equipped with three

electrodes. The bioelectrode was the working electrode. In both aqueous and non-aqueous experiments, a saturated calomel electrode (SCE) was used as reference electrode and a Pt-foil as counter electrode.

Steady state amperometric measurements were done as follows: the bioelectrode was immersed in 10 ml of testing solution (aqueous or non-aqueous) at room temperature, and poised at the desired value of the applied potential. When the recorded signal attained a stable value, a known volume of standard solution of substrate (phenol) was added under a vigorous stirring. Subsequently, the signal variation corresponding to the reduction of enzymatically produced o-quinone was recorded for 1-2 min. Thus, the calibration curve was constructed by means of successive additions of small volumes of standard aqueous solution of substrate. Before using the bioelectrode was kept at 5^{o} C in a humid atmosphere. The procedure presented above was repeated unchanged in all tests carried out using the amperometric bioelectrode in both aqueuos and chloroform solutions.

The bioelectrode preparation

Amphiphilic polypyrrole matrix

The technique of enzyme entrapment into polypyrrole matrix consisted in the electro-polymerization of the amphiphilic pyrrole monomer, after the adsorption on electrode surface of a mixture of enzyme and monomer [7, 8]. Thus, 2.5 mg of monomer were ultrasonically dispersed in 1 mL of distillated water and 3 mg of PPO was added per mL of dispersion. A volume of 10μL from the above-described mixture was deposited on the Pt disk electrode (3mm diameter) and the water was removed by keeping the coated electrode during 2h hours under reduced pressure. Finally, the monomer-enzyme film was electropolymerized in a 0.1M $LiClO_4$ aqueous solution, by controlled potential electrolysis. Figure 3 presents the current-time dependence observed during the amphiphilic pyrrole electropolymerization.

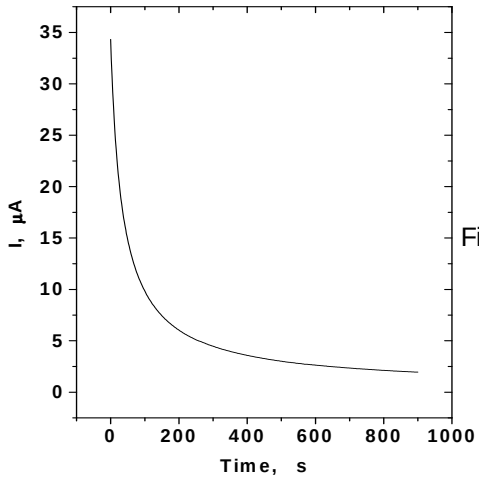

Figure 3. Current variation during potentiostatic electropolymerization of the amphiphilic pyrrole monomer. Experimental conditions: applied potential, 0.76 V *vs.* SCE; supporting electrolyte, 0.1M $LiClO_4$ aqueous solution.

Polyaniline matrix

3 mg of PPO was dispersed in 1 mL of fresh distilled aniline. The Pt disk electrode (φ = 3mm) was coated with 10 μL from the above-described mixture. Subsequently, the electrode was dried during 2h under reduced pressure and was covered with a polyethylene membrane. The aniline electropolymerization was performed at 0.45 V *vs.* SCE in a 0.1M $LiClO_4$ aqueous solution.

RESULTS AND DISCUSSION

The new strategy recently proposed to obtain reagentless phenol amperometric biosensors, based on PPO entrapment in a polypyrrole matrix obtained by "*in situ*" electropolymerization [7, 8], was first extended to polyaniline and finally used for phenol detection in a nonaqueous solvent ($CHCl_3$). Thus, two similar biolelectrodes using enzyme matrix based on polyaniline and a pyrrole derivative polymer were prepared and compared for phenol amperometric detection. Furthermore, the bioelectrode showing the best electroanalytic characteristics was checked for use in a nonaqueous solvent.

Comparison between polyaniline and amphiphilic polypyrrole matrix

Steady state amperometric measurements were performed with both investigated bioelectrodes at an applied potential of -180 mV *vs.* SCE. The corresponding calibration plots are shown in figure 4. The bioelectrode

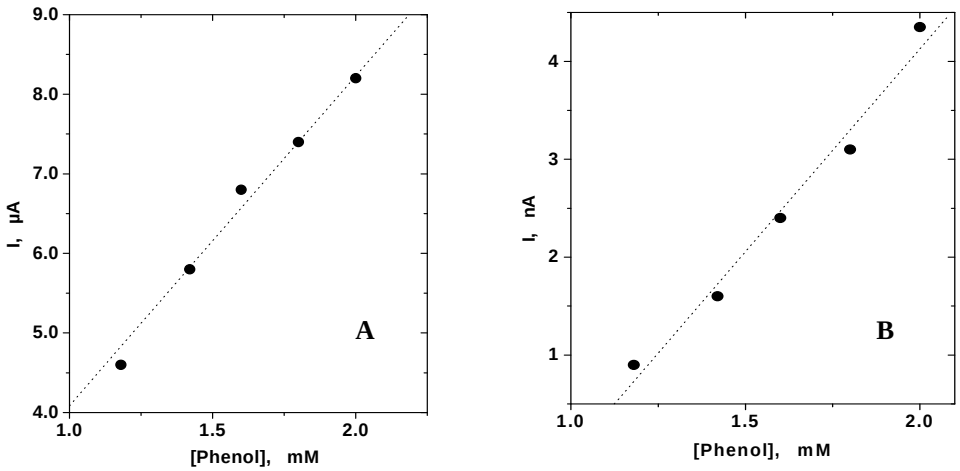

Figure 4. Amperometric response of the phenol biosensors: amphiphilic polypyrrole matrix ***(A)***; polyaniline matrix ***(B)***. Experimental conditions: working potential –180 mV *vs.* SCE; magnetically stirred buffer solutions (pH 7.0).

sensitivities, estimated as the slope of the linear range, were found to be strongly different: the bioelectrode based on polyaniline showed a sensitivity of (4,1 ± 0.3) μA M^{-1}, while that using amphiphilic polypyrrole had a higher sensitivity (4,4 ± 0.3) mA M^{-1}. The difference in the behavior of the two biosensors could be attributed to: (i) a higher efficiency for enzyme retention for the polypyrrole matrix; (ii) a high substrate permeability through the amphiphilic polypyrrole matrix; (iii) the matrix hydrophilicity, due to the amphiphilic structure of the pyrrole derivative [7, 8].

From figure 5 the response time for the bioelectrode using polypyrrole as polymer matrix for PPO entrapment can be estimated to be lower than 1 minute.

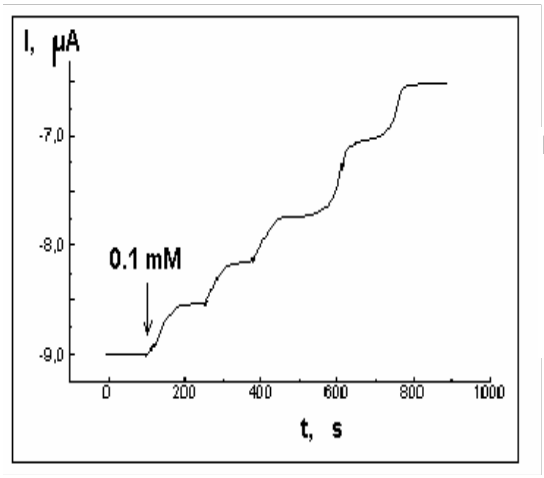

Figure 5. Amperometric response of the biosensor based on amphiphilic pyrrole matrix to successive additions of 0.1 mM phenol. Experimental conditions: see figure 4.

Summarizing, the bioelectrode using the polypyrrole matrix showed a high sensitivity, a low response time and a good operational stability. Thus, this variant was retained for all further investigations.

Phenol detection in chloroform

Cyclic voltammetry measurements performed in chloroform, in the absence and in the presence of phenol, proved that the bioelectrode based on polypyrrole matrix maintains its bioelectrocatalytic response for phenol (Figure 6). In the same time, it was noticed that even a lower applied potential than –180 mV *vs.* SCE can be used for amperometric measurements.

The chloroform being a hydrophilic compound it can remove water from the enzymatic environment [20, 21], and, consequently, only saturated with water the bioelectrode would keep its response due to the preservation of the hydration layer around the enzyme. In order to check the effect of

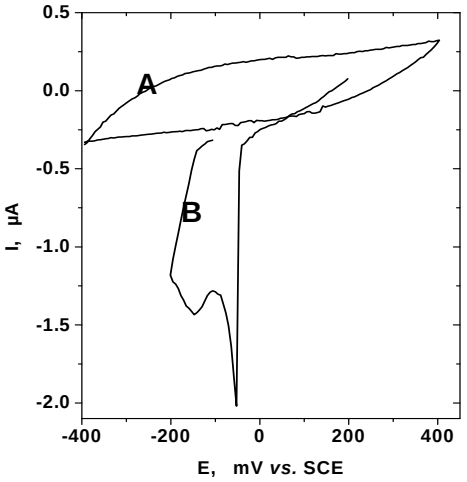

Figure 6. Cyclic voltammograms recorded in chloroform at tyrosinase based bioelectrode: in the absence of phenol ***(A)*** and in the presence of 0.1 mM phenol ***(B)***. Experimental conditions: working bioelectrode, tyrosinase entrapped in amphiphilic polypyrrole electropolymerized on Pt (3mm diameter); scan rate, 50 mV/s; starting potential, -400 mV ***(A)*** and +200 mV ***(B)***, *vs.* SCE.

chloroform on the operational stability of the polypyrrole based bioelectrode its amperometric response for 0.1 mM phenol was recorded after two hours of continuous immersion in chloroform. The remove of the enzyme hydration layer by chloroform was demonstrated by the absence of any response, if the experiment was done without any previous hydration. Contrarily, if the biosensor was kept one day in a humid atmosphere the signal to 0.1 mM phenol was recovered almost completly (~ 95%). The steady-state current was achieved typically after 5 min.

The calibration curve obtained by successive additions of standard phenol solution in chloroform (Figure 7) showed a linear response up to 2 mM with a lower sensitivity than that observed in water solutions (Table 1). The reason of the sensitivity decrease could be due to the gradual remove of the enzyme hydration layer and, as it was previously observed [22], to the difference between the solvent polarity, strongly influencing the reactivity of the enzyme active center.

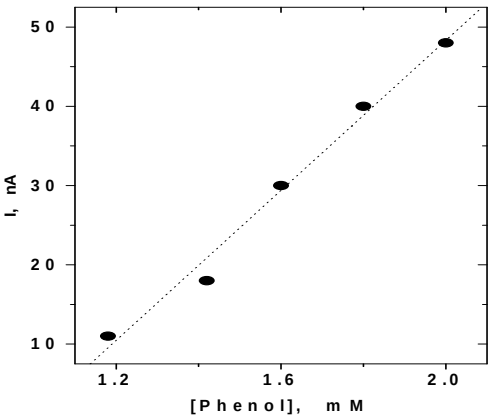

Figure 7. Calibration curve of the bioelectrode based on amphiphilic pyrrole matrix in chloroform containing 0.1M $C_6H_5CH_2N(CH_2)_3Cl$. Experimental conditions: applied potential, -50 mV *vs.* SCE; magnetically stirred solutions.

Table 1.

Sensitivity to phenol of the polypyrrole based biosensors recorded in two different media, at the same applied potential (-50 mV *vs.* SCE).

Solvent	**Sensitivity (nA/M)**	**Linear range (mM)**	**Regression coeff. / No. of exp. points**
H_2O	276	up to 2	0.9944 / 5
$CHCl_3$	47.3	up to 2	0.9934 / 5

CONCLUSIONS

This study demonstrates the advantages to use conducting polymers for bioelectrode construction, especially the amphiphilic polypyrrole, as polymer matrix for tyrosinase entrapment. It was observed a rapid stabilization of the background current, a high sensitivity to phenol and a good operational stability (higher than tree months) when tyrosinase was entrapped in amphiphilic polypirrole in order to construct amperometric biosensors.

On the other hand, a strong adherence of the enzyme matrix to the Pt electrode surface was observed in both water and chloroform solvent. Contrarily, the bioelectrode based on polyaniline matrix showed a low reproducibility and a poor operational stability.

Finally, this work demonstrated for the first time to our knowledge the suitability of organic phase tyrosinase bioelectrode using amphiphilic polypyrrole matrix for monitoring phenols in chloroform.

REFERENCES

1. I. Willner, E. Katz and B. Willner, Electroanalysis, 1997, **9**, 965.
2. B. Eggins, *Biosensors. An Introduction*, Wiley, New York, 1996, pp.1-201.
3. S. Cosnier and I. C. Popescu, Anal. Chim. Acta, 1996, **319,** 145
4. M.Trojanowicz and T. K. Krawczyk, Mikrochim. Acta*,* 1995, **121,** 167.
5. M. Sittig (ed.), *Priority Toxic Polluants. Healts Impacts and Allowable Limits*, Noyes Data Corporation, Park Ridge, New Jersey, U.S.A., 1980.
6. J. G. Schiller, A. K. Chen and C. C.Liu*,* Anal. Biochem., 1978, **85**, 25.
7. S. Cosnier and C. Innocent, J. Electroanal. Chem.,1992, **328**, 361.
8. S. Cosnier and C. Innocent, Bioelectrochem. Bioenerg, 1993, **31**, 147.
9. F. Ortega and E. Dominguez, J. Biotechnol.,1993, **31**, 289.
10. J. Wang and Y. Lin, Anal. Chim. Acta, 1993, **271**, 53.
11. .J. Wang, L. Fang and D. Lopez, Biosensors & Bioelectron.,1994, **9**, 9.
12. L. Campanella, T. Beone, M. P.Sammartino and M.Tomasseti, Talanta, 1994, **41**, 1397.

13. L. Campanella, T. Beone, M. P. Sammartino and M. Tomasseti, Talanta, 1994, **41**, 1015.
14. F. Liu, A. J. Reviejo, J. M. Pingarron and J.Wang, Talanta, 1994, **41**, 455.
15. H. Kotte, B. Grundig, K. D. Vorlop, B. Strehlitz and U. Stottmeister, Anal. Chem., 1995, **67**, 65.
16. K. M. Rogers, Biosensors Bioelectron., 1995,**10**, 533.
17. P. Onnerfjord, J. Emneus, G. Marko-Varga, L. Gorton, F. Ortega and E. Dominguez, Biosensors Bioelectron., 1995, **10**, 607.
18. S. Cosnier, Electroanalysis, 1997, **9**, 894.
19. H. Ju, D. Zhou, Y. Xiao and H. Chen, Electroanalysis, 1998, **10**, 541.
20. Q. Deng and S. Dong, Anal. Chem., 1995, **67**, 1357.
21. L. Campanella, T. Beone, M. P. Sammartino and M.Tomasseti, Analyst, 1993, **118**, 979.
22. I. C. Popescu, E. Csoregi and L. Gorton, Electroanalysis, 1996, **8**, 1014.

STUDIA UNIVERSITATIS BABEŞ-BOLYAI, CHEMIA, XLIV, 1-2, 1999

A NEW ORGANODITHIOPHOSPHORIC DERIVATIVE; SYNTHESIS AND STRUCTURAL CHARACTERISATION OF BIS(DIPHENYLBORANO)DITHIOPHOSPHORIC $[(C_6H_5)_2BO]_2P(S)SH$

CRETIU GABRIELA, TOROK REKA, BUGNARIU DELIA, JEMAN OXANA, IOAN SILAGHI-DUMITRESCU

Universitatea "Babeş-Bolyai", Facultatea de Chimie şi Inginerie Chimică, Cluj-Napoca, Ro-3400

ABSTRACT. A new organoderivative of dithiophosphoric acid $(RO)_2P(S)SH$ has been obtained by the reaction of phosphorus pentasulfide (P_4S_{10}) with diphenylborinic acid. IR, ^{1}H, ^{13}C, ^{11}B and ^{31}P NMR spectra of intermediates and the main product are discussed. Geometrical parameters (distances in Å, angles in degrees) for the minimum energy structure have been studied by ab initio RHF/3-21G* using Spartan version 5.0 installed on a SGI Octane.

INTRODUCTION

Diorganodithiophosphoric acids and their derivatives $(RO)_2P(S)SH$ ($R=(C_6H_5)_2B$) have a very reach chemistry which has been reviewed several times in the last years [1-3]. These acids are obtained by the reaction of phosphorus pentasulfide with alcohols (**1**).

$$P_4S_{10} + 8\ ROH \longrightarrow 4\ (RO_2)P(S)SH + 4\ H_2S \quad \textbf{(1)}$$

Boronic acids R_2BOH due to their polar OH group should react in a similar manner. In this paper, we investigate the reaction of diphenylborinic acid Ph_2BOH with phosphorus pentasulfide (***1***, $R=Ph_2B$-) which leads to bis(diphenylborano)ditiophosphoric acid. Such reactions afford an alternative route to new boron/phosphorus containing materials.

RESULTS AND DISCUSSION

Diphenylborinic acid has been synthesized following the general scheme ***(2)*** [4,5] with a few modifications (as described in the experimental part) which assure a better control of the product.

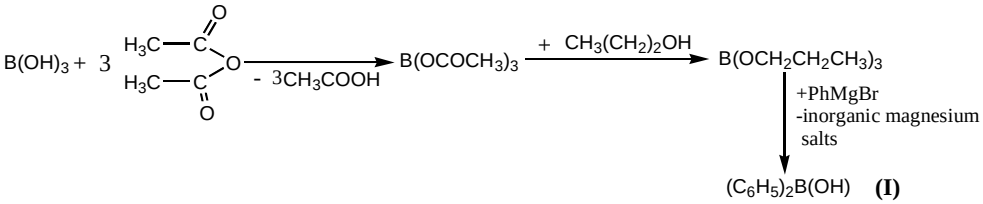

(**2**)

Reaction of diphenylborinic acid with phosphorus pentasulfide, P_4S_{10} (***1***, R=$(C_6H_5)_2B$), in 8:1 molar ration proceeds around at 36^0C in diethylether and the corresponding boron derivative of dithiophosphoric acid ***[(C$_6$H$_5$)$_2$BO]$_2$P(S)SH (II)*** results in a good yield.

Infrared spectral data for the new compound are collected in table 1. Table 2 contains NMR chemical shifts for ^{1}H, ^{11}B, ^{13}C and ^{31}P.

The IR spectra for bis(diphenylborano)ditiophosphoric acid show the bands due to BO, SiO, PO, and PS group vibrations in their characteristic regions [6,7]. The BO band in the IR spectra of diphenyl borinic acid is situated at 1371 cm^{-1}compared to 1350-1380 cm^{-1}, the range found for $B(OR)_3$ and $RB(OR)_2$ [6].

The stretching frequency of B-O bond in ***(II)*** (1346 cm^{-1})is slightly than in diphenylboronic acid ***(I)***, (1371 cm^{-1}). This shift is due to the presence of phosphorus atom that decreases the electron density on the bridging oxygen

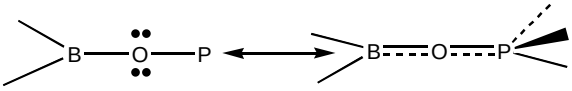

(**3**)

(I) **(II)**

The characteristic bands for the PO stretching group in compound ***(II)*** are situated in the range 980-1022 cm^{-1}, in agreement with the literature data [3]. The P-O bond stretching in ***(II)*** appears at high values than in classical dithiophosphates $R_2P(S)SH$.

The P-S bonds give the symmetric and antisymetric stretching at 450 cm^{-1} and 600 cm^{-1} respectively [3].

A possible explication of the B-O stretching frequencies might be described by the simple valence scheme ***(3)***. The electron pairs of oxygen are delocalised both to boron and phosphorus, which means that to B-O bond order in (II) can be lower than in $(C_6H_5)_2BOH$ ***(4)***.

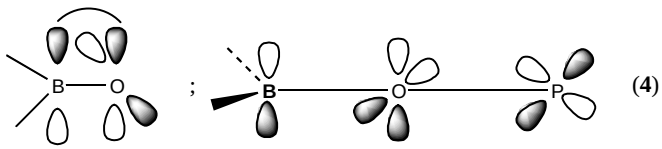

(**4**)

Table 1

Caracteristic vibration in infrared spectra of diphenylborinic, bis(diphenylborano)ditiophosphoric and bis(triphenylsilano)ditiophosphoric acids.

Compound	**ν(P-O) cm^{-1}**	**ν(B-O) cm^{-1}**	**ν(P-S) cm^{-1}**	**ν(S-H) cm^{-1}**
$[(C_6H_5)_2BOH$ (**I**)	-	1371	-	-
$[(C_6H_5)_2BO]_2P(S)SH$ (**II**)	1000-980	1346	600-555	2419

The ^{1}H, ^{13}C, ^{31}P, ^{11}B NMR studies has been effected. The results are shown in table 2.

Table 2

The chemical shifts (δ, ppm) in ^{1}H, ^{13}C, ^{31}P, ^{11}B NMR spectra, for diphenylborinic bis(diphenylborano)ditiophosphoric and bis(triphenylsilano)ditiophosphoric acids

COMPUS	**^{1}H aliphatic**	**^{1}H aromatic**	**^{13}C**	**^{31}P**	**^{11}B**
Ph_2BOH	2,2	7,37-7,39d (4) 7,44-7,49t (3,5) 7,61-7,63d (2,6)	138,2 (1) 128,2 (2,6) 136 (3,5) 129,4 (4)	-	29.45
$[Ph_2BO]_2P(=S)SH$	2,28	7,32-7,36m (4) 7,41-7,46m (3,5) 7,58-7,61dd (2,6)	141,65 (1) 127,65 (2,6) 129,2 (3,5) 127,75 (4)	130 s	29,80

See (**5**) for the atom numbering scheme.

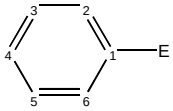

E=B, Si (**5**)

In the ^{1}H RMN spectra of $(C_6H_5)_2BOH$ the OH proton appears at δ(ppm) = 2.2(s), which reflects the greater acidity of this group than in alcohols (δ=3,15 ppm) [8] or in Me_2BOH (δ=6.65 ppm) [9].

In the ^{1}H NMR for bis(diphenylborano)ditiophosphoric acid appears one signal at 2,28 ppm for P(S)SH proton, comparable with the values in $(RO)_2P(S)SH$ [7], and the aromatic protons give a multiplet signal in the range 7.37-7.63 ppm (table 2).

The ^{13}C NMR spectra show four signals in normal range for phenyl group (table 2).

For the assignment of the protons attached to the phenyl groups we has used a 2D homocorrelation experiment COSY-45. This bidimensional experiment shows the coupling of the aromatic protons.

By ab initio RHF/3-21G* calculations using Spartan version 5.0 have been determined the geometrical parameters for the minimum energy structure of the bis(diphenylborano)ditiophosphoric acid. Some of the distances and angles for optimized geometry are comprised in table 3.

Table 3

Geometrical parameters (distances in Å, angles in degrees) for the minimum energy structure of bis(diphenylborano)ditiophosphoric acid

Distances (Å)		Angles and Torsiona Angles (degrees)	
B7-C11	1.546	P1-O5-B7	137.5
B7-C12	1.551	P1-O6-B8	136.98
B8-C9	1.547	C9-B8-C10	122.37
B8-C10	1.549	C11-B7-C12	121.97
B7-O5	1.361	O5-P1-S3	118.02
B8-O6	1.367	O5-P1-S2	106.71
P1-O5	1.585	O5-P1-O6	97.31
P1-O6	1.586	O6-P1-S3	120.94
P1-S2	2.106	O6-P1-S2	97.51
P1-S3	1.847	H-S2-P1	101.96
S2-H	1.336	B8-O6-P1-O5	72.98
		O6-P1-O5-B7	177.28

Since oxygen has lone pairs of electrons available for back donation into the formally empty p_z orbital of boron, the shortening of the bonds may be ascribed to partial double bond character, pπ-pπ interactions. The values (table 3) obtained are very similarly whit that described in literature [10].

The obtained molecular model with numbering of atoms is shown in fig.1.

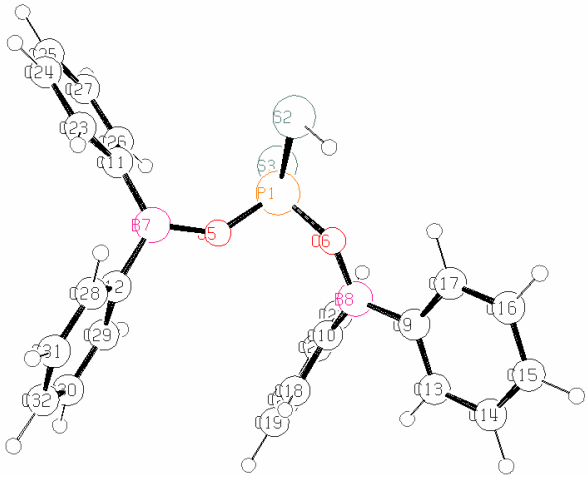

Fig. 1. Atomic numbering for the optimised structure of bis(diphenylborano)ditiophosphoric acid (depicted in ORTEP)

EXPERIMENTAL

Diphenylborinic acid has been synthesized [4] according to Scheme ***(2)***. All the reactions with the modification given in [11] have been carried out under inert atmosphere using anhydrous solvents. ^{1}H, ^{13}C, ^{31}P, ^{11}B NMR spectra were recorded on Varian Unity Plus instrument, 500 MHz. Melting points were measured on a Leitz microscope.

Ab initio RHF/3-21G* molecular orbital calculation have been carried out by using Spartan version 5.0 [12] installed on a SGI Octane

1. Diphenyl borinic acid $(C_6H_5)_2B(OH)$ (I)

To a 2.25 mol (255 g) of acetic anhydride is added to 0.75 mol (46,5 g) of boric acid. The mixture was warmed gradual on the water bath until the temperature arrived at 60-65^{0}C (the temperature of reaction mixture is 47^{0}C). At this point the boric acid passes in solution, the reaction starts and the temperature increases to 100-120^{0}C. Tri-acetyl borate precipitates on cooling as a white solid (m.p=120-124^{0}C, η=82%).

2.5 moli of n-propanol (220 ml) (50% excess) is added to 0,46 mol (97 g) $B(OAc)_3$. After two hour of stirring at reflux temperature the excess of alcohol is removed and than tri-n-propyl borate distils at 175-176^{0}C (18 ml, η=42%). Because of the sensitivity to water the product is used immediately.

Dropwise addition of the two equivalents tri(n-propilborate) in diethylether to one equivalent of Grignard reagent (4.6 g magnesium and 20 ml bromobenzenein diethylether) [13] leads to the diphenylborinic acid (scheme 2) which distils at 175-190^{0}C, and which turns on staying into a white solid (m.p.=52-54^{0}C, η=88%) IR: 3250 (νOH), 1385 (νBO), 1410 (νBPh), 1600, 1472, 700-730 (νPh).

2. Bis(diphenylborano)ditiophosphoric acid $[(C_6H_5)_2BO]_2P(S)SH$ (II)

To a diethylether solution of diphenyl borinic acid (0.08, 14.56 g moli in 20 ml diethyl ether) 0.01 moli (0.44 g) P_4S_{10} was added. After stirring at reflux temperature for 4 hours, the solvent was removed in vacuum resulting white solid. This precipitate is redissolved in the minimum pentane/ether mixture and after cooling at O^{0}C, $[(C_6H_5)_2BO]_2P(S)SH$ as a white solid (m.p.=46-48^{0}C, η=87%).

IR: 3029 (νPh), 1460 (B-Ph); 1366-1340 (B-O), 1000-980(P-O), 600 (P=S), 555(P-S), 1550(ν_{CC}Ph) 750-720 (Ph)

REFERENCES and NOTES

1. I. Haiduc, D.B.Sowerby, S.f. Lu, *Polyhedron*, 1995, **14**, 3389
2. I. Haiduc, D.B.Sowerby, *Polyhedron*, 1995,**15**, 2469
3. H.P.S. Chauhan, *Coord. Chem. Rev*., 1998, **173**, 1
4. H.C.Brown, A.C.Gupta, V.J.V.N.Pasad, M.Srebnik*, J.Org.Chem., 1988,* **53***,* 1391
5. C.Orvig, S.J.Rettig, J.Trotter*, Can.J.Chem.,* 1987*,***65**, 540
6. A. Smith *"Applied Infrared Spectroscopy",John Wiley and Sons, New York,*1982
7. G.M. Kosolapoff, L. Maier, "Organic Phosphorus Compound" vol. 6-7, Wiley Interscience, a Division of John Wiley & Sons, Inc, New-York, 1973
8. E.I. Negishi, *J.Organomet.Chem.,* 1976, **108**, 281
9. Gmelin Handbook of Inorganic and Organometallic Chemistry, B, Organoboron Compounds, Part 16, 1983
10. T. Fjeldberg, G.Gundersen, T. Jonvik, H. Martin Seip, S. Saebo, *Acta. Chim. Scandinavica,* 1980,**34A,** 547
11. To maintain a thorough control of the reaction the mixture should by gently heated up to 47^0C. Sometimes it happens that the reaction does not start even above this temperature. In such cases the mixture is cooled to the room temperature and than the heating restarted. However, we noticed that few drops of acetic acid added to the cold mixture initials the reaction without any warming.
12. Spartan version 5.0, Wavefunction, Inc, 18401, Von Karman Avenue, Suite 370, Irvine, CA 92612 USA
13. E. C. Ashby; John Oswald*, J.Org.Chem*., 1988, **53,** 6068.

STUDIA UNIVERSITATIS BABEŞ-BOLYAI, CHEMIA, XLIV, 1-2, 1999

FLAME ATOMIC EMISSION DETERMINATION OF CALCIUM IN NATURAL WATERS USING THE METHANE-AIR FLAME

LADISLAU KÉKEDY-NAGY and EMIL A. CORDOŞ

Universitatea "Babeş-Bolyai" Facultatea de Chimie şi Inginerie Chimică
3400 Cluj-Napoca, Arany J. 11, România

ABSTRACT. The calcium content of some natural waters (lake, river, well, mineral water) and drinking water (tap) has been determined by flame atomic emission spectroscopy using the methane-air flame. It was studied and optimized the flame and instrumental parameters (flame composition, the observation height in the flame) on the emission of calcium. The best results were obtained with the calcium line of 422.67 nm at the observation height of 7 mm, with the flame composition of 1.12 (relative stoichiometric units, (RSU)). The effect of pH, Na, K, Mg, Al, Sr, La, ClO_4^-, SO_4^{2-}, and PO_4^{3-} on the emission of calcium was studied too. The calibration curve was linear in the 0.1-10 mg/L range (long optical path in the flame) and 0.1–100 mg/L range (short optical path), respectively. The detection limit of 0.050 ± 0.022 mg/L was obtained at a significance level of 0.05 using the two-step Neyman-Pearson criterion. The calcium content of waters has been determined after suitable dilution of the sample, in the presence of 0.01 N $HClO_4$, using the calibration curve and the standard addition method. In the presence of interferences the best results were obtained with the standard addition method.

INTRODUCTION

Calcium is a common element of all natural waters. The industrial, household, biological etc. applicability of the water, among the other constituents, depends on the calcium content of the water. Flame atomic emission spectrometry (FAES) is a recommended method for the determination of calcium in waters. As excitation source usually C_2H_2-air, C_2H_2-O_2, C_2H_2-N_2O flames are used. The optimal flame conditions for the determination of calcium in these flames were established, the detection limits being of order of $1\text{-}10^{-3}$ μg/L [1-7]. The most sensitive is the atomic line of 422.67 nm. Calcium ionises partially in the acetylene flames, this phenomenon can be suppressed by adding K, Cs, Sr salts to the sample in excess [5-7]. Calcium forms the refractory CaO and CaOH in the flame, in the presence of

Al, Mg, Si, etc. the refractory mixed oxides (spinell-type), with well- defined composition [8-12]. Refractory compounds are formed with the SO_4^{2-} and PO_4^{3-} ions too [13-15]. The depletion of the calcium emission signal caused by these interferents can be avoided by using a hotter flame [16,17]; by adding an organic solvent [18-22], or La, Sr salt (releasing agent) [23-26]; EDTA, glycerol, or $HClO_4$ acid (matrix modifier) to the sample [27-29].

Propane-butane-air (PB-A) and the natural gas-air (NG-A) flames are used in low performance commercial flame-photometers, designated for routine analysis. The methane-air flame (M-A) has similar properties with the PB-A and NG-A flames, exhibiting lower temperature, burning velocity than the C_2H_2 ones. To our best knowledge the behaviour of calcium in the M-A flame was not reported. The aim of this work is to study the behaviour of calcium in the M-A flame, to optimize the flame and instrumental parameters and the determination of calcium in natural waters, respectively.

EXPERIMENTAL

Instrumentation

The measurements were carried out with a HEATH-701 (Heath Co., Benton Harbor, MI, USA) spectrophotometer using a HEATH EU-700 scanning monochromator, a HEATH EU-700-30 type photomultiplier module and a 1P28A (RCA, USA) photomultiplier (-700 V). The photomultiplier signal was recorded with a K-201 (Carl Zeiss Jena) strip chart recorder. The pneumatic nebulizer-spray chamber-burner system was used from an AAS -1 (Carl Zeiss Jena) atomic absorption spectrophotometer. The original 100 mm slot type burner head (for C_2H_2 - air flame) was replaced with a similar, Mecker type, developed by us, for the M-A flame [30,31]. In order to increase the nebulization efficiency the original 8 mm glass ball impactor was replaced with an 1 mm cylindrical one, placed at optimal distance of 5 mm from nebulizer head [32]. The air flow-rate was kept constant, 500 L/h, the flow rate of the methane being varied as a function of the gas mixture wanted. As CH_4 source the city gas of 99 % purity was used, from the pipe.

Reagents

Stock standard solutions (1000 mg/L) were prepared by dissolving the appropriate amounts of metals (La, Mg and Al (Specpure, Johson Matthey Chemicals Limited, England)) and compounds ($CaCO_3$, $SrCO_3$ (Specpure, Johnson Matthey Chemicals Limited, England) in corresponding acid. KCl, NaCl (analytical grade, Reactivul, Bucuresti, Romania), HCl, H_2SO_4, $HClO_4$ and H_3PO_4 (analytical grade, Merck, Darmstadt, Germany)) were dissolved and diluted in double distilled water, respectively. For further dilutions double distilled water was used in all cases.

Sampling and sample handling

The water samples were collected in the Cluj-Napoca city area: from the Someş river, from the central park lake and from some wells outside of the city. The waters were sampled and handled in accordance with the EPA-recommendations [4]. All determinations were carried out within 24 hours after sampling. The drinking water (tap water) from the laboratory was acidified and analysed just after sampling. The mineral waters (commercial available, "Anavie", "Izvorul Minunilor","Perla") were analysed after the sealed bottles were opened, acidified and degassed by shaking. The samples were diluted properly before measurements. The optimal pH of 1.5-2 of the solutions (in agreement with the literature data) was determined experimentally. The solutions were prepared just before the measurements.

Procedure

The behaviour of calcium in the M-A flame was studied up to h = 18 mm over the burner head (1mm steps), at three different flame compositions: 0.88; 1.00; 1.12 (expressed in relative stoichiometric units (RSU)). Four replicate measurements were made. The mean, the standard deviation, the S/N and the signal-to-background (S/B) ratio were calculated for each h and flame composition investigated. The homogeneity of the means was tested by the F test at a significance level of 0.05. The burner was held parallel to the optical axis of the spectrophotometer, unless stated otherwise. The slit width of the monochromator was of 0.1 mm, the sensitivity of the strip chart recorder was different in different spectral domains, in function of the intensity of the emission lines and the background observed. For a given set of determinations the sensitivity was kept constant.

RESULTS AND DISCUSSION

The emission spectrum of calcium, determination of the analytical emission line

The emission spectrum of calcium in the M-A flame was determined first (recording the spectrum of the flame alone, in the 200 - 800 nm spectral range, then that of the flame in the presence of calcium), by nebulizing of a calcium solution of 100 mg/L in the flame. Using spectral Tables [6] it was identified only the atomic line with wavelength of 422.67 nm and two molecular bands in the 420–650 nm spectral domain with the most intensive band heads with wavelength of 555 nm and 623 nm respectively, belonging to refractory CaO and $Ca(OH)_2$ formed in the flame [1-7].

Optimization of the flame and instrumental parameters

The aim is to obtain those values for the flame composition and observation height h for whose the S/N ratio is maximal. The composition of the flame was kept constant, at 1.12 RSU. The concentration of the calibration solution was of 10 mg/L. The analytical signal, intensity (I), was measured at 422.67 nm, 555 nm, and 623 nm and the background intensity (in the presence of calcium), at the base of the atomic emission line studied, at 423.2 nm. The variation of the line intensities versus observation height over the burner head is represented in Fig.1.

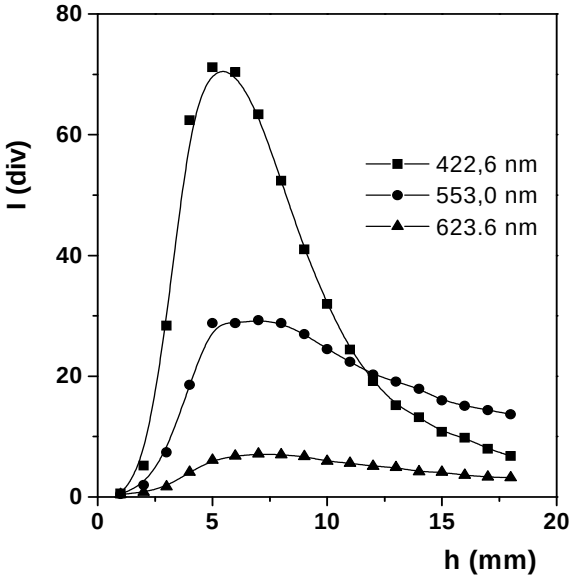

Figure 1**.** The intensity of different calcium lines versus observation height (h)

For the quantitative estimation of the results at different wavelengths only the maximal value of the analytical signal (I_{max}) for each line was selected. In order to get comparable data it was calculated the corrected intensity (I_{cor}) and the relative intensity (I_{rel}) for each line, considering the sensitivity of the chart recorder. The reference sensitivity of 1.10^{-9} A/div and the reference line was the weakest one. The S/B ratio was determined in the same way. The results are summarised in Table I.

Table I

The relative intensities of the emission lines of calcium in the M-A flame

Wavelength (nm)	h (mm)	I_{max}	$I_{Corr.}$	I_{rel}	S / B
422.67	7	35.6	71.2	10.20	1.41
555.00	7	29.3	29.3	4.12	7.32
623.00	7	7.1	7.1	1.00	4.73

The most intensive line is the atomic line of 422.67 nm, being excited in the interconal reaction zone of the flame, observed at 7 mm over the burner head. The S/B ratio is low, due to the high value of the background. The maximum of molecular emission appears at the same height, their emission are less influenced by excitation conditions in the flame. The influence of the flame composition and of observation height on the analytical signal for the most sensitive line was investigated using three flame compositions (0.88, 1.00, 1.12 RSU), at the concentration level of 10 mg/L. The data were processed by using the MicroCal Origin™ Software package, version 5.0 (MicroCal Software Inc., MA, USA) and plotted as 2D contour map (Fig.2).

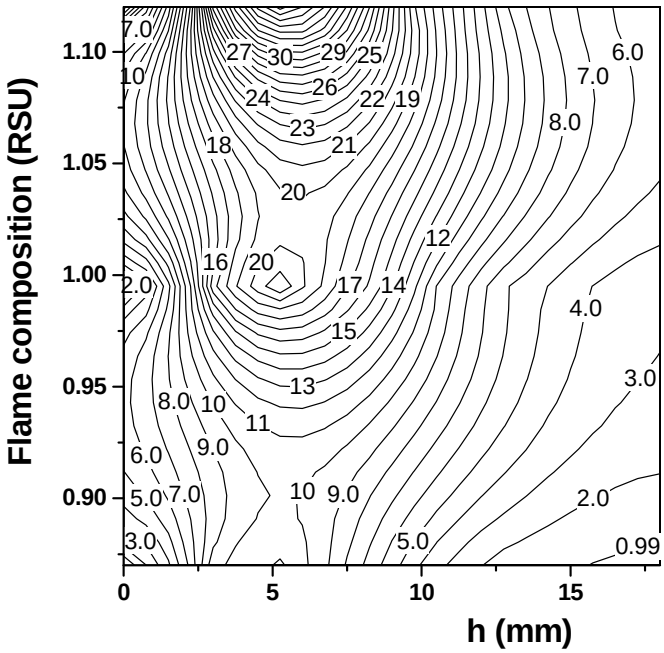

Figure 2. The 2D contour map of the emission of the 422.7 nm calcium-line vs. observation height and flame composition relation. The data labels on the plot indicate the grid matrix values

The results shows, that the analytical signal depends both of observation height and flame composition and increases with the increase of the methane content in the flame. The I-h curves are of Gaussian-shape, with the maximum between h = 5-7 mm. The analytical signal varies in the same manner as the concentration of the OH and CN radicals, fact which suggests that excitation of the calcium atoms take place *via* these radicals [33]. The

standard deviation of all means were homogeneous, the magnitude of the S/N ratio being decided by the magnitude of the mean. In conclusion, the optimal conditions for the quantitative determination of calcium in the M-A flame are λ = 422.67 nm, h = 7 mm, flame composition 1.12 RSU.

Interferences

The effect of Na, K, Mg, Al, SO_4^{2-} and PO_4^{3-} on the emission signal of calcium of 10 mg/L was investigated, as possible inorganic interferents, present in natural waters. The effect of Sr, La and $HClO_4$ were tested too, as releasing agents or as matrix modifier, respectively. The experimental conditions were the optimal ones, determined previously. In the case of Na, K and Sr the background signal was measured at 423,3 nm. The variation of the emission signal versus the concentration of the interferents are represented in Fig 3.

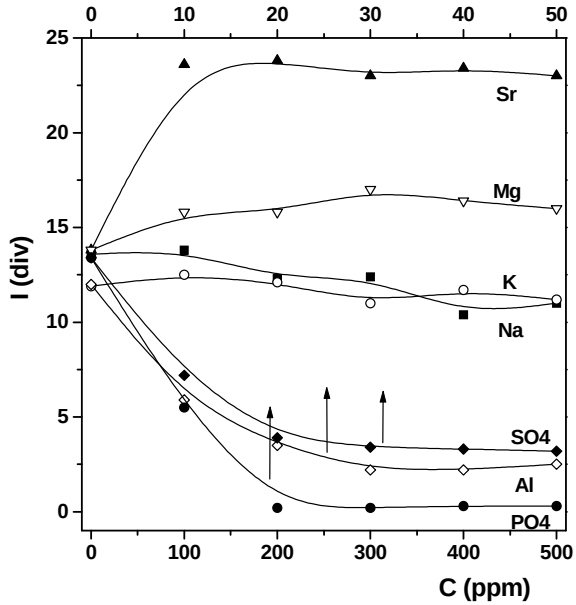

Figure 3. Influence of Na, K, Mg, Al, Sr, SO_4^{2-}, and PO_4^{3-} on the emission signal of calcium of 10 mg/L.

K acts as ionisation suppressor, enhancing simultaneously the calcium and the flame background signal. The influence of Na is lower, and is mainly due to the background enhancement. Surprisingly, Mg increases the calcium emission signal, acting as releasing agent. Al, SO_4^{2-} and PO_4^{3-} ions decrease drastically the calcium emission signal even at low concentrations. In contrast with the acetylene flames, La is not efficient. Sr enhances the flame background and exhibits a good releasing effect (as shown in figure 3), in

accordance with observed in the acetylene flames, acting as ionization suppressor too. It releases the analyte partially only (90% till 40-fold excess of Al, 79% till 10-fold excess of SO_4^{2-} and PO_4^{3-}). The low efficiency of these agents is the consequence of the low temperature of the M-A flame. $HClO_4$ as matrix modifier, enhances the calcium emission signal with 15.2 %, without enhancing the flame background.

Calibration, determination of the detection limit

For the determination of the detection limit the variation of the analytical signal versus concentration was studied. The calibration curves were plotted in the 0.1-100 mg/L calcium concentration range of. One curve covered only one order of magnitude of concentration. Each calibration curve was established by using six standard solutions. Six replicate measurements were made at each concentration level. The homogeneity of the means and the linearity of the calibration curve was tested, it was calculated the equation of the regression line, the confidence limits, the coefficient of correlation (r), with the least squares method. The detection limit was calculated using the two step Neyman-Pearson model [34,35], for the fixed values of $(P_{10})_0 = 0.025$ and $(P_{11})_d = 0.975$. In order to increase the sensitivity of the determinations, and lover the detection limit the calibrations were carried out in the presence of 100 ppm Sr and 1000 ppm $HClO_4$ too. The optimal concentrations of these agents were determined experimentally. The results are summarised in Table II.

Table II

The calibration data of calcium determination in the M-A flame

Nr.	Concentration range (mg/L)	Sensitivity (A/div)	Equation of the calibration curve	r
(1)	100 – 10	$10*10^{-9}$	$I = -0.022 + 0.788*C – 0.0027*C^2$	0.9988
(2)[@]	100 – 10	$2*10^{-9}$	I = 0.2 2 + 0.472*C	0.9999
(3)[@]	100 – 10	$10*10^{-9}$	$I = 1.46 + 0.504*C – 0.0014*C^2$	0.9972
(4)	10 – 1	$2*10^{-9}$	I = -0.193 + 4.892*C	0.9997
(5)[*]	10 – 1	$2*10^{-9}$	I = 1.27 + 7.525*C	0.9994
(6)[@]	10 – 1	$1*10^{-9}$	I = -0.78 + 2.695*C	0.9999
(7)[#]	10 – 1	$2*10^{-9}$	I = 0.31 + 7.505*C	0.9998
(8)	1 – 0.1	$1*10^{-9}$	I = -0.41 + 8.380*C	0.9922
(9)[*]	1 – 0.1	$2*10^{-9}$	I = 0.11 + 7.160*C	0.9977

[@] burner held perpendicular to the optical axis, optical path 8 mm through the flame
* 100 ppm of Sr added
[#] 1000 ppm of $HClO_4$ added

In the 10-100 mg/L domain the concentration-intensity relationship is linear only in the case of short optical path through the flame and in the absence of Sr (eq.(2)). Otherwise the relationship could be estimated best with a second order polynomial function. In the lower concentration ranges (eq.(4) - (9)) this phenomenon disappears even in long optical path. The linear correlation can be improved (eq.(6)) by keeping the burner perpendicular to the optical axis. The presence of Sr and $HClO_4$ enhances simultaneously the sensitivity and the linearity of the calibration curve (higher slope and r values). The detection limit was calculated only in the 0.1 - 1ppm concentration range, in the presence of Sr, being of 0.050 ± 0.022 mg/L.

Determination of calcium in water samples

The calcium content of the water samples was determined by the calibration and the standard addition method, the later being used as reference method due to the absence of certified reference material. The determinations were carried out keeping the burner parallel to the optical axes, the other parameters were the optimal ones. The measurements were carried out in the presence of Sr and $HClO_4$ too, regardless of method used. Four parallel measurements were made in each case. To minimise the effect of the interferences and to bring the final concentration of the sample within the linear range the samples were properly diluted before measurements. The measuring sample solutions were prepared in 25 mL volumetric flasks. In the case of standard addition method 100 µL of concentrated calcium standard was added to the 25 mL of diluted sample. Three additions of standard were made, in 1 ppm concentration steps. It was calculated the regression line, the calcium content was determined from the intercept with the abscissa of the line. Using the data set, first it was tested the reproducibility of the standard addition method. The recoveries were the closest, within 95-114 %, in the presence of Sr or $HClO_4$, depending on the salt content of the water. The recovery values are close to 100 %, with most samples within the error of determination, so the standard addition method could be used as reference method.

Comparing the calibration curves, the slope of calibration curves corresponding to the standard additions are significantly lover then of the calibration, fact, which suggests the existence of the chemical interference and the partial release of calcium from its compounds. By using Sr or $HClO_4$ in the sample, the slopes became higher and closer, they do not differ significantly. The best results were obtained in the presence of $HClO_4$. The results of the determination of calcium content of waters in the presence of 0.01 N $HClO_4$ are summarized in Table III.

The results of the two methods agree, they are within the errors of the determinations, for the low salt content waters (tap, lake, river and mineral water). The differences between the two methods are greater for the higher salt content waters. In these cases the standard addition method offers better results, closer to the real calcium content of waters. In conclusion calcium can

be determined precisely in natural waters in the presence of 0.01 N $HClO_4$ using the M-A flame. For the low salt content waters the calibration method gives acceptable results, for the higher salt content waters the standard addition method is recommended.

Table III

Results of analysis of water samples

Sample		Dilution	Concentration (ppm, calibration)	Concentration (ppm, standard addition)
Tap water		1:10	25.8 ± 1.3	27.5 ± 2.1
Lake water		1:25	16.2 ± 1.9	17.6 ± 2.1
River water		1:25	21.8 ± 1.8	23.9 ± 2.0
Mineral water	"Anavie"	1:50	72.4 ± 2.7	77.3 ± 3.0
	"Izvorul Minunilor"	1:10	34.6 ± 2.1	44.3 ± 2.7
	"Perla"	1:50	67.6 ± 4.8	68.0 ± 4.0
Well water	Nr. 1	1:50	108.4 ± 5.6	119.0 ± 6.2
	Nr. 2	1:50	171.5 ± 7.6	180.8 ± 8.1
	Nr. 3	1:50	151.7 ± 6.8	162.5 ± 7.1
	Nr. 4	1:50	122.4 ± 7.4	133.6 ± 7.8

CONCLUSIONS

In the M-A flame calcium exhibits atomic and molecular spectrum, the most intensive is the atomic line of 422.7 nm. The intensity of this line varies with the composition of the flame and observation height, the optimal observation height over the burner head is 7 mm, in fuel rich flame (RSU = 1.12). The presence of Mg, Al, SO_4^{2-}, and PO_4^{3-} decreases the emission of calcium. 100 ppm of Sr or 0.01 N $HClO_4$ exhibits the best releasing effect. This effect is partially, as consequence of the low temperature of the M-Aflame. The intensity-concentration relationship is linear in the 0.1-10 ppm range, the detection limit in the presence of 100 ppm Sr is of 0.050 ± 0.022 mg/L. This value is low and lies between the values obtained with cool and hot flames. The calcium content of natural waters can be determined precisely in the presence of $HClO_4$ using the calibration or the standard addition method. For the higher salt content waters the standard addition method is recommended. In conclusion, M-A flame is a suitable excitation source for precise determination of calcium in natural waters.

REFERENCES

[1] S.M.V. Fernandes, A.O.S.S. Rangel, J.L.F.C. LIMA, *J.Agric.Food.Chem.*, 1997, **45**, 1269.
[2] W. Frenzel, D. Schepers, G. Schulze, *Anal.Chim.Acta*, 1993, **277**, 103.
[3] G. Schwedt, *LaborPraxis*, 1990, **14**, 620.
[4] *Standard Methods for examination of water and wastewater*, 17th Edition, Edited by

L.S. Clesceri, A.E. Greenberg, R.R. Trussel, 1-30, 1989 APHA – AWWA – WPCF
[5] J.D. Winefordner, *Spectrochemical methods of analysis*, Wiley Interscience, New York, 1971.
[6] R. Mavrodineanu, H. Boiteux, *Flame spectroscopy*, Wiley Interscience, New York, 1965.
[7] E. Pungor, *Flame photometry*'', Akadémiai Kiadó, Budapest, 1967.
[8] J.H. Gibbson, W.E. Grossman, W.D. Cooke, *Anal.Chem.*, 1963, **35**, 266.
[9] M. Margoshes, B.L. Vallee, *Anal.Chem.*, 1956, **28**, 180.
[10] D.R. Demers, D.W. Ellis, *Anal.Chem.*, 1968, **40**, 860.
[11] W.W. Harrison, W.H. Wadlin, *Anal.Chem.*, 1969, **41,** 374.
[12] C.TH.J. Alkemade, *Anal.Chem.*, 1966, **38**, 1252.
[13] J.A. Dean, *Flame photometry*, Mc.Graw-Hill Book Company, Inc., New York, 1960.
[14] J.W. Hasking, N.B. Snell, B.T. Sturman, *J.Chem.Educ.*, 1977, **54**, 128.
[15] G.L. Long, C.B. Boss, *Anal.Chem.*, 1982, **54**, 2496.
[16] E.E. Pickett, S.R. Koirtyohann, *Anal.Chem.*, 1969, **41**, 28A.
[17] I. Rubeska, M. Miksovsky, *Chem.Listy.*, 1972, **66**, 1191.
[18]. J. Mohay, *Magy. Kém. Foly.*, 1973, **25**, 79.
[19]. J.D. Winefordner, C.T. Mansfield, T.J. Vickers, *Anal.Chem.*, 1963, **35**, 1607.
[20] J. Elhanan, W.D. Cooke, *Anal.Chem.*, 1966, **38**, 1062.
[21] A.J. Lemonds, B.E. Mc.Clellan, *Anal.Chem.*, 1973, **45**, 1455.
[22] B.W. Bailey, J.M. Ramkin, *Anal.Chem.*, 1971, **43**, 219.
[23] V.A. Fassel, D.A. Becker, *Anal.Chem.*, 1969, **41**, 1523.
[24] W.H. Foster, D.N. Hume, *Anal.Chem.*, 1959, **3**, 2033.
[25] W.A. Magill, G. Svehla, *Z.Analyt. Chem.*, 1974, **270**, 177.
[26] J.I. Dinnin, *Anal.Chem.*, 1960, **32**, 1475.
[27] A.C. West, W.D. Cooke, *Anal.Chem.*, 1960, **32**, 1471.
[28] A.C. West, *Anal.Chem.*, 1964, **36**, 310.
[29] L.A. Elfers, P.F. Hallbach, R.J. Velten, *Anal.Chem.*, 1964, **36**, 540.
[30] E. Cordoş, L.N. Kékedy, R. Hui, *Patent* RSR, nr. 67867 / 1977.
[31] E. Cordoş, L. Kékedy Nagy, *Studia*, 1992, **37**, 61.
[32] L. Kékedy-Nagy, *Talanta*, 1997, **44,** 1919.
[33] L. Kékedy Nagy, *Studia*, 1992, **37**, 109.
[34] C. Liteanu, I. Rîcã, *Statistical Theory and Methodology of Trace Analysis,* John Wiley, New York, 1980.
[35] D.L. Massart, B.G.M. Vandeginste, S.N. Deming, Y. Michotte, L. Kaufman, *Chemometrics: a textbook,* Elsevier, New York, 1988.

STUDIA UNIVERSITATIS BABEŞ-BOLYAI, CHEMIA, XLIV, 1-2, 1999

LEACHING OF CHALCOPYRITE CONCENTRATE WITH SULPHURIC ACID IN ABSENCE AND PRESENCE OF OXIDIZING AGENTS

CAMELIA LUMINITA VARGA[1], LIVIU ONICIU[2]

[1] *Department of Chemistry, North University of Baia Mare, 4800 Baia Mare, Romania*
[2] *Department of Physical Chemistry, University "Babeş-Bolyai", 3400 Cluj-Napoca, Romania*

ABSTRACT. The kinetic leaching characteristics of chalcopyrite concentrate were investigated in sulphate media. The experiments were carried out on chalcopyrite concentrate obtained by flotation of the ores from mines around Baia Mare. The concentrate has the following chemical composition: 30.38% Cu, 4.2% Zn, 1.93% Pb, 28.89% Fe and 34.49% S. Three stages of the leaching process were established. The apparent activation energy suggests a dependence on the period of leaching and on the presence of ferric ion and oxygen as oxidizing agents in the leaching solution. Also, an attempt was made to determine the rate controlling reaction step, according to both the activation energies, and the analytical expressions for each period. The parameters that were modified during experiments were: the leaching time, the leaching temperature and the quantity of ferric sulphate and of oxygen as oxidizing agents.

INTRODUCTION

Hydrometallurgical processes for chalcopyrite copper concentrates can be categorized according to the type of lixiviants used, the most common lixiviants being chloride, nitrate, ammine and sulphate. The sulphate-based processes have some potential advantages over the others in that the leaching chemistry is generally simpler and better understood, and copper recovery from sulphate media (by solvent extraction/electrowinning) is easy. Unfortunately, the sulphate processes have a critical disadvantage in that chalcopyrite leaches slower in sulphate media than in the other media. Initial reaction rates tend to decline rapidly with time, leading at the conclusion that a passivating layer forms on the mineral surface.

The study of the reaction rate between chalcopyrite and leaching agents is important because a prolongation of the leaching process considerably raises the operational costs, owing to the necessity of treating large volumes of dilute solutions.

The literature on chalcopyrite leaching concerning the theoretical and practical aspects, reveals that the dissolution of chalcopyrite is governed by a parabolic kinetic caused by the progressive formation of a compact layer of elemental sulphur or other products on the solid/liquid

interface. This layer may not be entirely impermeable and it can be abraded or peeled off by the pulp stirring.

A number of papers [1-11] have reported the leaching kinetic of pure or synthetic chalcopyrite having the ferric ion as oxidizing agent. In most of these papers [3-5, 7, 8], the ferric chloride was used because its availability and recoverability, but it is also much more aggressive than sulphate, due to the ability to accelerate dissolution of the mineral owing to the formation of complexes.

The apparent activation energy depends on the period of leaching, as well as on the presence of oxidizing agents Fe^{3+} or O_2 in the leaching solution. Some attempts were made to determine the rate controlling reaction steps for each period of leaching from the kinetics. The dissolution kinetics vary sensibly with the leaching temperature, and the quantity of ferric sulphate and/or of oxygen added as oxidizing agents.

The scattering values of apparent activation energy, presented in literature, can be mainly attributed to:

- the significant variation of the different chalcopyrite concentrates reactivity with the location of origin [3];
- the presence of flotation reagents which seemed to have minor effects on the leaching behavior;
- the major difference in the electroleaching rates caused mainly by electrical conductivity variations;
- the admixtures and impurities as well as the influence of real structure of the investigated material.

EXPERIMENTAL

The leach tests were carried out on chalcopyrite concentrate obtained by flotation of ores from mines around Baia Mare. The chemical and mineralogical composition of the investigated concentrate is shown in table 1 and table 2, respectively.

Table 1.

The chemical composition of concentrate.

Element	Cu	Zn	Pb	Fe	S
%	30.38	4.2	1.93	28.89	34.49

Table 2.

The mineralogical composition of concentrate.

Mineral	Chalcopyrite $CuFeS_2$	Pyrite FeS_2	Sphalerite ZnS	Galena PbS
%	85.5-86.5	5-6	6-7	2-3

The particle size of chalcopyrite concentrate ranged between 0.071-0.1 mm. As leaching medium, a solution of 8.0 N H_2SO_4 was used. Each leaching experiment was performed with 2 g chalcopyrite and 15 ml leaching solution therefore, a ratio solid/liquid of 1/7.5.

The chalcopyrite concentrate leaching experiments were carried out at the following temperatures: 20, 30, 40, 50 and 60°C. For each leaching temperature, the leaching time was: 5, 10, 15, 20, 30, 45, 60, 90, 120, 150, 180, 240, 360, 480, 600, 720 and 1440 minutes.

To increase the copper dissolution, the ferric sulphate as oxidizing agent was added to the leaching solution. The tested concentration of ferric sulphate in 8.0 N H_2SO_4 was 10, 20 and 30 g/l. Also, the leaching pulp was stirred by air bubbling at 200 l/hour in a volume of 210 ml leaching agent, at a same ratio solid/liquid. For leaching tests, in which the oxidizing agents (Fe^{3+} and/or O_2) were used, the leaching temperatures were 40 and 60°C.

After filtration, the copper concentration in solution was analyzed by spectrophotometric method.

RESULTS AND DISCUSSIONS

The leaching results of chalcopyrite concentrate, in the temperature region of 20-60°C, at atmospheric pressure, are represented in figure 1.

The shape of the leaching curves indicates three periods of leaching. The attempt to treat the first two periods as one resulted in a exponential dependence with an exponent less than one, it is not recommended, because from figure 1 it is obvious that the initial stage is characterized by linear kinetics.

The change of the leached copper percent in that first period could be described by the analytical expression:

$$c_1 = k_1 t \tag{1}$$

where c_1 is the leached copper percent in time t ($t \leq 0.3333$ h), and k_1 is a constant representing the slope of the respective plot (% of leached copper/h).

The second period could be described by a power function having the form:

$$c_2 = c - c_1 = k_2 (t - t_1)^a \tag{2}$$

where c is the total leached copper percent in time t (in this case $t \in$ [0.5-4 h), k_2 is a constant representing the intercept on the ordinate axis in the log-log plot, a is the coefficient related to the slope in the log-log plot, and c_1 is the maximum leached copper percent in first period at time t_1 (t_1 = 0.333 h).

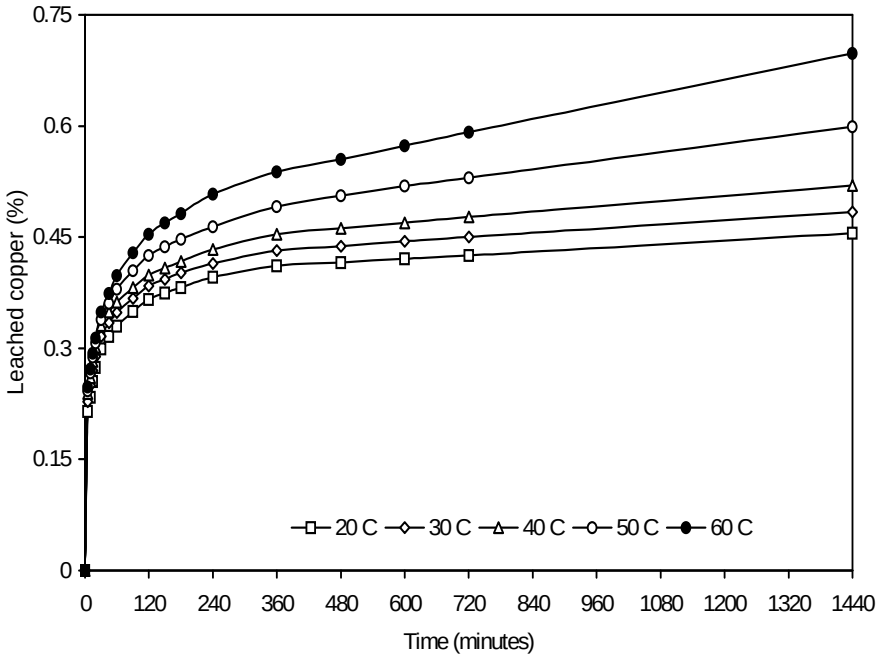

Figure. 1. The chalcopyrite concentrates leaching curves as a function of time at different temperatures.

The third period was characterized by linear kinetics, the corresponding analytical expression having the form:

$$c_3 = c - c_2 = k_3\left(t - t_2\right) \tag{3}$$

where c is the total leached copper percent in time t (in this case $t \geq 6$ h), k_3 is constant representing the slope of the respective plot (% of leached copper/h), and c_2 is the maximum leached copper in the second period at t_2 ($t_2 = 4$ h).

The experimental data for all the three periods of chalcopyrite concentrate leaching, with sulphuric acid at 20°C, are given in table 3. The bolded values of this table represent the values of c_1 and t_1 of equation (2), and c_2 and t_2 of equation (3), respectively.

The values of the rate constants k and exponents a, obtained as function of temperature, for chalcopyrite concentrate leaching curves are listed in table 4.

Table 3.

The experimental data of chalcopyrite concentrate leaching with sulphuric acid at 20°C.

First period			Second period						Third period				
c_1 (%)	t (h)	k_1 (%/h)	c (%)	t (h)	C_2 (%)	$t-t_1$ (h)	k_2 (%/h^a)	a	c (%)	t (h)	c_3 (%)	$t-t_2$ (h)	k_3 (%/h)
0.215	0.083	0.237	0.299	0.50	0.025	0.167	0.0668	0.521	0.411	6	0.015	2	0.00226
0.234	0.167		0.316	0.75	0.042	0.417			0.416	8	0.020	4	
0.255	0.250		0.330	1.00	0.056	0.667			0.421	10	0.025	6	
0.274	0.333		0.350	1.50	0.076	1.167			0.425	12	0.029	8	
			0.366	2.00	0.092	1.667			0.455	24	0.059	20	
			0.375	2.50	0.101	2.167							
			0.384	3.00	0.110	2.667							
			0.396	4.00	0.122	3.667							

Table 4.

The values of the constants *k* and exponents *a*.

Temperature (°C)	Period			
	I	II		III
	k_1 (%/h)	k_2 (%/h^a)	a	k_3 (%/h)
20	0.237	0.0668	0.521	0.00226
30	0.243	0.0698	0.504	0.00288
40	0.249	0.0733	0.484	0.00365
50	0.255	0.0860	0.522	0.00590
60	0.263	0.1000	0.561	0.00891

Accordingly, with the results represented in figure 1, the leaching of chalcopyrite in acidic media is characterized by an increase with temperature. The quantitative expression of the temperature influence can be obtained by the Arrhenius relation represented in figure 2.

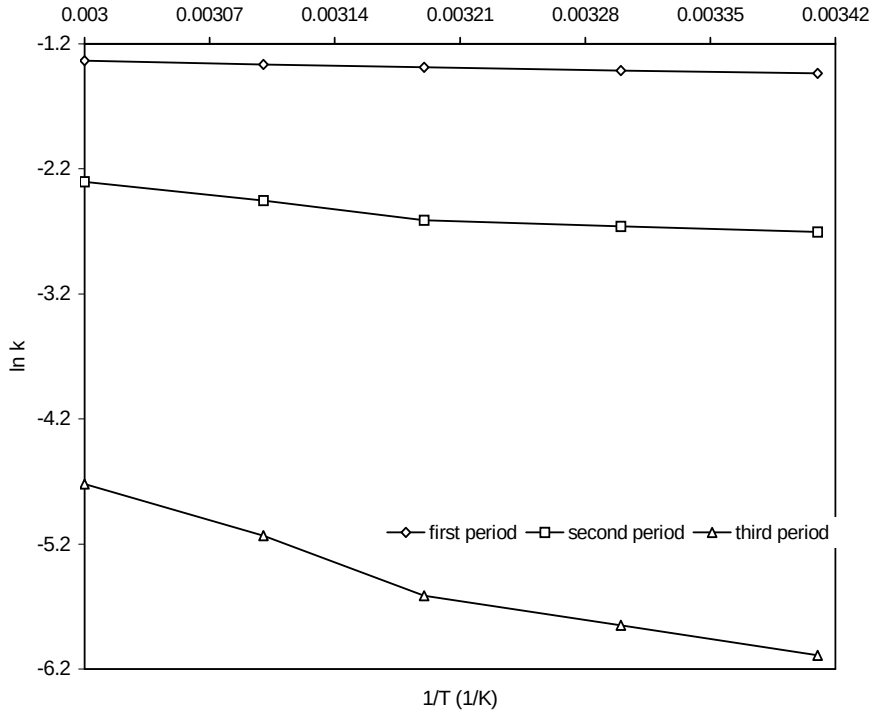

Figure. 2. The dependence of apparent activation energy on the period of leaching

The values of apparent activation energy, obtained from the Arrhenius plot showed in figure 2, are presented in table 5.

To increase the copper dissolution from chalcopyrite concentrate with sulphuric acid, oxidizing agents were added into leaching solution. Therefore, the influence of the ferric sulphate and/or oxygen addition, as oxidizing agent, on the rate of chalcopyrite concentrate was studied too.

Table 5.

The apparent activation energy.

Period of leaching	Temperature range (°C)	E_a (kJ/mol)
I	20-60	2.023
II	20-40	3.538
	40-60	13.446
III	20-40	18.267
	40-60	38.707

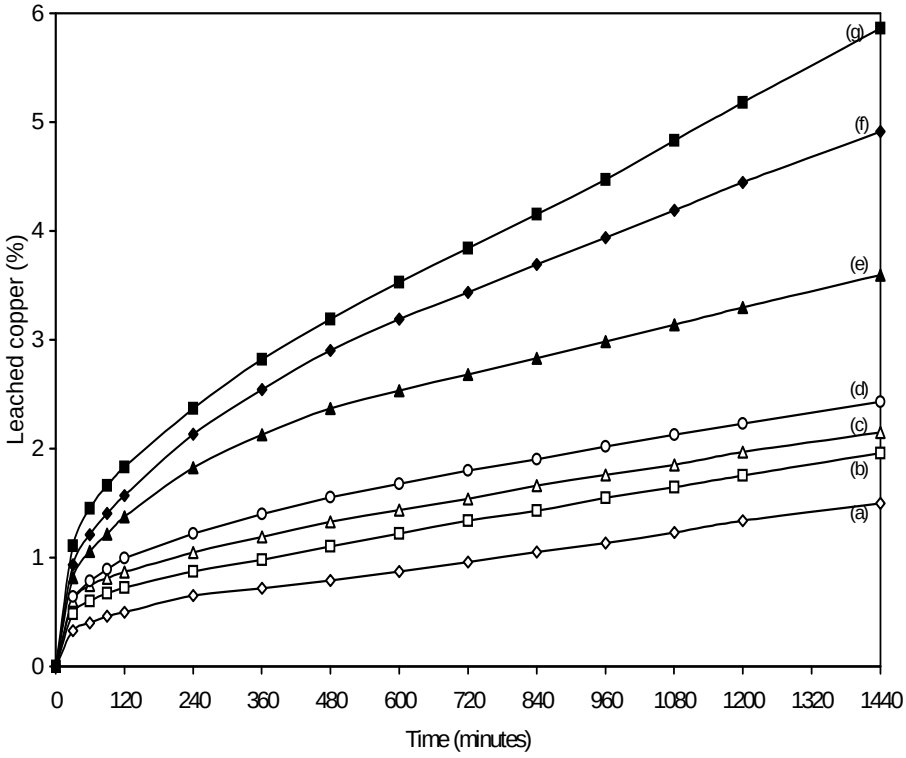

Figure. 3. The chalcopyrite concentrate leaching curves, using oxidizing agents, as function of time.

The shapes of the oxidative leaching curve points out an increase of the second period time until 480 minutes in (c)–(g) cases. The rate constants *k* and apparent activation energies, in the range of temperature 40-60°C, for third period of chalcopyrite concentrate leaching, with sulphate acid, in the presence of oxygen or oxygen and ferric sulphate (30 g/l), are presented in table 6.

Table 6.

The rate constants and apparent activation energies, for third period of chalcopyrite concentrate leaching.

Oxidizing used agents	Temperature (°C)	k_3 (%/h)	E_a (kJ/mol)
oxygen	40	0.0223	38.894
	60	0.0523	
Oxygen and ferric sulphate (30 g/l)	40	0.0547	52.675
	60	0.1763	

CONCLUSIONS

The obtained apparent activation energies are comparable with these found in literature: about 69 kJ/mol for ferric chloride chalcopyrite leaching, in the range 40-100°C [8]. Also, the small leached copper percent obtained for ferric sulphate chalcopyrite (about 6% in 24 hours) can be compared with the literature values, which are about 7% [8] for ferric chloride chalcopyrite leaching, in the similar conditions (the fraction of concentrate sample: 0.071-0.1 mm; the chemical composition of fraction: 32.3% Cu, 28.4% Fe, 31.9% S; the ratio solid/liquid: 1/25; the leaching agent concentration: 1.0 M $FeCl_3$ in 0.2 M HCl; the leaching time: 240 minutes; the temperature: 60°C; the stirring speed: 300 rpm).

The leached copper percent for ferric chloride chalcopyrite leaching, a little increased, can be explained by the fact that the ferric chloride is much more aggressive than sulphate, due to the ability to accelerate dissolution of the mineral, owing to the formation of complexes, as well as by the fact that a high stirring speed was applied to the pulp.

The examination of the rate constants, exponents and apparent activation energy values obtained leads to the following conclusions:

(a) according to the apparent activation energy (~2 kJ/mol) in the range 20-60°C, the rate controlling reaction step in the first period of leaching is diffusion of leaching agent from bulk solution to the grain surface (external diffusion);
(b) in the initial stage of dissolution, fast leaching rates have been observed due to dissolution of the fine portions of chalcopyrite, the high concentration gradients at the interface, as well as the fact that the start of the process is not retarded by layers of elemental sulphur, formed on the leached surface;
(c) the second period of leaching is much longer than the first, and the values of the apparent activation energy (~3.5 kJ/mol in the range 20-40°C, and ~13.5 kJ/mol in the range 40-60°C, respectively) indicates the diffusion of reactants and products over the passivating layer (internal diffusion), as the rate controlling reaction step;
(d) the analytical form of the expression describing the kinetics of leaching in the third period indicates linear kinetics, and the values of the apparent activation energy (~18 kJ/mol in the range 20-40°C, and ~39 kJ/mol in the range 40-60°C, respectively) indicates the same rate controlling reaction step, like in second period;
(e) the same behavior was observed when the oxidizing agents were used;
(f) the increase of the apparent activation energy for the third period, when the oxidizing agents were used, can be ascribed to the change of chemical reaction mechanism.

REFERENCES

1. D u t r i z a c, J. E., *Met. Trans. B*, **1978**, 9B, 431;
2. D u t r i z a c, J. E., *Met. Trans. B*, **1981**, 12B, 371;
3. D u t r i z a c, J. E., *Met. Trans. B*, **1982**, 13B, 303;
4. H a v e r, F. P., W o n g, M. M., *J. Met*., **1971**, February, 25;
5. H i r a t o, T., K i n o s h i t a, M., A w a k u r a, Y., *Met. Trans. B*, **1986**, 17B, 19;
6. M a j i m a, H., A w a k u r a, Y., H i r a t o, T., T a n a k a, T., *Can. Metallurg. Q.*, **1985**, 24(4), 283;
7. O 'M a l l e y, M. L., L i d e l l, K. K., D u t r i z a c, J. E., *Met. Trans. B*, **1987**, 18B, 505;
8. H a v l i k , T., K a m m e l, R., *Minerals Engineering*, 1995, **8**(10), 1125;
9. A k r e t c h e, D. E., S l i m a n e, S. K., K e r d j o u d i, H., *Hydrometallurgy*, **1995**, 38, 189;
10. H a c k l, R. P., D r e i s i n g e r, D. B., P e t e r s, E., K i n g, J. A., *Hydrometallurgy*, **1995**, 39, 25;
11. H a v l i k, T., S k r o b i a n, M., B a l a z, P., K a m m e l, R., *Int. J. Miner. Process*, **1991**, 43, 61.

STUDIA UNIVERSITATIS BABEŞ-BOLYAI, CHEMIA, XLIV, 1-2, 1999

SPECTROSCOPIC CHARACTERIZATION OF SOME CHROMIUM O-ALKYLDITHIOCARBONATES

RADU FLORIN SEMENIUC[a], RODICA MICU SEMENIUC[a], IONEL HAIDUC[a] AND ONUC COZAR[b]

a) "Babes-Bolyai" University, Department of Chemistry, 3400 Cluj-Napoca, Romania.
b) "Babes-Bolyai" University, Department of Physics, 3400 Cluj-Napoca, Romania.

ABSTRACT. Four chromium O-alkylditiocarbonates, with the general formula $Cr(S_2COR)_3$, where R = methyl, ethyl, i-propyl and metoxiethyl, were prepared and characterized by elemental analysis, IR and UV-VIS spectra. All the compounds show a reduced thermal stability and decomposition was observed on heating. The CrS_6 cromophores exhibit a distorted octahedral geometries. The transition $^4T_{1g}(P)<---^4A_{2g}(F)$ was not solved, the calculated value lies in the range 33.600 - 33.930 cm^{-1}. The nephelauxetic parameter, with values from 0.428 to 0.445 suggests, as expected, a high degree of covalency. The same conclusion results from EPR spectra. The IR spectra showed strong absorption bands at 1260-1230 cm^{-1} (νOC), which certified an important contribution of resonance form $^{-2}S_2CO^{+}$-R to the resonance hybrid. On the basis of these values a high degree of covalency was estimated (0,74 - 0,86), also.

INTRODUCTION

O-alkyldithiocarbonates of transition metals and main group elements was studied in detail and revised [1,2]. The overall structure of these compounds is a resonance hybrid of canonical forms presented in figure 1.

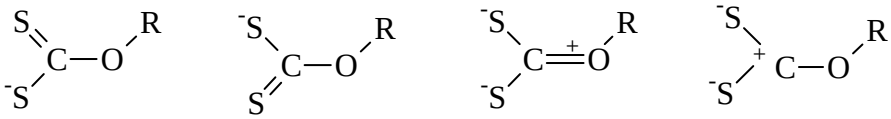

I II III IV

Figure 1. Canonical forms of xanthate moiety.

Chromium O-alkyldithiocarbonates were the subject of synthesis studies [3,4] and they were studied by electronic [5,6] and infrared spectra [7,8]. A number of X-ray structure analyses have become available [9,10]. In an

attempt to find more information about chromium xanthates, we prepared four compounds with the general formula $Cr(S_2COR)_3$, where R = $-CH_3$, $-C_2H_5$, $-{}^iC_3H_7$ and $-CH_2CH_2-OCH_3$ and we investigated them by electronic, infrared and EPR spectra.

RESULTS AND DISCUSSION

The compounds were prepared by mixing the aqueous solutions of $Cr(NO_3)_3 \cdot 9H_2O$ and the corresponding potassium xanthates. The yield was rather low, because during the precipitation of the compounds, a partial decomposition of the xanthate ligand occurred. The complexes were studied by elemental analysis, electronic, IR and EPR spectra. The yields, melting points and elemental analysis data are listed in Table 1.

The yields of chromium(III) xanthates were lower than in the other cases, the presence of chromium(III) nitrate leading to the decomposition of the desired compounds. During the study of the thermal behavior of chromium(III) xanthates, decomposition was observed on heating. This is suggested by color change of the compounds and by release of gas bubbles. As can be seen in table 1, the melting points decrease with the increase of the number of carbon atoms in the organic radical. On the other hand, the decomposition of chromium complexes is quite different: $Cr(S_2COCH_3)_3$ decompose to the melting point, but the decomposition points of $Cr(S_2COCH_2CH_3)_3$, $Cr(S_2COCH(CH_3)_2)_3$ and $Cr(S_2COCH_2CH_2OCH_3)_3$ are by 10, 40 and 50 degrees higher than the melting point.

ELECTRONIC SPECTRA

The electronic spectra were recorded in aqueous solution for potassium xanthates and in acetone solution for chromium(III) xanthates. The results of electronic spectra are listed in Table 2. An increase of 10Dq parameter, which fits with the first transition, is observed, along with the increase of the chain of alkyl groups.

The two bands in the visible region were used in the calculation of the nephelauxetic parameter (β). The small value of this parameter covers a small range (0.425 -0.445) like in the other cases for CrS_6 cromophores [11-13]. This value certifies a high degree of covalency of the metal-sulfur bonds. On the basis of literature data [14], we have also approximated the position of the $\nu 3$ band corresponding to the $^4T_{1g}(P) \leftarrow\!- {}^4A_{2g}(F)$ transition (table 2) with values situated between 33660 and 33930 cm^{-1}. A rigorous assignment is not possible, because of the presence in the near environment of a strong band due to π-π^* transition, characteristic of the xanthate moiety. On the other hand, the shoulder at 28700 -29400 cm^{-1} region can be associated with $\nu 3$ band. The high value of the molar extinction coefficient, ε, is explained by the intensity transfer from the nearby π-π^*.

Table 1.

Elemental Analysis and Some Properties of Compounds (*)

Compound	η (%)	Color	% Cr		% S		Thermal behavior (°C)
			calc.	found	calc.	found	
KMexn (147)	85	bright yellow	-	-	43.53	41.75	205-210 melting with gas release 225-brown-redish;
$Cr(Mexn)_3$ (373)	36.1	indigo	13.94	14.15	51.47	50.25	147-150 melting with gas release;
KEtxn (161)	82	white	-	-	39.75	38.12	209 melting with gas release; 250-oil;
$Cr(Etxn)_3$ (415)	21.68	dark blue	12.53	12.05	46.26	45.02	130-132 melt, the color becomes green; 145 gas release;
K^{i}Prxn (175)	70.5	white yellowish	-	-	36.57	35.50	219 beige; 260 brown oil;
$Cr(^{i}Prxn)_3$ (457)	23.75	blue-indigo	11.37	11.82	42.01	40.85	121-122 melt, the color becomes green; 165 gas release;
KMeOEtxn (191)	68.48	white yellowish	-	-	33.50	32.35	200-202 orange; 260 waxy oil;
$Cr(MeOEtxn)_3$ (505)	19.8	blue	10.29	9.85	38.01	36.85	68-69 melt; 129-130 gas release;

*)Mexn = O-methyldithiocarbonate; Etxn = O-ethyldithiocarbonate; ^{i}Prxn = O-izo-propyldithiocarbonate; MeOEtxn = O-methoxyethyldithiocarbonate

We can also see (table 2) that the positions of π-π* and n-σ* bands decrease by coordination with values from 550 to 700 cm^{-1} and from 7400 to 8540 cm^{-1} respectively, printing out the electronic structure modifications in the ligand along with the formation of complex combinations as can be seen in table 3.

The distorted Oh geometry of the CrS_6 chromophore is suggested by the large ν1 and ν2 bands in the visible region. The values of the bands half widths are quite large (table 3). However, the bands are not split, so we can assume that the distortion is not so pronounced.

Table 2.

Electronic spectra of Cr(III) O-alkyldithiocarbonates *

Compound	$^4T_{2g}(F) \leftarrow {}^4A_{2g}(F)$ ν_1 (ε)	$^4T_{1g}(F) \leftarrow {}^4A_{2g}(F)$ ν_2 (ε)	$^4T_{1g}(P) \leftarrow {}^4A_{2g}(F)$ ν_3(calc)	B (cm^{-1}) (β)	π→π* (ε)	n→σ* (ε)
$Cr(Mexn)_3$	15974 ($1.77 \cdot 10^2$)	20449 ($1.82 \cdot 10^2$)	33661	410 (0.445)	29428 u ($3.6 \cdot 10^3$) 32573 ($1.57 \cdot 10^3$)	35842 ($1.138 \cdot 10^4$)
$Cr(Etxn)_3$	16025 ($1.76 \cdot 10^2$)	20325 ($1.8 \cdot 10^2$)	33660	391 (0.425)	28818 u ($3.6 \cdot 10^3$) 32258 ($1.56 \cdot 10^4$)	35460 ($1.136 \cdot 10^4$)
$Cr(^iPrxn)_3$	16080 ($1.75 \cdot 10^2$)	20480 ($1.78 \cdot 10^2$)	38825	402 (0.437)	32240 ($1.50 \cdot 10^4$)	35652 ($1.31 \cdot 10^4$)
$Cr(MeOEtxn)_3$	16160 ($1.71 \cdot 10^2$)	20480 ($1.77 \cdot 10^2$)	33932	394 (0.428)	28735 u ($3.8 \cdot 10^3$) 32258 ($0.919 \cdot 10^4$)	35974 ($1.30 \cdot 10^4$)

*) transitions (cm^{-1}) and ε ($l \cdot mol^{-1} \cdot cm^{-1}$)

Table 3.

Some characteristic features of the bands from the electronic spectra

R	π-π* (cm^{-1})		Δ	n-σ*		Δ	Δ ν1/2	
	xanthate ion	complex		xanthate ion	complex		ν1	ν2
$-CH_3$	33200	32573	627	44320	35842	8478	5140	3575
$-C_2H_5$	32800	32528	542	44000	35400	8600	4576	3000
$-{}^iC_3H_7$	33040	32240	800	43400	34900	8500	4720	3200
$-C_2H_4OCH_3$	32960	32258	702	44240	35971	8269	4862	2860

INFRARED SPECTRA

IR spectra were recorded for both chromium(III) xanthates and the corresponding potassium xanthates. For KS_2COCH_3, $KS_2COCH_2CH_3$, $Cr(S_2COCH_3)_3$ and $Cr(S_2COCH_2CH_3)_3$ our IR spectra are similar to the literature spectra [7,8,15,16]. For the other compounds $KS_2CH(CH_3)_2$, $KS_2COCH_2CH_2OCH_3$, $Cr(S_2CH(CH_3)_3)_3$ and $Cr(S_2COCH_2CH_2OCH_3)_3$ there are no detailed studies of their IR spectra.

The IR spectra were interpreted by comparison with the results obtained by normal coordinate analysis on free and coordinated ion $S_2COCH_3^-$ [16,17]. The vibrational assignments for the absorption bands (cm^{-1}) of the infrared spectra are listed in table 4.

For KS_2COCH_3 and $Pt(S_2COCH_3)_2$ the potential energy distribution of the vibrational states is listed, considering only the components with a contribution higher than 10 %. It was found that almost all vibration are strongly coupled, so an interpretation of the IR spectra is very difficult to make.

When the IR spectra of chromium(III) xanthates are compared with those of potassium xanthates we can see a major change in the 1300 - 1200 cm^{-1} region, where the νOC stretching is located (νOC is the stretching vibration of carbon-oxygen bond in the O-CS_2 group and νCO is the stretching vibration of carbon-oxygen bond in the R-O group).

Table 4.

Vibration frequencies of $Cr(S_2COR)_3$ (cm^{-1})

Assignments	(1)	(2)	(3)	(4)	(5)	(6)
ν_aCH_3	2995	3020	3025	2995 (2953)	2979	2987
ν_sCH_3	2937	2980	2939	2928	2930	2931
δ_aCH_3	1447	1455	1453 u	1455	1459	1467
δ_sCH_3	1429	1442	1438	1446 1434	-	1440
$\rho CH_3+\nu_aCS_2$	1189	1183 ρCH_3(61) +δCOC (17)	1171	1143	1183	1187
$\rho CH_3+\nu_a CS_2$	1114	-	1123	1119	-	1115
νCO(78)+ νOC(25)+ ν_sCS_2(15)	1055	1024 νCO(36)+ν_aCS_2(30) 949 νCO(71)+ν_aCS_2(24)	1037 942	1029	1034 934	1053 987 973
νOC(80)+ νCO(25)+ ν_sCS_2(15)	945	1290 νOC(89)+ν_sCS_2(17)	1243	1274 1246	1268 1242	1247 1220
ν_sCS_2(41)+ δCOC(26)	664 618	610 ν_sCS_2(45)+ν_aCS_2(15)	-	650	654	513
γCS_2	580	455 δCOC(30)+ ν_aCS_2(25)+ν_sCS_2(22)	458	441	463	
δCOC(28)+ ν_sCS_2(28)+ ν_aCS_2(12)	472	364 ν_aPtS_2(89)	376	397 359	391	
δCS_2(87)	333	332 δCS_2(97)+ν_sPtS_2(45) 291 ν_sPtS_2(77)	324 -	321 -	321 -	

1= $S_2COCH_3^-$; 2= $Pt(CH_3OCS_2)_2$; 3= $Cr(S_2COCH_3)_3$; 4= $Cr(S_2COC_2H_5)_3$; 5= $Cr(S_2CO^iC_3H_7)_3$; 6= $Cr(S_2COEtOCH_3)_3$

In the 1300-1200 cm^{-1} region there are no bands for KS_2COCH_3 and $KS_2CH(CH_3)_2$ while for $KS_2COCH_2CH_3$ and $KS_2COCH_2CH_2OCH_3$ there are

one and two bands respectively of low intensity. For the corresponding chromium(III) complexes this region is dominated by large and strong bands. The presence of these bands is correlated with the increase of double character of the O-C bond. This fact is confirmed by X-ray diffraction studies, which reveal in most of the cases of metallic xanthates, smaller values for O-C bonds length as compared to the length of C-O bonds. For $KS_2COCH_2CH_3$ the length of O-C and C-O bonds are 1.35 Å and 1.48 Å respectively and for $Cr(S_2COCH_2CH_3)_3$ the corresponding values are 1.297 Å and 1.471 Å respectively [9]. The increase of the O-C bond length as compared to the C-O bond length is correlated with a greater participation of the canonical form III (fig.1) to the overall structure. For $Cr(S_2COCH_2CH_3)_3$ the contribution of canonical form III was calculated to be 36 % [9]. The smaller the length of this band, the greater the participation of the limit structure III.

The positions of bands in the 1300-1200 cm^{-1} region for chromium(III) complexes, as compared to the corresponding positions for potassium xanthates are the following:

R	**$-CH_3$**	**$-CH_3CH_2$**	**$-CH(CH_3)_2$**	**$-CH_2CH_2OCH_3$**
K^+	945w	1008w	-	1270w
		1286vw	-	1230w
Cr(III)	1243vw	1274vs	1268vs	1277vs
		1246vs	1242vs	1230vs

where vw = very weak, w = weak, vs = very strong.

Assuming the idea that the greater covalent bond character appears in $Pt(S_2COCH_3)_2$ for the series of transition metals due to the great affinity of platinum ion for sulfur, on the basis of a simple formula we can approximate the covalency degree:

$$\gamma = \frac{\nu OC[\,complex\,] - \nu OC[\,free\ anion\,]}{\nu OC[\,Pt(S_2COCH_3)_2 - \nu OC[\,free\ anion\,]} = \frac{\Delta\nu'}{\Delta\nu''}$$

The results are listed in table 5.

The values of gamma parameter, from 0.74 to 0.95 indicates a high covalecy degree in chromium(III) xanthates.

Table 5.

Empirical evaluation of covalency coefficients of xanthate compounds

Compound	νOC	νOC free anion	Δν'	γ
$Cr(S_2COCH_3)_3$	1243	945	298	0.86
$Cr(S_2COC_2H_5)_3$	1260	1008	257	0.73
$Cr(S_2CO^iC_3H_7)_3$	1265	927	328	0.95
$Cr(S_2COC_2H_5OCH_3)_3$	1233	975	258	0.74

The calculations carried out so far [16,17] have shown that the frequencies of carbon-sulfur vibrations are distributed in several domains of the IR spectrum, both for the free anion and for the coordinated one (table 4). With a certain prudence concerning the assignments made in table 4, we can admit that the νCS_2 frequencies decrease from the free anion to complexes, or new bands appear as related to non-coordinated anions. Frequencies of the νNiS vibrations, located between 376 and 397 cm^{-1}, could also be identified in the IR spectra of the complexes.

EPR SPECTRA

The shapes of the EPR spectra (Fig. 2 a-c) depends on length of the alkyl radicals and are typical for the isolated Cr^{3+} ions in a pseudo-octahedral geometry (mononuclear species) [18]. At g_{eff} 2, a broad band characteristic for strongly exchange coupled Cr(III) ions prevails (dimeric or polynuclear species) [19,20]. The number of clustered ions decreases with the dimension of alkyl radicals. The shape of the spectra is also dependent by the radical nature, the spectra being simple for methyl and ^{i}propyl, but more complex for ethyl.

EPR spectra were interpreted in term of the following spin Hamiltonian [21]:

$$H = g\,\mu_B\, B\cdot S + D\left[S_z^2 - \frac{1}{3}S(S+1)\right] + E\left(S_x^2 - S_y^2\right)$$

where μ_B is the Bohr magneton, S_x, S_y and S_z are the components of the electron spin S, D and E are the axial and rhombic zero field splitting parameters, respectively.

The perturbation theory in the second-order approximation leaded to the following three resonance fields [22]:

$$B_1 = B_0 - D(3\cos^2\theta - 1)$$

$$B_2 = B_0 + \frac{3\sin^2\theta}{B_0} D \cdot E, \quad with\ B_0 = \frac{h\nu}{g\mu_B}$$

$$B_3 = B_0 + D(3\cos^2\theta - 1)$$

For the complex $Cr(S_2COC_2H_5)_3$ (Fig. 2.a) the zero field splitting parameters D and E were estimated by considering $\theta = 0^o$ in the B_1 and B_3 expressions (and which correspond to B_1 and B_5 values in the spectrum) (table 6). The relative great value of the E parameter is due to the important rhombic distorsion of the local symmetry around the metallic ions.

The broad line at $g \approx 2$, assigned to coupled Cr^{3+} ions, can be described by the following spin Hamiltonian, in which only the isotropic exchange and Zeeman interactions were taken into account, all other interactions being negligible:

$$H = J\,S_1 \cdot S_2 + g\mu_B(S_1 + S_2)$$

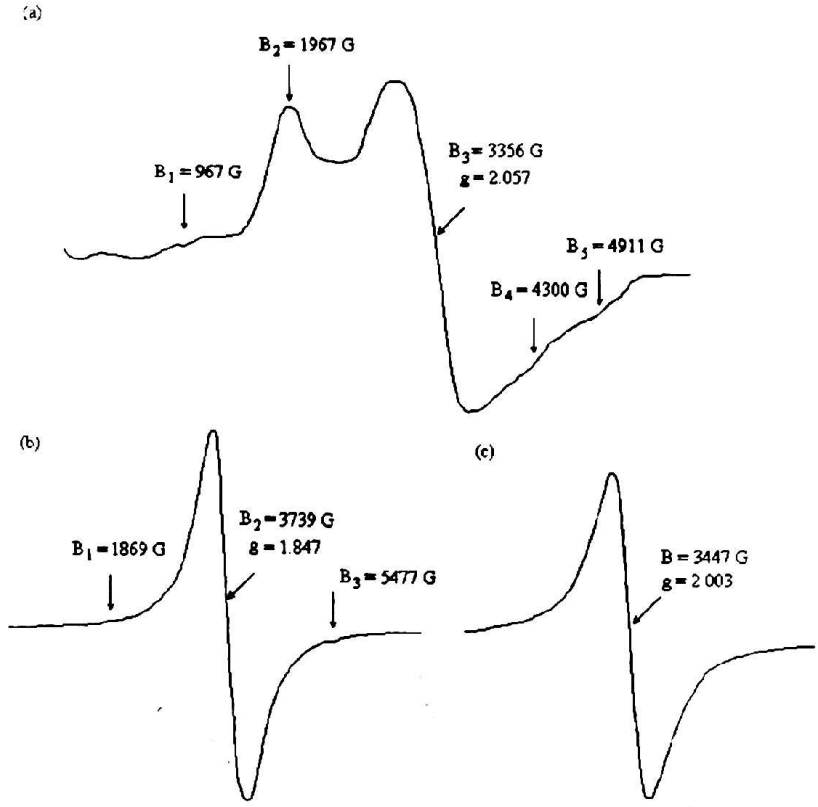

Figure 2. Powder EPR spectra of Cr(III)-tris-O-alkyldithiocarbonates at room temperature.

The exchange term is dominant and the large value of the spin-spin coupling parameter J not allows any transition between the S (=1,2,3) states. The allowed ($\Delta M_s = \pm 1$) transitions between the multiplets of the same spin state occur at g_{eff} = 2 [19]. The appearance of the coupled species is also confirmed by the mean of the value of 3.63 MB obtained for the effective magnetic moment of the studied compounds (table 6) which is smaller than the spin only value (μ_S = 5.92 MB). The values of the magnetic moments (table 6) increase with the length of the organic radicals due to the presence of weaker metal-metal interaction.

Table 6.

EPR parameters of the investigated Cr(III) compounds

Compound	g	D[G]	E[G]	B_1[G]	B_2[G]	B_3[G]	B_4[G]	B_5[G]	μ_{eff} [MB]
$Cr(S_2COC_2H_5)_3$	2.057	986	414	967	1967	3356	4300	4911	3.70
$Cr(S_2COCH_3)_3$	1.847	-	-	-	1869	3739	-	5477	3.60
$Cr(S_2CO^iC_3H_7)_3$	2.003	-	-	-	-	3447	-	-	3.63

EXPERIMENTAL

Reagents and Procedure.

The starting materials and all solvents were commercial products of analytical grade purity and were used as supplied.

Electronic spectra were recorded on an ATI UNICAM-UV/VIS apparatus and IR spectra were recorded as follows: the spectra of KS_2COCH_3, $KS_2COCH_2CH_3$, $KS_2COCH(CH_3)_2$, $Cr(S_2COCH_3)_3$, $Cr(S_2COCH_2CH_3)_3$ and $Cr(S_2COCH(CH_3)_2)_3$ on a Perkin Elmer 1330 spectrometer and the spectra of $KS_2COCH_2CH_2OCH_3$ and $Cr(S_2COCH_2CH_2OCH_3)_3$ on a SPECORD apparatus (KBr pellets).

EPR spectra were recorded at 9.4 GHz (X band) using a standard JEOL-JES-3B equipment with a magnetic field modulation of 100 KHz. Magnetic moments studies were carried out on a Faraday balance.

Synthesis of potassium xanthates.

The synthesis of potassium xanthates were prepared from the appropriate alcohol, potassium hydroxide and carbon disulfide, with excess alcohol acting as solvent. All chromium xanthates were prepared by a similar procedure given for $Cr(S_2COCH_3)_3$.

Synthesis of $Cr(S_2COCH_3)_3$.

To a solution of $Cr(NO_3)_3 \cdot 9H_2O$ (0.4 g, 0.001 moles in 25 ml H_2O) was added, under stirring, a solution of KS_2COCH_3 (0.438 g, 0.003 moles in 50 ml H_2O). After standing 5 hours at room temperature, the precipitate was filtered off, washed with 50 ml H_2O and dried over P_4O_{10}.

The chromium content was determined by titration with EDTA and the sulfur content by oxidation to S(VI) followed by precipitation as barium sulfate.

REFERENCES

1. G. Winter, *Revs. Inorg. Chem.*, **2**, 253 (1980).
2. E.R.T. Tiekink and G. Winter, *Revs. Inorg. Chem.*, **12**, 183 (1992)
3. J.V. Dubsky, *J. Prakt. Chem.*, **93**, 142 (1916)
4. G.W. Watt and B.J. McCormik, *J. Inorg. Nucl. Chem.*, **27**, 898 (1965)
5. F. Galsbol and C. Schiffer, *Inorg. Synth.*, **10**, 42 (1967)
6. W.J. Mitchell and M.C. De Armand, *J. Molec. Spect.*, **41**, 33 (1972)
7. G.W. Watt and B.J. McCormik, *Spectrochim. Acta.*, **21**, 753 (1965)
8. U.A. Lakshami and P.B. Rao, *Inorg. Chim. Acta.*, **2**, 337 (1968)
9. S. Merlino and F. Sartori, *Acta Cryst.*, **B28**, 972 (1972)
10. S. Boharagava, R. Bohra and R.C. Mecrota. *J. Cryst. Spectr. Res.*, **21**, 281 (1961)
11. F.N. Tebbe and E.L. Muettetis, *Inorg. Chem*., **9**. 629 (1970)
12. J.D. Lebedda and R.A. Palmer, *Inorg. Chem*., **10**, 2709 (1971)
13. A.A.G. Tomlinson, *J. Chem. Soc*., **1971**, 1409.
14. A.B.P. Lever, *J. Chem. Educ.*, **45**, 711 (1968)
15. L.H. Little, G.W. Poling and J. Leja, *Can. J. Chem.*, **39**, 747 (1961)
16. R. Mattes and G. Pauleickhoff, *Spectrochim. Acta.*, **29A**, 1339 (1973)
17. R. Mattes and G. Pauleickhoff, *Spectrochim. Acta.*, **30A**, 379 (1974)
18. J.R. Landry, J.T. Fourier, C.G. Young, *J. Chem. Phys*., **46**, 1285 (1967)
19. M. Vicens, J.J. Fiol, A. Terron, V. Moreno, D.M.L. Goodgame and R.N. Sheppard, *Inorg. Chim. Acta*., **192**, 139 (1992)
20. M. de la Fuente, O. Cozar, L. David, R. Navarro A. Hernanz and I. Bratu, *Spectrochim. Acta., Part A*, **53**, 637 (1997)
21. F.E. Mabbs and D. Collins, Electron Paramagnetic Resonance of d Transition Metal Compounds, Elsevier, Amsterdam, 1992
22. Al. Nicula, Rezonanta magnetica, Ed. Did. şi Ped., Bucharest, 1980

STUDIA UNIVERSITATIS BABEŞ-BOLYAI, CHEMIA, XLIV, 1-2, 1999

EFFECT OF CURING ON THE PERFORMANCE OF LEAD-ACID BATTERY POSITIVE PLATES

ELEONORA MARIA RUS and DELIA MARIA CONSTANTIN

"Babes-Bolyai" University, Faculty of Chemistry and Chemical Engineering, 11, Arany Janos str., 3400, Cluj-Napoca, Romania

ABSTRACT. The performance of a lead-acid battery depends on the structure and composition of positive active mass, a mixture of α-PbO_2 and β-PbO_2. The amounts of these two crystal PbO_2 modifications that are formed in the positive active mass depend on the processing plate history and on its formation conditions. The curing process is the longest step in the manufacture of lead-acid batteries. In this work the effect of three different curing methods on the physico-chemical and electrochemical properties of positive plates was studied. IR spectra, X-ray diffraction, scanning electron microscope observations and wet-chemical analysis were used as techniques of investigation. It has been observed that curing conditions (duration, humidity and temperature) strongly influence electrode phase-composition and electrical performance. A continuous recrystallization process and a growth of crystal size were observed during curing at low temperature and inadequate humidity and temperature.

INTRODUCTION

It is generally accepted that a good automotive lead-battery should have both high initial and reserve capacity and long deep-discharge cycle life [1-3]. In a major part, this performance depends on the structure and composition of positive active mass, which consists of a mixture of two PbO_2 crystal modifications: α-PbO_2 (orthorhombic) and β-PbO_2 (tetragonal) [4-7]. The amounts of α-PbO_2 (formed in a neutral or alkaline environment) and β-PbO_2 (formed in an acidic environment) in the positive active mass depend on the processing plate history (leady oxide preparation, mixing and curing of positive materials) and of the plates formation conditions (sulfuric acid concentration, time of soaking, charge current density and temperature) [8-10].

Applying a paste of "leady oxide", water and diluted sulfuric acid onto a lead or lead-alloy grid structure produces the positive plates.

The "leady-oxide" usually comprises about three-part lead monoxide (α-PbO and β-PbO) to one-part fine lead particles (so-called "free lead") [3]. Sometimes, the oxide is blended with a minor percentage of red lead (Pb_3O_4) as well as with certain proprietary additives that are thought to benefit the manufacturing procedure and/or battery performance.

From the steps involved in the positive plate manufacturing process, curing is a key stage, while the paste is converted into a cohesive, porous mass, with a good adherence to the grid. Poor control of the process will diminish the mechanical strength and the electrical performance of the plates during battery service life [11]. The transformations that take place during the curing are dependent on the composition of starting materials and processes which occurs in the mixing and pasting steps [12-16].

It has been established that the following processes, either separately or simultaneously, occurs during the curing of pasts [1,2,4,11,16]:

- oxidation of free lead particles to lead monoxide with liberation of heat;
- conversion of lead monoxide to mono, three or tetra - basic lead sulfates ($PbO{\cdot}PbSO_4$-1BS; 3 $PbO{\cdot}PbSO_4{\cdot}H_2O$-3BS; 4 $PbO{\cdot}PbSO_4$-4BS);
- recrystallization and interconversion of basic lead sulfates;
- development, of basic lead carbonate ($2.PbCO_3.Pb(OH)_2$ - HC) on the surface of the plate;
- corrosive attack of the metallic grids;
- evaporation of water from plates.

It has been found that the positive active mass obtained from 3BS rich paste contains small PbO_2 crystals. Due to their high surface area they assure a high initial capacity, being appropriate to the manufacture of automotive batteries [2,11]. The plates formed from 4BS rich paste have a lower capacity and an inferior charge acceptance, but a longer cycle life and could be used for industrial batteries [7,13-16].

The relative amounts of 3BS and 4BS in the positive paste are influenced by: a) the proprieties of starting leady-oxide (composition, morphology, particles size, etc); b) the quantities of water and sulfuric acid added in the mixing stage; c) the temperature, duration and method of mixing; d) the temperature, humidity and duration of curing; e) the stand time of the paste before pasting on the grid [3,14-16].

This paper describes the work that has been carried out in order to investigate more fully the effect of three different methods of curing on the physicochemical behavior of positive plates before, and after, formation in sulfuric acid solution.

We aim to find the conditions under which 3BS are formed and to detect the correlation between the phase composition of plates in the cured and formed states.

EXPERIMENTAL

Paste and Plates Preparation

Positive paste was prepared in a laboratory mixer system, by mixing leady-oxide powder namely Balox (Barton pot variety) with a definite quantity of water, and 8%(wt.) with respect to the leady-oxide, sulfuric acid (1.4 g/cm^3) [17]. The prepared paste was applied to grid cast from Pb-Sb alloy (4% Sb). The resulting positive plates were cured according to the following three methods:

A. In an industrial curing micropilot provided with temperature and humidity controls and air recirculation system, in two steps a) at 36^{0}C and 75% relative humidity (RH) for 16h and b) at 40^{0}C and 40% RH for 48h.

B. Air-dried at 20^{0}C in a closed curing chamber for 36h, without any control of humidity. The moisture content of the plates provided the humidity themselves.

C. Air-dried at 20^{0}C, closed in a polyethylene sheet for 72h.

After curing all plates were dried at 70^{0}C until the moisture content not exceed 2.0 %(wt).

Samples of leady-oxide, uncured and cured pastes were analyzed by X-ray diffraction (XRD) phase-analysis method, scanning electron microscopy (SEM) and wet chemical analysis. The XRD patterns were recorded with a C. Zeiss Jena URB-1988 diffractometer using CuK_α radiation and with an APX-60 complex program the phase composition was determined. SEM studies using a TESLA BS-340-1999 scanning electron microscope were carried out for crystal morphology and structure analysis. By wet analysis, the lead, lead oxide (free and bond in basic sulfates) and lead sulfates (free and bond) were determined.

Plates Formation

A series of test cells with 1 positive and 2 negative (produced under factory conditions) dried plates were assembled. After a soaking for 72h in H_2SO_4 (sp.g. 1.05 g/cm^3) the plates were formed in 0.8M H_2SO_4 solution according to the following protocol: 2h-1A/cell; 1h break; 10h-1.85A/cell; 1h break; 4h-1.50A/cell; 3h-0.85A/cell. Samples of these formed plates, after washing in running water and drying at 125^{0}C for 10h were subjected to phase compositions, morphology and chemical composition analysis.

Battery Performance

Electrical performance tests (nominal capacity, cold cranking ability, charge acceptance and reserve-capacity) were carried out on a series of 12V/45A batteries manufactured using the three cured types of plates.

RESULTS AND DISCUSSION

The changes in phase composition and crystal structure of materials were observed as a function of curing method. Samples of leady oxide uncured and cured paste and formed plates were subjected to X-ray diffraction and wet chemical analysis. The morphology of the materials was examinate by scanning electron microscopy.

1. Leady-oxide

The phase composition and the physico-chemical characteristics of leady-oxide precursor are presented in Table 1.

The crystal structure, obtained by SEM, shows that the oxide phase consists mainly of individual "particles" of varying shape and diameters in the range 2-10 μm (Fig.1a).

Table 1.

Phase composition and physico-chemical characteristic of leady-oxide.

Pb (wt.%)	α-PbO (wt.%)	β-PbO (wt.%)	Acid adsorption (mg H_2SO_4/g)	Water adsorption (ml H_2O/Kg)	Density (g/cm^3)
24	71.40	4.60	185	139	3.50

SEM micrography obtained at higher magnification show that the "particles" are in fact aggregates of various tiny grain which contains numerous small pores (Fig.1b). These pores serve to increase the surface area and explain the high reactivity of leady-oxide (Table 1).

From the above results (Fig. 1. and Table 1.) we have seen that the leady-oxide used as precursor in this work is of good quality [5,7,9].

2. Uncured Paste

The mixing times (30 min.) and temperature (55 - 60^{0}C) were selected so that the only basic lead sulfate formed was 3BS [5].

Chemical analysis data of the prepared paste show that during the mixing, the level of free lead remains largely unchanged but a significant part of PbO converts to lead sulfates (Table 2).

Table 2.

Composition (wt.%) of the prepared positive paste.

Pb	PbO	$PbSO_4$	H_2O	Density (g/cm^3)
22.50	44.22	22.70	10.58	3.78

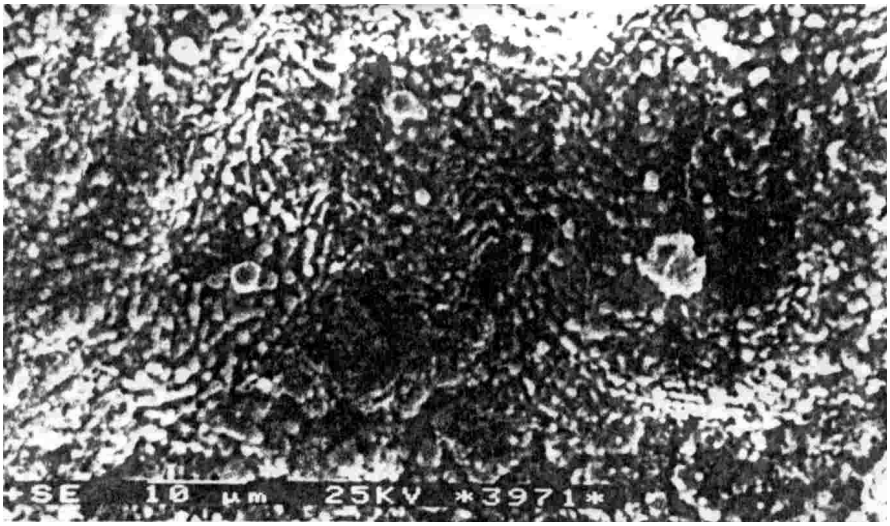

a)

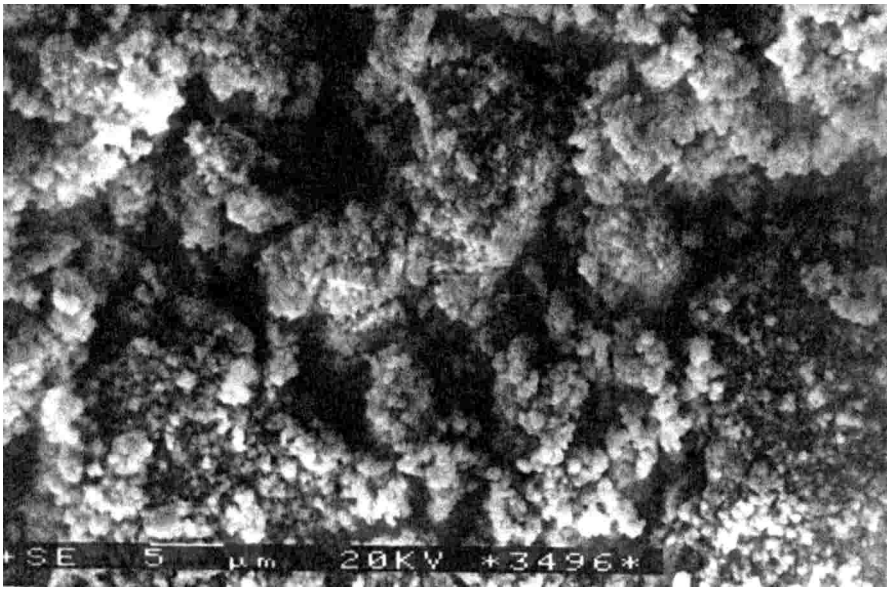

b)

Fig.1. Scanning electron micrographs of leady-oxide. Magnification bar: a)10 µm and b) 5µm.

The SEM investigations show clearly that the phase morphology of the paste changes from the spherical shape of the precursor oxide to the needle-like form of three basic lead sulfate crystals (Fig. 2).

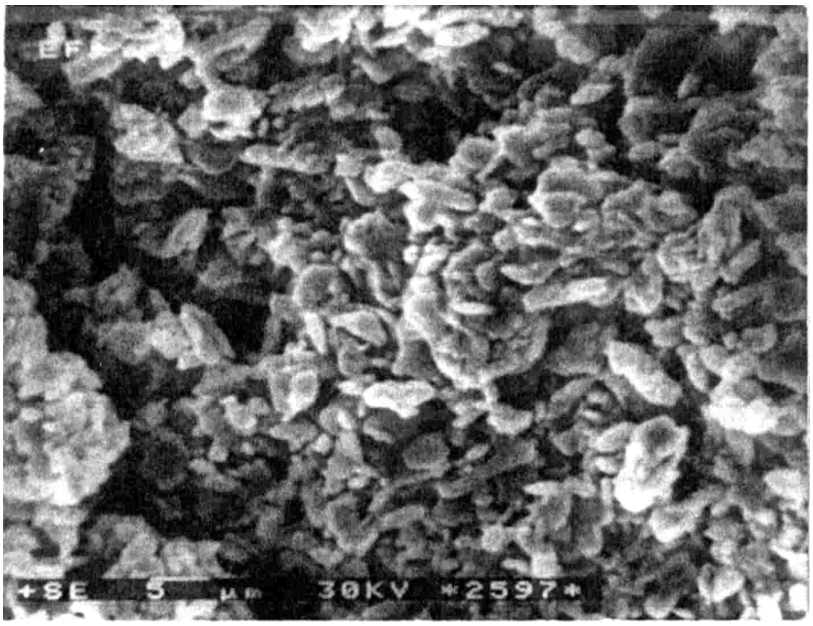

Fig. 2. Scanning electron micrograph of uncured paste.

Because the prepared positive plates were set aside under ambient conditions (up to 8h) until the production run was completed, an investigation was made to determine whether this residence time before curing exerted an influence on the paste composition. Accordingly, phase analysis were conducted every 2h. For all analyzed samples the average $PbSO_4$ content was about 23 wt.%. This fact shows that the paste had already reached a stable composition during mixing and remained virtually unchanged throughout the stand period before curing.

3. Cured Plates

The results of phase composition analysis performed by X-ray diffraction on cured materials are given in Table 3.

Table 3.

Phase-analysis for different cured positive plates.

Curing method	α-PbO (wt.%)	3BS (wt.%)	1BS (wt.%)	HC (wt.%)	Pb (wt.%)
Method A	56.00	36.20	-	7.80	-
Method B	64.05	26.67	-	3.65	5.63
Method C	56.54	30.84	2.87	6.29	3.46

It can be seen that at the end of curing the lead content in paste decreased considerably in all three curing methods due to their conversion to α-PbO. No 4BS were formed. Very little amount of 1BS (variety, which is harmful to battery performance,) was formed in the plates cured under polyethylene sheet.

Basic lead carbonate (HC) is formed in all the curing methods. The formation of carbonate roughens the surface of 3BS crystal [13]. This improves the contact between the crystals and, consequently the toughness of the paste.

The amount of 3BS, the predominant species of basic lead sulfate in active cured materials depends on curing method. It is clearly that during curing in a highly humid atmosphere, method A, the remaining metallic lead from the precursor paste is oxidized, while the 3BS phase content increases.

The level of 3BS in plates materials cured under polyethylene sheet is higher than those cured by method B (in closed chamber) but the first contains 1BS and cracking and partial shedding of pastes were observed.

The higher free lead content of plates cured after method B and C provides evidence that the curing process was incomplete (has been stalled probably, by the lower humidity level existent in the chamber).

The above observations confirm that the cured material phase-composition is largely dependent on the humidity level and its variation during the process.

From the SEM micrographs of different cured plates it is seen that the curing has affected the material crystal structure (Fig. 3. a, b and c). In general the small sized crystals of various shapes interconnected in a homogenous structure are attributed to 3BS and to unreacted α-PbO.

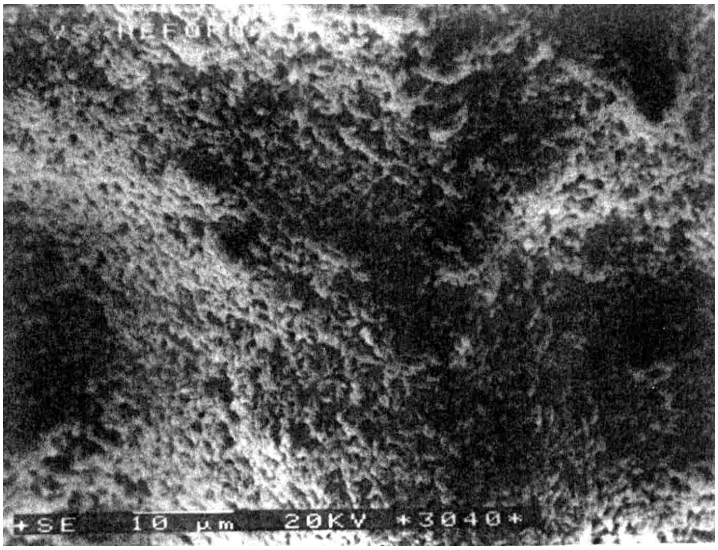

a)

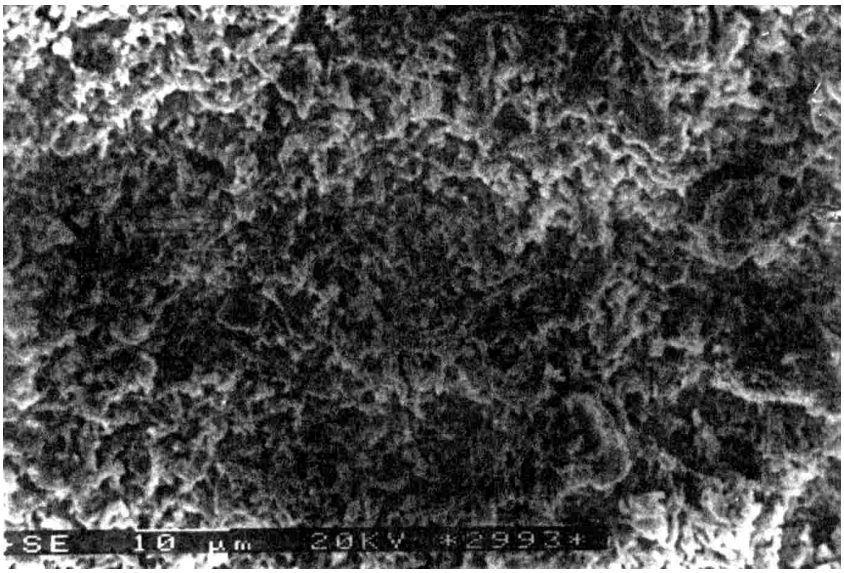

b)

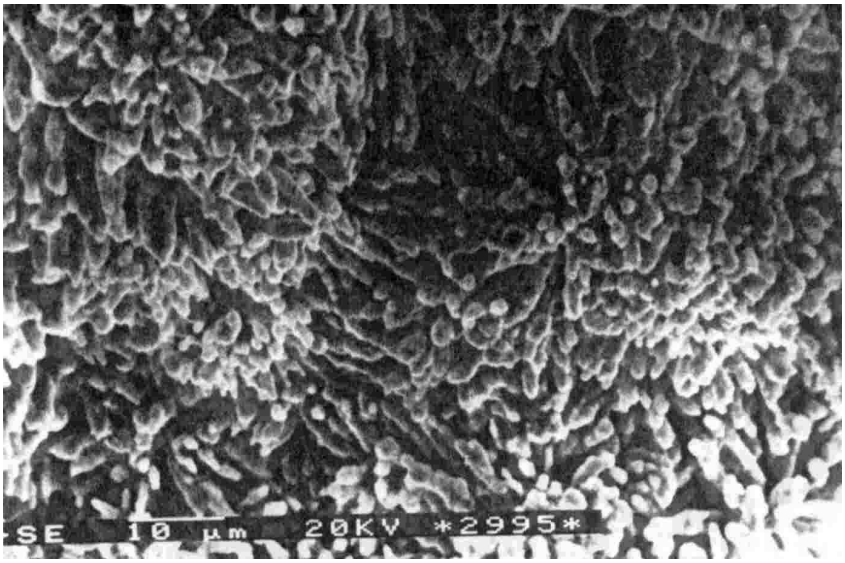

c)

Fig. 3. Scanning electron micrographs of different cured plates:
a) micropilot; b) closed chamber and c) polyethylene covered.

Pavlov [2] and Zerroual [7] reported similar micrographs on synthesized 3BS from PbO and H_2SO_4.

The 3BS formed during curing (A method) consists of needles with relative equal size (1.5-2.0 μm), while the 3BS crystals formed in the plates cured after C method are slightly larger (3-7 μm) without definite shape (Fig. 3 a and b).

From the electron micrographs given in Fig. 2 and Fig. 3 (b and c) we can say that the 3BS cured material crystals is slightly larger that those in the precursor paste. This indicated that at low temperature (20^0C) a recrystallization of 3BS has occurred during curing process but no recrystallization has occurred at higher temperature (method A).

4. Formed Plates and Battery Tests

During formation two main reactions can be distinguished. First, due to the soaking of plates in the electrolyte, the basic lead sulfates are partially converted into lead sulfate. Simultaneously, the lead and/or the lead basic sulfate are electrochemically oxidized leading to charge active material PbO_2. Table 4 gives the XRD analysis of the formed active materials.

Table 4.

X-ray diffraction analysis of formed active mass (wt.%).

Curing method	PbO	$PbSO_4$	Pb	PbO_2	α-PbO_2	β- PbO_2
Method A	9.33	1.68	-	88.99	7.83	81.16
Method B	12.43	5.35	2.76	79.46	12.18	67.28
Method C	12.38	3.56	0.73	83.33	10.09	73.24

The results shows that the active mass of plates previously cured after method A lead to a higher PbO_2 content than those cured under conditions B and C. In addition, the formed active material cured in micropilot contains after oxidation more β-PbO_2 and the formed plates derived from material cured after method B and C still contains appreciable levels of unoxidized residues, i.e. PbO, $PbSO_4$ and Pb. It can be concluded therefore that the conditions of curing have a notable effect on the level of PbO_2 active mass formation. From the above results we can seen that the larger the amount of 3BS paste content, the larger will be the β-PbO_2 amount in the formed active mass (Table 3 and 4).

After formation, the fully charged state of the cell was achieved by applying a constant current (2.25 A) until both the terminal voltage and the acid density (1.28 g/cm^3) were kept constant for two hours.

For the determining of nominal capacity, C_{20}, the full charged batteries were discharged at a constant current of 2,25 A until the terminal voltage fell to 10.5 V. The product between the current intensity and the discharge time yields the nominal capacity.

For the determining of charge acceptance, the fully charged batteries were discharged with a constant current I = $0.1C_{20}$ A, at 25^0C. The batteries were then kept at 0^0C for 25 hours and fully charged at a 14.4 V constant voltage. The current intensity value after 10 min. charge was recorded.

In the reserve-capacity tests, the fully charged batteries were subjected to two complete C_{20} charge-discharge cycles and deposited for 28 days at (20 $\pm$ 5)^{0}C. The batteries were then discharged at 0.05 C_{20} A, until the terminal voltage was 10.5 V. The measured reserve capacity was reported to the initial capacity. In the cold-cranking ability tests, after three complete C_{20} charge-discharge cycles, the fully charged batteries were kept at -18^0C for 24h. The batteries were then discharged at 3.5 C_{20} A and the recorded time until the terminal voltage to fell to 6 V was taken as a measure of cold-cranking ability.

Table 4 summarizes the electrical testing results of batteries manufactured using the three different cured plates. The results were recorded after technical requirements for quality included in Romanian STAS 444/1 - 74.

Table 5.

Electrical batteries parameters.

Electrical characteristics	Method of curing (A)	(B)	(C)
Initial capacity, $E_{xp.}/C_{20}$ (%)	109.8	100	104
Charge acceptance (A)	6.85	6.15	7.55
Reserve capacity (%)	93	83	85
Cold-cranking ability (sec.)	185	182	184

In the light of these results, it can be seen that the positive plate active mass previously cured by method A gives the highest electrical performance.

This could be attributed to the large β-PbO_2 and total PbO_2 contents since the capacity of β-PbO_2 (0.164 Ah/g) is larger than that of α- PbO_2 (0.135 Ah/g) [18]. Because during lead-battery discharge, the potential of negative plate is the first to reach the cut-off value, the cold-cranking ability (deep discharge at - 18^0C) of battery is "negative-potential limited" [4]. Thus this propriety is not so much affected by positive plate structure.

The obtained results give us ground to conclude that curing methods B and C are not a successful technology for positive plates production.

CONCLUSIONS

The above investigation illustrates that curing conditions are determinant for the modifications of the chemical and phase composition of positive active mass and for the electrochemical performance. Thus, a better understanding of the curing mechanisms is required in order to optimize the positive plate's performance.

It has been observed that the key to successful curing is the maintenance of an exact balance between the moisture contient, temperature and duration of process (method A). It is essential to conduct the curing in an enclosed chamber that allows precis regulation of the ambient conditions.

Further experimental work is required to determine in detail, the influence of these parameters on curing reactions.

REFERENCES

1. H. Bode, *"Lead-Acid batteries*", J. Wiley, New York, 1997, 204 - 280.
2. D. Pavlov and N. Kapkov, *J. Electrochem.Soc.*1990, **137**,16 - 21.
3. D. A. J. Rand, R. J. Hill and M. McDouagh, *J. Power Sources*, 1990, **31**, 203 - 215.
4. H. Ozgun, L. T. Lam, D.A.J. Rand and S.K. Bhargava, *J. Power Sources*, 1994, **52,** 159 - 171.
5. L. T. Lam, A. M. Vecchio-Sadus, H. Ozgun and D. A. J. Rand, *J. Power Sources,* 1992, **38**, 87 - 102.
6. L. T. Lam, H.Ozgun, L.M.D.Cranswick and D.A.J.Rand, *J. Power Sources,* 1993, **41,** 55 - 70.
7. L. Zerroual, F. Tedjar, J. Guitton and A. Mousser, *J. Power Sources,* 1993, **41,** 231 - 138.
8. D. Pavlov and N. Kapkov, *J. Electrochem.Soc.* 1990, **137**, 21 - 28.
9. L. Zerroual, N. Chelali, F. Tedjar and J. Guitton, *J. Power Sources*, 1994, **51,** 425 - 431.
10. S. Grugeon-Dewaele, J.B. Leriche, J.M. Tarascon, A. Delahaye-Vidal, L. Torcheux, F. Henn and A. De Guibert, *J. Power Sources*, 1997, **64**,71 - 80.
11. S. Ruevski and D. Pavlov, *J. Power Sources*, 1990, **31,** 217 - 223.
12. D. Pavlov and E. Bashtavelova, *J. Power Sources*, 1990, **31,** 243 - 254.
13. Nakamichi Yamasaki, Jia-jun Ke and Wei-ping Tang, *J. Power Sources*, 1991, **36,** 95 - 110.
14. F. Vallat-Joliveau, A. Delahaye-Vidal, M. Figlarz and A. De Guibert, *J. Power Sources*, 1995, **55,** 97 - 100.
15. J.K. Vilhnnen and E. Kantti, *J. Power Sources*, 1992, **38,** 273 - 280.
16. S. Laruelle, S. Grugeon-Dewaele, L. Torcheux and A. Delahaye-Vidal, *J. Power Sources*, 1999, **77**, 83 - 89.
17. T.Antonescu, Eleonora - Maria Rus, T.Fărcaş, E.Neagoş, *Producerea, transportul şi utilizarea energiei,* 1997**, *vol. XV***, 194 - 202.
18. L.Oniciu and Eleonora Maria Rus, "*Surse electrochimice de putere",* Ed. Dacia, Cluj-Napoca, 1987, 163 - 176.

STUDIA UNIVERSITATIS BABEŞ-BOLYAI, CHEMIA, XLIV, 1-2, 1999

INFLUENCE OF ULTRASOUNDS IN ELECTROCHEMICAL PROCESSES

VIRGINIA DANCIU, VERONICA COSOVEANU, EVA BARABAS, IOANA CARMEN LADIU

"Babeş-Bolyai" University, Faculty of Chemistry and Chemical Engineering
3400 Cluj-Napoca, 11, Arany Janos St., Romania

ABSTRACT. Sonoelectrochemistry is an emergent and interdisciplinary field of research which couples the power of ultrasound to electrochemical systems in order to both achieve and develop new process and allow their measurement and quantification in combination with ultrasound associated reaction kinetics. The present review focuses on the influences of ultrasounds on mass transport at the electrode, induced surface electrode effects and electrode processes. Based on the tools and methods now available it is hoped that the application of ultrasound in areas as diverse as electroanalytical and synthetic electrochemistry will be beneficial and new innovative approaches employing the various mechanical and chemical effects of ultrasound will result.

Introduction

Ultrasound is defined as sound of a frequency beyond that to which the human ear can respond. The normal range of hearing is between 16 Hz and about 18 kHz and ultrasound is generally considered to lie between 20 kHZ to beyond 100 MHz. Sonochemistry uses frequencies between 20 KHz and 2 MHz.

Like all sound energy, ultrasound is propagated *via* a series of compression and rarefaction waves induced in the molecules of the medium through which it passes. At sufficiently high power the rarefaction cycle may exceed the attractive forces of the molecules of the liquid and cavitation bubbles will form. These bubbles will grow over a few cycles taking in some vapour or gas from the medium to an equilibrium size which matches the frequency of bubble resonance to that of the sound frequency applied. The acoustic field experienced by the bubble is not stable because of the interference of other bubbles forming and resonating around it. As a result some bubbles suffer sudden expansion to an unstable size and collapse violently. It is the fate of these cavities when they collapse which

generates the energy for chemical and mechanical effects. Each cavitation bubble acts as a localised microreactor which, in aqueous system, generates temperature of several thousand degrees and pressures in excess of one thousand atmospheres.

In addition to the generation of extreme conditions within the bubble there are also major mechanical effects produced as a result of its rapid collapse.

An empirical classification of sonochemical reactions based upon purely chemical effects induced by cavitation was proposed by J.-L. Luche [1]:

- Homogeneous systems which proceed *via* radical or radical-ion intermediates. This implies that sonication is able to affect reactions proceeding through radicals and further that it is unlikely to affect ionic reactions [2-5].
- Heterogeneous systems proceeding *via* ionic intermediates. Here the reaction is influenced primarily through the mechanical effects of cavitation such as surface cleaning, particle size reduction and improved mass transfer [6,7].
- Heterogeneous reactions which include radical pathway or a mixed mechanism *i.e.* radical and ionic. Radical reactions will be chemically enhanced by sonication but the general mechanical effect referred to above may well still apply. If the radical and ionic mechanisms lead to different products, ultrasound should favour the radical pathway and this could lead to a switch in the nature of the reaction products [2,8-10].

It was observed that if cavitation bubbles are formed at or near to any large solid surface (heterogeneous systems), the bubble collapse will no longer be symmetrical. The large solid surface hinders liquid movement from that side and so the major liquid flow into the collapsing bubble will be from the other side of the bubble. As a result of this a liquid jet will be formed which is targeted at the surface with speeds in excess of 100m s^{-1}. Depending upon the conditions used this powerful jet can activate surface catalysis, force the impregnation of catalytic material into porous supports and generally increase mass and heat transfer to the surface by disruption of interfacial boundary layers [11].

Coupling of power ultrasound to electrochemical systems leads to an emergent and interdisciplinary field of research *sonoelectrochemistry.* Sonoelectrochemistry may be compared to other synergistic approaches in which two independent sources of energy or activation are coupled. The result is a new powerful metodology for the study of each source of activation on its own but furthermore capable of the detection of new processes induced by dual activation [12]. The particular advantages of the sonoelectrochemistry include:

(a) degassing at the electrode surface,

(b) disruption of the diffusion layer which reduces depletion of electroactive species,

(c) improved mass transport of ions across the double layer and

(d) continuous cleaning and activation of the electrode surfaces.

All of these effects combine to provide enhanced yield and improved electrical efficiency.

2. The Influence of Ultrasound on Mass Transport at the Electrode

As stated in the introduction, the application of ultrasound to a solution may drastically increase the rate of mass transport of material to a solid surface. Mass transport is a very important aspect of electrochemical processes as well as heterogeneous processes in general. Many heterogeneous reactions proceed under mass transport control and the variation of the flux of material transported to and from an interface has been reported to cause in some cases a “switching” to a different reaction pathway [8, 13]. The corresponding parameter describing the mass transport in electrochemistry is the diffusion layer thickness, δ, which can be used intentionally to control the nature of a chemical process [14].

The use of the diffusion layer thickness is based on the diffusion layer model [15] which allows an approximate description of the mass transport at the electrode-solution boundary by assuming a laminar sublayer close to the surface and an approximately linear concentration gradient across a thin layer adjacent to the electrode. Using this simple concept, the mass transport to the electrode is described by the equation (1):

$$I_{lim} = nFDA\,(c_{bulk} - c_{surface})/\delta \qquad (1)$$

where: n = the number of transferred electrons, F = the Faraday constant, D = the diffusion coefficient, A = the electrode area, c = the concentration, δ = the diffusion layer thickness.

Figure 1 shows two voltammograms of which the first was obtained in the absence (a) and the second in the presence (b) of ultrasound at Pt disk electrode for the oxidation of Cp_2Fe ($Cp = \eta\text{-}C_5H_5$) in acetonitrile [16].

The transport limited current is significantly enhanced as compared to the silent case, and the form of voltammogram is qualitatively changed from that of a familiar cyclic voltammogram to a sigmoidal shape, indicative of a constant rate of transport of the electroactive species to the electrode surface so as to sustain an, in average, steady current. The magnitude of the current is considerably greater than that of the peak current seen under silent conditions.

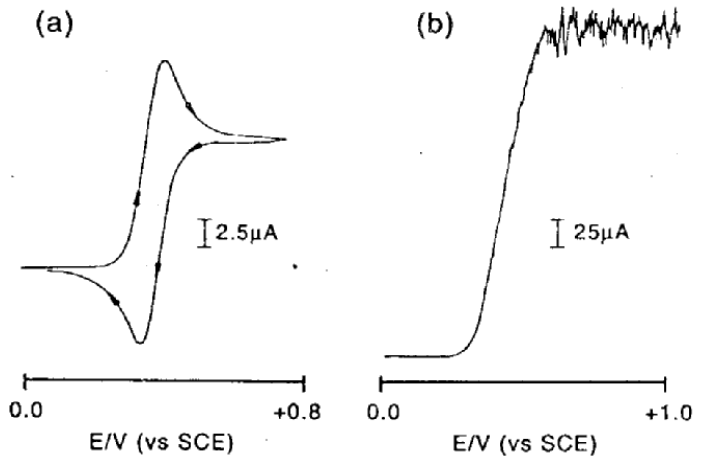

Figure 1. a) Cyclic voltammogram and b) sonovoltamogram (20 kHz, power 50 W cm^{-2}, distance 40 mm) for the oxidation of 2 mM ferrocene in acetonitrile (0,1 M NBu_4ClO_4), at Pt-disk electrode (2mm diameter); v = 20 mV s^{-1} [24].

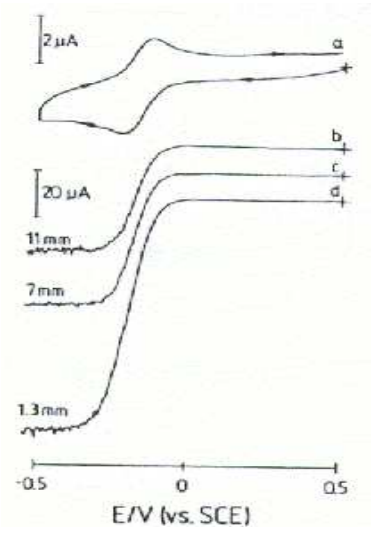

Figure 2. Voltammograms for the reduction of 0,23 mM $Ru(NH_3)_6^{3+}$ in aqueous 0,1 M KCl obtained at 22^0 C using a 2mm diameter Pt electrode under (a) silent condition (scan rate 50 mV s^{-1}), and in the presence of ultrasound (scan rate 20 mVs^{-1}, ultrasonic power 30 Wcm^{-2}), (b) 11, (c) 7, (d) 1,3 mm electrode-horn separation [17].

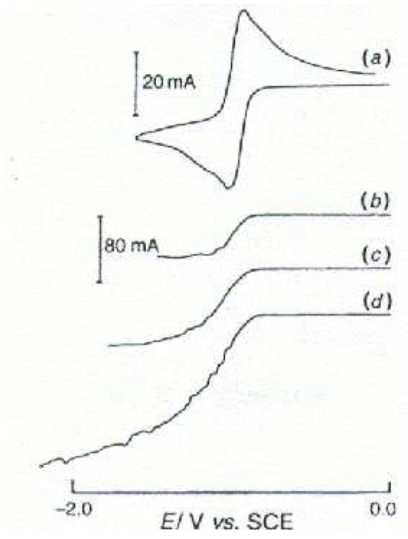

Figure 3. Voltammograms for the reduction of 5 mM $CoCp_2(PF_6)$ at a 23,8 mm^2 area glassy carbon plate electrode in acetonitrile (0,1M NBu_4PF_6) at 25^0C; (a) silent condition (scan rate 100mV s^{-1}),and in the presence of ultrasound (scan rate 100 mVs^{-1}, ultrasonic frequency 20 kHz), (b) 6, (c) 18, (d) 30 W cm^{-2} ultrasonic power [18].

The sonocurrent is found to increase as the electrode-horn tip separation is reduced (fig. 2) and the magnitude of the ultrasonic intensity applied to the system is increased (fig. 3). “Steady state” sonovoltammograms shown in figs. 2(b)-(d) exhibit slopes of 60 mV in mass-transport-corrected Tafel plots (plot of $\log[1/I - 1/I_{lim}]$ versus E [19]), in agreement with fast electron transfer. From the limiting current, I_{lim}, the diffusion layer thickness, δ, for this reaction may be determinate [20] using Eq. (2):

$$\delta = nFc_bDA/I_{lim} \quad (2)$$

where $D = 9{,}1 \cdot 10^{-6}$ $cm^2\ s^{-1}$, was independently determined by rotating disk voltammetry.

The fact that no irreversible signal occurs even at average diffusion layer thicknesses down to 0,65 μm (corresponding to an electrode horn distance of 1,3 mm) allows a lower limit for the apparent standard rate constant for heterogeneous electron transfer, k_0 to be estimated (using $k_0 > D/\delta$) as $k_0 >$ 0,14 cm s^{-1}.

Commonly, the electrode material, the electrode pre-treatment and the solution environment strongly influence the rate of heterogeneous electron transfer [21-23].

The enhancement of the mass transport is very dependent upon the geometry of the ultrasonic horn relative to the electrode surface. It have been studied three alternative geometries (fig. 4) [24]:

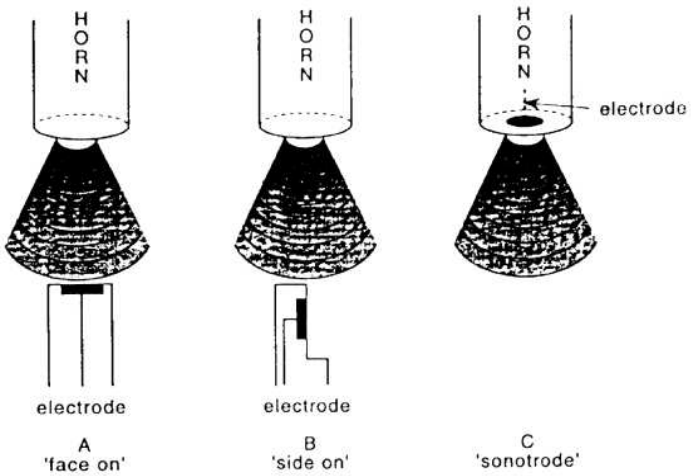

Figure 4. Types of electrode geometries used in sonovoltammetric experiments

- the conventional or “face-on” geometry,
- the “side-on” electrode geometry with the electrode placed perpendicular to the tip of the ultrasonic horn with the centre of the electrode at the

same separation from the tip as the surface of the electrode in the "face-on" geometry,

- "sonotrode" - the actual tip of the ultrasonic horn may be used as the working electrode directly or after insertion of an isolated metal disk.

In the "side-on" case, the mass transport of material to the electrode could be crudely modelled as the flow of material over a metal plate embedded in a nonconducting surface, a problem which has been treated by Levich [25]. In this case, the diffusion layer is nonuniform, its thickness being proportional to the square root of the distance along the electrode. The fact that a model using an intensity dependent flow over the electrode surface could be used successfully implies that acoustic streaming, a process induced by intense sound waves in which a macroscopic jet of liquid originating from the sound source is formed, is governing the mass transport properties in this experimental arrangement [26, 27]. In these cases, the diffusion layer thickness was empirically found to be dependent on the diffusion coefficient following a $\delta \propto D^{1/3}$ law. This result is in marked contrast to the dependence observed in acetonitrile solutions in which the diffusion layer thickness was found to be independent of the diffusion coefficient. The empirically observed non linear dependence is in agreement with a whole range of other "classical" hydrodynamic techniques [28], as well as with turbulent voltammetry [29] and the behaviour predicted by Perusich [30] all of which rely on a convective flow of liquid past on electrode surface. The individual contribution of the macroscopic jet and, on the other hand, of the microjets induced by cavitation may depend on the experimental conditions, but the use of an immersion horn appears to strongly favour the contribution from macroscopic turbulent streaming.

In the third and last case of alternative electrode geometries, the titanium alloy tip surface of the ultrasonic horn can be used directly, as described by Reisse et al. [31] for the case of an immersion horn with tip being connected to the potentiostat. In general it was found that this "sonotrode" design vastly improved the yield and current efficiency for the reduction of Cu^{2+} to Cu, however in the case of the titanium immersion horn [31] details of the nature of the electrode process are not clear and background processes as hydrogen evolution may occur. The work conducted on a similar system by Compton et al. [32] suggested that the "sonotrode" surface consisted of a TiO_2 containing layer with the characteristic properties of an n-type semiconductor. The voltammograms observed for the reduction of Cu^{2+} were only slightly effected by insonation and it was suggested that under these conditions the observed electrode current was not mass transport limited. Further, in the electrochemistry of a number of simple electron transfer systems (i.e., the reduction of ferricyanide, the oxidation of 1,4-N,N,N',N'-tetramethyl-phenylenediamine) was found a change in the reversibility of the simple reductive electron transfers and no voltammetry was observed for the oxidative systems in accord with the electrode surface behaving like an n-type

semiconductor. Using a modified sonotrode - a Pt electrode inserted into the tip of ultrasonic horn - it was found that even for low powers this system was restricted to huge enhancements in the rate of mass transport of the electroactive material to the Pt electrode surface for the oxidation of ferrocene (in acetonitrile) and the reduction of benzoquinone (in water) [24].

In summary it can be stated that ultrasound enhances the mass transport of electroactive material to an electrode surface. This enhanced mass transport can, for the case of the "face-on" geometry, simply be described by a thinning of the diffusion layer. The enhancement of the mass transport is very dependent upon the geometry of the ultrasonic horn relative to the electrode surface. A good approximation of the effect of ultrasound on the mass transport at the electrode surface, is possible by considering only the effect of "acoustic streaming" and by treating the system similar to related cases in hydrodynamic voltammetry [33, 34].

3. Ultrasound Induced Surface Effects

Effects of ultrasounds on heterogeneous processes include most notably erosion at solid surfaces induced by asymmetric cavitation close to a solid-solution interface [35, 36]. This process is thought to be responsible for the damage to the surface as well as for cleaning the surface of particles and adherent films.

There is a wide range of ex-situ and in-situ methods available for the investigation of surface properties. First of all microscopy allows the detailed study of changes in the surface morphology caused by ultrasound [37, 38]. Electrochemical AC impedance methods are well suited for in-situ monitoring of changes in surface roughness and capacitance [38].

Different types of damages were observed for glassy carbon and gold electrodes after a period of ultrasound treatment in 0,1 M NaOH [37, 38]. After 30 min. of ultrasound (20 kHz, 60 Wcm^{-2}) treatment the atomic force microscopy of a gold surface shows a roughening in the 10 μm scale, as well as in a smaller scale with little (ca. 0,1 μm) sized pits. Under similar conditions, the glassy carbon electrode surface shows cracks caused by high amplitude vibrations. This kind of severe damage occurs only after a prolonged treatment with high intensity ultrasound at a close distance between electrode and immersion horn. Voltammetric experiments, however, require shorter periods of time and usually a lower sound intensity with much more subtle changes in the surface properties.

The study of a platinum electrode surface in acetonitrile solutions and of aluminium and nickel electrodes in aqueous environments [37] also demonstrated the destructive effect of sonication which is possibly in most cases attributable to cavitational collapse of bubbles close to the surface. In figure 5 cyclic voltammograms for the oxidation of a nickel electrode immersed in aqueous 1M KOH are shown. In the presence of ultrasound,

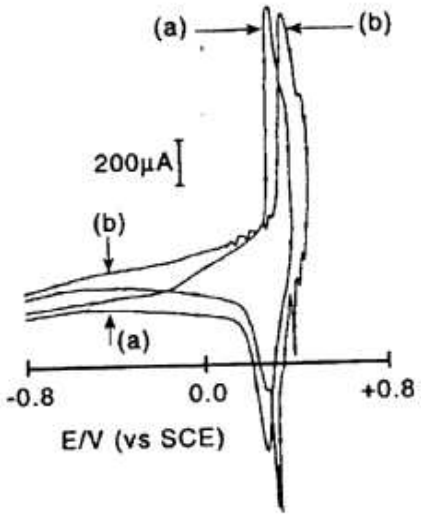

Figure 5. Cyclic voltammograms for the oxidation of a nickel electrode in 1M aqueous KOH solution a) in the absence and b) in the presence of ultrasound (20 kHz, 60 Wcm^{-2}, scan rate 100 mVs^{-1})

the magnitude of the observed current and the overall shape of the signal apart from added current fluctuations remains unchanged, consistent with surface confined processes independent of mass transport in the solution phase. The potential shift, up to 60 mV, towards more anodic potentials - depending on the applied ultrasound intensity - may be attributed to ultrasound causing an effect, such as surface cleaning, which could compete with the film growth. Alternatively, a local change of the temperature may also be considered due to direct cavitation on the surface of the electrode.

An other example for ultrasound affecting electrode properties and surface confined electrode processes is presented in figure 6 [24]. In the presence of ultrasound the oxidation process proceeds with a higher current whereas the reduction process is split into two signals. Further, in the presence of ultrasound at elevated temperature (50^0C) a massive change occurs with high anodic currents being detected even on the reverse scan. In figure 6f, the presence of a cathodic process can only be assumed from the presence of a small peak superimposed onto the oxidation response which is caused by a ultrasonically enhanced gold depassivation process. Three potential regions may be identified corresponding to the processes at the gold electrode with an inert region at lower potential, a corrosion region in which gold dissolution is possible, and a passivation region at very positive potentials.

Further examples for the cleaning effect of ultrasound have been given for the electrode poisoning by $Cr(CO)_6$ by Compton et al. [37] and for the case of the formation of a polymer film [39-42].

Coury has shown that sonication of an insulating polymer film prepared by electropolymerisation of o-phenylendiamine results in the formation of a microarray electrode [39]. This effect is explained on the

basis of microjetting, i.e. the microjets of solution are pitting microscopic holes through the insulating film. Another example of the formation of a microarray electrode by sonication of the electrode covered by a passivating film is presented by Klima [42]. Their study of sonassisted electroxidative polymerisation of salicylic acid shows that whereas all the acoustic streaming, turbulence of solution and microjetting, can accelerate electrochemical processes by mass transfer enhancement, only the last one, i.e. microjetting, can reactivate the electrode covered by passivating polymeric film. Consequently, as the microjets are connected with transient collapses, the electrode reactivation can be observed only in the points in the cell with high acoustic intensity where transient cavitation takes place, whereas the acoustically induced increase of electrochemical current can be observed even at an electrode in areas in the cell with lower acoustic intensity where no transient cavitation is present.

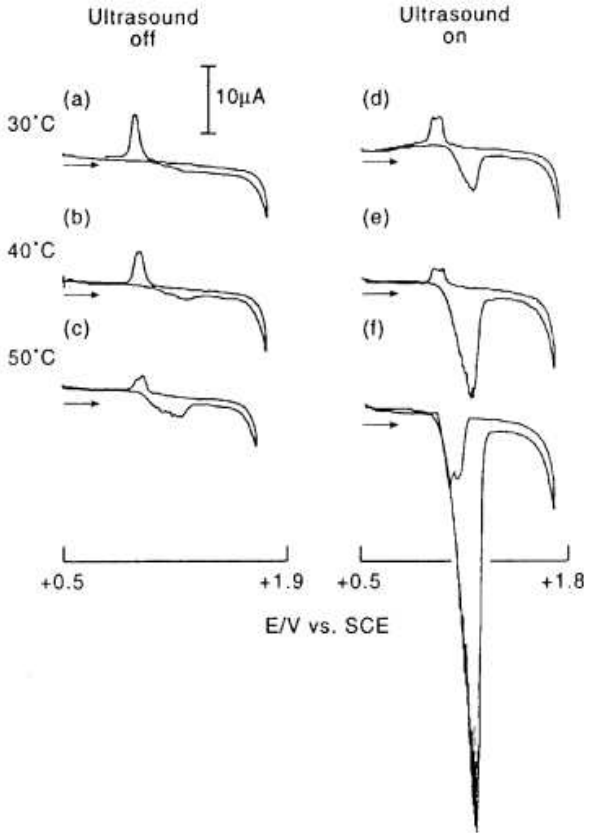

Figure 6. Cyclic voltammograms for the oxidation of a 1mm diameter gold electrode in aqueous 1M $HClO_4$ at temperatures of 30, 40 and 50^0 C under silent conditions (a-c) and in the presence of ultrasound (d-f) (20 kHz, 40 W cm^{-2}, scan rate 100 mVs^{-1}).

3. The Influence of Ultrasound on Electrode Processes

The potential of ultrasound to enhance the rate or to alter the pathway of heterogeneous chemical reactions has been exploited by workers in organic and inorganic electrochemistry for many years [43-45]. The nature of the processes involved varies from the surface activation of solid reactants to the generation of active radical species and to great changes in the transport leading to new dominant reaction pathways and is in many cases not fully known.

The electrode reactions may be grouped into two categories:

- the surface confined reactions, such as the heterogeneous electron transfer and surface catalytic or adsorption steps,
- the large group of homogeneous reactions which may be coupled to the electrode process by mass transport.

Ultrasound may affect chemical reaction which occur in a simple liquid phase mainly via four possible routes:

⇒ enhanced mass transport;
⇒ thermal fluctuation caused by cavitation or “hot spots”;
⇒ the formation of highly reactive intermediates, e.g., radical species in the solution near a “hot spots”;
⇒ strong shear forces which can effect large molecules, particles or surfaces.

The sonication of systems comprising simple one-electron transfer reactions, in aqueous solutions, e.g. $Ru(NH_3)_6^{3+/2+}$, $Eu^{3+/2+}$ [17] and $Fe^{3+/2+}$ [46, 47] showed that even with high intensity ultrasound the deviation of the measured rate constants for heterogeneous electron transfer at the electrode-solution interface remain within the experimental error unaffected. Data on other important and more complex reaction, such as the H_2 and the O_2 evolution processes would be interesting for comparison. Gas evolution processes in the presence of ultrasound were studied very early in the history of sonoelectrochemistry [48-51] and a significant depolarisation effect has been reported. In the presence of ultrasound, gases appear to be very effectively removed from the electrode surfaces.

Until recently there have been relatively few studies on the effect of ultrasound on electrode reaction mechanisms involving homogeneous as well as heterogeneous chemical steps. The Kolbe reaction [52, 53] and an electrochemically induced aromatic substitution reaction [54] were found to benefit from or be affected by the application of ultrasound, and in the case of the Kolbe reaction a significant change in the reaction pathway in the presence of ultrasound was reported. Different reaction pathways exist under different kinetic regimes, and adsorption and other electrode phenomena are known to be important, all of which might be influenced to differing extents by ultrasound. Scheme 1 gives the usual and plausible scheme to account for the range of products obtained from electrooxidation of a typical carboxylate anion. The general mechanisms break down into a

pathway involving one electron per molecule of starting material, giving products from the radical intermediate, and a two electron pathway per starting molecule, giving products from an intermediate cation.

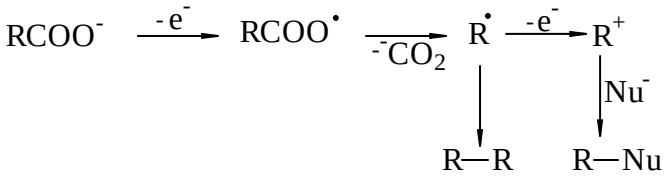

Scheme 1.

The Coventry group chose to examine a system almost at balance where both pathways operate [55] in order to best identify any sonoelectrochemical effect on mechanism [52]. Table 1 shows product ratios (by GLC) from the electrooxidation of partially neutralised cyclohexanecarboxylate in

Table 1.

Electrooxidation of cyclohexane carboxylate[a,b]

Product	**Amount [%]**	
	without ultrasound	with ultrasound
Bicyclohexyl	49.0	7.7
Cyclohexane	1.5	2.6
Cyclohexene	4.5	32.4
Methoxy-cyclohexane	24.9	34.3
Methyl-cyclohexanoate	17.0	2.5
Cyclohexanol	2.1	6.8

[a] - relative product ratios after the passage of 2,2 F· mol^{-1}

[b] - average cell potential to maintain current density of 200 mA cm^{-2} is 8,3 V in the absence and 7,3 V in the presence of ultrasound

methanol at Pt electrode, at a current density of 200 mA·cm^{-2} . The column 2 (tab. 1) shows the effect on product ratio of ultrasonic irradiation from a Kerry Pulsatron cleaning bath (35 kHz, 50 W) during electrolysis. The preponderance of cyclohexene over cyclohexane shows its formation by proton loss from the carbocation intermediate, since free-radical routes to cyclohexane also produce cyclohexane in equal if not greater amounts [55, 56]. It is also noted in column 2 that the parasitic formation of methyl cyclohexanoate ester is lessened under ultrasound, perhaps suggesting enhanced adsorption of carboxylate with concomitant suppression of solvent discharge. This has precedent since ultrasound is thought to enhance adsorption phenomena in dissolving-metal chemical reactions [57].

Other procedural benefits in the electrooxidation of cyclohexane carboxylate under ultrasound include a drop in overall cell voltage from 8.3 to 7.3 V needed to maintain the same cd for the galvanostatic system. The reaction approached completion in a shorter time-span despite the apparent switch to the two-electron process, suggesting diminution of parasitic processes.

Overall, ultrasound appears to favour the two-electron mechanism, but the greatest effect of sonication upon product distribution was the substantial enhancement of alkene formation.

Table 2 shows relative product ratios for electrooxidation of phenylacetate, where is no proton-loss pathway from the intermediate carbocation, in similar conditions to those used for cyclohexane carboxylate but employing 100 $mA \cdot cm^{-2}$ [58].

Table 2.

Electrooxidation of Phenylacetate[a,b]

Product	**Amount [%]**			
	without ultrasound		with ultrasound	
	no pyridine	13% pyridine	no pyridine[c]	13% pyridine
Bibenzyl	0	59.8	52.7	51.3
Toluene	0	0.4	3.1	1.5
Benzyl methyl ether	0	21.1	32.3	27.8
Methyl phenylethanoate	0	10.2	6.2	4.2

[a] - relative product ratios after the passage of 1.1 $F \cdot mol^{-1}$

[b] - average cell potential to maintain current density of 100 mA cm^{-2} is 7.9 V in the absence and 6.6 V in the presence of ultrasound

[c] - a fine white powder precipitate was formed in these conditions

Because the simple electrolysis of the partially neutralised salt in methanol causes a very rapid increase in applied cell voltage, due to the coating of the anode with a pale-coloured material that causes the reaction to cease, is necessary to add pyridine (up to 50% v/v) to keep the electrode clean, presumably by simply solubilizing the inhibiting layer. A major component of the remaining (8%) material is benzaldehyde, a persistent by-product of arylacetate electrooxidations whose exact mechanistic origin remains uncertain.

The column 3 (table 2) shows the effect of ultrasound upon the product ratio from methanol / pyridine; the results suggest only a slight shift towards the two-electron products, but with an overall diminution of solvent discharge and side reactions. Phenylacetate electrooxidation, however, is known to favour the one-electron route to bibenzyl in a wide range of conditions [59], and to be much less sensitive to mechanistic switches by

manipulation of parameter than is cyclohexane carboxylate electrooxidation [56]. This trend remains even under ultrasound.

The column 4 (table 2) shows the product ratios under ultrasound in the absence of pyridine; there is the same trend with the electrolyse without sonication in the presence of 13% pyridine, namely a slight shift from one-electron towards two-electron pathway, although here there seems to be a higher yield of benzaldehyde-derived by-products.

The most significant factor is that there is no evidence of electrode fouling, and the reaction maintains cd at a steady and lower voltage. In addition, a fine white powder (a polymer containing aromatic rings as well as two types of methylene groups and an aliphatic ester carbonyl) was formed during the electrolysis, which was isolated by filtration (14%). It may be supposed that enhanced mass transport under ultrasound and the abrasion effect near the electrode surface has swept the inhibiting species into solution, thus keeping the electrode clean. There is much less of this powder under ultrasound in the presence of pyridine, suggesting that it is indeed solubility factors that demand the use of the cosolvent in silent conditions.

The obviation of pyridine under ultrasound represents a significant procedural enhancement since its presence considerably hampers work-up, and also has environmental implications. A further feature is again the lowering of the applied cell voltage from 7.9 to 6.6 V under ultrasound, representing an energy saving.

The same conclusions were obtained by Japanese workers [60] who employed crossed Kolbe electrolyses of phenylacetates, succinates, variously deuterated and palmitates.

The Coventry group has also examined the behaviour of p-chlorophenyl acetate electrooxidation under ultrasound [58]. This substrate is known to markedly favour the two-electron mechanism [56], showing that the choice of reaction pathway is more dependent on substrate nature than upon manipulation of electrolysis parameters. A further feature of this system is the appreciable yield of p-chlorobenzaldehyde-derived products. The sonication produces little change in relative product ratio. An unexpected advantage of sonication was found here. There was no formation of polymeric coating on the anode, tending to confirm that the free para-position of unsubstituted phenylacetate is necessary for production of the inhibitory species; instead the cathode became coated in a black deposit as the electrolysis proceeded. It is possible to envisage a reductive cleavage process occurring on the protonated acid molecule with loss of chloride ion to yield species that could polymerise on the cathode.

The origin of ultrasonic effect upon carboxilate electrooxidation is not straightforward to establish in view of complex mechanism of the reaction with different kinetic regimes, the loss of carbon dioxide, and also the role of

adsorption and other electrode phenomena. It has also been suggested that the second electron transfer to give the carbocation need not occur in bulk solution, although this requires methoxyradicals from solvent discharge or other species to act as redox mediators in the solution phase [61].

The Coventry group also examined the use of higher ultrasonic frequencies (500 and 800kHz) [5]. It would seem that higher frequencies are more suitable for the insonation of these reaction systems, although this is not straightforward to explain since cavitation phenomena, effects of acoustic impedance, cell geometry implications and other factors all change with frequencies.

Cavitation is substantially more difficult to induce at higher frequencies and since these experiments were performed at the same ultrasonic power, suggests that the observed sonoelectrochemical benefits are not cavitational in origin. However, it may be simply an effect of the shorter wavelength at higher frequency. Thus in the 20 - 60 kHz frequency region, the half-wavelength is of the order of centimetres so that only a limited number of nodes and antinodes span the dimensions of the electrolysis cell used; in the 500 -800 kHz region, however, the distance between nodes and antinodes is only in the order of millimetres. If, as seems likely from electroanalytical studies, certain sonoelectrochemical benefits originate from nodes or positive regions of the wave, but antinodes or negative regions of wave do not interfere, then simplistically an increase in the number of nodes within the active region of the cell will produce more uniform and effective sonoelectrochemical phenomena.

One of potentially most useful preparative-scale electroreduction reactions involves the transformation of aryl nitrocompounds to amino derivatives 62-67], but in practice this is a complicated system in which there are a number of competing reactions including, for example hydrodimerization to hydrazo compounds [14a, 68].

A schematic description of the electrochemical reduction of nitrobenzene, a model voltammetric system, as proposed by Laviron et al. [69] is given in scheme 2. At pH 13, in aqueous media, the first reduction is followed by a protonation step. The second reduction then leads, after loss of OH^-, to nitrosobenzen as an intermediate. After further transfer of two electrons and uptake of two protons, the product phenylhydroxyamine is generated.

Side products due to a condensation reaction may also be observed under certain conditions [70].

Despite the multipathway nature of nitroelectroreductions, there appears to be no further reports of sonoelectrochemical studies on this type of reaction.

The nitrobenzene radical-anion is known to be only metastable in alkaline solution due to slow disproportionation [71]. This and the fact that certain electrode materials appear to allow catalysis [72,73] of the decay of

the nitrobenzene radical-anion allow several aspects of the effect of ultrasound to be studied.

Scheme 2. Reaction pathway for the electrochemical reduction of nitrobenzene in aqueous media at pH 13

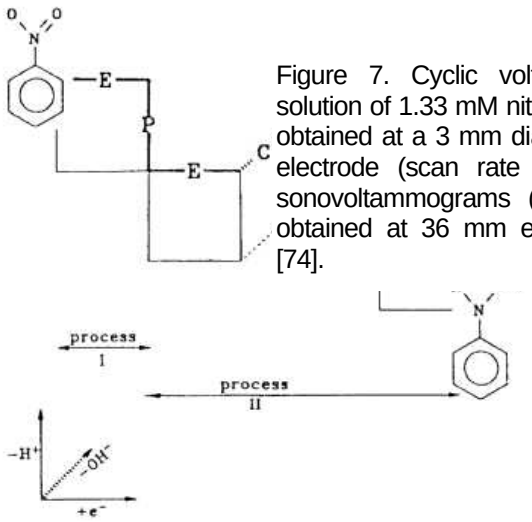

Figure 7. Cyclic voltammograms (a,b) of a solution of 1.33 mM nitrobenzene in 0.1 M NaOH obtained at a 3 mm diameter glassy carbon disk electrode (scan rate 50 mVs^{-1}, T=25^{0}C) and sonovoltammograms (c,d) (20mVs^{-1}, 25Wcm^{-2}) obtained at 36 mm electrode to horn distance [74].

In voltammetric studies in 0.1 M NaOH, glassy carbon electrodes

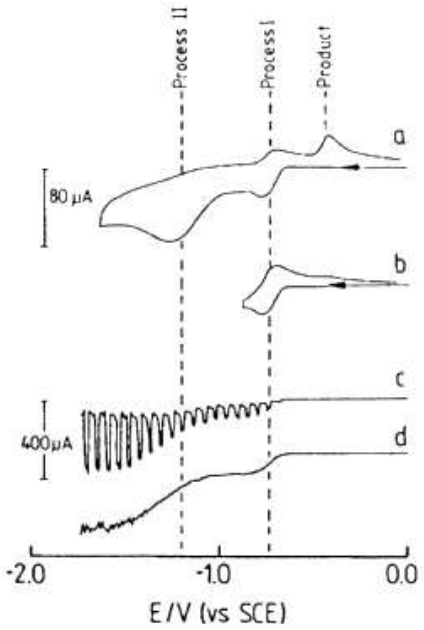

allow well-defined voltammograms to be recorded both under silent conditions and under sonication and over a wide potential range [74]. In fig. 7 it may be observed a reversible one-electron reduction (process I) at $E_{1/2}$ = - 0.73 V/SCE followed by an overall three-electron reduction (process II) with a peak potential E_p = -1.25 V/SCE. A product signal at E_p = -0.43 V/SCE can be identified as a two-electron / two proton oxidation process from phenylhydroxylamine to nitrosobenzene [73]. The sonovoltammograms (fig. 7 c,d) using pulsed (providing important additional information, e.g. on back-ground processes [75, 76]) and continuous ultrasound are in agreement both with the one- and the three-electron nature of the reduction process. The variation of the distance between horn and electrode allowed almost linear variation of the average diffusion layer thickness δ from 1.3 to 5.8 μm. The number *n* of electron transferred, calculated using the limiting currents for the reduction of nitrobenzene, remains in good approximation, constant at one (process I) and three (process II) without any obvious effect of the soundfield.The reduction of nitrobenzene on gold electrodes occurs with a mechanism of considerably high complexity. Voltammetric studies on mercury and on gold electrodes with a single four- electron reduction process for nitrobenzene in aqueous alkaline media have been reported [77,78], and a surface catalytic process was suggested involving the protonation of the adsorbed nitrobenzene radical anion [79].

Figure 8 (a) shows that upon continuos cycling, a complex change occur: a dramatic increase in current for process I accompanied by a shift of the peak potential for process II towards more positive potentials. After only 5 cycles one reduction process (of the four electron) is observed, followed by a new and uncharacterised reduction peak at E_p =1.29 V / SCE. Figure 8 (b,c) demonstrates the change in mechanism using gold rotating disk voltammetry. The negative scan direction consists of the anticipated $1e^-$ and $3e^-$ processes, but the positive scan direction exhibits only one $4e^-$ wave. This phenomenon has been described [80] and attributed to a change of the gold surface properties. The sonovoltammograms (fig.8 d-f) exhibit similar behaviour, although at decreasing diffusion layer thickness the effect of the electrocatalyst diminishes. There are two possible mechanisms likely responsible for this effect. On the one hand the loss of catalyst from the electrode surface due to ultrasonic cleaning or, alternatively, a purely kinetic effect due to high mass flux. In the presence of intense ultrasound (or a high rate of mass transport), the homogenous reaction pathway (one-reduction) could out-run the rate of the heterogeneous reaction pathway (chemical step such as protonation) hence, a different mechanistic pathway would dominate the overall reaction. Marken et al. [74] proposed a simplified reaction scheme which supposes that the nitrobenzene radical-anion, formed by one-electron reduction of nitrobenzene at the gold surface electrode, than diffuse away, or

after surface catalytic protonation, takes up three more electron before diffusing into the bulk solution. Their kinetic results, obtained for the reduction of nitrobenzene in aqueous NaOH, suggests that sonovoltammetry may be applied in mechanistic studies using the concepts which apply to rotating disk voltammetry, such as an average uniform diffusion layer and the reaction layer concept.

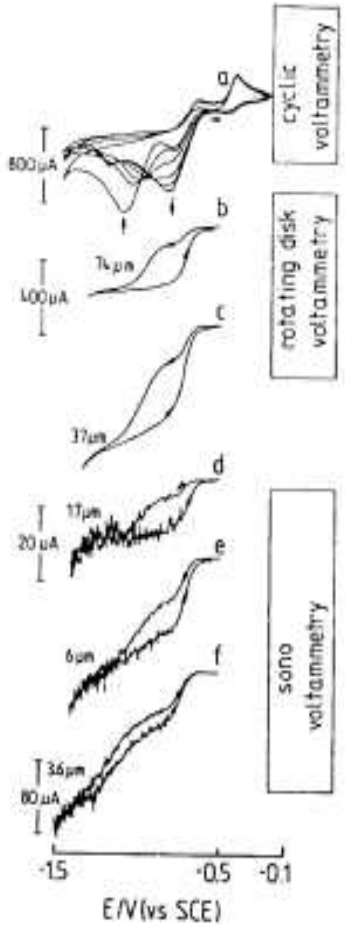

Figure 8. Cyclic voltammograms (a) of a solution of 10 mM nitrobenzene in 0.1 M NaOH obtained at a 7 mm diameter gold electrode (scan rate 100 mVs^{-1} , $T=25^0C$). Rotating disk voltammograms (b,c) and sonovoltammograms (d-f) of 1 mM nitrobenzene in 0.1 M NaOH obtained at a 7 mm (b,c) and 1mm (d,f) diameter gold electrode (scan rate 20 mVs^{-1}) with (d,e) 37mm and (f) 4mm electrode to horn separation and (d) 15 W cm^{-2} , (e,f) 30 Wcm^{-2}. The average diffusion layer thickness obtained are indicated [74].

Recent works from the group at the Tokyo Institute of Technology have been specifically directed at ultrasonic control of product selectivity in electroreductions. Thus the electroreduction of benzaldehydes [81-83] can lead to either the hydrodimer in a one-electron per substrate molecule process, or to the benzyl alcohol in a two-electron process, as indicated in scheme 3.

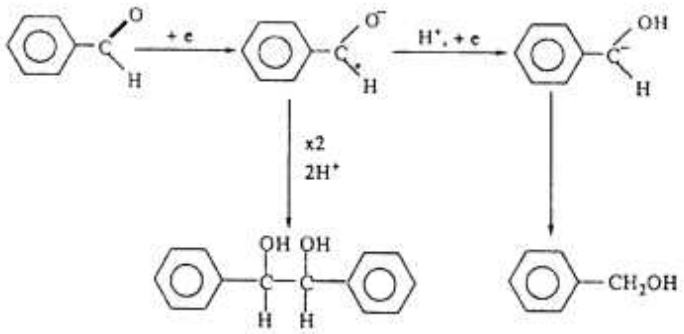

Scheme 3.

Using a lead cathode in dilute methanolic sulphuric acid at constant current of 20 mA cm^{-2}, the benzyl alcohol was the major product from unstirred solution, while mechanical stirring reversed the position to favour the hydrodimer. However, ultrasonic irradiation from a cleaning bath (100 W, 36 kHz) so strongly favoured the hydrodimer that the alcohol was barely evident. The current efficiency for reduction and product selectivity for the corresponding hydrodimeric products were increased with increasing ultrasound oscillating power in different manners on the cathode. The lateral cathodes could exhibit the effect at relatively low ultrasonic powers compared with the sectional one (see fig. 9).

In addition, higher efficiency and selectivity were obtained at the lateral loop cathode than at the node one (see tab.3). Interfacial layers of the lateral electrodes (LN and LL cathodes) are reciprocally sheared by the parallel vibration, while those of the TSL cathode are cyclically compressed and expanded. In a sense, the vibrating lateral electrode may affect an electrochemical reaction in a way a little similar to a rotating cylindrical electrode. It is suggested that a reciprocal shearing phenomenon in the ultrasonically vibrating lateral cathode interfaces causes the clear increase in efficiency and selectivity as well as the cyclic compression/ expansion phenomenon in the ultrasound irradiated and oscillating sectional cathode interfaces. On another basis, the ultrasonic effects observed on the lateral electrodes may be caused by a peculiar interaction of stationary surface waves occurring on the electrode (solid) with the solution (liquid), though the physical mechanism has not been verified at present.

The reduction of benzoic acid at a lead cathode in an aqueous 0.05M H_2SO_4/0.2 M citric acid solution gives not the corresponding hydrodimeric product but hydro-monomeric 2- and 4- electroreduction products such as benzaldehyde and benzyl alcohol. Here ultrasound produces some switch towards the two-electron product; thus in all studied

cases the authors found that ultrasound favoured the process involving the smaller number of electrons per molecule [82]. This is opposite to the sonoelectro-chemical effect seen in carboxylate electrooxidation [52,58] where the process involving the greater of electrons was favoured by ultrasound, and shows that in the present state-of-the-art generalisations are inappropriate. The nature of the electrochemical system is an important consideration in the establishment of sonoelectrochemical phenomena.

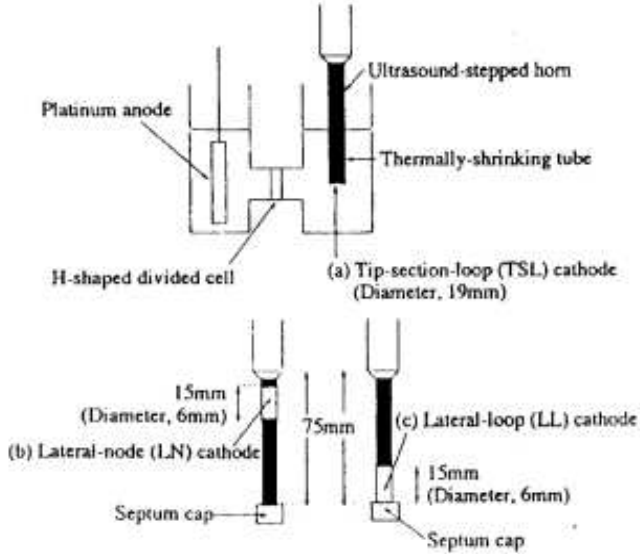

Figure 9. Ultrasound vibrating electrodes [83]

Table 3.
Electroreduction of 40 mM benzaldehyde in 0.25 M H_2SO_4-50% CH_3OH catholyte on the tip-section loop cathode an ultrasound stepped horn [83].

Ultrasound power [W]	Current density [mA cm^{-2}]	Current efficiency [%]	Selectivity for hydrodimer [%]
0	20	5	29
50	20	26	36
0	40	3	39
80	40	25	47
0	80	4	46
50	80	18	61

The group at Tokyo Institute of Technology have also examined the electro-reduction of methyl and benzyl halides at a reactive tin and respectively, lead cathodes [5,82]. The first example is a different type of electrochemical system in which the cathode is a reactive metal. For

reduction of CH_3I in DMF/Bu_4NClO_4 at room temperature and 10 mA cm^{-2}, an unstirred reaction gave 1:10 ratio distannane to stannane, while ultrasound, from a 20 kHz probe, increased the dimmer to give 1:5 ratio.

CONCLUSIONS

Ultrasonic irradiation produces a number of significant benefits in a wide range of electrochemical systems. Insonation of an electrosynthetic reaction can produce altered product ratios, greater efficiencies, lessened cell power requirements and a diminution of detrimental electrode fouling. The technique also provide a probe into fundamental physico-chemical principles of electrolyte solutions, electrode phenomena, and associated processes.

The best established effect of ultrasound in electrochemistry is the diminution of the diffusion layer and the enhanced limiting currents so produced. This is of benefit towards sensitivity improvement in electrochemical sensors, and is also the origin of many sonoelectrochemical phenomena. Ultrasound also affects electrode surfaces and has a beneficial effect during electrolysis.

It is hoped that applied as well as fundamental aspects of sonoelectrochemistry will develop over the next decade or so similar to the development in sonochemistry, in general.

REFERENCES

[1] T.J. Mason, J.P. Lorimer, Sonochemistry, Theory, Applications and Uses of Ultrasound in Chemistry, Ellis Horwood Publishers, Chichester, 1988
[2] P. Reisz, Advances in Sonochemistry, ed. T.J. Mason, JAI Press, London, 1991, vol. 2
[3] K.S. Suslick, S.B. Choe, A.A. Chichowlas, M.W. Grimstaff, Nature, 1991, **353**, 414
[4] T.H. Hyeon, M.M. Fang, K.S. Suslick, J. Am. Chem. Soc. 1996, **118**, 5492
[5] D.J. Walton, S.S. Phull, Sonoelectrochemistry, Advances in Sonochemistry, ed.T.J. Mason, JAI Press, London, 1996, vol. 4
[6] S. Moon, L. Duchin, J.V. Cooney, Tetrahedron Lett., 1979, **20**, 3917
[7] T.J. Mason, Practical Sonochemistry. A users guide to applications in chemistry and chemical engineering. Ellis Horwood Publishers, Chichester 1991
[8] T. Ando, P. Bauchat, A. Foucaud, M. Fujita, T. Kimura, H. Sohmiya, Tetrahedron Lett., 1991, **32**, 6371
[9] M.J. Dickens, J.L. Luke, Tetrahedron Lett., 1991, **32**, 4709
[10] J. Einhorn, C. Einhorn, J.L. Luke, Tetrahedron Lett., 1988, **29**, 2183
[11] T.J. Mason, Chemical Society Reviews, 1997, **26**, 443
[12] R.G. Compton, R.A.W. Dryfe, Prog. Reaction Kinetics, 1995, **20**, 245

[13] T. Ando, S. Sumi, T. Kawate, J. Ichihara, T. Hanafusa, J. Chem. Soc. Chem. Commun., 1984, 439
[14] a) C. Amatore, Organic Electrochemistry, (Ed. H. Lund, M.M. Baizer), Marcel Dekker, New York, 1991, b) C. Amatore, J.M. Saveant, J. Electroanal. Chem., 1981, **123**, 189
[15] P.H. Rieger, Electrochemistry, 2nd ed., Chapman & Hall, New York, 1994
[16] R.G. Compton, J.C. Eklund, S.D. Page, T.J. Mason, D.J. Walton, J. Appl. Electrochem., 1996, **26**, 775
[17] F. Marken, J.C. Eklund, R.G. Compton, J. Electroanal. Chem., 1995, **395**, 335
[18] F. Marken, R.G. Compton, S.G. Davies, S.D. Bull, T. Thiemann, M. L. Melo, A.C. Neves, J. Castillo, C.G. Jung, A. Fontana, J. Chem. Soc. Perkin Trans., 1997, **2**, 2055
[19] A.J. Bard, L.R. Faulkner, Electrochemical Methods, J.W.Wiley & Sons, New York, 1980
[20] R.G. Compton, J.C. Eklund, S.D. Page, J. Phys. Chem., 1995, **99**, 4211
[21] P.J. Daly, D.J. Page, R.G. Compton, Anal. Chem., 1983, **55**, 1191
[22] R.L. McCreery in A.J. Bard (Ed.), Electroanalytical Chemistry, Marcel Dekker, New York, 1991, vol. 17, p. 221
[23] M.J. Weaver, J. Phys. Chem., 1980, **84**. 568
[24] R.G. Compton, J.C. Eklund, F. Marken, Electroanalysis, 1997, **9(7)**, 509
[25] V.G. Levich, Physicochemical Hydrodynamics, Prentice Hall, Englewood Cliffs, NJ, 1962
[26] W. Le Mars Nyborg, Physical Acoustics, (Ed. W.P. Mason), Academic Press, New York, 1965, p. 265
[27] H.A.O. Hill, Y. Nakagawa, F. Marken, R.G. Compton, J.Phys. Chem, 1996, **100**, 17395
[28] C.M.A. Brett, A.M.O. Brett, Electrochemstry, Oxford University Press, Oxford, 1993, p. 93
[29] F. Barz, C. Bernstein, W. Vielstich, Adv. Electrochem. Electrochem. Engineer. 1984, **13**, 261
[30] S.A. Perusich, R.C. Alkire, J. Electrochem. Soc., 1991,**138**, 700; 708
[31] J. Reisse, H.H. Francois, J. Vandercammen, O. Fabre, A. Kirsch-de Mesmaeker, C. Maerschalk, J.L. Delplancke, Electrochim. Acta, 1994, **39**, 37
[32] R.G. Compton, J.C. Eklund, F. Marken, D.N. Waller, Electrochim. Acta, 1996, **41**, 315
[33] H. Huck, Ber. Bunsenges. Phys. Chem., 1987, **91**, 648
[34] C.R.S. Hagan, L.A. Coury Jr., Anal. Chem., 1994, **66**, 599
[35] W.J. Tomlinson, Adv. Sonochem, 1990, **1**, 173
[36] A. Henglein, D. Herburger, M. Gutierrez, J.Phys. Chem., 1992, **96**, 1126
[37] R.G. Compton, J.C. Eklund, S.D. Page, G.H.W. Sanders, J. Booth, J.Phys. Chem., 1992, **94**, 12410
[38] F. Marken, S. Humbhat, G.H.W. Sanders, R.G. Compton, J. Electroanal. Chem. 1996, **414**, 95
[39] N.A. Madigan, C.R.S. Hagan, L.A. Coury Jr., J. Electrochem. Soc, 1994, **141**, 23
[40] U. Akbulut, L. Toppare, B. Yurrtas, Polymer, 1986, **27**, 803

[41] S. Osawa, M. Ito, K. Tanaka, J. Kuwano, Synthetic Metals, 1987, **18**, 145
[42] J. Klima, C. Bernard, J. Electroanal. Chem.,1999, **462**, 181
[43] a) S.V. Ley, C.M.R. Low, Ultrasound in Synthesis, Springer, Berlin, 1989, b) Current Trends in Sonochemistry (Ed. G.J. Price) the Royal Society of Chemistry, London, 1992
[44] Ultrasound: Its Chemical, Physical and Biological Effects (Ed. K.S. Suslick) VCH Weinheim, 1988
[45] Sonochemistry: the Uses of Ultrasound in Chemistry (Ed. T.J. Mason) the Royal Society of Chemistry, London, 1990
[46] A. Fontana, The 5th Meeting of the European Society of Sonochemistry, 7-11 July 1996, Cambridge, U.K.
[47] L.A. Coury Jr., The 5th Meeting of the European Society of Sonochemistry, 7-11 July 1996, Cambridge, U.K.
[48] J.O'M. Bockris, A.K.N. Reddy, Modern Electrochemistry, vol 2, Plenum, New York, 1970, 1170
[49] G. Schmid, L. Ehret-Stuttgart, Z. Elektrochem. 1937, **43**, 597
[50] a)F. Cataldo, J. Electroanal. Chem.,1992, **332**, 325; b) D.J. Walton, L.D. Burke, M.M. Murphy, Electrochim. Acta, 1996, **41**, 2747
[51] F. Marken, Q. Hong, R.G. Compton, J. Electrochem. Soc., 1997,**144 (9)**, 3019
[52] D.J. Walton, A. Chyla, J.P. Lorimer, T.J. Mason, G.J. Smith, J. Chem. Soc., Chem. Commun., 1989, 603
[53] D.J. Walton, S.S. Phull, D. Colton, P. Richards, A. Chyla, T. Javed, L. Clarke, J.P. Lorimer, T.J. Mason, Ultrason. Sonochem. 1994, **1**, S 23
[54] C. Degrand, J. Chem. Soc., Chem. Commun., 1986, 1113
[55] G.E. Hawkes, J.H.P. Utley, G.B. Yates, J. Chem. Soc., Perkin Trans., 1976, **2,** 1709
[56] L. Eberson, J.H.P. Utley, (ed. M.M. Baizer, H. Lund) Organic Electrochemistry, (2nd Ed.) Marcel Dekker, 1982
[57] S.L. Luche, C. Einhorn, J. Einhorn, Tet.Lett., 1990, **31**, 4125
[58] D.J. Walton, A. Chyla, J.P. Lorimer, T.J. Mason, Synth. Commun. 1990, **20**, 1843
[59] J.P. Coleman, R. Lines, J.H.P. Utley, B.C.L. Weedon, J. Chem. Soc., Perkin Trans., 1974, **2,** 1064
[60] M. Tashiro, H. Tsuzuki, H. Goto, S. Makata, Chemistry Express, 1991, **6**, 403
[61] Y.B. Vasiliev, V.A. Grinberg, J. Electroanal. Chem., 1991, **308**, 1
[62] V. Danciu, A-M. Martre, P. Pouillen, G. Mousset, Electrochim. Acta 1992, **37**, 1993
[63] V. Danciu, A-M. Martre, P. Pouillen, G. Mousset, Electrochim. Acta 1992, **37**, 2001
[64] A-M. Martre, V. Danciu, G. Mousset, Can. J. Chem. 1993, **71**, 1136
[65] A-M. Martre, G. Mousset, V. Cosoveanu, V. Danciu, New J. Chem. 1994, **18**, 1221
[66] A-M. Martre, G. Mousset, V. Cosoveanu, V. Danciu, Can. J. of Chem., 1996, **74**, 1409
[67] A-M. Martre, G. Mousset, V. Danciu, V. Coºoveanu, Electrochim. Acta, 1998, **43 (21-22**), 3217

[68] S. Torii, Electroorganic Syntheses, Part 2 Electroreductions, Kodansha 1986
[69] E. Laviron, A. Vallat, R. Meunier-Prest, J. Electroanal. Chem., 1994, **379**, 427
[70] H.Lund, Organic Electrochemistry, (Ed. H. Lund, M.M. Baizer), Marcel Dekker, New York, 1991, p. 411
[71] B. Kastening, Electrochim. Acta, 1964,**9**, 241
[72] C. Nishihara, H. Shindo, J. Electroanal. Chem., 1987, **221**, 245
[73] I. Rubinstein, J. Electroanal. Chem., 1985, **183**, 379
[74] F. Marken, S. Kumbhat, G.H.W. Sanders, R.G. Compton, J. Electroanal. Chem., 1996, **414**, 95
[75] H.D. Dewald, B.A. Peterson, Anal. Chem., 1990,**62**, 679
[76] R.G. Compton, F.M. Matysik, Electroanal., 1996, **8**, 218
[77] P. Zuman, Z. Fijalek, J. Electroanal. Chem.,1990, **296**, 583
[78] A. Cyr, P. Huot, G. Belot, J. Lessard, Electrochim. Acta, 1990, **35**, 147
[79] B. Kastening, L. Holleck, J. Electroanal. Chem., 1970, **27**, 355
[80] C. Nishihara, H. Shindo, J. Eletroanal. Chem., 1987, **221,** 245
[81] Y. Ono, Y. Nishiki, T. Nonaka, Chem. Lett. 1994, 1623
[82] K. Matsuda, M. , T. Nonaka, Chem. Lett. 1994, 1619
[83] M. Atobe, T. Nonaka, J. Electroanal. Chem.,1997, **425**, 161

STUDIA UNIVERSITATIS BABEŞ-BOLYAI, CHEMIA, XLIV, 1-2, 1999

LEACHING OF LOW-GRADE CHALCOCITE-COVELLITE-CHALCOPYRITE ORE WITH SULPHURIC ACID. THE INFLUENCE OF THE OXIDIZING AGENTS ON THE KINETICS OF COPPER LEACHING

CAMELIA LUMINITA VARGA[1], LIVIU ONICIU[2], IOAN BALDEA[2]

[1] *Department of Chemistry, North University of Baia Mare, 4800 Baia Mare, Romania*
[2] *Department of Physical Chemistry, "Babes-Bolyai" University, 3400 Cluj-Napoca, Romania*

ABSTRACT. The leaching characteristics of low-grade chalcocite-covellite-chalcopyrite ore from the Cavnic Mine were investigated in sulphate medium. The chemical composition of ore was: 0.37% Cu, 1.50% Zn, 2.00% Pb, 0.38 g/t Au, 45.70 g/t Ag, 7.52% Fe, 7.92% S and 53.40% SiO_2. During the experiments, the following parameters were modified: the leaching time, the leaching temperature and the quantity of ferric sulphate and of oxygen as oxidizing agents. From the shape of the leaching curves, three stages of the process were observed. The apparent activation energy depends on the period of leaching as well as on the presence of ferric ion and oxygen as oxidizing agents in the leaching medium. The study intends to establish the rate controlling reaction step, according to both the activation energies, and the analytical expressions for each period.

INTRODUCTION

In the last years there has been a renewed interest for copper recovery by processing the low-grade ores or complex ores with hydrometallurgical methods. The most common hydrometallurgical processes for copper recovery are based on the solubilization in sulphuric medium. The sulphate-based processes exhibits some potential advantages over the others systems because the leaching chemistry is generally simpler and better understood, and copper recovery by solvent extraction and electrowinning from sulphate medium is easier. The dissolution of copper from the low-grade chalcocite-covellite-chalcopiryte ore involves a complex mechanism. The most studied copper mineral is chalcopyrite, which in sulphate medium leaches by a parabolic kinetic [1-3], caused by the progressive formation of a sulphur layer or other products at the external surface. It behaved as passivation layer.

From the kinetic and surface science studies, the following reaction sequence has been proposed to describe the oxidative leaching and passivation of chalcopyrite in sulphate medium [3]:

$$CuFeS_2 \longrightarrow Cu_{1-x}Fe_{1-y}S_2 + x\,Cu^{2+} + y\,Fe^{2+} + 2(x+y)\,e^- \text{ (fast)}, \quad y >> x,\ x + y \approx 1 \qquad (1)$$

$$Cu_{1-x}Fe_{1-y}S_2 \longrightarrow Cu_{1-x-z}S_2 + z\,Cu^{2+} + (1-y)\,Fe^{2+} + 2(z+1-y)\,e^- \text{ (slow)}, \qquad (2)$$

$$Cu_{1-x-z}S_2 \longrightarrow (1-x-z)z\,Cu^{2+} + 2\,S^{2+} + 2(1-x-zy)\,e^- \text{ (the slowest)}. \qquad (3)$$

Within the fast initial period, the iron leaches preferentially as compared to copper. An intermediate disulphide phase is formed, $Cu_{1-x}Fe_{1-y}S_2$, where $y >> x$ and $x + y \approx 1$. In the second slow stage, the disulphide phase is further oxidizer to form copper polysulphide, $Cu_{1-x-z}S_2$, alternatively expressed as CuS_n where $n=2/(1-x-z)$. The copper polysulphide acts on chalcopyrite as a passive layer. The rate controlling reaction step was considered the slow decomposition of the copper polysulphide to cupric ions and elemental sulphur, with the polysulphide chains restructuring to form S_8 rings. The elemental sulphur is porous enough that the rate is not limited by reactant/ product diffusion through sulphur unless the sulphur melts during leaching when higher temperatures are used.

The attempts to dissolve of chalcocite with acidic ferric sulphate solutions has proved that the process occurs in two stages [4-6]:

$$Cu_2S + 2\,Fe^{3+} = Cu^{2+} + CuS + 2\,Fe^{2+}, \qquad (4)$$

$$CuS + 2\,Fe^{3+} = Cu^{2+} + S + 2\,Fe^{2+}. \qquad (5)$$

Afterwards, in presence of the ferric sulphate added to leaching of natural chalcocite the following sequence of reactions has been identified [7]:

$$5\,Cu_2S = 5\,Cu_{1.8}S + Cu^{2+} + 2\,e^-, \qquad (6)$$

$$5\,Cu_{1.8}S = 5\,Cu_{1.2}S + 3\,Cu^{2+} + 6\,e^-, \qquad (7)$$

$$5\,Cu_{1.2}S = 5\,S + 6\,Cu^{2+} + 12\,e^-. \qquad (8)$$

The intermediate product $Cu_{1.8}S$, digenite, was found to be rapidly formed. At 30°C and 48x65 mesh Cu_2S, particles were completely covered to $Cu_{1.8}S$ after 3.5 minutes in 0.03M ferric sulphate solutions. The final product at 30°C, and low ferric sulphate concentrations, was blue remaining covellite, $Cu_{1.2}S$, which leaches at a much slower rate. Normal covellite, CuS, was never observed as a product of reaction at 30°C. At higher temperature values (75°C) the final product was cupric ion.

The kinetics of synthetic covellite dissolution in aqueous acidic ferric sulphate solutions reveals a linear dependence of dissolved copper concentration upon the leaching time, with the exception of the initial induction period which was very short [8-10].

EXPERIMENTAL

The investigations were carried out by using samples of low-grade chalcocite-covellite-chalcopyrite ore obtained from the Cavnic Mine. The chemical and mineralogical composition of the investigated ore is given in table 1 and table 2, respectively.

Table 1.

The chemical composition of low-grade ore.

Element	Cu (%)	Pb (%)	Zn (%)	Au (g/t)	Ag (g/t)	Fe (%)	S (%)	SiO_2 (%)
Cavnic Mine Ore	0.37	1.50	2.00	0.38	45.70	7.52	7.92	53.40

The fraction 100-160 μm of low-grade ore was separated by screening and used for leaching. A solution of 8.0 N H_2SO_4 was used as leaching medium. Each leaching experiment was performed with 2 g low-grade ore and a ratio solid/liquid of 1/7.5.

The low-grade chalcocite-covellite-chalcopyrite ore leaching experiments were carried out at various temperature values.

To increase the copper dissolution, the ferric sulphate as oxidizing agent was added to the leaching solution. The tested concentration of ferric sulphate in 8.0 N H_2SO_4 was 10, 20 and 30 g/l. Also, the leaching pulp was stirred by air bubbling at 200 l/hour in a volume of 210 ml leaching agent, at a same ratio solid/liquid. For leaching tests, in which the oxidizing agents (Fe^{3+} and/or O_2) were used, the leaching temperatures were 40 and 60°C.

Table 2.

The mineralogical composition of low-grade ore.

Element	Compounds	Mineralogical composition reported at ore	Mineralogical composition reported at element
Cu (%)	sulphates	0.003	0.80
	carbonates and oxides	0.013	3.49
	chalcocite and covellite	0.144	38.70
	chalcopyrite	0.212	56.98
Pb (%)	sulphates	0.140	9.33
	carbonates	0.110	7.33
	sulphides	1.010	67.33
	oxidic compounds	0.240	16.00
Zn (%)	sulphates	0.005	0.27
	carbonates and oxides	0.065	3.24
	silicates	0.080	3.98
	sulphides	1.855	93.49

After filtration, the copper concentration in solution was analyzed by spectrophotometrical method using cuprizon as complexing agent.

RESULTS AND DISCUSSIONS

The leaching results of low-grade chalcocite-covellite-chalcopyrite ore, in the temperature range of 20-60°C, at atmospheric pressure, are presented in figure 1.

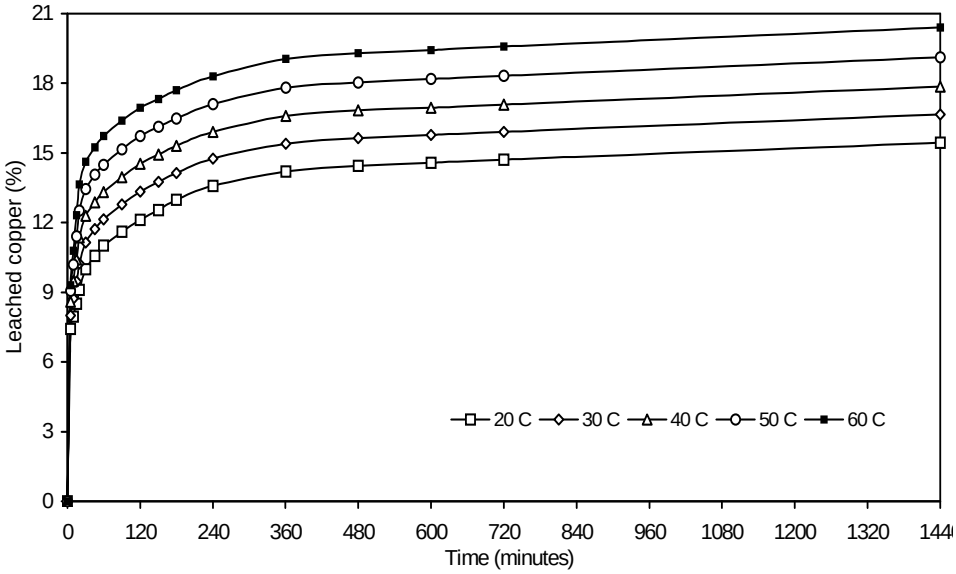

Fig. 1. The low-grade chalcocite-covellite-chalcopyrite ore leaching curves as a function of time at different temperatures.

The shape of the leaching curves indicates three periods of leaching. Making an analogy with the shrinking-core model for gas-solid noncatalytic reaction [11], the three rates - diffusion of reagents through the boundary layer, diffusion through the layer of product, and reactions at the interface of unreacted core – are observed. We were encouraged to use this shrinking-core model by the fact that particle size did not modify after the leaching process. By drying the remaining solid material and separation by screening, the same size (100-160 μm) has been obtained.

It is obvious that the initial stage of solubilization is characterized by linear kinetics. In this stage, the rate controlling reaction step is the external diffusion (the diffusion of reagents from the bulk solution to the particle surfaces). The change of the leached copper percent in this initial period could be described by the analytical expression:

$$\frac{t}{t_\infty} = 1-(1-x) = k_1 t \qquad (1)$$

where t is the leaching time (for this period $t \in 5 \div 30$ minutes), t_∞ represents the time for complete copper conversion if the process followed the same

mechanism throughout, and *x* is the copper fractional recovery. The ratio $1/t_{\infty} = k_1$ represents the rate constant (time^{-1}).

The second period of solubilization could be described by a power function having the form:

$$\frac{t}{t_{\infty}} = 1 - 3(1-x)^{\frac{2}{3}} + 2(1-x) = k_2 t \qquad (2)$$

where *t* (for this period t∈45÷240 minutes), t_{∞} and *x* have the same signification as for the first stage. Now, the rate controlling reaction step is the internal diffusion through the product layer adherent to the original material.

The third period was characterized by the following analytical expression:

$$\frac{t}{t_{\infty}} = 1 - (1-x)^{\frac{1}{3}} = k_3 t \qquad (3)$$

where *t* (for third period t∈360÷1440 minutes), t_{∞} and *x* with the previous signification like on equations (1) and (2). In this stage, the rate controlling reaction step seems to be the chemical reactions.

The experimental data for all the three periods of low-grade ore leaching, with sulphuric acid at 20°C, are presented in table 3. The apparent rate constant has been obtained using a standard least-square method. The linear dependence described by eqs. (1)-(3) is quite good, with correlation coefficients of 0.9970, 0.9866 and 0.9880 respectively.

Table 3.

The experimental data of low-grade ore leaching with sulphuric acid at 20°C.

First period			Second period			Third period		
x	t min	$10^3 k_1$ min^{-1}	x	t min	$10^5 k_2$ min^{-1}	x	t min	$10^6 k_3$ min^{-1}
0.0742	5	1.05	0.1057	45	1.37	0.1420	360	4.12
0.0795	10		0.1100	60		0.1445	480	
0.0850	15		0.1161	90		0.1458	600	
0.0910	20		0.1212	120		0.1471	720	
0.1000	30		0.1254	150		0.1543	1440	
			0.1298	180				
			0.1358	240				

The values of the rate constants, obtained as function of leaching temperature, for low-grade chalcocite-covellite-chalcopyrite ore solubilization curves, are listed in table 4. As seen, important enhancement of rate constant is obtained within the first stage, and only small enhancement within the following two stages as temperature values was risen.

Table 4.

The values of the rate constants.

Temperature °C	10^3 k_1 min^{-1}	10^5 k_2 min^{-1}	10^6 k_3 min^{-1}
20	1.05	1.37	4.12
30	1.29	1.54	4.28
40	1.55	1.69	4.30
50	1.86	1.83	4.44
60	2.30	1.96	4.69

Linear Arrhenius relation can express the quantitative dependence on the temperature. From the linear plots the values of apparent activation energy were determined. They depend upon the period of leaching and are given in table 5.

Table 5

The apparent activation energy.

Period	Temperature range (°C)	E_a (kJ/mol)
I	20-60	15.7
II	20-60	7.2
III	20-60	2.4

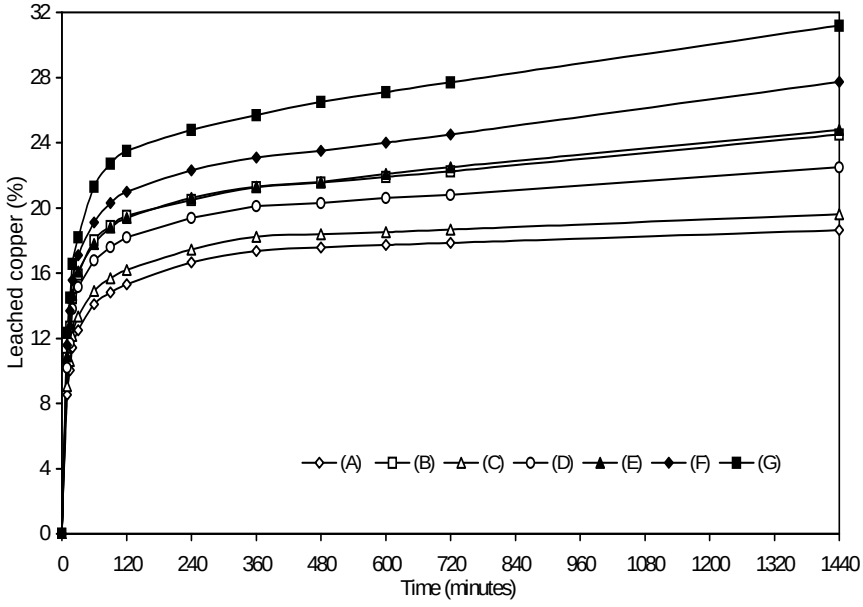

Fig. 2. The low-grade chalcocite-covellite-chalcopyrite ore leaching curves, using oxidizing agents, as function of time.

Table 6.

The R^2 values, for all of three oxidizing leaching period of the low-grade chalcocite-covellite-chalcopyrite ore.

Time range (minutes)	R^2									
	$k_1 t = 1-(1-x)$		$k_2 t = 1-3(1-x)^{\frac{2}{3}}+2(1-x)$				$k_3 t = 1-(1-x)^{\frac{1}{3}}$			
	10÷20	10÷30	30÷240	30÷360	60÷240	60÷360	60÷120	240÷1440	360÷1440
40°C, O_2	0.9991	0.9355	0.9061	0.9017	0.9824	0.9649	0.9937	0.8787	0.9928
40°C, O_2, Fe^{3+}	1.0000	0.9393	0.8902	0.8979	0.9651	0.9632	0.9861	0.9018	0.9996
60°C, O_2	0.9990	0.9392	0.8058	0.8254	0.9175	0.9374	0.9892	0.9917	0.9982
60°C, Fe^{3+}	0.9991	0.9391	0.8519	0.8552	0.9209	0.9295	0.9809	0.9978	0.9984
60°C, O_2, Fe^{3+}	0.9997	0.9402	0.7887	0.7944	0.8944	0.9107	0.9826	0.9950	0.9986

To increase the copper dissolution from low-grade chalcocite-covellite-chalcopyrite ore with sulphuric acid, oxidizing agents were added into leaching solution. Therefore, the influence of the ferric sulphate and/or oxygen addition, as oxidizing agent, on the rate of chalcopyrite concentrate was studied too. The low-grade chalcocite-covellite-chalcopyrite ore leaching curves, with sulphuric acid using the following conditions, are presented in figure 2: (A) the addition of oxygen at 40°C;(B) the addition of oxygen at 60°C;(C) the addition of oxygen and ferric sulphate (30 g/l) at 40°C;(D)the addition of ferric sulphate (10 g/l) at 60°C; (E) the addition of ferric sulphate (20 g/l) at 60°C;(F) the addition of ferric sulphate (30 g/l) at 60°C;and the addition of ferric sulphate (30 g/l) at 60°C; The data handling using the eqs. (1)-(3), in order to split the points into three periods, leads to the R^2 values presented in table 6. From these values it can be observed a decrease of second period leaching time at 60°C, when oxidizing agents are used.

The rate constants and apparent activation energies, within the temperature range 40-60°C, for all of three period in the presence of oxidizing agents, are presented in table 7.

Table 7

The rate constants and apparent activation energies, for all of three oxidizing leaching period of the low-grade chalcocite-covellite-chalcopyrite ore.

Oxidizing agents	Period	Temperature °C	k min^{-1}	E_a kJ/mol
O_2	I	40	2.09×10^{-3}	10.6
		60	2.67×10^{-3}	
	II	40	1.58×10^{-5}	35.9
		60	3.62×10^{-5}	
	III	40	4.40×10^{-6}	45.9
		60	12.68×10^{-6}	
O_2 and Fe^{3+}	I	40	2.24×10^{-3}	13.8
		60	3.08×10^{-3}	
	II	40	1.68×10^{-5}	59.4
		60	6.62×10^{-5}	
	III	40	4.92×10^{-6}	64.2
		60	21.66×10^{-6}	

CONCLUSIONS

The examination of the rate constants and apparent activation energy obtained values leads to the following conclusions:

(a) According to the apparent activation energy (~16 kJ/mol) in the range 20-60°C, the rate controlling reaction step in the first period of leaching is diffusion of leaching agent from bulk solution to the grain surface (external diffusion);

(b) In the initial stage of dissolution, fast leaching rates have been observed due to dissolution of the fine portions of low-grade chalcocite-covellite-chalcopyrite ore, the high concentration gradients at the interface, as well as the fact that the start of the process is not retarded by layers of elemental sulphur or other weak reactive products, formed on the leached surface;

(c) The second period of leaching is much longer than the first, and the values of the apparent activation energy (~7 kJ/mol) indicates the diffusion of reactants and products over the passivating layer (internal diffusion), as the rate controlling reaction step;

(d) The values of the apparent activation energy (~2 kJ/mol) indicates the same rate controlling reaction step, like in second period;

(e) The increase of the apparent activation energy for the second and third period, when the oxidizing agents were used, can be ascribed to the change of mechanism. It is highly probable that the copper polysulphide layer can release copper ions (see eqs. (3), (6)-(7)) in the interaction with the oxidizing agents, and the chemical control is installed.

REFERENCES

1. L e H o u l l i e r, R., G h a l i, E., *Hydrometallurgy*, **1982**, *9*, 169.
2. D u t r i z a c, J.E., *Can. Metall. Q.*, **1989**, *28*(4), 337;
3. H a c k l, R. P., D r e i s i n g e r, D. B., P e t e r s, E., K i n g, J. A., *Hydrometallurgy*, **1995**, *39*, 25;
4. T h o m a s, G., I n g r a h a m, T., M c. D o n a l d, R., *Can. Metall. Q.*, **1967**, *6*(2), 153;
5. T h o m a s, G., I n g r a h a m, T., M c. D o n a l d, R., *Can. Metall. Q.*, **1967**, *6*(3), 281;
6. W a d s w o r t h, M., *Metall. Treatises*, Tien, J.K., Elliot, J.F., Metall. Soc. AIME Warrendall, **1981**, p. 1-22;
7. M a r c a n t o n I o, P., "*Chalcocite Dissolution in Acidic Ferric Sulphate Solutions*", Ph. D. Thesis, Department of Mining, Metallurgical and Fuels Engineering, University of Utah, **1976**;
8. G r i z o, A., P a c o v i c, N., P o p o s k a, F., K o n e s k a, Z., *Hydrometallurgy*, **1982**, *8*, 5;
9. B u t t i n e l l i, D., L a v e c c h i a, R., P o c h e t t i, F., G e v e c i, A., G u r e s i n, N., T o p k a y a, Y., *Int. J. Miner. Process.*, **1992**, *36*, 245;
10. G r e w a l, I. S., D r e i s i n g e r, D. B., K r u e g e r, D., T y r o l e r, P.M., K r a u s e, E., N i s s e n, N.C., *Hydrometallurgy*, **1992**, *29*, 319;
11. S m i t h, J. M., *Chemical Engineering Kinetics*, Mc.Graw-Hill, Kagacusha Ltd, Tokyo, 2nd Ed., **1970**, p. 571-596.

STUDIA UNIVERSITATIS BABEŞ-BOLYAI, CHEMIA, XLIV, 1-2, 1999

L'INFLUENCE DU MATERIAU CATHODIQUE ET DE LA COMPOSITION DE L'ELECTROLYTE SUR L'ELECTRODEPOSITION DU MANGANESE DES SOLUTIONS AQUEUSES DE $MnSO_4$. COURBES DES POLARISATIONS SUR L'ELECTRODE DISQUE TOURNANTE

PETRU ILEA*, PAUL TISSOT, LIVIU ONICIU***

** Université "Babes-Bolyai", Département de chimie physique, Cluj-Napoca, ROMANIA,*
*** Université du Genève, Département de Chimie Minérale, Analytique et Appliqué, 30 quai Ernest. Ansermet, CH-1211 Genève 4, SUISSE*

RÉSUME. L'influence des substrats cathodiques, utilisés pour l'électrodéposition du manganèse (edMn), est analysée par l'intermédiaire des courbes des polarisations sur l'électrode à disque tournante. Les courbes de polarisation tracées sur le platine montrent que la edMn est stimulée par la présence simultanée du H_2SeO_3 et des ions Mn^{2+} qui exercent un effet synegétique en ce qui concerne le surpotentiel de la réaction de dégagement d'hydrogène. Les courbes de polarisation sur une cathode en carbone vitreux, révèlent une incompatibilité épitaxiale entre le substrat et le Mn déposé. La présence du H_2SeO_3 améliore la compatibilité entre les deux structures cristallines (carbone vitreux et le manganèse). Parmi les autres substrats cathodiques étudiés, Ti, Cu, Al et acier inoxydable, le dernier présente les meilleures performances.

INTRODUCTION

L'étude de l'électrodéposition du manganèse par voltammétrie sur l'électrode stationnaire [1, 2] a montré les caractéristiques spécifiques de ce processus et en même temps la nécessité d'une étude sur l'électrode tournante pour diminuer les influences qui proviennent de l'absence d'un transport de masse intensif. En plus, les changements du pH autour de la cathode stationnaire, à cause du dégagement d'hydrogène, empêchent l'électrodéposition du manganèse. Il s'agit, de même, du blocage de la surface d'électrode par les bulles d'hydrogène. C'est le motif pourquoi nous avons décidé d'étudier l'électrodéposition du manganèse sur l'électrode à disque tournante (EDT). A la fois, nous avons été intéressé d'élucider l'effet du matériau d'électrode et de la présence de H_2SeO_3 sur l'edMn. Ce-ci permettra d'éviter l'alcalinisation très forte à la proximité de la cathode [3] et de chasser les éventuelles bulles d'hydrogène qui se forment sur la surface de l'électrode.

RESULTATS ET DISCUSSIONS

La manière de travail adoptée c'est tout à fait comparable à celle décrite au cas de l'électrode stationnaire [1,2]. Ainsi qu'en ce cas on a commencé par étudier le système le plus simple, H_2O-$(NH_4)_2SO_4$, lequel représent le fond électrolytique (FE), sur ***la cathode en platine***. Sur les courbes on n'observe que la rdH à son commencement vers -0,350 V/EHN (fig. 1.a, courbe 1).

L'adjonction du H_2SeO_3 dans l'électrolyte a pour effet une légère augmentation du potentiel cathodique (fig. 1.A, courbes 2 et 3). Le fait peut être attribué à l'augmentation du pH, quoique l'effet tampon du $(NH_4)_2SO_4$ limite ce processus, ou bien à la réduction du sélénium déjà formé sur la surface de la cathode:

$$Se + 2e^- \rightarrow Se^{2-}, \qquad \varepsilon° = - 0{,}92 \text{ V/EHN [5].}$$

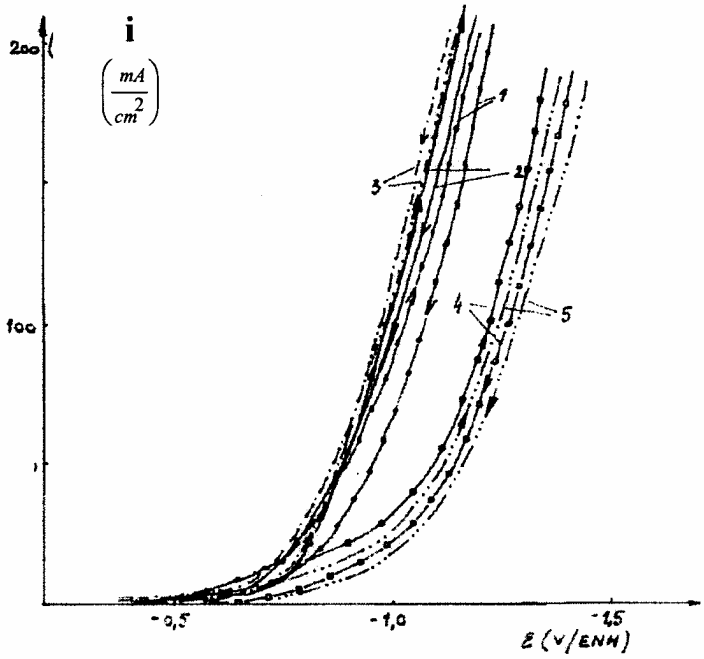

Fig.1.A. Courbes de polarisations sur la cathode en platine correspondant aux systèmes: FE (courbe 1); FE + H_2SeO_3 0,4 mM (courbe 2); FE + H_2SeO_3 1 mM (courbe 3); FE + $MnSO_4$ 0,4 mM (courbe 4); FE + $MnSO_4$ 1 mM (courbe 5).

La présence du $MnSO_4$ dans l'électrolyte (fig. 1.A, courbe 4) déplace le potentiel cathodique vers de valeurs plus négatives, d'à peu près 250 mV, déplacement sensible à la concentration en Mn^{2+} (fig. 1.A, courbes 4 et 5).

Le balayage anodique ne relève pas la réaction d'oxydation du dépôt de manganèse, éventuellement formé, à cause de la superposition de celle-ci avec la rdH.

Dans la présence simultanée de $MnSO_4$ et H_2SeO_3 dans l'électrolyte (fig. 1.B.), on observe des modifications substantielles. Bien que la rdH commence à l'approximativement même valeur en potentiel, la vitesse de réaction reste toujours basse ce qui permet d'observer les processus dont le début précède le dégagement d'hydrogène. Au balayage cathodique on remarque l'existence de deux ondes mal délimitées. Celles-ci précèdent le dégagement d'hydrogène - déplacé avec 250 mV vers des valeurs plus négatives par rapport à la présence du H_2SeO_3.

La première onde (attribué à la réduction du sélénium élémentaire) située à -0,900 V/EHN est influencé par la concentration du H_2SeO_3. Cette onde est absente pour une concentration de H_2SeO_3 0.4 mM (fig.1.B. courbe 2) et apparaît pour une concentration de H_2SeO_3 1 mM (fig.1.B. courbe 3). Etant donné que pendant le balayage cathodique la surface de la cathode commence à rougir est évident que dans une première étape se forme le sélénium élémentaire. La valeur du potentiel ainsi que la présence sur la surface de l'EDT, du sélénium rouge constituent des arguments pour une certaine appréciation.

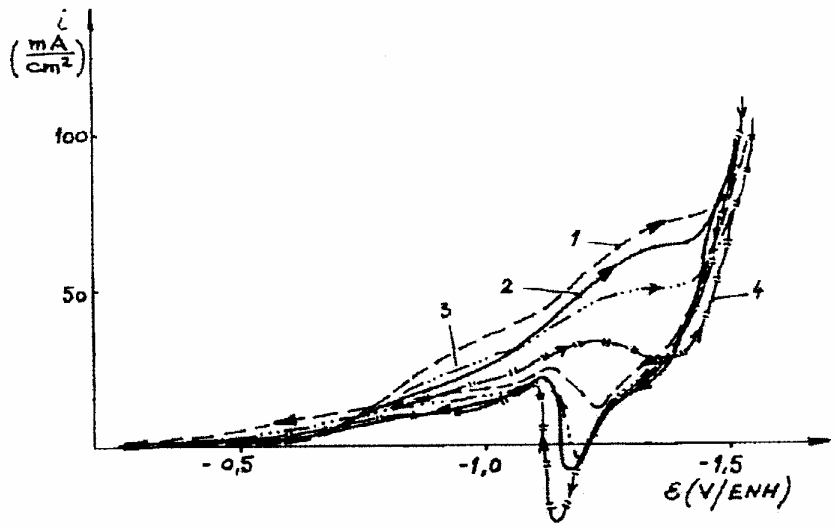

Fig.1.B. Les courbes de polarisations sur la cathode en platine correspondant aux systémes: FE + $MnSO_4$ 0,4 mM + H_2SeO_3 1 mM (courbe 1); FE + $MnSO_4$ 1 mM + H_2SeO_3 0,4 mM, (courbe 2); FE + $MnSO_4$ 1 mM + H_2SeO_3 1 mM (courbe 3); FE + $MnSO_4$ 2 mM +H_2SeO_3 1 mM (courbe 4).

La vitesse de réduction en étapes du H_2SeO_3 est influencée par la présence du Mn^{2+}, l'augmentation de la concentration du Mn^{2+} inhibe la réduction du H_2SeO_3 (fig.1.B. courbes 1, 3 et 4). Le balayage anodique montre un maximum qui corresponde à l'oxydation du manganèse déposé.

En comparant les courbes 1, 2, et 4 (fig. 1.B.) on observe que lorsque la concentration en Mn augmente, la deuxième onde se déplace vers des potentiels positifs et que celle-ci ressemble plutôt à un maximum. Ce maximum est attribué à la réduction des ions Mn^{2+}; sa présence est moins marque à des faibles concentrations en Mn^{2+} à cause du dégagement simultané d'hydrogène. La diminution de la vitesse de la rdH avec l'augmentation de la concentration en Mn est confirmée d'ailleurs par la croissance du maximum d'oxydation anodique du métal. Le même maximum baisse avec la l'augmentation de concentration en H_2SeO_3 (courbes 2 et 3, fig.1.b.) ce qui s'explique si on accepte que l'additif exerce aussi un effet d'inhibition sur la edMn elle-même [6].

Sur les courbes tracés en utilisant des électrolytes aqueux (A): $(NH_4)_2SO_4$ 1M + 100 g/l $MnSO_4$ et (B): $(NH_4)_2SO_4$ 1M + 100 g/l $MnSO_4$ + H_2SeO_3 1mM (Fig.1.C.) est à remarquer la diminution de la rdH en présence d'H_2SeO_3 (Fig.1.C. courbe 2) ainsi que le déplacement du maximum anodique vers des valeurs plus positives, d'à peu près 80 mV, ce qui prouve aussi la croissance de la stabilisation du dépôt en Mn, comparativement au processus de corrosion électrochimique.

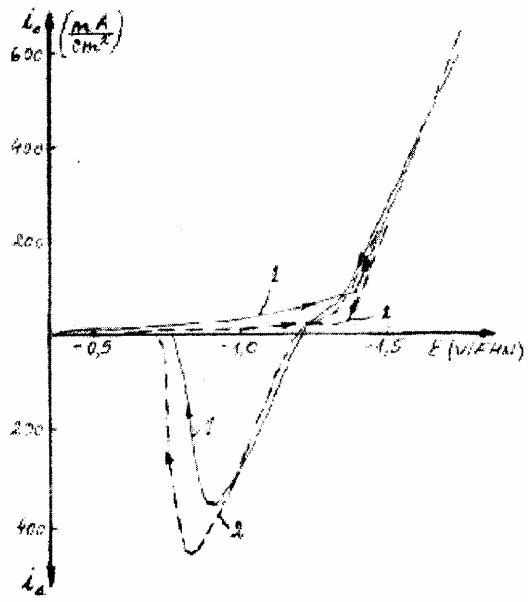

Fig. 1.C. Courbes de polarisations sur la cathode en platine correspondant aux systèmes: FE + $MnSO_4$ 100 g/l (courbe 1), FE + $MnSO_4$ 100 g/l + H_2SeO_3 1 mM (courbe 2).

Sur la cathode en Pt il est difficile de séparer nettement l'edMn et la rdH à cause de son effet catalytique sur la rdH. Pour cela, le substrat en Pt a été changée par ***la cathode en carbone vitreux*** (fig. 2.A - 2.B), connu pour sa grande valeur de surpotentiel de rdH [6].

En absence d'ions Mn^{2+} on observe l'augmentation du surpotentiel de la rdH. Par exemple sur la platine pour une densité de courant, i = 50 mA/cm^2, le potentiel cathodique est -0,870 V/EHN (Fig.1A, courbes 1- 3) par rapport à celui sur carbone vitreux -1,650 V/EHN (Fig.2A. courbes 1 et 3).

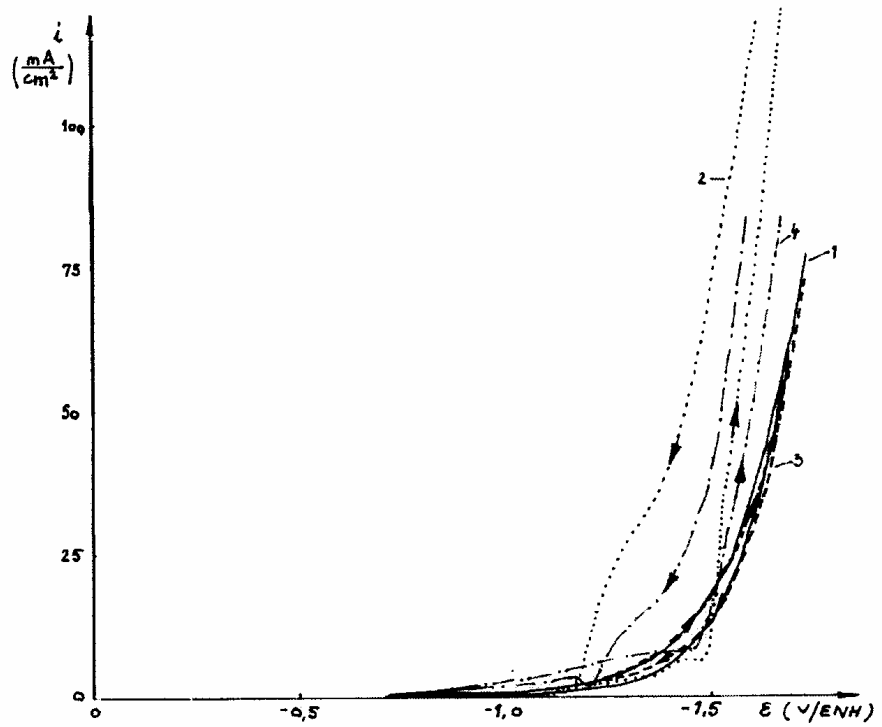

Fig.2A. Courbes de polarisations sur la cathode en carbone vitreux correspondant aux systèmes: FE (courbe 1), FE + $MnSO_4$ 1 mM (courbe 2), FE + H_2SeO_3 1 mM (courbe 3), FE + H_2SeO_3 1 mM + $MnSO_4$ 1 mM (courbe 4).

Au balayage anodique, sur toutes les courbes, on remarque l'existence d'un domaine de potentiel dans lequel la vitesse du processus cathodique reste plus élevé qu'au balayage cathodique. Cette situation est spécifique pour les cas où le processus d'électrode s'accomplit par l'apparition d'une nouvelle phase -l'éléctrocristalysation [7].

Ce comportement s'explique par le fait qu'à l'électrodéposition d'un métal, sur un substrat différent la germination nécessite un plus grand surpotentiel. Par la suite, au balayage cathodique l'électrodéposition ne

commence qu'au moment où ce surpotentiel a été atteint, mais une fois la nucléation initiée, la vitesse du processus augmente d'une manière spectaculaire. Au balayage anodique, le métal existe déjà à la surface de l'électrode, pour cela l'électrocristalisation continue tant qu'il est possible du point de vue thermodynamique et cinétique; ensuite le dépôt métallique commence à se dissoudre.

À la fin du balayage anodique on observe sur les courbes, un maximum anodique (Fig.2A courbe 4). L'absence de ce maximum sur la courbe 2 (Fig.2A) s'explique par une possible oxydation chimique du dépôt par les ions capables à libérer l'hydrogène lorsque la polarisation cathodique est diminuée. Le processus n'est pas accompagné par le transfert d'électrons, donc il n'est pas visible sur la courbe.

En traçant les courbes correspondantes à l'électrolyte (A) (fig. 2.B, courbe 1), on observe la conservation du comportement des solutions diluées dans le domaine des courants cathodiques, et l'apparition du maximum de la dissolution anodique.

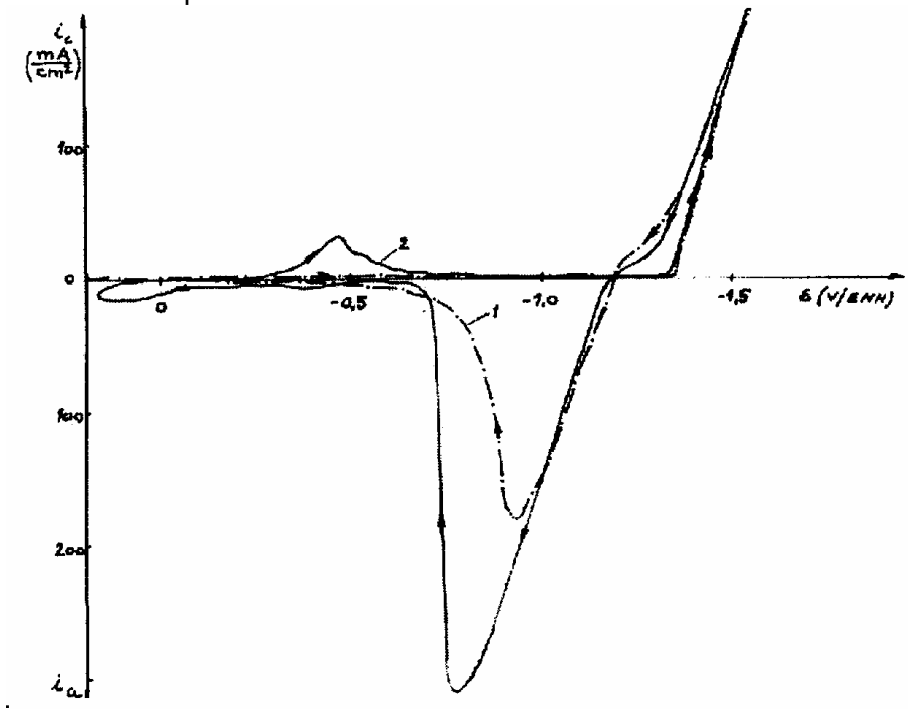

Fig.2B. Courbes de polarisations sur la cathode en carbone vitreux correspondant aux systèmes: FE + $MnSO_4$ 100 g/l (courbe 1), FE + H_2SeO_3 1 mM + $MnSO_4$ 100 g/l (courbe 2).

La courbe du système (B) (fig. 2B. courbe 2) présente un maximum cathodique à -0,470 V/EHN et un maximum anodique à -0,390 V/EHN. Ceux-ci peuvent être attribués à la réaction:

$$SeO_3^{2-} + 4e^- + 3H_2O \rightarrow Se + 6OH^-, \quad \varepsilon° = -0{,}366 \text{ V/EHN} \quad [5],$$

caractérisée dans les conditions expérimentales (c = 1mM) par un potentiel réversible de 0,455 V/EHN. Sur la fig.2B on observe aussi que la présence de H_2SeO_3 ne modifie pas le surpotentiel nécessaire à la germination. La différence relative entre les deux maximes anodiques d'oxydation du manganèse électrodéposé révèle un rendement de courant supérieur en présence du sélénium.

La cathode en acier inoxidable est le matériel le plus fréquemment employé comme matrice cathodique pour l'électrodéposition du manganèse [8-15]. L'évolution de la edMn et de la rdH sur acier inoxydable 316 est représentée dans les fig. 3A et 3B. A cause d'une faible reproductibilité des courbes ayant comme potentiel de départ +0,156 V/EHN, pour ce matériel on est parti d'un potentiel plus négatif, d'environ -0,500 V/EHN. L'apparition d'un maximum au balayage cathodique à -1,230 V/EHN en absence du Mn et du sélénium (fig.3A, courbe 1) est due probablement à la réduction du film d'oxyde existant à la surface de la cathode. Ce maximum disparaît en présence du sélénium grâce au fait que le Se élémentaire couvre la surface de l'électrode.

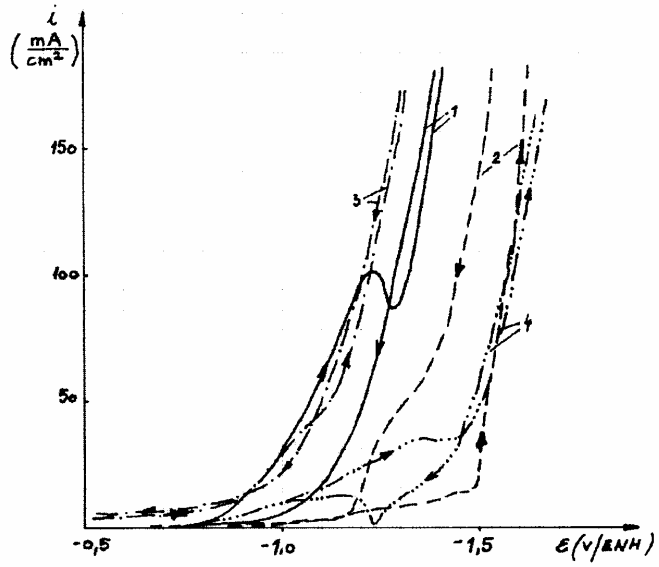

Fig.3A. Courbes de polarisations sur la cathode en acier inoxydable correspondant aux systèmes: FE (courbe 1), FE + $MnSO_4$ 1 mM (courbe 2), FE + H_2SeO_3 1 mM (courbe 3), FE + H_2SeO_3 1 mM + $MnSO_4$ 1 mM (courbe 4).

L'apparition des germes de Mn sur l'acier inoxydable se déroule avec un surpotentiel plus bas en présence de H_2SeO_3 (Fig.3A. courbes 2 et 4) qu'en absence de celui-ci. Au balayage anodique, le courant cathodique décroît plus rapidement (Fig.3A. courbe 4) dans la situation où le sélénium manque (Fig.3A. courbe 2). Sur la courbe 4 on trouve même un maximum anodique, dans le domaine des courants cathodiques qui peut être expliqué par la dissolution du manganèse électrodéposé, dissolution qui s'arrête au potentiel d'équilibre Mn^{2+}/Mn.

A des concentrations élevées en Mn^{2+} (fig. 3B) il y a assez de manganèse déposé lors du balayage cathodique pour former un maximum net à la polarisation anodique. Le dépôt obtenu en présence de H_2SeO_3 (Fig.3B. courbe 4) est plus stable et le potentiel du maximum anodique et déplacé vers des valeurs plus positives d'environ 100 mV.

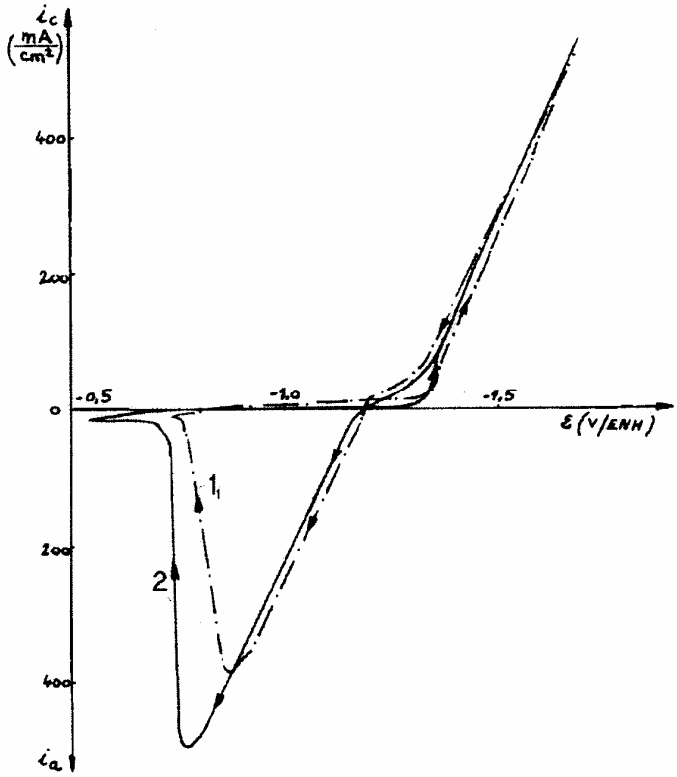

Fig.3B. Courbes de polarisations sur la cathode en acier inoxydable correspondant aux systèmes: FE + $MnSO_4$ 100 g/l (courbe 1), FE + H_2SeO_3 1 mM + $MnSO_4$ 100 g/l (courbe 2).

La courbe sur ***la cathode en titane*** aux faibles concentrations en manganèse révèle le fait qu'en ce cas la présence du sélénium (fig.4.A, courbes 2 et 4) n'augmente pas le surpotentiel de la rdH, mais au contraire, on remarque aussi un effet réduit à des concentrations plus élevées en manganèse (fig. 4B).

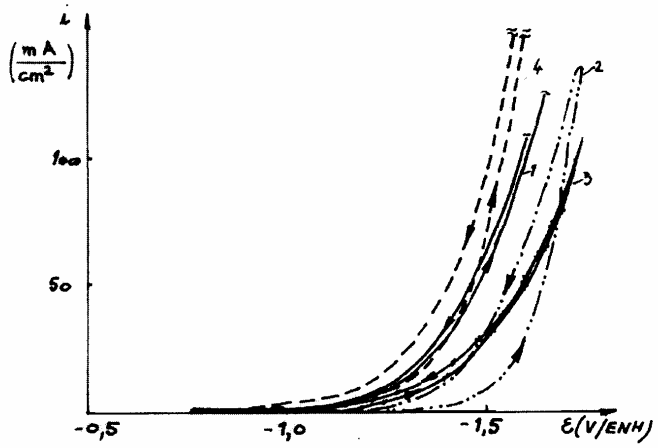

Fig. 4A. Les courbes de polarisations sur la cathode en titane correspondant aux systèmes: FE (courbe 1), FE + $MnSO_4$ 1 mM (courbe 2), FE + H_2SeO_3 1 mM (courbe 3), FE + H_2SeO_3 1 mM + $MnSO_4$ 1 mM (courbe 4).

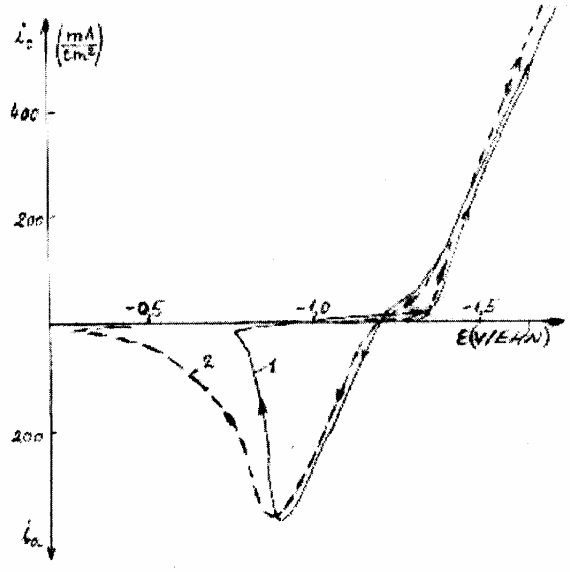

Fig.4B. Les courbes de polarisations sur la cathode en titane correspondant aux systèmes: FE + $MnSO_4$ 100 g/l (courbe 1), FE + H_2SeO_3 1 mM + $MnSO_4$ 100 g/l (courbe 2).

De l'allure du maximum anodique (fig. 4B courbe 2) on peut conclure que le dépôt manganèse est plus difficile à réoxyder, sa dessolution n'étant pas terminée à un potentiel plus positif que -0,500 V/EHN.

Le comportement de ***la cathode en aluminium*** est représenté dans les fig. 5.A et 5.B. On observe qu'en absence des ions Mn^{2+} (fig.5.A. courbes 1 et 3) la vitesse de la rdH, est faible. En ajoutant du manganèse, le courant cathodique augmente beaucoup si on dépasse le potentiel de -1,500 V/EHN (fig.5A, courbe 2), mais il peut se modifier peu en présence simultanée du sélénium (fig. 5A, courbe 4).

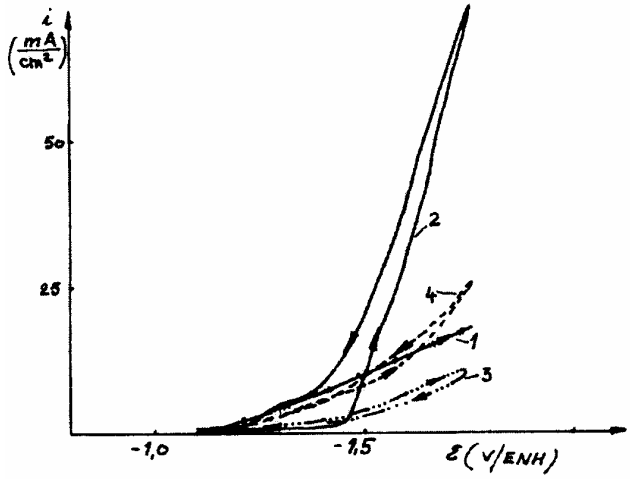

Fig. 5A. Les courbes de polarisations sur la cathode en Al correspondant aux systèmes: FE (courbe 1), FE + $MnSO_4$ 1 mM (courbe 2), FE + H_2SeO_3 1 mM (courbe 3),FE + H_2SeO_3 1 mM + $MnSO_4$ 1 mM (courbe 4).

A des concentrations élevées en manganèse on constate un comportement semblable (fig.5.B). De nouveau, le rendement d'électrodéposition en présence du Se (Fig.5B, courbe 2) est inférieur au celui constaté dans son absence (Fig.5B, courbe 1). Par la suite, sur l'Al la présence du sélénium n'améliore pas le rendement d'électrodéposition du manganèse.

La cathode en cuivre présente quelques particularités révélées sur les courbes tracées pour une faible concentration en manganèse (fig. 6A), ainsi qu'à une concentration plus élevée (fig. 6B). La germination sur cuivre est moins difficile comparativement à la croissance ultérieure du dépôt (fig. 6a, courbe 2) comportement semblable à celui sur platine (fig. 1A, courbe 5), mais le surpotentiel du processus cathodique est plus élevée sur cuivre (d'environ 150 mV). Aux concentrations plus élevées et en présence du sélénium (fig.6B, courbe 2) on constate la plus faible vitesse du processus cathodique de tous les matériaux testés.

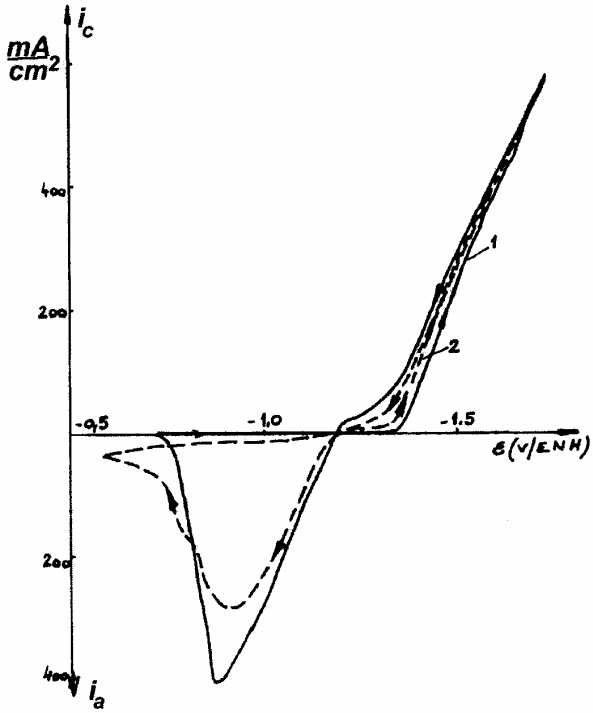

Fig.5B. Les courbes de polarisations sur la cathode en Al correspondant aux systèmes: FE + $MnSO_4$ 100 g/l (courbe 1); FE + H_2SeO_3 1 mM + $MnSO_4$ 100 g/l (courbe 2).

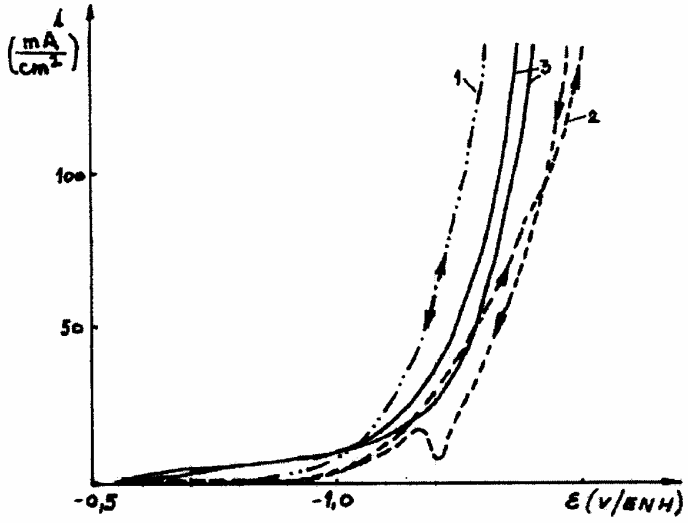

Fig.6A. Les courbes de polarisations sur la cathode en Cu correspondant aux systèmes: FE (courbe 1), FE + $MnSO_4$ 1 mM (courbe 2), FE + H_2SeO_3 1 mM (courbe 3).

La cathode en cuivre présente quelques particularités révélées sur les courbes tracées pour une faible concentration en manganèse (fig. 6A), ainsi qu'à une concentration plus élevée (fig. 6B). La germination sur cuivre est moins difficile comparativement à la croissance ultérieure du dépôt (fig. 6a, courbe 2) comportement semblable à celui sur platine (fig. 1A, courbe 5), mais le surpotentiel du processus cathodique est plus élevée sur cuivre (d'environ 150 mV). Aux concentrations plus élevées et en présence du sélénium (fig.6B, courbe 2) on constate la plus faible vitesse du processus cathodique de tous les matériaux testés.

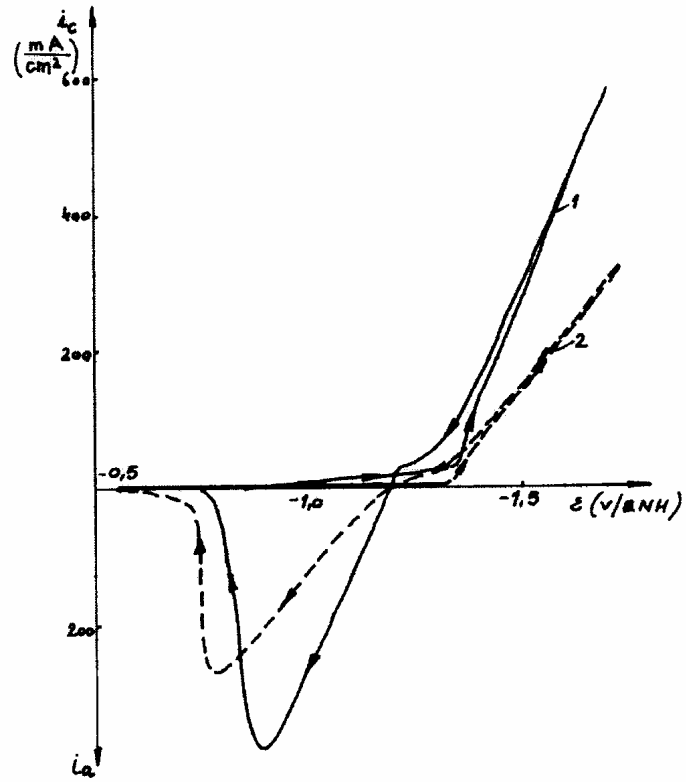

Fig. 6B. Courbes de polarisations sur la cathode en Cu correspondant aux systèmes: FE + $MnSO_4$ 100 g/l (courbe 1), FE + H_2SeO_3 1 mM + $MnSO_4$ 100 g/l (courbe 2).

Les courbes de polarisation cyclique peuvent servir à l'évaluation du rendement de courant [6]. Pour cela, on a fait l'intégration de la quantité d'électricité consommée, pour le processus anodique, respectivement cathodique. Si le processus qui accompagnent la déposition cathodique du métal (par ex. rdH) n'est pas réversible, on peut estimer que pratiquement toute la quantité d'énergie consommée pendant la polarisation anodique, est employée pour que le dépôt de métal obtenu au balayage direct soit réoxydé.

Ainsi, à l'électrodéposition du Mn métallique de solutions ayant un contenu important en manganèse on peut estimer qu'au balayage cathodique le courant consommé est dû à la edMn et à la rdH et que, lors de la polarisation anodique, est dû à la disollution du manganèse électrodéposé. Dans cette situation, le rapport entre la quantité d'électricité consommée d'une part, à la polarisation anodique, d'autre part, de la polarisation cathodique représente la mesure du rendement de courant d'électrodéposition du manganèse.

En employant les courbes de polarisation tracés en présence des concentrations élevées en manganèse (fig. 1C, 2B, 3B, 4B, 5B et 6B) on a calculé les rendements de courant pour les deux types d'électrolyte. Les résultats obtenus à la suite de ces calculs sont résumés dans le tableau 1.

Tableau 1

Rendement en courant, (%), évalue sur la base des courbes de polarisation cyclique

Matériaux cathodique → / **Électrolyte ↓**	**Pt**	**Al**	**Carbone vitreux**	**Ti**	**Cu**	**Acier inox**
$(NH_4)_2SO_4$ 1M $MnSO_4$ 100 g/l	31	35	28	33	35	39
$(NH_4)_2SO_4$ 1M $MnSO_4$ 100g/l H_2SeO_3 1 mM $MnSO_4$ 100g/l	51	31	51	47	45	48

Pour platine, dans l'électrolyte (A), le faible rendement de courant est à cause de son faible surpotentiel pour rdH. Le carbone vitreux, dans l'électrolyte (A), présente le plus faible rendement de courant à cause de la difficulté de la germination du manganèse sur ce substrat cathodique (une incompatibilité épitaxiale entre le substrat et le Mn déposé).

Les autres matériaux pressentent un rendement en courant qui augmente dans l'ordre suivant: Ti < Cu < Al < acier inoxydable.

En présence du H_2SeO_3, électrolyte (B), à l'éxception de l'Al tous les autres matériaux pressentent un rendement de courant élevé par rapport à celui observé en absence du sélénium.

Une situation digne d'etre remarquée est la très forte influence du sélénium sur Pt, carbone vitreux mais aussi sur Ti et acier inoxydable.

CONCLUSIONS

Les courbes de polarisation tracés sur platine constituent "l'étalon" pour les comparaisons avec les autres matrices cathodiques mais aussi l'occasion pour mettre en évidence l'influence du H_2SeO_3 dans le cas d'un support cathodique ayant un caractère électrocathalytique pour rdH. Ces courbes montrent que la edMn est stimulée par la présence simultanée du sélénium et des ions Mn^{2+} qui exercent un effet sinegétique en ce qui concerne le surpotentiel de la rdH.

Pendant le balayage cathodique, l'acide H_2SeO_3 est réduit tout d'abord en sélénium élémentaire, ayant $\varepsilon\,° = -0{,}366$ V/EHN (i), puis en Se^{2-} ayant $\varepsilon\,° = -0{,}920$ V/EHN (ii) [5], les deux processus devançant la edMn [16]. Le processus (ii) peut avoir lieu en même temps avec la rdH, en milieu plus acide; ou bien peut commencer avant la rdH en milieu basique. Par conséquent, en présence d'acide H_2SeO_3, edMn démarre après l'apparition de Se^{2-}. Dans ces conditions il est possible que l'ion Mn^{2+} forme les complexes [Mn(HSe)(HO)] et MnSe [17]. Si on considère les données fournies par Mehra [17] concernant l'apparition du complexe [Mn(HSe)(HO)], pour une concentration en Mn^{2+} de 10^{-3} mol/l on trouve une constante de stabilité de $10^{11,5}$.

Les courbes de polarisation sur une cathode en carbone vitreux, révèlent une incompatibilité épitaxiale entre le substrat et le Mn déposé. La présence du sélénium améliore la compatibilité entre les deux structures cristallines (carbone vitreux et le manganèse).

Parmi les autres matrices cathodiques l'acier est supérieur aux autres (Al, Cu, Ti), conclusion confirmée également par des mesures de rendement de courant (voir le tableau 1).

En ce qui concerne la stabilité de dépôts du manganèse sur différentes matrices cathodiques, les données obtenues (figures 1C, 2B, 3B, 4B, 5B et 6B), sont présenté synthétiquement dans le Tableau 2.

Pour l'électrolyte (A) le potentiel anodique maxime se déplace vers de valeurs positives en fonction de la nature des matrices cathodique dans l'ordre suivant:

Carbone vitreux < Pt ≅ Ti < Cu < Al ≅ acier inoxydable,

en même temps la densité de courant maxime augmente dans l'ordre suivant:

Carbone vitreux < Pt = Ti < Cu < acier inoxydable < Al.

Pour l'électrolyte (B) le potentiel anodique maxime se déplace vers de valeurs positives en fonction de la nature des matrices cathodique dans l'ordre suivant:

Al < Ti < Pt < Cu < Carbone vitreux = acier inoxydable,

en même temps la densité de courant maxime augmente dans l'ordre suivant:

Cu < Al < Carbone vitreux < Ti < Pt < acier inoxydable.

Tableau 2

Les parametres des maximes anodiques des courbes de polarisation cycliques sur differentes materiau cathodiques et electrolytes (A) et (B)

Materiau cathodique	**Electrolyte**	**Potential du maxim anodique, *mV / EHN***	**Densite de courant du maxime anodic, *mA / cm²***
Pt	A	- 900	370
	B	- 820	460
Carbon vitreux	A	- 930	180
	B	- 770	310
Acier inoxidable	A	- 870	390
	B	- 770	495
Ti	A	- 900	370
	B	- 870	355
Al	A	- 870	400
	B	- 930	280
Cu	A	- 890	380
	B	- 780	270

PARTIE EXPERIMENTALE

Les expérimentations ont été effectuées dans une cellule en verre, ayant 3 électrodes: l'électrode de travail - une électrode disque tournante (EDT) type Tacussel CTV 101T, l'anode (un disque en Pt, ϕ = 50 mm) et une électrode de référence de type METROHM , en sulfate mercureux (+ 0,656V/EHN). Les cathodes ont été en Pt, Al, Ti, Cu, acier inoxydable (ϕ = 2mm), ou Mn et carbone vitreux (ϕ = 3mm).

Les détails concernant cellule et les électrodes nous les avons précisés auparavant [4].

Avant chaque mesure les cathodes ont été polies sur papiers émeris, dans l'ordre 1000, 1200, 2000, puis rincées, dégraissées et séchées. La vitesse de rotation de l'électrode était de 5000 rot/min; de plus une agitation magnétique de l'électrolyte assurait l'élimination des bulles d'hydrogène à la surface de la cathode. Le potentiostat employé a été du type Scanning potentiostat 362, EG&G-PAR, EUA). Pour enregistrer les courbes, nous avons utilisé un enrgistreur X-Y (BBC - Goerz Metrowatt, type SE780).

La solution d'électrolyte a était préparée à base des réactifs FLUKA, puriss, p. a. et de l'eau distillée. Le volume d'électrolyte était toujours 250 ml, et le pH = 7,8. Les expériences ont été effectuées sous atmosphère d'argon.

Les courbes ont été tracées avec la vitesse de balayage de 100 mV/s.

REMERCIEMENTS

L'un d'entre nous (Petru Ilea) remercie au Département de Chimie Minérale, Analytique et Appliqué de L'Université du Genève pour la bourse de recherche. Des remerciements s'adressent au Professeur Ionel - Catalin Popescu pour son intérêt manifesté pendant la rédaction de cet article. Nous remercions égalmant à Madame H. Lartique pour son assistance technique.

BIBLIOGRAPHIE

1. L.Oniciu, P. Ilea, I.C. Popescu et Melania Urda, Studia Universitatis Babeö-Bolyai, Serie Chemia, 1992. 1-2, 29.
2. P. Ilea, Teza de doctorat, Universitatea "Babes-Bolyai" Cluj-Napoca, 1994.
3. R.U. Bondar, I.V. Gamali et V.V. Stender, Prikl. Khim., 1967. **40**, 5, 1025.
4. P. Ilea, P. Tissot, L. Oniciu, Chem. Bull. "Politehnica" Univ. Timişoara, 1997. **42**, (56), 5.
5. J. Bard, "Encyclopedia of Electrochemistry of the Elements" Vol. IV, pag. 362, Marcel Dekker, Inc., New York and Basel, 1975.
6. M. Gonsalves et D.Pletcher, J. Electroanal. Chem., 1990, **285**, 185.
7. D. Pletcher,"A first course in electrode processes", pag. 174, Alresford Press Ltd., England, 1991.
8. R.S. Dean, "Eectrolytic Manganese and it's alloys", Ronald Press, New-York, 69, 1952.
9. M.A. Qazi et J. Leaj, J. Electrochem. Soc., 1971. **118**, 548.
10. C.L. Mantell et G.R. Ferment, U.S. Pat., 1959. 3 455 799.
11. N. Dhananjayan, J. Electrochem. Soc., 1959. **117**, (8), 1006.
12. J.E. Lewis, P.H. Scaife et D.A.J. Swinkels, J. Applied Electrochem., 1976. **6**, (3), 453-462
13. P. Radhakrishnamurthy et A.K.N. Reddy, J. Applied Electrochem., 1977. **7**, (1), 113-117
14. G.D. Bagley et M.C. Carosela, U.S. Pat. , 1956. 2 755, 241
15. J. Holasek, V. Tokar, J. Alberty et I. Chladecky, Brevet Czech., 1963. 109 049
16. J. Bard, "Encyclopedia of Electrochemistry of the Elements" Vol. I, pag. 351, Marcel Dekker, Inc., New York and Basel, 1973.
17. M.C. Mehra et A.O. Gubeli, J.Less-Common Metals, 1970. 22, 281.

STUDIA UNIVERSITATIS BABEŞ-BOLYAI, CHEMIA, XLIV, 1-2, 1999

STRUCTURAL INVESTIGATIONS AND THERMAL ANALYSIS OF THE COMPLEX COMPOUND OBTAINED THROUGH THE REACTION OF 1,3-PROPANEDIOL WITH $Ni(NO_3)_2 \cdot 6H_2O$

M. NICULESCU*, N. VASZILCSIN* and P. BUDRUGEAC**

** "Politehnica" University of Timisoara, Industrial Chemistry and Environmental Engineering Faculty, Piata Victoriei 2, 1900, Timisoara, Romania*

*** ICPE – Research and Development Institute for Electrical Engineering, Splaiul Unirii 313, Sector 3, Bucharest 74204, Romania*

ABSTRACT. In this paper the authors present the results of an investigation concerning the reaction between 1,3-propanediol and $Ni(NO_3)_2 \cdot 6H_2O$, leading to a complex containing as ligand the β-hydroxypropionate anion (L). The obtained solid homopolynuclear combination, $[Ni_2(OH)_2L_2(H_2O)_2 \cdot 0.5H_2O]_n$, has been investigated by thermal analysis, electronic and IR spectroscopy and magnetic methods. Nickel oxide obtained by thermolysis of this coordinative compound was characterized by IR and X-ray spectroscopy.

Keywords*:* 1,3-propanediol; nitrate; homopolynuclear combination; β-hydroxypropionate; thermal analysis.

INTRODUCTION

The thermal conversion of homo- and hetero-polynuclear complexes with anions of carboxylic acids as ligands have been carried out to oxide systems with irreducible structure and properties, required by the modern technology in various fields (heterogeneous catalysis, electrocatalysis, electronics, ceramic pigments, physical supports (carriers, brackets) for the stockade and processing of information, drug industry)[1-4]. Such ligands include the anions glyoxylate, malonate, succynate and lactate. These complexes have been obtained by the oxidation reaction between some diols and metal nitrates, under different reaction conditions [5-9]. In a recent paper [10] we have reported the results of the study of the oxidation reaction between 1,3-propanediol and $M(NO_3)_2 \cdot 6H_2O$ (M: Co, Ni), in the presence of dilute nitric acid solution. Ni and Co complex combinations synthesized in this way contain malonate anion as ligand.

The determination of the formation conditions of nonstoichiometric oxides of Ni and Co led to a original method for obtaining anodes with

electrocatalytically active films for the oxygen evolution at the electrolysis of alkaline solutions [8, 9].

This paper presents the results obtained at the investigation of 1,3-propanediol oxidation with $Ni(NO_3)_2.6H_2O$, in a weak acid medium, due to the hydrolysis of the metal nitrate. The obtained coordination compound was investigated with respect to the composition and physical-chemical properties. It will be shown that it can be a precursor for the NiO obtaining at relatively low temperature.

EXPERIMENTAL

For the synthesis of the coordination compound, $Ni(NO_3)_2.6H_2O$, "Reactivul" – Bucharest, with minimal purity of 98%, and 1,3-propanediol, "BDH Chemical Ltd. Poole "- England with purity of 97% were used. The impurities from the reagents do not influence the synthesis and purity of the obtained compound as they are removed in the subsequent purification step.

The elaborated method of synthesis of the complex compound is based on the oxidation reaction of 1,3-propanediol in an alcohol-water system by nickel nitrate and the simultaneous isolation of the complex compound in the reaction system.

A solution of water + diol + $Ni(NO_3)_2 \cdot 6H_2O$ in the molar ratio: 1,3-propanediol : $Ni(NO_3)_2 \cdot 6H_2O$ = 3:2 was prepared. This mixture was heated gradually during 20 h in a thermostat up to 120^0 C. The reaction was considered completed when no more gas evolution was observed.

Refluxing from acetone-water mixture purified the solid reaction product. After that the solution was filtered and the solid product was washed with acetone and finally was maintained in air until constant mass.

The evolution of the reaction between 1,3-propanediol and $Ni(NO_3)_2.6H_2O$ was investigated by IR spectroscopy. As the reaction advances the bands due to nitrate ion decreases in intensity, proving that the nitrate ion is consumed in reaction [11]. In the same time, the appearance and the increase of the band intensity in the range 1580 – 1680 cm^{-1} (ν_{as} COO^-) is observed, which is specific to complexes ligands which contain at least two oxygen atoms as donors such as the carboxylic anions of the acids.

The elemental analysis results (Table 1) as well as the IR investigation confirm the following empirical chemical formula for the coordination compound: $Ni(OH)L(H_2O) \cdot 0.25H_2O$, where L is the β-hydroxypropionate anion.

The heating curves (TG, DTG, DTA) corresponding to the decomposition of the coordination compound were recorded on a Q-1500D MOM-Budapest type Paulik-Paulik-Erdey derivatograph, in static air atmosphere and the temperature range 20 – 500^0C, at heating rates: 1.25 $K \cdot min^{-1}$, 2.5 $K \cdot min^{-1}$, 5 $K \cdot min^{-1}$ and 10 $K \cdot min^{-1}$; reference material: α-Al_2O_3.

The coordination compound was also characterized by the following methods: chemical analyses, IR-spectroscopy, electronic spectroscopy (diffuse reflectance technique) and magnetic methods.

The IR spectrum was recorded on a Specord IR 75 Carl Zeiss Jena spectrometer using the technique of KBr pellets, in the range 400 – 4000 cm^{-1}.

Table 1.

Composition and elemental analysis data

Compound (compound formula)	Ni(II) %		C %		H %	
	calc.	exper.	calc.	exper.	calc.	exper.
$Ni(OH)L(H_2O)\cdot 0.25H_2O$	31.35	31.10	19.23	19.40	4.54	4.73

The electronic spectrum was recorded by diffuse reflectance technique using MgO as a reference material.

The magnetic measurements were performed according to Faraday's method, at room temperature, using $Hg[Co(NCS)_4]$ as a standard.

The characterization of the nickel oxide obtained by thermal decomposition of the investigated coordination compound was performed by IR and X-ray spectroscopy. XR-diffractogrames were recorded on a DRON 3 diffractometer.

RESULTS AND DISCUSSION

The experimental results as well as those previously reported [5] concerning the oxidation of 1,2-propanediol with M(II) nitrate (M= Ni, Co) suggest that the oxidation of the 1,3-propanediol with $Ni(NO_3)_2\cdot 6H_2O$ occurs at one primary hydroxyl, which is oxidized to carboxylate ion. Consequently, we suggest the following mechanism for the reaction between 1,3-propanediol and $Ni(NO_3)_2$:

a) $HO\text{-}CH_2\text{-}CH_2\text{-}COO^- + 4e + 5\,H^+ \rightleftharpoons HO\text{-}CH_2\text{-}CH_2\text{-}CH_2\text{-}OH + H_2O$

b) $NO_3^- + 3e + 4\,H^+ \rightarrow NO + 2\,H_2O$

---

c) $3HO\text{-}CH_2\text{-}CH_2\text{-}CH_2\text{-}OH + 4NO_3^- + H^+ \rightleftharpoons 3HO\text{-}CH_2\text{-}CH_2\text{-}COO^- + 4NO + 5H_2O$

d) $[Ni(H_2O)_X]^{2+} + H_2O \rightleftharpoons [Ni(OH)(OH_2)_{X-1}]^+ + H_3O^+$

(1) $C_3H_5O_3^- + [Ni(OH)(OH_2)_{X-1}]^+ \rightarrow Ni(OH)C_3H_5O_3\cdot yH_2O + (x\text{-}1\text{-}y)H_2O$

Ni(II)-β-hydroxypropionate

(2) $NO + 1/2\,O_2 \rightarrow NO_2$

From this reactions one may notice the necessity of the presence of protons involved in the c) stage in order to potentiate the oxidation activity of the nitrate ion. The necessary protons are generated by the hydrated Ni(II) cation hydrolysis, as shown in the d) process.

The suggested formula of the coordination compound as well as information concerning its structure are going to be confirmed by the results which will be presented in the following.

Electronic reflexion spectrum of Ni(II)- β-hydroxypropionate

The electronic spectrum of the coordination compound shows the presence of two characteristic bands due to the Ni(II) hexacoordinated ion.

Table 2 shows the wave numbers, which correspond to the diffuse reflectance spectral bands together with their assignments. The results are in good agreement with those from the literature [12].

Table 2.

Diffuse reflectance spectral data of the investigated compound

ν_1 [cm^{-1}]	ν_2 [cm^{-1}]	ν_3 [cm^{-1}]
-	15873 $^3T_{1g}(F) \leftarrow {}^3A_{2g}$	26316 $^3T_{1g}(P) \leftarrow {}^3A_{2g}$

In order to calculate the electronic parameters 10 Dq, B and β, we followed the classical procedure, employing König's formula [13]. Table 3 shows the calculated electronic parameters. The values of the spectral parameters show that the coordinated ligands at Ni(II), H_2O, HO^-, L, are in the spectrometric series of Ni(II) of close strength [12].

Table 3.

Calculated electronic parameters

10 Dq (kK)	B (kK)	β
9.804	0.816	0.78

The value of the effective magnetic moment 3.15 MB, is also in accordance with the octahedral configuration of the Ni(II) ion – maximal spin, higher than that corresponding to the spin value (2.83 MB). The difference could be explained through the coupling spin-orbit, which is also found for the slight splitting in the electronic spectrum of band ν_2. Therefore the Ni(II) ion is to be found in the state of maximal spin $t_{2g}^6 e_g^2$ ($^3A_{2g}$).

The electronic spectrum suggests a pseudooctahedral configuration of the Ni(II) ion; water molecules from the apical position are coordinated at two Ni(II) ions from adjacent layers.

IR vibrational spectrum of Ni(II)-β-hydroxypropionate

The infrared spectrum (Table 4) and the green color of the complex verified the above supposition.

Table 4.

Characteristic absorption bands in IR for Ni(II)-β-hydroxypropionate and the corresponding assignments

ν (OH) [cm^{-1}]	ν_{as} (COO) [cm^{-1}]	ν_s (COO) [cm^{-1}]	ν_s (CO)+ δ(OCO) [cm^{-1}]	ν (C-OH) [cm^{-1}]	ν (OH bridge) [cm^{-1}]	δ(OCO) +ν(MO) [cm^{-1}]	ρ_w (H_2O) [cm^{-1}]
3300	1600	1420 1380	1310	1118 1088	1047	800	670

The intensive and large band in the range 3200 – 3600 cm^{-1} with maximum at ≈ 3300 cm^{-1} is attributed to the formation of the hydrogen bonds between water molecules and the alcoholic hydroxyl [14, 15].

The intensive band at 1600 cm^{-1} is attributed to asymetrical vibration of the carboxylate ion and the values show that the resonance from the carboxylate group is maintained during complex formation, metal-carboxylate bond being prevalent on the ionic one [16].

The low intensity band with maximum at 1420 cm^{-1} is attributed to symmetric vibration ν_s(COO). As the difference between ν_{as} - ν_s is greater than 170 cm^{-1} one may say that the metal-carboxylate bond is really preponderantly ionic, and the carboxylate group acts as a bidentate ligand [16, 17]. Also, the existence of the two bands for ν_s(COO) could be explained through the octahedral deformation [18].

The band at 1310 cm^{-1} confirms that the carboxylate group is acting as a bidentate ligand [19].

Two bands are present at 1118 cm^{-1} and 1088 cm^{-1}, both attributed to C-OH vibration.

The band at 1047 cm^{-1} is attributed to the vibration of the OH bridge group [20].

The band of mean intensity at 800 cm^{-1} is attributed to the group of vibrations δ(OCO) + ν(MO), the same as in the case of Fe(III) Ni(II) oxalate complexes [19].

The coordination of the two water molecules to the M(II) ion is further confirmed by the presence in the vibrational spectrum of the complex combination of the band at 670 cm^{-1}. This is in a good agreement with the results obtained by Serov et al. [21].

In accordance with Nagase et al. [22], the 480 cm^{-1} band, obtained for the investigated complex, can be attributed to ν(MO)-oxygen vibration belonging to the COO^- group from the anion.

The obtained compound is insoluble in water, ethanol and ether, but it is hardly destroyed by concentrated solutions of HCl or H_2SO_4. These statements as well as the above mentioned data suggest a polynuclear structure which corresponds to the following formula: $[Ni_2(OH)_2L_2(H_2O)_2 \cdot 0.5H_2O]_n$.

Thermal analysis of Ni(II)-β-hydroxypropionate

In order to confirm the composition and the configuration of the coordination compound ($[Ni_2(OH)_2L_2(H_2O)_2 \cdot 0.5H_2O]_n$) as well as to establish the conversions to NiO which promote catalytic activity, the thermal analysis methods have been used. The thermogram corresponding to the decomposition of the $[Ni_2(OH)_2L_2(H_2O)_2 \cdot 0.5H_2O]_n$ in static air atmosphere, at a heating rate of 2,5 K/min is shown in figure 1.

Similar thermograms have also been obtained for the other heating rates.One may observe that through the progressive heating of the studied complex three processes (noted I, II, III) take place with volatile products forming. The process I is endothermic, while the processes II and III are exothermic. We consider the apparent conversion degree of $[Ni_2(OH)_2L_2(H_2O)_2 \cdot 0.5H_2O]_n$ as being given by the expression:

$$\alpha = \frac{\%\Delta m}{\%\Delta m_t} \tag{1}$$

in which:%Δm represents the percentage of the mass loss at a certain temperature and $\%\Delta m_t$ - the percentage of the total mass loss.

The TG curve in (α,T) coordinates for the heating rate β = 2.5 K/min is shown in figure 2.

Similar curves have also been obtained for the other heating rates.

Figure 3 shows the curves $\ln(d\alpha/dt) \equiv \ln\beta(d\alpha/dt)$ as a function of T, corresponding to the 4 heating rates (t represents the time; dα/dt - the decomposition rate; β - the heating rate, expressed in K/s). In the drawing of the curves in figure 3, the local heating rates have been used, calculated for temperature intervals of maximum 50°C. The curves in this figure are equivalent to the DTG - curves.

The figures 2 and 3 reconfirm the fact that at the progressive heating of $[Ni_2(OH)_2L_2(H_2O)_2 \cdot 0.5H_2O]_n$ three main decomposition processes take place. Table 5 gives the main parameters of the processes I, II, and III.

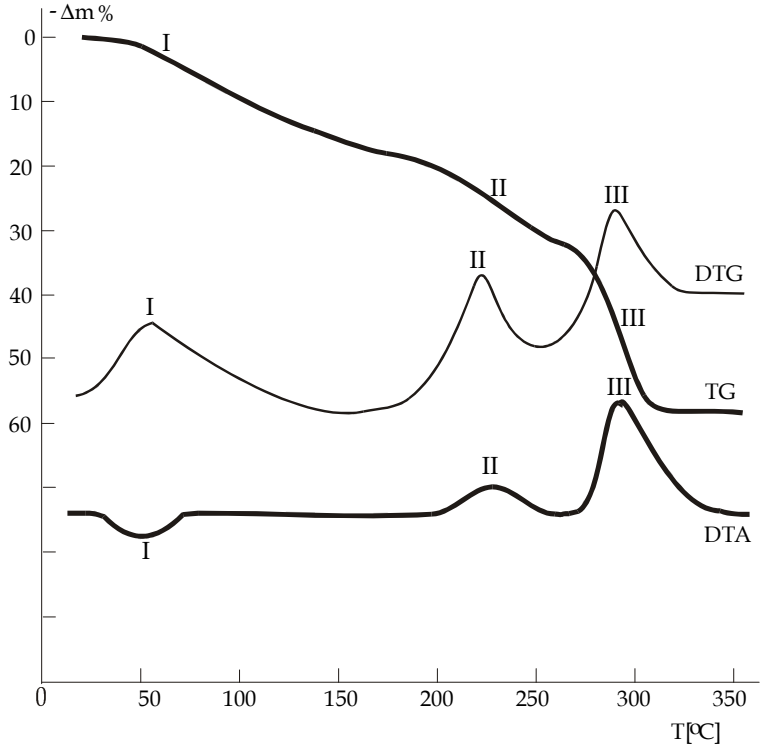

Fig. 1. Thermal analytical curves for the complex combination $[Ni_2(OH)_2L_2(H_2O)_2 \cdot 0.5H_2O]_n$

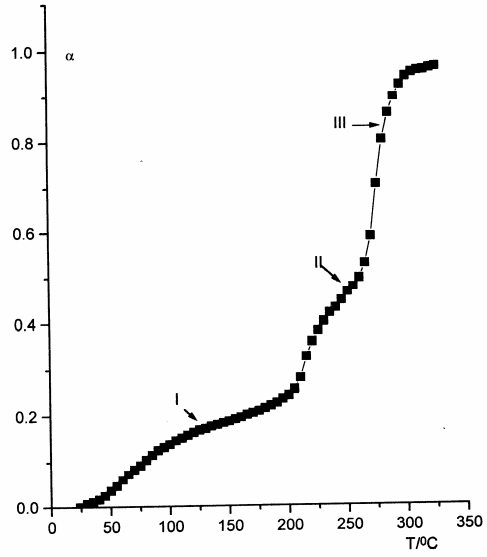

Fig. 2. α - curve as a function of T at the heating rate β = 2.5 K/min.

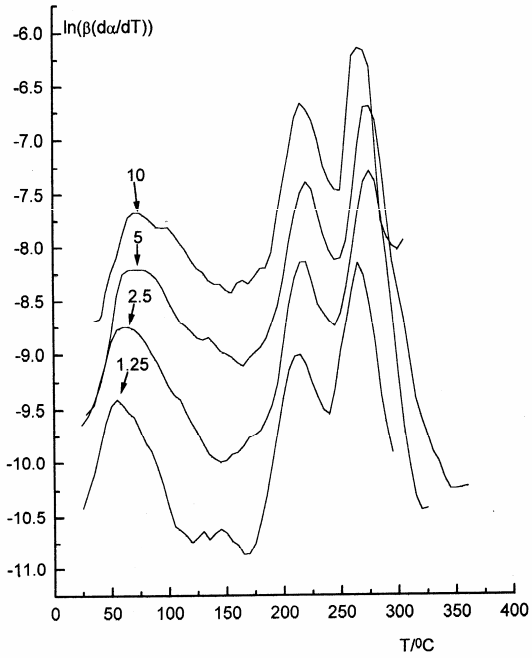

Fig. 3. lnβ(dα/dt) - curves as a function of T at the heating rates for which the thermograms have been recorded.

Table 5.

Characteristic parameters of the processes I, II, and III.

β K/min	Process I			
	ΔT ºC	%Δm_1	T_{DTA} ºC	T_{DTG} ºC
1,25	25-170	12.0	-	55
2,5	24-175	12.9	56	58
5	28-180	13.1	65	56
10	28-200	13.1	80	72
β	Process II			
K/min	ΔT ºC	%Δm_2	T_{DTA} ºC	T_{DTG} ºC
1,25	170-245	16,1	-	213
2,5	175-255	16,6	235	217
5	180-250	15,3	230	215
10	200-255	13,9	240	217

β	Process III			
K/min	ΔT °C	%Δm_3	T_{DTA} °C	T_{DTG} °C
1,25	245-295	32,9	272	266
2,5	255-305	32,5	280	275
5	250-315	35,4	275	275
10	255-305	36,0	273	267

ΔT - represents the temperature interval in which the process takes place;

%Δm_i - the percentage of the mass loss in the process i (i = 1,2,3);

T_{DTA} - the temperature minimum (for the process I) or the maximum (for the processes II and III) DTA;

T_{DTG} - the temperature of the DTG - maximum;

%Δm_t - the percentage of the total mass-loss.

It must be specified that the delimitation between the processes pointed out in the thermograms is only approximate, which explains the differences of the corresponding mass-losses at different heating rates. Nevertheless, these differences are not very high

($12\% \le \%\Delta m_I \le 13{,}1\%$; $13{,}9\% \le \%\Delta m_{II} \le 16{,}6\%$; $32{,}5\% \le \%\Delta m_{III} \le 36\%$).

The total mass-loss also varies between 61,0% and 63,8%, which may be explained through the unavoidable errors in such determinations. Finally, one may observe, that with the exception of process II, the T_{DTA} values are close to those of T_{DTG}. The process II is characterized through a flat exothermic DTA - peak, which leads to errors in the evaluation of T_{DTA}.

Based on the obtained results, we suggest the following steps for the decomposition of the complex (at the heating rate β = 2.5 K/min):

$$[Ni_2(OH)_2(HO\text{-}CH_2CH_2COO^-)_2(H_2O)_2\cdot 0.5H_2O] \xrightarrow{I\,(24\text{-}175^\circ C)\ -\ 2.5\,H_2O}$$

$$[Ni_2(OH)_2(HO\text{-}CH_2CH_2COO^-)_2] \xrightarrow{II\,(175\text{-}255^\circ C)\ -\ H_2O\ -\ CO_2}$$

$$[Ni_2O(C_5H_{10}O_4)]$$

$$\xrightarrow{III\,(255\text{-}305^\circ C)\ +\ 6\,O_2\ -\ 4\,H_2O\ -\ 6\,CO_2} 2\ NiO$$

Data from table 6 confirm the proposed conversion mechanism.

Table 6.

Mass-loss at the thermal conversion in air of the complex compound, at the heating rate β = 2.5 K/min

Step	I	II	III	I - III
Δm % (calculated)	12.00	16.50	31.50	60.10
Δm % (experimental)	12.90	16.60	32.50	61.90

Ni(II) oxide was the only component of the conversion products as it was proved by X-Ray diffraction, the obtained wave length being in agreement with ASTM 4-835.

Analysing the obtained results, one can observe that the calculated mass-losses are - within the experimental errors - in good agreement with the experimental ones, which supports the proposed formula for the complex compound.

The kinetic analysis of the nonisothermic data has been carried out through the isoconversional method, independently proposed by Flynn and Wall and by Ozawa [23], being based on the expression:

$$\ln \beta = \ln F(\alpha) + \ln \frac{AE}{R} - 2.315 - 1.052 \frac{E}{RT}$$

in which β represents the heating rate, F(α) - the conversion function, E - the activation energy, A - the preexponential factor, T - the thermodynamic temperature and R - the universal gas constant.

According to this relation, at α = constant, the dependence of lnβ as a function of 1/T should be a straight line; from its slope one may evaluate the activation energy, and from the ordinate at the origine - the preexponential factor.

The Flynn-Wall-Ozawa diagrams obtained for the decomposition of $[Ni_2(OH)_2L_2(H_2O)_2 \cdot 0.5H_2O]_n$ are shown in the figures 4 and 5.

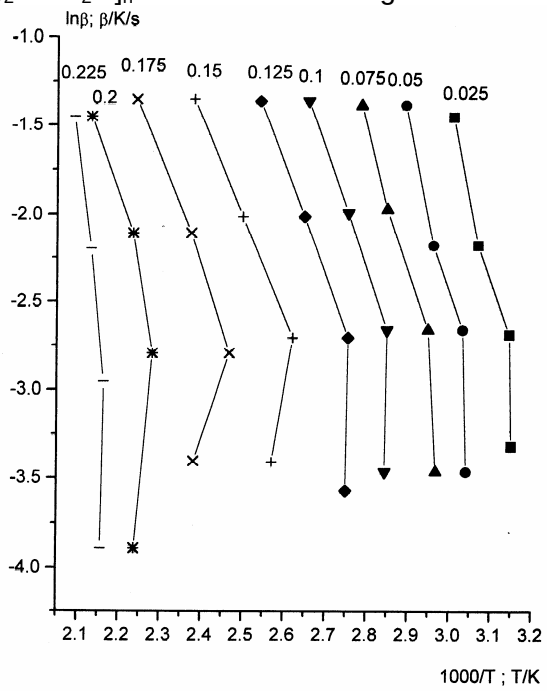

Fig. 4. Flynn-Wall-Ozawa diagram for the decomposition of

$[Ni_2(OH)_2L_2(H_2O)_2 \cdot 0.5H_2O]_n$, $0{,}025 \leq \alpha \leq 0{,}225$.

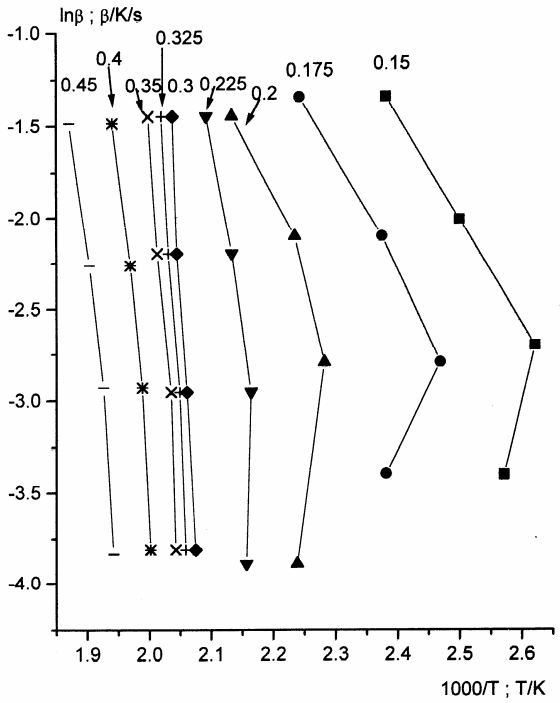

Fig. 5. Flynn-Wall-Ozawa diagram for the decomposition of $[Ni_2(OH)_2L_2(H_2O)_2 \cdot 0.5H_2O]_n$, $0{,}15 \leq \alpha \leq 0{,}45$.

One may establish that for all the considered α values, the curves $\ln\beta$ as a function of 1/T are not linear, which ascertains that the mechanisms of the decomposition steps of the investigated complex compound suffer modifications with the heating rate and the conversion degree. The use of other differential or integral methods for the evaluation of the kinetic parameters presumes the knowing of the conversion function.

Simplifying assumptions with respect to the analytical form of the conversion function lead to incorrect values for the activation parameters (E and A).

CONCLUSIONS

The coordination compound reported in this paper is a homopolynuclear combination having the formula $[Ni_2(OH)_2L_2(H_2O)_2 \cdot 0.5H_2O]_n$.

The thermal conversion product obtained at $\approx 300^0$C is NiO.

The kinetic analysis of the nonisothermic data has been carried out through the isoconversional method. The complex character of the processes

I, II, and III of the decomposition of $[Ni_2(OH)_2L_2(H_2O)_2 \cdot 0.5H_2O]_n$ makes the evaluation of their kinetic parameters impossible.

REFERENCES

1. M. Lalia-Kantouri, G. A. Katsoulos, C.C. Hadgi-Kostas and A. D. Magri, *J. Thermal Anal.,* 1989. 35. 2411.
2. T. V. Albu, S. Plostinaru, L. Patron and E. Segal, *J. Thermal Anal.,* 1997. 50. 425.
3. O. Carp, E. Segal, M. Brezeanu, R. Barjega and N. Stanica, *J. Thermal Anal.,*1997. 50. 125.
4. Pocol, L. Patron, O. Carp, M. Brezeanu, E. Segal, N. Stanica and D. Crisan, *J. Thermal Anal.,*1999. 55. 143.
5. M.Bîrzescu, M. Niculescu, M. Ştefănescu and N. Vaszilcsin, *Chem. Bull. "Politehnica" Univ. Timisoara*, 1995. 40. 83.
6. N.Vaszilcsin, M.Birzescu, M.Stefanescu and M.Niculescu, *Bulg.Chem.Comm.*, 1996/1997. 29. 293.
7. M. Niculescu, N. Vaszilcsin, C. Muntean, C.M. Davidescu and M. Bîrzescu, *Chem.Bull. "Politehnica" Univ. Timisoara*, 1998. 43(57). 259.
8. Radoi, M. Birzescu, Fr. Golumbioschi and M. Stefanescu, *Rev. Chim. (Bucharest)*, 1985. 36. 832.
9. Fr. Golumbioschi, M. Birzescu, M. Stefanescu and M. Nemes, *Proc. Applied Electrochemistry Symp.,* Timisoara, 1985, p.399.
10. M. Niculescu, N. Vaszilcsin A.Magda and M. Medeleanu, *Chem. Bull. "Politehnica" Univ. Timisoara,* 1998. 43(57). 149.
11. B. M. Antti, *Acta Chem. Scand.,* 1973. 27. 3513.
12. Fischinger, A. Sarapu and A. Companion, *Can. J. Chem.,* 1969. 47. 2629.
13. E. Konig, *Structure and Bonding,* 1972. 9. 175.
14. P. Spacu, L. Patron, S. Plostinaru, A. Contescu and N. Stanica, *Rev. Roumaine Chim.,* 1989. 34. 1275.
15. M. Brezeanu, L. Patron, O. Carp, M. Andruch and N. Stanica, *Rev. Roumaine Chim.,* 1991. 36. 545.
16. K. Nakamoto, Y. Morimoto and A. E. Martell, *J. Am. Chem. Soc.,* 1961. 83. 4528.
17. P. V. Khadikar, *J. Thermal Anal.,* 1987. 32. 737.
18. Burbaciuc and V. P. Sokolov, *Zh. Obsc. Himii,* 1974. 44. 1626.
19. O. Ilie, *PhD Theses, Politechnical Institute of Bucharest,* 1985.
20. M. Maneva, N. Petroff and M. Pankova, *J. Thermal Anal.,*1990. 36. 577.
21. V. A. Sarov, T. M. Jdanovsky and E. A. Nikonanko, *Z. Neorg. Himii,* 1979. 24. 1489.
22. K. Nagase, K. Sato and N. Tanaka, *Bull. Chem. Soc. Japan,* 1975. 48. 439.
23. E. Segal and D. Fătu, *Introduction in nonisothermal kinetics*, Editura Academiei, Bucureşti, 1981.

STUDIA UNIVERSITATIS BABEŞ-BOLYAI, CHEMIA, XLIV, 1-2, 1999

LITHIUM INTERCALATION INTO TRANSITION METAL DICHALCOGENIDES

GEORGETA ŢARĂLUNGĂ*, SILVIA FEŞNIC, L.D. BOBOŞ, CS. BOLLA, L. ONICIU

"Babeş-Bolyai" University, Faculty of Chemistry and Chemical Engineering, 3400 Cluj-Napoca, Romania
**University of Agricultural Sciences and Veterinary Medicine, 3400 Cluj-Napoca, Romania*

ABSTRACT. The electrochemical processes of the lithium batteries are based on the intercalation phenomenon of the lithium ions into a host lattice of transition metal dichalcogenides.

This paper presents some theoretical aspects concerning the intercalation of Li^+ into TiS_2 electrodes. The physical and structural characteristics and the electrochemical behaviour of the TiS_2 electrodes were investigated by X-ray diffraction, and charge-discharge curves in galvanostatic regime.

INTRODUCTION

It is well known that lithium batteries are one of the most promising devices for light and compact power sources because of their high power, high energy density and long cycle life.

Various types of active materials for rechargeable lithium batteries have been investigated by research groups worldwide. Among these, titanium disulphide has been thought to be one of the desirable cathode materials for a high energy density secondary battery [1-6]. Its high current characteristics and good reversibility are due to the fact that the electrochemical reaction is an intercalation reaction of lithium into the van der Waals layer of titanium disulphide [7-11].

The disulphides are formed by two hexagonally close-packed sulphur layers between which reside the transition metal ions. These metal ions are found either in sites of octahedral symmetry or in ones of trigonal prismatic symmetry. The transition metals of the group IV B (Ti, Zr, Hf) are in octahedral symmetry, the group VI B (Cr, Mo, W) in the trigonal prismatic sites, but Nb and Ta of the group V B are found in both [12-14].

In Fig. 1 is shown the ordering of the Ti and S layers, as well as the octahedral symmetry sites. The S and Ti atoms are covalent bonded, but the sandwich-type building units are maintained together by van der Waals forces.

The compound is nonstoichiometric, the titanium or sulphur excess founding in the van der Waals layer. The titanium excess stabilized the compound, but a subsequent intercalation becomes more difficult, and sulphur excess led to the moulding of the titanium trisulphide, which has been unable for reversible intercalation.

The cell reaction, which results in the moulding of the intercalation compounds, is given by:

$$x\,Li + xe^- + TiS_2 \rightarrow Li_xTiS_2 \quad (1)$$

where $0 < x < 1$.

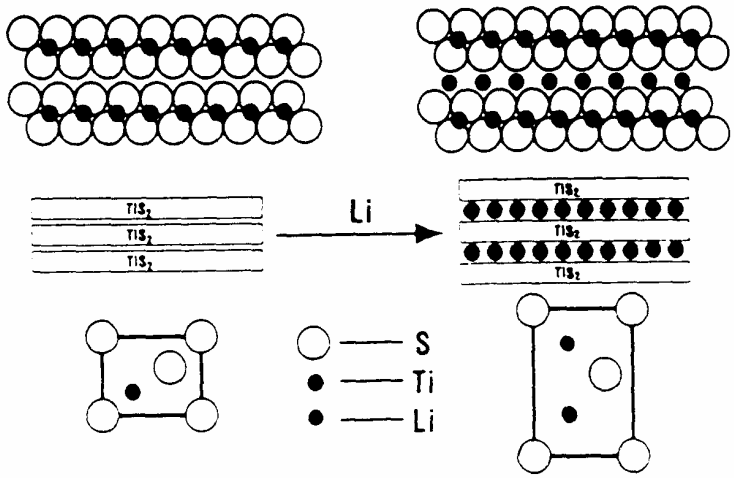

Fig. 1. Diagram representing intercalation of lithium ions in TiS_2 layered crystalline structure.

The diffusion of the lithium ions takes place only in the van der Waals layer, there being non-significant mobility perpendicular to these places. Therefore, the diffusion is bidimensional and there is not diffusion through the sulphide layers [15].

The structure of the Li_xTiS_2 intercalation compound is about the same with the crystalline structure of the host dichalcogenide.

The Li/TiS_2 cell consists of an elemental lithium anode (negative electrode), a titanium disulphide cathode (positive electrode), and a lithium salt dissolved in an aprotic nonaqueous solvent as the electrolyte. During discharge of the cell, lithium ions intercalate in the TiS_2 cathode forming Li_xTiS_2 and elemental lithium at the anode is oxidized to lithium ions.

In this paper are presented:

a) the preparation and the physical and structural characterization of TiS_2 active mass;
b) the electrochemical behaviour of TiS_2 electrodes.

In literature [16,17] there are several methods for obtaining TiS_2:

- by direct reaction between titanium and sulphur at 600^0C;
- by disproportion reaction of TiS_3 at 600^0C;
- by reaction of $TiCl_4$ and H_2S at 550^0C;

The first two methods are not advantageous because the temperature in the reaction zone must be kept rigorously. In addition, titanium disulphide obtained presents crystalline imperfections, which determine a structural reduction of the Li^+ mobility during the intercalation.

EXPERIMENTAL

We obtained TiS_2 by the third method, based on the reaction between $TiCl_4$ and H_2S:

$$TiCl_4 + 2H_2S \xrightarrow{475-550^0\,C} TiS_2 + 4HCl \qquad (2)$$

The reaction occurred in a tubular quartz reactor, placed vertically and having external heating system. The temperature in the reactor was rigorously maintained in 475-550^0 C range to avoid the decomposition of H_2S and the formation of undesired compounds (TiS_2, $TiOCl_2$).

The physical characteristics of prepared TiS_2 powder were determined by gravimmetric analysis [18].

The structural characteristics of TiS_2 active mass were investigated by X-ray diffraction (XRD) with a Dron 3 powder diffractometer, using CuK_α radiation.

TiS_2 electrodes were realized from prepared TiS_2 as active mass, graphite as electronic conductor, and teflon as binder, having different compositions.

The electrochemical behaviour of these electrodes has been investigated by charge-discharge curves in galvanostatic regime, at room temperature. The charge-discharge curves were performed for Li/ TiS_2 button batteries.

RESULTS AND DISCUSSION

The gravimmetric analysis of TiS_2 powder, having a dark tint and golden lustre, is presented in Table 1.

Table 1.

Titanium content of TiS_2 samples.

Sample	Ti (%wt)	S (%wt)
1	39.68	60.32
2	41.08	58.92
3	40.12	59.88
4	39.20	60.80
5	40.06	59.94

It can be seen that the values for titanium content are very near of theoretical value (42.76%wt) [18].

The X-ray diffraction pattern of TiS_2 prepared powder is showed in Fig. 2. and is evidenced that the X-ray diffractogram contained the specific diffractional lines of titanium disulphide.

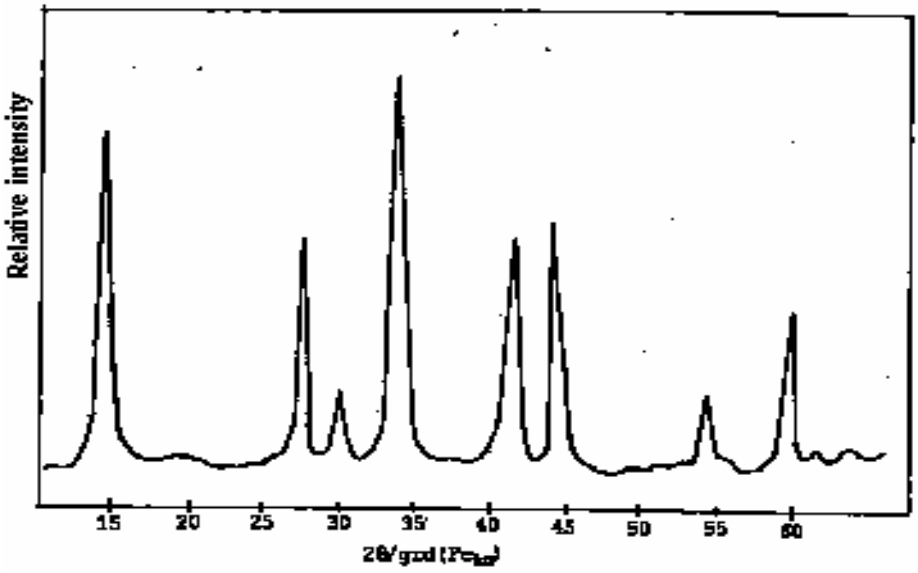

Fig. 2. X-ray diffractional patterns of TiS_2.

The electrochemical behaviour of TiS_2 electrodes was studied by testing in Li/TiS_2 cells. The discharge and charge curves presenting the voltage (U) vs. specific masic capacities (C) are illustrated in Fig. 3.

From the slopes of performance curves it comes out that Li/TiS_2 cells are reversible systems; the charge and discharge processes unfold in one stage.

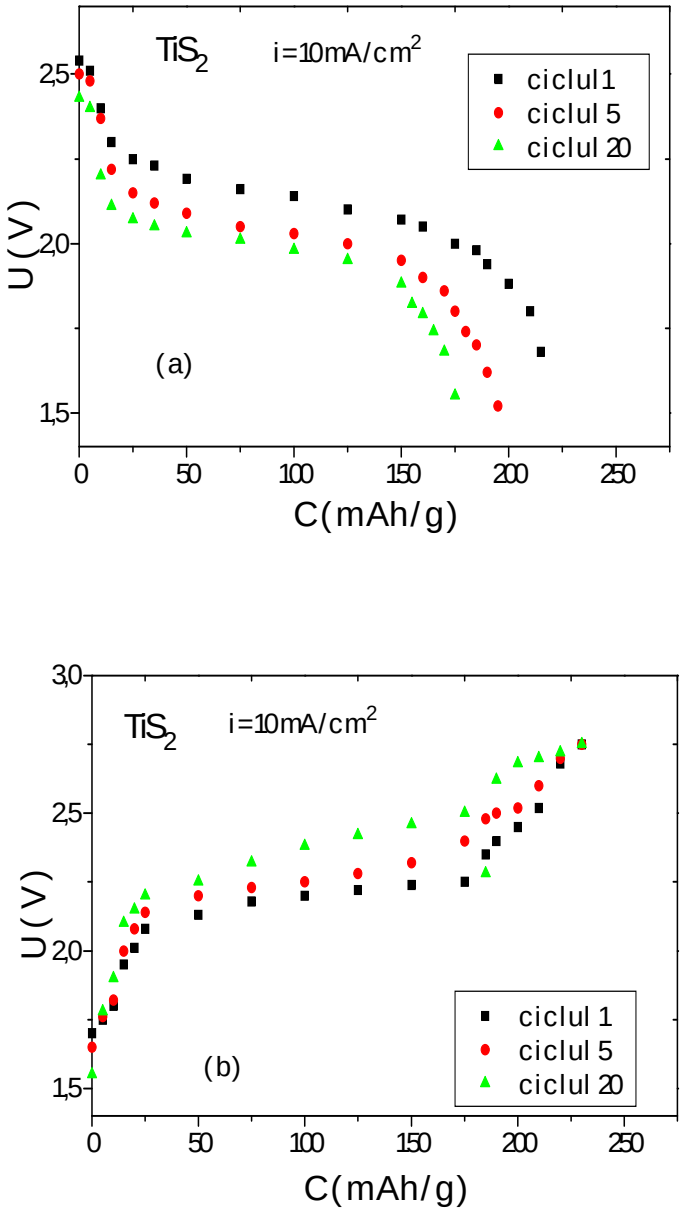

Fig. 3. Performance curves of Li/TiS_2 cell with 93.33%wt TiS_2, 0%wt graphite, and 6.67%wt teflon cathode composition; (a) discharge curves, and (b) charge curves.

The discharge curves have a slight downwarded plateau, therefore intercalation of lithium ions takes place in a larger voltage domains (2.10 - 1.90 V vs. Li/Li^+). The voltage for lithium intercalation depends on cathodic composition and on number of charge-discharge cycles.

Because the titanium disulfide is characterized by a very high electronic conductivity, it was possible to prepare electrodes without graphite or with a very small amount of graphite.

In accordance with the cathode composition, were realized three Li/TiS_2 button batteries. The opencircuit voltage cells is situated at 2.4 - 2.5 V vs. Li/Li^+, and the batteries are considered entirely discharged for 1.7 - 1.8 V vs. Li/Li^+ open circuit voltage. This value corresponds to a maximum intercalation degree of lithium ions in TiS_2 crystalline structure (x = 1).

The charge of batteries was made until the open circuit voltage was arrived at 2.7 V vs. Li/Li^+. The discharge and charge processes were performed at the same current density ($i = 10\ mA/cm^2$).

From the experimental data, corresponding to the different cycles, were calculated the discharge capacities, C_{disch}, charge capacities C_{ch}, the utilization coefficient of active material, u, and efficiency of batteries r_F. The electrochemical characteristics of TiS_2 depolarisants are shown in Table 2.

Table 2.

Electrochemical characteristics of TiS_2 electrodes.

Cycle	C_t [mAh/g]	t_{disch} [h]	C_{disch} [mAh/g]	t_{ch} [h]	C_{ch} [mAh/g]	r_F [%]	u [%]
Electrode composition: 93.33 %wtTiS_2; 0%wt graphite; 6.67%wt teflon							
1	223	7.5	210.26	8	224.28	93.74	96.28
5	223	7	196.25	8	224.28	87.50	88.00
20	223	6.2	173.83	8	224.28	77.50	77.94
Electrode composition: 89.2 %wtTiS_2; 4.47%wt graphite; 6.33%wt teflon							
1	213.18	7	205.42	8	234.76	87.49	96.36
5	213.18	6	176.07	8	234.76	74.99	82.59
Electrode composition: 85.4 %wtTiS_2; 8.53%wt graphite; 6.08%wt teflon							
1	204.08	6.7	205.44	7.5	229.98	89.32	**100.66**
5	204.08	6	183.98	7.5	229.98	79.89	90.15
12	204.08	5	153.32	7.5	229.98	66.66	75.12

As can be seen from Table 2, the best performance was obtained with the batteries without graphite in composition of the cathode. For these cells were obtained 20 charge-discharge cycles, with good efficiencies (77-94%) at high utilized degree of active mass.

The displacement between the discharge and charge curves is due almost solely to resistance losses in the electrolyte, except at the extreme values of x, where polarization becomes important.

CONCLUSION

From the obtained results it can be establish that TiS_2 electrodes present good electrochemical characteristics, the intercalation phenomenon taking place by diffusion of the lithium ions only in the van der Waals layer, there being non-significant mobility through the sulfide layers.

The electrochemical behaviour of the electrodes is influenced by the crystalline structure of active material, TiS_2, by preparation conditions, and by electrode composition (graphite and teflon ratio).

The galvanic system with TiS_2 cathodes is reversible, observing plateau regions on charge-discharge curves, which corresponds to intercalation and deintercalation of lithium ions.

The reversibility of the electrode processes descrease with the number of charge-discharge cycles, because the oxidation process becomes more difficult in the presence of lithium ions.

REFERENCES

1. L. Aselage, E.E. Hellstrom, *J. Electrochem. Soc.,* 1987,**134**, 1932.
2. S.S. Wang, *J. Electrochem. Soc.,* 1988, **135**, 1675.
3. M. Eisenberg, *Electrochim. Acta,* 1981, **26**, 955.
4. Z.I. Takemara, Z. Ogumi, *J. Electrochem. Soc.,* 1991, **138**, 1574.
5. R.H. Friend, A.D. Yoffe, *Adv. Phys.*, 1987, **36**, 1.
6. E.J. Plichta, W.K. Behl, D. Vujic, W.H.S. Chang, D.M. Schleich, *J. Electrochem. Soc.,* 1992, **139**, 1509.
7. T. Jacobsen, K. West, S. Atlung, *Electrochim. Acta*, 1982, **27**, 1007.
8. M.A. Santa-Ana, V. Sanchez, G. Gonzales, *Bol. Soc. Chil. Quim.*, 1992, **37**, 157.
9. G.L. Henriksen, D.R. Wissers, A.A. Chilenskas, *J. Power Sources*, 1995, **54**, 134.
10. M.S. Whittingham, *Prog. Solid State Chem.,* 1978, **12**, 41.
11. K. Kanehori, F. Kirino, T. Kudo, K. Miyauchi, *J. Electrochem. Soc.,* 1991, **138**, 2217.
12. K. Kanehori, F. Kirino, T. Kudo, K. Miyauchi, *J. Electrochem. Soc.*, 1991, **138**, 2216.
13. S.A. Safran, *Solid State Phys.*, 1987, **40**, 183.
14. O. Tillement, J. Angenault, J.C. Couturier, M. Quarton, *Solid State Ionics,* 1992, **53-56**, 391.
15. S.R. Narayanan, D.H. Shen, S. Surampudi, A.I. Attia, G. Halpert, *J. Electrochem. Soc.,* 1993, **140**, 1854.

16. M.B. Armand, *Materials for Advanced Batteries*, Edited by D.W. Murphy and J. Broadhead, p. 145, 1984.
17. E.J. Frazer, S. Phang, *J. Power Sources,* 1981, **6**, 307.
18. Georgeta Țarălungă, *Ph. D. Thesis,* "Babeş-Bolyai" University Cluj-Napoca, Romania, 1998.

STUDIA UNIVERSITATIS BABEŞ-BOLYAI, CHEMIA, XLIV, 1-2, 1999

ELECROSYNTHESIS OF HYDROGEN PEROXIDE BY PARTIAL REDUCTION OF OXYGEN IN ALKALINE MEDIA. PART III. WALL-JET RING ELECTRODE FOR HYDROGEN PEROXIDE AMPEROMETRIC DETECTION

VICTOR ROSCA, PETRU ILEA and IONEL CATALIN POPESCU

Department of Physical Chemistry, University "Babeş–Bolyai", 3400 Cluj-Napoca, Romania

ABSTRACT. A wall-jet ring electrode system was selected as a convenient electrochemical device for amperometric detection of hydrogen peroxide, particularly when it was "in situ" generated by partial electro-reduction of dissolved oxygen in a flow-injection set-up. Steady-state amperometric measurements were performed at an applied potential corresponding to the diffusion-controlled plateau, previously reported for hydrogen peroxide oxidation on stainless steel ring electrode. The experimental parameters, electrolyte flow rate and inlet capillary nozzle to ring electrode distance, were established to ensure a wall-jet hydrodynamic regime. In these experimental conditions, a good linear dependence between the ring limiting current *vs.* hydrogen peroxide concentration was observed. Thus, it was proved that the hydrogen peroxide obtained during electro-reduction of dissolved oxygen at wall-jet disc electrode could be successfully monitored at a ring electrode, part of a wall-jet ring disc electrode.

INTRODUCTION

Because of environmental pressure on the use of chlorine chemistry, hydrogen peroxide has been displacing some uses of chloride based chemicals in the paper and pulp industry (bleaching of mechanical pulp, brightening of chemical pulp etc.) [1-4], as well as in wastewater treatment as an oxidizing agent for electrochemical and chemical incineration of various pollutants [5-9]. These and many other reasons motivate continuous interest in electrosynthesis and detection of H_2O_2, particularly in alkaline media. Electrosynthesis of H_2O_2 by partial electro-reduction of oxygen (PERO) and the subsequent use of H_2O_2 solutions in industrial processes require a rigorous control of its concentration [10].

Several techniques, as for example thermometric, potentiometric, optical, conductivity measurements etc. were adapted to measure H_2O_2 concentration. However, until now, none of them gave satisfactory results in terms of continuous and/or in-line monitoring, reliability, stability, and low cost. An important advance along this line was achieved by elaboration of new modified electrodes for H_2O_2 selective detection. For example, should be mentioned amperometric sensors based on glassy carbon electrodes modified with nickel tetra-aza-macrocyclic complexes [12], polyaniline films and platinum particles co-modified carbon fiber microelectrodes [13], peroxidase based biosensors [14,15] etc. This approach permits to improve especially the selectivity of the H_2O_2 detection.

On the other hand, electrochemical sensors are easily adapted to measurements in flow-injection systems. Thus, they can satisfy most of requirements for an ideal flow-through cell as, for example, good washing characteristics, low dead volume, fast response, and simple maintenance [16, 17]. Among the different used hydrodynamic configurations, the wall-jet one was recognized as one of the most convenient for a flow-injection detector [18]. That is why, a wall-jet electrochemical system was selected in our investigation of PERO on carbonaceous materials [18,10].

In this context, the present work was done in order to prove that the hydrogen peroxide obtained during electro-reduction of dissolved oxygen at wall-jet disc electrode could be successfully monitored by measuring the limiting current developed at ring electrode during its oxidation on a wall-jet ring disc electrode (WJRE). For this purpose, the influence of the main experimental parameters, electrolyte flow rate, inlet capillary nozzle to ring electrode distance, and hydrogen peroxide concentration, on the sensor out-put was investigated.

EXPERIMENTAL

Reagents and materials

All reagents were of analytical grade and used without any further purification. 1M NaOH aqueous solution was used as supporting electrolyte for all electrochemical measurements. All solutions were prepared with doubly distilled water.

The working ring electrode was made of stainless steel (AISI 304).

Electrochemical measurements

The wall-jet ring disc electrode was a part of a wall-jet electrochemical cell [19] (Figure 1) equipped with a homemade ring disc electrode [18]. Accordingly to the purpose of this study the disc electrode was deactivated, and hence the WJRE resulted. A Pt wire was used as counter electrode and an Ag/AgCl, KCl 1M served as reference electrode.

In order to construct the ring working electrode (r_{out} = 3 mm, r_{inn} = 2 mm) a stainless steel ring was mounted in a Perspex body, and was sealed with epoxy resin. Before use, the ring electrode was carefully wet polished with emery paper (grit 400 and 600, Carbochim, Romania) and Al_2O_3 (1 μm).

The upper part of the electrochemical cell, where the WJRE was inserted, has a thread with 1 mm step, allowing a fine-tuning of distance (d) between the inlet capillary nozzle (ϕ = 0.5 mm) and the WJRE surface. The electrochemical cell was inserted into a single line flow system, consisting of a peristaltic pump (Alitea-XV, Sweden), equipped with a silicone tubing (0.16 $cm^3\,m^{-1}$).

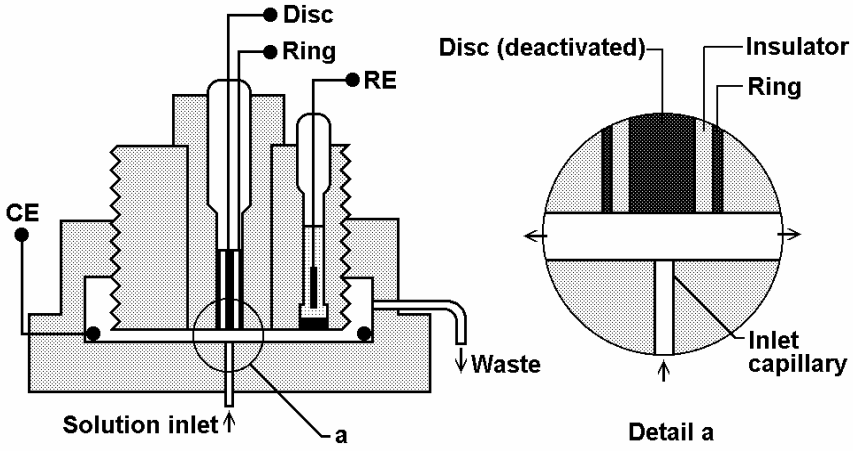

Figure 1. Scheme of the wall-jet electrochemical cell equipped with a ring disc electrode.

The three electrodes of the electrochemical cell were connected to a low current custom-made potentiostat, controlled by an IBM-PC (Olivetti 486/33) through a data acquisition card (AT-MIO-16F-5, National Instruments, USA). The software for monitoring the set-up and to perform data acquisition was based on LabVIEW 3.1 software [20].

Steady-state amperometric measurements were performed at an applied potential selected in the diffusion-controlled plateau, previously observed for hydrogen peroxide oxidation on stainless steel electrode [18].

RESULTS AND DISCUSSIONS

The limiting current, observed in a WJRE system is strongly influenced by the hydrodynamic conditions under which the system is operated [21]. In addition, the potential of the ring electrode has to be established in the domain controlled by mass transfer.

In this context, for this work an alternative procedure to that described previously [18] was followed. Thus, basically hydrogen peroxide was oxidized at WJRE when its potential was linearly swept with a slow rate, between + 0.1 and + 0.48 V *vs.* Ag/AgCl, KCl 1M. Modifying the hydrogen peroxide concentration, the distance between the inlet capillary nozzle and the ring plane for different electrolyte flow rate it was tried to establish simultaneously two goals: (i) the optimum hydrodynamic regime; (ii) the linear range of the dependence between the limiting current and the hydrogen peroxide concentration.

In order to check the assumption that, for the selected experimental conditions, the WJRE is working under wall-jet hydrodynamic regime the following equation was used [22]:

$$i_L = 1.59knFCD^{2/3}\upsilon^{-5/12}a^{-1/2}A^{3/8}V_f{}^{3/4}r_{in}{}^{3/4}\beta^{2/3}$$

where, $\beta = (r_{out}^q - r_{in}^q)/r_{in}^q$ and for a wall-jet system q = 9/8 [22]

k is a constant determined by experimental way to be 0.86 [23];
a – inlet capillary nozzle diameter, cm;
A – electrode aria, cm^2;
C – concentration, mol cm^{-3};
F – Faraday constant; C eq^{-1}
D – diffusion coefficient; $cm^2\ s^{-1}$;
ν – cinematic viscosity; $cm^2\ s^{-1}$;
V_f – volume flow rate; $cm^3\ s^{-1}$
n – number of exchanged electrons.

In Table 1 are presented the slopes and the correlation coefficients of the regression lines obtained for linear fitting of log i_L *vs.* log V_f, at two values of the distance between the inlet capillary nozzle and the ring electrode. It can be seen that for the distance of 2 mm, the hydrodynamic regime is well a wall-jet one: the slope of the log i_L *vs.* log V_f dependence is closed to the theoretical value (0.75). For a smaller value of the distance, 1 mm, the hydrodynamic regime was not well defined (experimental data are not shown). For a higher value, 3 mm, the hydrodynamic regime starts to deviate significantly from a wall-jet one (the slopes differ significantly from 0.75).

The second step consisted of the analysis of i_L *vs.* hydrogen peroxide concentration dependence in the domain of wall-jet hydrodynamic regime predomination. In figure 2 are represented i_L *vs.* C_m (H_2O_2) plots for 6 volume flow rates and two different distances.

First of all, we can notice a good linearity between the limiting current and H_2O_2 concentration, for all flow rates when the distance was 2 mm (see also Table 2). This fact can be attributed to the stability of the wall-jet regime in the selected working conditions.

Table 1.

Linear fitting parameters of log i_L *vs.* log V_f dependencies.

d = 2 mm		d = 3 mm	
$[H_2O_2]$ mM	**Slope / R / N**	**$[H_2O_2]$ mM**	**slope / R / N**
1.5	0.7845 / 0.97824 / 5	1.5	0.7826 / 0.9484 / 5
2.3	0.7536 / 0.9859 / 5	2.3	0.6821 / 0.9716 / 5
3.1	0.7832 / 0.9969 / 5	3.1	0.8164 / 0.9819 / 5
3.8	0.7445 / 0.9982 / 5	3.8	0.5894 / 0.9713 / 5
4.6	0.7817 / 0.9817 / 5	4.6	0.70655 / 0.9678 / 5
R – the correlation coefficient N – the number of experimental points			

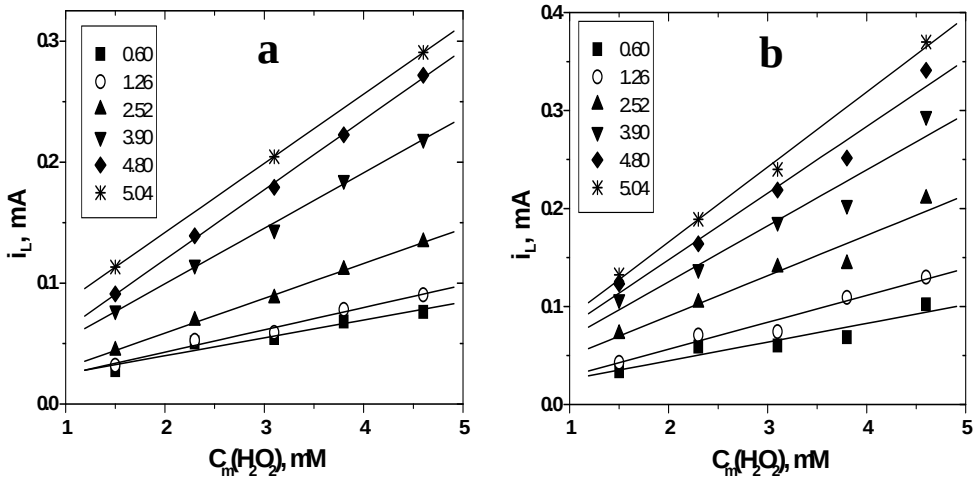

Figure 2. Dependence of the WJRE limiting current *vs.* hydrogen peroxide concentration: (*a*) d = 2 mm; (***b***), d = 3 mm. Numbers in the legend are the values of volume electrolyte flow rate (cm^3 min^{-1}). Experimental conditions: applied potential, + 400 mV *vs.* Ag/AgCl, KCl 1M; flow carrier, 1M NaOH solution.

The best linear fittings are observed for intermediate flow rates. This can be explained by the instability of the hydrodynamic regime at low flow rates, and by the decrease of the limiting current plateau at high flow rates, both involving an increasing error in the evaluation of the limiting current value. Analyzing the similar data for the distance of 3 mm it can be noticed that for a mixed hydrodynamic regime a worse linearity was observed.

In order to demonstrate the performances of the investigated system, the values of main analytical parameters are given below. Thus, for an electrolyte flow rate of 4.80 cm^3 min^{-1}) we found: the minimum sample volume, 500 μL; number of samples per hour, 30 s/h; sensitivity, 15.5 mA/mM;

detection limit, 0.71 mM (for S/N = 3). It should be added the an important advantage of the proposed detection technique is the possibility to slightly increase the system sensitivity by increasing the electrolyte flow rate.

Table 2.

Parameters of linear regression lines for i_L *vs.* C_m (H_2O_2) dependencies.

Inlet capillary nozzle to ring electrode distance			
2 mm		**3 mm**	
V_f (cm^3 min^{-1})	**Cor. coeff. / No. of points**	**V_f (cm^3 min^{-1})**	**Cor. coeff. / No. of points**
0.60	0.9822 / 5	0.60	0.9411 / 5
1.26	0.9940 / 5	1.26	0.9778 / 5
2.52	0.9988 / 5	2.52	0.9802 / 5
3.90	0.9981 / 5	3.90	0.9813 / 5
4.80	0.9994 / 5	4.80	0.9868 / 5
5.04	0.9999 / 3	5.04	0.9976 / 4

CONCLUSIONS

Experimental data demonstrate two important points:

(i) The wall-jet hydrodynamic regime is remarkably stable at small variations of the electrolyte flow rate and the distance between the inlet capillary nozzle and the electrode.

(ii) For the wall-jet hydrodynamic regime (d = 2 - 3 mm and V_f = 2.5 - 5.0 cm^3 min^{-1}) a strong linear regression between the ring limiting current (i_L) and the H_2O_2 concentration (up to 5 mM) was observed.

Taking into consideration these electroanalytical characteristics we can conclude that the wall-jet configuration render to the electrochemical response of the WJRE a high stability and a good sensitivity, qualities that often are decisive to establish the level of performance for a flow-injection method of analysis. Concluding, the WJRE system can by recommended as an alternative method for "in-line" amperometric detection of H_2O_2.

ACKNOWLEDGEMENT

Financial support from CNCSIS (Grant 53/109-1999) is gratefully acknowledged. The single line flow system is a kindly gift from Dr. Lo Gorton, Lund University, Sweden. The authors thank Adrian Nicoara for the data acquisition software. We also thank Sorin Dorneanu for his technical assistance.

REFERENCES

1. E.E. Kalu and C. Oloman, J. Appl. Electrochem., 1990. **20.** 932.
2. B.V. Tilak, in "Electrochemistry for a Cleaner Environment", J.D. Genders and N.L. Weinberg (eds.), p. 387, The Electrosynthesis Company Inc, New York, 1992.
3. J.A. McIntyre, The Electrochemical Society Interface, 1995, **4**(2), 29.
4. O. Savadogo and S. Leclerc, Résumés des Comunications, Journées d`Electrochimie, Montréal, 1997.
5. P. Westbroec, E. Temmerman and P. Kiekens, Anal. Commun., 1998, **35**, 21.
6. J.-S. Do and C.-P. Chen, J. Appl. Electrochem., 1994, **24**, 936.
7. C. Ponce de Leon and D. Pletcher, J. Appl. Electrochem., 1995, **25**, 307.
8. Y.-L. Hsiao and K. Nobe, J. Appl. Electrochem., 1993, **23**, 943.
9. J.-S. Do and W.-C. Yeh, J. Appl. Electrochem., 1996, **26**, 673.
10. O. Serdan, C. Ghiurutan, P. Ilea and I.C. Popescu, unpublished results.
11. R. Toniolo, N. Comisso, G. Bontempelli, G. Schiavon, Electroanalysis, 1996, **8**,151.
12. J. Taraszewska and G. Roslonek, J. Electroanal. Chem., 1994, **371**, 223.
13. Yu. Wang, J. Huang, J. Wei and X. Zhou, Electroanalysis, 1998, **10**, 776.
14. D. Wilke, H. Muller and N. Kolytsheva, Fresenius J. Anal. Chem., 1997, **357**, 534.
15. Z. Zhang, C. Lei, W. Sun, H. Liu and J. Deng, J. Electroanal. Chem., 1996, **419**, 85.
16. W. Frenzel, Analyst, 1988, **113**, 1039.
17. J.G. Douglas, Anal. Chem., 1989, **61**, 922.
18. P. Ilea, S. Dorneanu and I.C. Popescu, J. Appl. Electrochem., 2000, **30**, .
19. R. Appelqvist, G. Marko-Varga, L. Gorton, A. Torstensson and G. Johansson, Anal. Chim. Acta, 1985, **169**, 237.
20. A. Nicoara, L. Oniciu and S. Dorneanu, Rev. Roumaine Chim., 1998, **43**, 823.
21. H. Gunasingham and B. Fleet, in A.J. Bard (Ed.) "Electroanalytical Chemistry", vol. 16, Marcel Dekker, New York. 1989, 96.
22. W.J. Albery and C.M.A. Brett. J. Electroanal. Chem., 1983, **148**, 201.
23. D.C. Johnson and R.E. Allen, Talanta, 1973, **20**, 305.

STUDIA UNIVERSITATIS BABEŞ-BOLYAI, CHEMIA, XLIV, 1-2, 1999

REMOVAL OF SODIUM LINEAR ALKYLBENZENE SULPHONATE BY ELECTROCOAGULATION-ELECTROFLOTATION

G.A. CIORBA[1], C. RADOVAN[2], I. VLAICU[3] and A. IOVI[4]

[1] ECOIND Branch in Timisoara, University "Politehnica", P.O. Box 254, Of.1, 1900 Timisoara, Romania
[2] West University of Timisoara, Str. Pestalozzi No.16, 1900 Timisoara, Romania
[3] AQUATIM, Str. Paris No. 2, 1900 Timisoara, Romania
[4] University "Politehnica" of Timisoara, P-ta Victoriei No. 2, 1900 Timisoara, Romania

ABSTRACT. This paper took into consideration the behaviour of an aluminium electrode in the presence and in the absence of sodium linear alkylbenzene sulphonate. It acted as the organic component of a simulated wastewater. In addition, the effect of the organic load (surfactant concentration) on the separation of the surfactant from water was studied. The characterisation of the electrode material was carried out by polarisation measurements under potentiostatic and galvanostatic conditions with scan rates of 0.02 V/s and 0.0001 A/s, respectively. The electrode processes could be stimulated or inhibited depending on the history of the electrode and the composition of the simulated wastewater. The change of the anodic inhibition or activation was interpreted by the character of the superficial oxide film and partially de-filming process. The simulated wastewater treatment was carried out in an electrocoagulation-electroflotation cell in galvanostatic conditions. The efficiencies of treatment ranged between 70-80% as Chemical Oxygen Demand (COD) removal. The increase of surfactant concentration over 0.75 g/L caused a sharp fall of the treatment efficiency.

INTRODUCTION

The removal of synthetic surfactants from aqueous solution (industrial and rinsing wastewaters) is not so easy to accomplish. The diphilic feature of surfactant molecules and hydrophilic interactions of their micelles determine a rather difficult separation from water.

Electrocoagulation alone or together with electroflotation provides effective separation and can offer a better treatment than the conventional ne with reagents. This method implies wastewater electrolysis using soluble metal anodes, coagulant generation and pollutant separation by combined effects [1-10].

Various aspects of aluminium behaviour have been reported extensively by many authors [7-20]. However, case studies concerning the behaviour of aluminium in wastewater containing surfactant have been reported less frequently [4-10].

This paper investigated the interactions between sodium linear alkylbenzene sulphonate (LABS) and aluminium anode with consequences regarding the effective separation of surfactant from water. The working conditions referred to low concentration of sodium chloride (Cl^- as activator), sodium sulphate as supporting electrolyte and the absence or the presence of surfactant. The pH of 4.0 was in agreement with the initial pH in an operating electrocoagulation-electroflotation cell. Other objectives of this paper were to study the effect of the organic load on the separation of the surfactant and to find out a limiting surfactant concentration.

RESULTS AND DISCUSSION

The first series of voltammetric measurements aimed to reveal the behavioural pattern of the aluminium electrode in selected conditions of sulphate content and low chloride concentration. Fig. 1 gives the plots of current (logarithmic scale) against potential at 0.02 V/s scan rate. The passivation sector was substantially wider for sulphate (curve 1) than the equivalent one for chloride (curve 2). This was in good agreement with previously reported data for higher concentrations of anions [12-16].

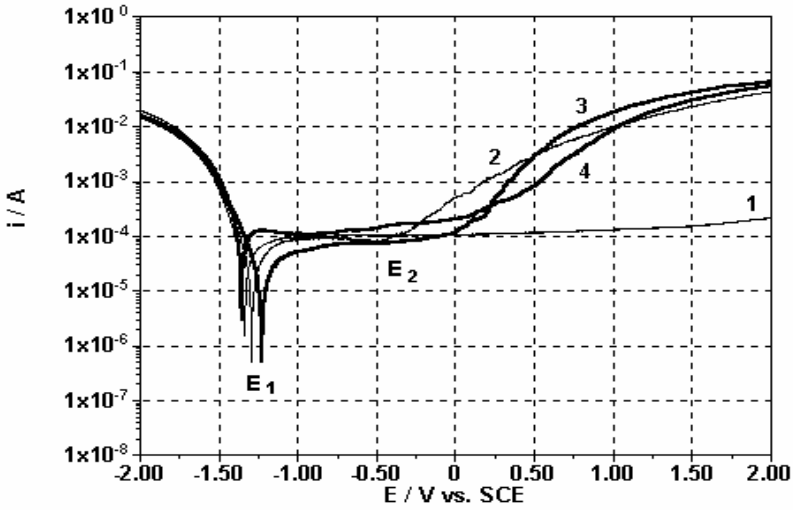

Fig. 1. Potentiostatic polarisation data for aluminium electrode at 0.02 V/s in Na_2SO_4 0.1 M (***1***); Na_2SO_4 0.1 M + NaCl 0.01 M (***2***); Sodium Linear Alkylbenzene Sulphonate (LABS) 0.5 g/L + Na_2SO_4 0.1 M + NaCl 0.01 M (***3***) and LABS 1.5 g/L + Na_2SO_4 0.1 M + NaCl 0.01 M (***4***); pH 4.0

The lower limit of the passivation potential range could be set up for potential E_1, which corresponded to zero current passage. E_1 can be considered conventionally as a "corrosion potential". The upper limit, E_2, is the breakdown potential, pointing out the beginning of the active dissolution that occurred mostly in presence of chloride (almost two orders of magnitude vs. sulphate). The cathodic prepolarisation generated OH^- ions, which then were involved in the formation of a superficial "film" (hydrated oxide) with the anodically generated aluminium ions. Two effects were overlaid on the anodic branch: diffusion limitations and the formation of the superficial layer. The latter aspect implied the permeability of that layer, which could be also a limiting factor.

The shape of polarisation curves was not changed essentially in the presence of sodium linear alkylbenzene sulphonate. The higher the concentration of the surfactant the longer the passivation sector corresponding to E_1-E_2.

The cyclic voltammograms in Fig. 2, in the presence and in the absence of the surfactant, pointed out again the activating effect of chloride ion. The aluminium electrode was practically passivated over an extended range of potential (curve 1) in the presence of sulphate as the only component of the solution. Curves 2, 3 and 4 pointed out a supplementary and remanant activation on the backward branch due to enough induction time for the film breakdown, increased roughness of the active surface and diffusion of anodically generated species. The increase of LABS concentration determined lower currents both on the forward and backward branches of the curves. Even in the presence of the surfactant (curves 3 and 4), the behavioural pattern of the electrode was predominant. However, the involvement of surfactant in electrode processes might be discussed as a wetting effect at controlled potential and pH change on the very surface of the electrode.

Galvanostatic polarisation data were required for a better approach to the common galvanostatic conditions in electrochemical wastewater treatment (electrocoagulation-electroflotation). Comparable and reproducible data could be obtained by cathodic prepolarisation followed by galvanostatic scan from –0.020 A to +0.020 A. Those values corresponded to the upper limits of current density in an electrocoagulation-electroflotation cell.

The cathodic prepolarisation also generated OH^- ions, which interacted with anodically generated aluminium ionic species. Duration of diffusion, formation of the superficial layer and defilming by chloride activation were correlated with the scan rate. The scan rate of 0.1 mA/s was chosen for all measurements to provide enough time for activation and diffusion of the anodic products. Without cathodically controlled prepolarisation, the formation of the superficial layer occurred randomly.

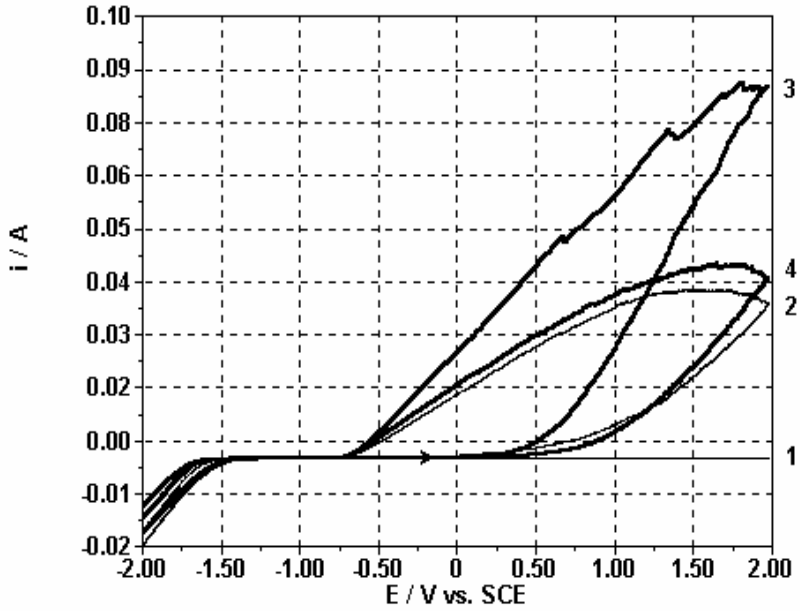

Fig. 2. Potentiostatic cyclic voltammograms for aluminium electrode at 0.02 V/s in Na_2SO_4 0.1 M (***1***); Na_2SO_4 0.1 M + NaCl 0.01 M (***2***); Sodium Linear Alkylbenzene Sulphonate (LABS) 0.5 g/L + Na_2SO_4 0.1 M + NaCl 0.01 M (***3***) and LABS 1.5 g/L + Na_2SO_4 0.1 M + NaCl 0.01 M (***4***); pH 4.0

Figure 3 shows the effect of the surfactant and the inorganic components at pH 4.0. The formation of the superficial layer determined the increase of polarisation. The most pronounced increase was given by sulphate. The anodic peaks were smaller in the presence of LABS, but at higher current densities, the curve 4 corresponded to an increase of polarisation. This aspect could be interpreted as an increase of thickness and permeability of the layer.

The experiments for the separation of the anionic surfactant were carried out in an electrocoagulation-electroflotation cell taking into account the galvanostatic polarisation data and the fact that LABS is widely used in various compositions of detergents. The current density ranged between 50-200 A/m^2. In all separation experiments, the initial pH was 3.1. The initial concentration of LABS ranged between 0.1-2.5 g/L to simulate various compositions of wastewater.

Tables 1 to 4 show the influence of the current density on the treatment efficiency and power consumption. At 200 A/m^2 the process developed very intensively, but the improvement of the treatment efficiency was not significant in comparison with the lower current densities. The effect of surfactant concentration on the evolution of treatment by electrocoagulation-

electroflotation was studied for a current density of 50 A/m^2. Two situations of 0.15 and 0.30 Ah quantity of electricity are shown in Fig. 4. In comparable conditions of quantity of electricity, the treatment efficiencies decreased with the increase of surfactant load. It would have been necessary higher quantities of electricity to get higher removal of chemical oxygen demand.

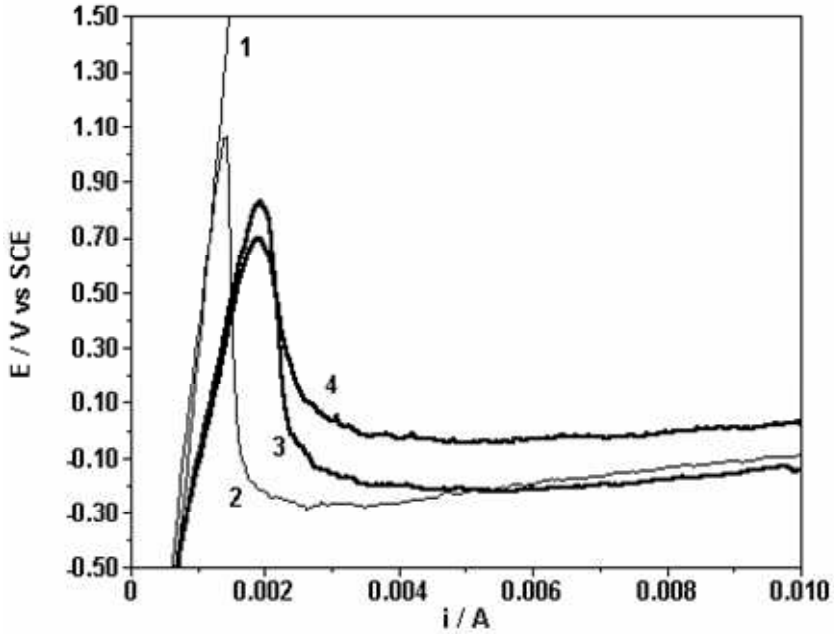

Fig. 3. Galvanostatic polarisation data for aluminium electrode at 0.0001 A/s in Na_2SO_4 0.1 M (***1***); Na_2SO_4 0.1 M + NaCl 0.01 M (***2***); Sodium Linear Alkylbenzene Sulphonate (LABS) 0.5 g/L + Na_2SO_4 0.1 M + NaCl 0.01 M (***3***) and LABS 1.5 g/L + Na_2SO_4 0.1 M + NaCl 0.01 M (***4***); pH 4.0

Table 1.

The evolution of treatment by electrocoagulation-electroflotation for the separation of sodium linear alkylbenzene sulphonate (i_A 50 A/m^2; C_i 0.5 g/L; COD_i 915 mg O_2/L; pH_i 3.1; NaCl 1 g/L; at 22 ℃)

Q (Ah)	U (V)	pH_f	COD (mg O_2/L)	COD removal (%)	W_{sp} (kWh/m^3)
0.05	1.30	3.4	352	61.5	0.1
0.10	1.35	4.4	337	63.2	0.2
0.15	1.35	4.7	222	75.7	0.3
0.20	1.35	4.8	177	80.7	0.4
0.30	1.35	5.0	162	85.7	0.6

Q-Quantity of electricity; U-Cell voltage; i_A- Current density; C_i-Initial surfactant concentration; COD-Chemical Oxygen Demand; pH_i, pH_f-Initial and final pH; W_{sp}-Specific electric energy consumption

Table 2.

The evolution of treatment by electrocoagulation-electroflotation for the separation of sodium linear alkylbenzene sulphonate (i_A 100 A/m^2; C_i 0.5 g/L; COD_i 915 mg O_2/L; pH_i 3.1; NaCl 1 g/L; 22 ℃)

Q (Ah)	U (V)	pH_f	COD (mg O_2/L)	COD removal (%)	W_{sp} (kWh/m^3)
0.05	2.0	4.6	402	56.1	0.1
0.10	2.0	4.9	254	72.2	0.3
0.15	2.0	5.2	178	80.5	0.4
0.20	2.0	6.0	178	80.5	0.6
0.30	2.0	7.0	147	83.9	0.9

Table 3.

The evolution of treatment by electrocoagulation-electroflotation for the separation of sodium linear alkylbenzene sulphonate (i_A 150 A/m^2; C_i 0.5 g/L; COD_i 915 mg O_2/L; pH_i 3.1; NaCl 1 g/L; 22 ℃)

Q (Ah)	U (V)	pH_f	COD (mg O_2/L)	COD removal (%)	W_{sp} (kWh/m^3)
0.05	2.8	4.6	406	55.6	0.2
0.10	2.7	4.8	266	70.9	0.4
0.15	2.7	5.3	239	73.9	0.6
0.20	2.7	6.2	217	76.3	0.8
0.30	2.6	7.1	180	80.3	1.1

Table 4.

The evolution of treatment by electrocoagulation-electroflotation for the separation of sodium linear alkylbenzene sulphonate (i_A 200 A/m^2; C_i 0.5 g/L; COD_i 915 mg O_2/L; pH_i 3.1; NaCl 1 g/L; 22 ℃)

Q (Ah)	U (V)	pH_f	COD (mg O_2/L)	COD removal (%)	W_{sp} (kWh/m^3)
0.05	3.2	4.6	516	43.6	0.2
0.10	3.3	4.8	262	71.4	0.5
0.15	3.1	5.3	213	76.8	0.7
0.20	3.2	5.9	174	81.0	0.9
0.30	3.2	7.0	150	83.6	1.2

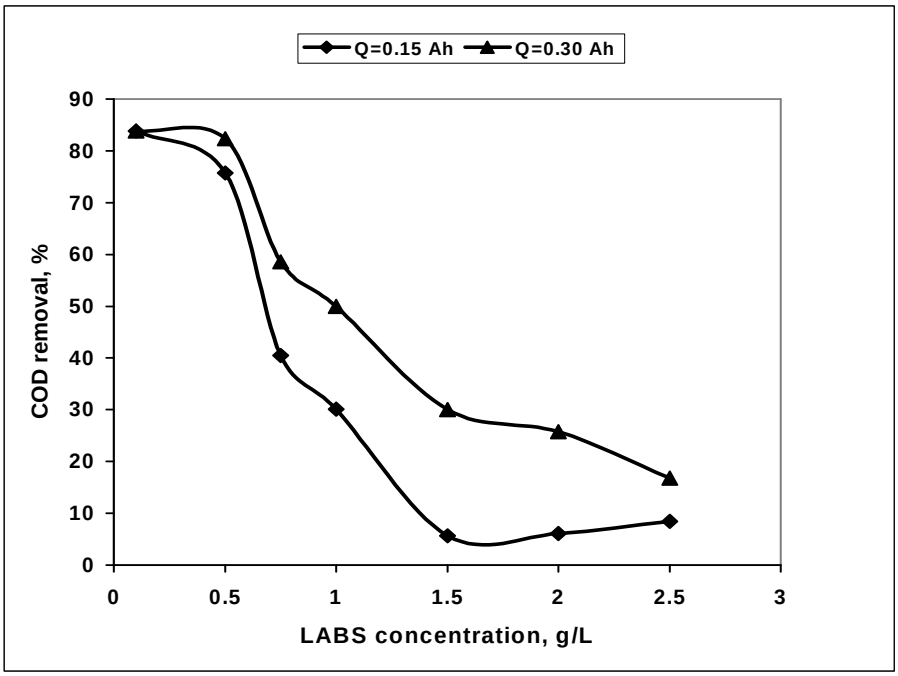

Fig. 4. The influence of sodium linear alkylbenzene sulphonate concentration on treatment efficiency.

The separation of the surfactant was badly affected over concentration of 0.75 g/L when the destabilisation of surfactant micelles was more difficult to accomplish. The effect of the organic load could be associated with hydrophilic interactions within the bulk of solution. The colloidal system consisting of aluminium hydroxocomplexes was stabilised by the presence of the surfactant.

At surfactant concentration below 0.7 g/L, the treatment was conducted in conditions of satisfactory power consumption (0.2-0.3 kWh/m^3) and chemical oxygen demand removal (60-80%). The voltage of the cell did not reflect any limitations of aluminium dissolution, the only limiting interactions resulting from the increase of the organic load were in the bulk of solution. The effect of the organic load was more significant in the experiments of water treatment than in those ones concerning polarisation curves.

EXPERIMENTAL

The behaviour of aluminium electrode (Al 99.3%, an ALRO Company product) was investigated in potentiostatic and galvanostatic conditions. The working electrode in voltammetric measurements was cleaned with two-grade emery paper, filter paper, degreased with acetone and washed

carefully. The aluminium cylindrical working electrode (2.8 mm diameter) was mounted vertically and had an exposed surface area of 1 cm^2. Thus, current (A) was equivalent to current density (A/cm^2). The counter electrode was made of aluminium and had a large surface area. A saturated calomel electrode (SCE) was used as a reference electrode. The cell used for the voltammetric measurements had no separated anodic and cathodic compartments.

The device used was the system Autolab-Ecochemie PGstat 20. The overall anodic and cathodic processes were studied by voltammetric techniques: cyclic voltammetry (linear scan), linear sweep voltammetry (current integration) and linear sweep voltammetry (galvanostatic). The potential ranged from -2 to +2, V vs. SCE in potentiostatic measurements and the current ranged from –0.020 A cathodic current to +0.020 A. The scan rates were 0.02 V/s and 0.0001 A/s, respectively. The static working electrode was pre-polarised cathodically (3 minutes) to provide conventionally reproducible conditions.

The electrocoagulation-electroflotation cell used in the wastewater treatment experiments is shown in Fig. 5.

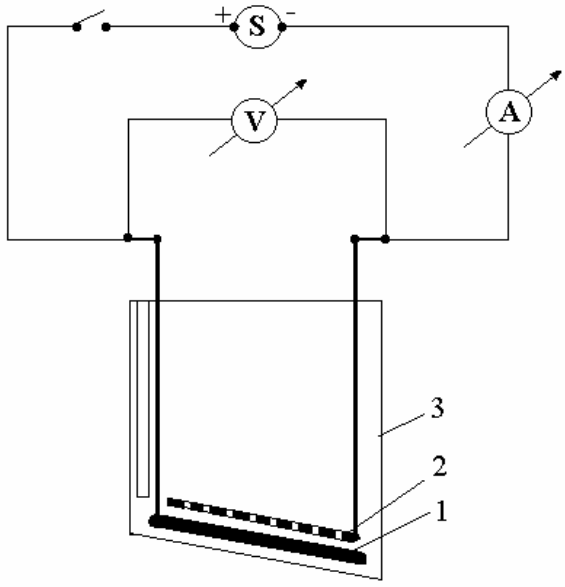

Fig. 5. Schematic diagram for experimental set-up of surfactant separation in an electrocoagulation-electroflotation cell: 1-Anode: aluminium plate, surface area, 60 cm^2; 2-Cathode: grid of stainless steel wires, Φ 3 mm; Surface area ratio, S_A/S_C 1.44; 3-cell, made of plexiglass; Surfactant concentration: 0.1-2.5 g/L; Batches of 0.7 L were run into the cell;

The reagents were NaCl and Na_2SO_4 p.a. (Rompar), technical grade sodium linear alkylbenzene sulphonate: CH_3-$(CH_2)_{11}$-C_6H_4-SO_3Na supplied by Romtensid Romania and doubly distilled water. The supporting electrolyte used for voltammetric measurements contained Na_2SO_4 0.1M and NaCl 0.01 M as activator. The temperature was 22±1℃.

CONCLUSION

The behaviour of aluminium as electrode material was studied in various solutions (low sodium chloride concentration, sodium sulphate and sodium linear alkylbenzene sulphonate anionic) and at pH 4.0. The overall anodic and cathodic processes were studied by voltammetric techniques: cyclic voltammetry and linear sweep voltammetry in potentiostatic and galvanostatic variants.

The potentiostatic polarisation curves were analysed as resultant curves. Even in the presence of the surfactant, the behavioural pattern of the electrode was predominant. However, the involvement of the surfactant in electrode processes might be discussed as a wetting effect at controlled potential and pH change on the very surface of the electrode.

The change of the anodic inhibition or activation was developed more clearly in conditions of galvanostatic polarisation of the electrode and interpreted by the character of superficial film and partially defilming process. The formation of the superficial layer determined the increase of polarisation. The effect of LABS correlated partially with the increase of the surfactant concentration, when polarisation was higher towards higher current densities. This aspect could be interpreted as an increase of thickness and permeability of the layer.

The simulated water treatment was carried out in an electrocoagulation-electroflotation cell in galvanostatic conditions. In addition to the electrode processes, reactions in the bulk of solution influenced the processes that occurred at the adsorption surface of the electrochemically-generated coagulant.

The wastewater treatment by electrocoagulation-electroflotation at 50 A/m^2 current density yielded higher separation efficiency (70-80%) even at 0.15 Ah and low specific energy consumption (0.2-0.3 kWh/m^3) for surfactant concentrations of 0.1-0.5 g/L. The increase of surfactant concentration over 0.75 g/L caused a sharp fall of the treatment efficiency and the method was no longer feasible. The limiting surfactant concentration of 0.75 g/L was associated with the hydrophilic interactions and the stabilisation of the colloidal system.

Usually, high concentrations of surfactants are not common in rinsing and industrial wastewater. Some of our experiments with real wastewater pointed up the same high treatment efficiencies as those for the treatment simulations.

REFERENCES

1. S.V. Yakovlev, I.G. Krasnoborod'ko and V.M. Rogov, *Technologhiya elektrokhimicheskoi ochistki vody*, Stroizdat, L., 1987.
2. L. A. Kulskyi, P.P. Stokach, V.A. Slipenko and E.I. Saigak, *Ochistka Vody Electrokoagulyatsei*, Budivelnik, Kiev, 1978.
3. K. Scott, *Electrochemical Processes for Clean Technology*, The Royal Society of Chemistry, London (1995).
4. C. Berset, H. Jaskiewicz, C. Tran Manh Sung and F. Sandret, *Trib. CEBEDEAU* 1979, **427**, 79.
5. S. P. Novikova, T. L. Skorbatova and E. Ya. Sokol, *Khim. Tekh. Vody*, 1982,**4**, 352.
6. V. Cocheci, C. Radovan, A. Bugarski and L. Andres, *Rev. Chim.*, 1989, **40**, 446.
7. C. Radovan, I. Vlaicu, G.A. Ciorba and M. Adam-Stoia, in *Proceedings of the Symposium "Energy and Electrochemical Processing for a Cleanner Environment"*, (Edited by C.W. Walton and E.J. Rudd), **27-28**, p. 427, ECS, Pennington, N.J. 1998.
8. C. Radovan, I. Vlaicu, G.A. Ciorba and M. Adam-Stoia, *Annals of West University of Timisoara, Ser. Chem.*, 1997, **6**, 259.
9. C. Radovan, G.A. Ciorba and I. Vlaicu, *Annals of West University of Timisoara, ser. chem.*, 1997, **6**, 267.
10. G. Ciorba, C. Radovan, I. Vlaicu, L. Pitulice, submitted to *Electrochimica Acta*
11. M. Pourbaix, *Atlas of Electrochemical Equilibria in Aqueous Solutions*, Pergamon Press, London 1966.
12. A.D. Davydov and A.N. Kamkin, *Eletrokhimiya*, 1978, **14**, 979.
13. M. Kliskic, J. Radosevic, S. Gudic and M. Smith, *Electrochim. Acta*, 1998, **43**, 3241.
14. D.M. Drazic, S.K. Zecevic, R.T. Atanasoski and A.R. Despic, *Electrochim. Acta*, 1983, **28**, 751.
15. R.M. Stevanovic, A.R. Despic and D.M. Drazic, *Electrochim. Acta*, 1988, **33**, 397.
16. L. Tomcsany, C. Varga, I. Bartik, G. Horanyi and E. Maleczky, *Electrochim. Acta*, 1989, **34**, 855.
17. L. Chen, N. Myung, P.T.A. Sumodjo and K. Nobe, *Electrochim. Acta*, 1999, **44**, 2751.
18. E. Brillas, P.L. Cabot, F. Centelas, J.A. Garido, E. Perez and R.M. Rodriguez, *Electrochim. Acta*, 1998, **43**, 799.
19. S.M. Moon and S. Pyun, *Corros. Sci*, 1997, **39**, 399.
20. S. Real, M. Urquidi-Macdonald and D.D. Macdonald, *J. Electrochem.Soc.*, 1988, **135**, 1633.